Toward a Mass-Limited Catalog of Galaxy Clusters from the Atacama Cosmology Telescope

Adam Douglas Hincks

A DISSERTATION PRESENTED TO THE FACULTY OF PRINCETON UNIVERSITY
IN CANDIDACY FOR THE DEGREE OF DOCTOR OF PHILOSOPHY

RECOMMENDED FOR ACCEPTANCE BY THE DEPARTMENT OF PHYSICS
ADVISER: LYMAN A. PAGE, JR.

SEPTEMBER 2009

Abstract

The Atacama Cosmology Telescope (ACT) is a six meter observatory in the Andes of northern Chile. It is currently in its third season of operation, observing the cosmic microwave background (CMB) with about 1000 detectors each at 148 GHz, 218 GHz, and 277 GHz. Capable of producing high sensitivity maps of the CMB at arcminute resolution, the ACT will contribute to our knowledge of cosmology by constraining the parameters describing the early universe as well as by studying its subsequent evolution. One of the more important tools for investigating the latter will be the Sunyaev-Zel'dovich (SZ) effect, by which large clusters of galaxies leave distinct imprints in the CMB, the strength of which is nearly independent of redshift. In this dissertation, we present maps of the first SZ clusters to be detected by the ACT, showing that we are beginning to reach our objective of creating a large, mass-limited catalog of clusters for probing the growth of structure in the universe. Extensive data analysis is required to produce our CMB maps, so, after describing the telescope itself, much of the dissertation is devoted to presenting some of the mapmaking elements. In particular, we have developed a pipeline which specializes at removing atmospheric contamination from the data to produce small, clean maps suitable for cluster analysis. It has also been used to make high precision beam maps, crucial for interpreting all of the measurements made by the ACT.

הַשָׁמַ֗יִם מְֽסַפְּרִ֥ים כְּבֽוֹד־אֵ֑ל
וּֽמַעֲשֵׂ֥ה יָ֝דָ֗יו מַגִּ֥יד הָרָקִֽיעַ

The heavens catalog the glory of God,
And the expanse makes known the work of his hands.

Acknowledgments

An famous Oxford don believed that the relationship between a professor and his protégé should not to be that of schoolmaster and pupil, but rather that of collaborators. “The student is, or ought to be, a young man who is already beginning to follow learning for its own sake, and who attaches himself to an older student, not precisely to be taught, but to pick up what he can. From the very beginning the two ought to be fellow students.”[1] I have been fortunate to have many outstanding “fellow students” during my academic career and it is a pleasure to offer my deep gratitude to them here.

My interest in cosmology matured as an undergraduate at the University of Toronto, much of it due to the enthusiasm and cheerfulness of Barth Netterfield, in whose lab I worked for two summers. Dick Bond and Carlo Contaldi were also important influences during my work with them at CITA.

When I arrived at Princeton, I was fairly certain I wanted to work with Lyman Page. My experience over five years has confirmed the wisdom of this initial inclination. He has given me the latitude to pursue my own interests within the bounds of our research, but at the same time has been eminently available, given insightful guidance, and always offered encouragement when most needed. I particularly thank him and his wife Lisa for their hospitality during the last few weeks of my work on this dissertation.

Formally I have had one doctoral advisor, but informally I have had several, at Princeton and beyond. I have very much enjoyed working with Mark Devlin, Joe Fowler, Mark Halpern, Norm Jarosik, Jeff Klein, Michele Limon, and Suzanne Staggs, all of whom have taught me a great deal. Their collective experience coupled with generous personalities have been indispensable to my growth as a researcher.

I have had the good luck of having wonderful officemates over the years: Asad Aboobaker, Ryan Fisher, Judy Lau, Toby Marriage, Mike Niemack, and Eric Switzer. Additionally, there are many members of our project with whom I have worked closely: Paula Aguirre, John William Appel, Elia Battistelli, Sudeep Das, Jo Dunkley, Rolando Dünner-Planella, Tom Essinger-Hileman, Amir Hajian, Matt Hasselfield, Madhuri Kaul, Danica Marsden, Mike “Dr. No” Nolta, Lucas Parker, Jon Sievers, David Spergel, Omelan Stryzak, Dan Swetz, Bob Thornton, and Yue Zhao. I have spent a lot of quality time at close quarters with most of these fine people in the field, and can truly say that I enjoy the company of each and every one of them.

From the wider collaboration I have benefited from interactions with Viviana Acquaviva, Mandana Amiri, Ben Brown, Bryce Burger, Jay Chervenak, Sarah Denny, Simon Dicker, Randy Doriese, Carlos Hernández-Monteagudo, Gene Hilton, Renée Hlozek, Anson Hook, Kevin Huffenberger, David Hughes, Jack Hughes, Polo Infante, Kent Irwin, Raul Jiminez, Jean-Baptiste Juin, Arthur Kosowsky, Yen-Tin Lin, Bob Margolis, Krista Martocci, Robert Lupton the Good, Felipe Menanteau, Harvey Moseley, Bruce Partridge, Beth Reid, Audrey Sederberg, Neelima Sehgal, Hy Trac, Licia Verde, Katerina Visnjic, and Ed Wollack.

I thank the staff in the department at Princeton whose assistance has been a great help through the years, particularly Claude Champagne, Angela Glenn, Laurel Lerner, Mike Peloso, Marixa Reyes, and John Washington.

[1] C. S. Lewis, “Our English Syllabus” in *Rehabilitations and Other Essays*, Oxford University Press, 1939.

I would be remiss not to mention our colleagues from Dynamic Structures and KUKA robotics, particularly those with whom I worked most closely: Walter Brzezik, Mike Cozza, Jeff Funke, Mel Yargeau, and Ye Zhou. Additionally, I thank the members of ALMA, ASTE, CBI/QUIET, NANTEN2, Astro-Norte, and APEX who gave much informal support in the field in Chile and are too many to list by name here.

I remember with fondness my two visits to the summer schools in South Africa, for which I received funding from the NSF PIRE program. I thank our collaborators Matt Hilton, Kavilan Moodley, Ryan Warne, and all of their fellow-organizers who helped make these trips so memorable. *Nkosi sikelel' iAfrika.*

I have been blessed with many friends in Princeton and, though sorely tempted, I cannot mention them all here. I will, however, give special thanks to Philip Eckhoff, Sam Feng, Nik Pavlov, Eric Switzer, and Tom Zanker, with whom I lived at various times in the past four years. Their friendship and good company have meant a great deal to me.

I gratefully acknowledge financial support from the Natural Sciences and Engineering Research Council of Canada, the United States' National Science Foundation (via a grant to the Princeton Gravity Group), and Princeton University.

The first school is the home and my most important teachers have been my family members, especially my parents. They have always given me the freedom to pursue my interests, and their love and support continues to help me become more fully alive.

Preface

When I arrived in Princeton in the autumn of 2004, the Atacama Cosmology Telescope (ACT) had just been funded by the National Science Foundation (NSF) and a contract for its construction awarded to AMEC Dynamic Structures. A vigorous campaign of detector fabrication and characterization for this new project was well underway and prototype cryogenic systems for cooling them to 300 mK were being developed. Now, as I reach the end of my doctoral program, the telescope is in the middle of its third season of observations, and we recently released our very first astrophysical results. Thus, I have had both the good fortune and the privilege of working on this project from the initial stages through to its fruition, and I have been involved in everything from instrumentation to analysis of celestial maps.

Much of the work that goes into an experiment is not of interest to the wider world. The substantial amount of time spent running cables, soldering, computer programming, pumping diesel, and so on, while necessary for the project and often rewarding in of itself for the laborer, cannot be represented with commensurate length in a scientific treatise. Consequently, I devote the majority of this dissertation to the data analysis I have worked on over the past year and a half. A project like the ACT is collaborative by its very nature, and I have done nothing in complete isolation from the rest of the group. Nevertheless, I have generally only included material which is substantially my own work, and have attempted to acknowledge specific contributions from colleagues whenever possible throughout the text.

This dissertation is structured to lead from a general understanding of the telescope hardware to our first measurements of distant clusters of galaxies. The first chapter is an introduction to the scientific motivation for the project and also provides an overview of the telescope and its receiver. Chapter 2 describes some of the control and data acquisition systems which I helped to realize. Chapter 3 is about low-level data analysis and Chapter 4 outlines the mapmaking algorithm I developed for the ACT data. Maps from this pipeline are used in Chapter 5 to make precision measurements of the telescope beam pattern, and in Chapter 6 for studying point sources and clusters of galaxies.

Large portions of the final two chapters are based on our first science paper (Hincks et al., 2009). Some material in the first and second chapter may also be found in Hincks et al. (2008).

Contents

Abstract . . . iii
Acknowledgments . . . vii
Preface . . . ix
List of Figures . . . xiv
List of Tables . . . xvii

1 Introduction **1**
1.1 Relict Radiation . . . 1
1.1.1 Hot and Cold Spots in the CMB . . . 2
1.1.2 Primary CMB Anisotropies . . . 3
1.1.3 Secondary CMB Anisotropies . . . 5
1.1.4 The Sunyaev-Zel'dovich Effect . . . 6
1.1.4.1 The Thermal SZ Effect . . . 6
1.1.4.2 The Kinematic SZ Effect . . . 8
1.1.4.3 Detection Limits . . . 9
1.1.5 Science from the Sunyaev-Zel'dovich Effect . . . 10
1.1.5.1 Distance Measurements and The Hubble Constant . . . 10
1.1.5.2 Gas Mass Fractions . . . 11
1.1.5.3 Peculiar Velocities . . . 11
1.1.5.4 Growth of Structure . . . 11
1.1.5.5 Manifestation in the Angular Power Spectrum . . . 13
1.2 The Atacama Cosmology Telescope . . . 14
1.2.1 Telescope Structure . . . 14
1.2.2 Detectors & Camera . . . 15
1.2.3 Site . . . 17
1.2.4 Commissioning History . . . 19
1.2.5 Summary of Data from First and Second Seasons (2007–2008) . . . 21

2 Telescope Control, Housekeeping and Data Acquisition **29**
2.1 Overview of Telescope Systems . . . 29
2.1.1 The Receiver and its Readout: the MBAC and MCE . . . 30
2.1.2 Fast Housekeeping and Control: the BLAST DAC . . . 32
2.1.2.1 Cryogenic Thermometers . . . 33
2.1.2.2 Cryogenic Heaters . . . 34
2.1.2.3 Ambient Instruments: Accelerometers, LVDT's, Magnetometer, Pressure Sensor . . . 34
2.1.3 Encoders . . . 34
2.1.4 Slow Housekeeping: ABOB . . . 34
2.1.5 Miscellaneous Readout . . . 35
2.2 Telescope Motion . . . 35
2.2.1 The Control System . . . 36

2.2.2 Motion Quality . . . 37
2.3 Timing and Synchronization of Data Acquisition . . . 37
2.3.1 Systems for Synchronization and Absolute Timing . . . 38
2.3.2 Evaluation of Timing Performance . . . 41
2.4 Software and Data Flow . . . 42
2.4.1 Data Acquisition Software . . . 42
2.4.1.1 MCE Acquisition Software . . . 42
2.4.1.2 Housekeeping Software . . . 44
2.4.2 Merging . . . 45
2.4.3 Data Flow and File Tracking . . . 45
2.4.4 Control and Monitoring Software . . . 46

3 Time Stream Analysis **47**
3.1 Time Stream Preprocessing . . . 47
3.1.1 Fourier Domain Deconvolutions and Downsampling . . . 47
3.1.2 Dark Mode Removal . . . 49
3.2 Detector Time Constant Measurements . . . 50
3.3 Pointing . . . 54
3.3.1 Measuring Pointing Offsets from Planet Observations . . . 55
3.3.2 Robust Determination of Relative Detector Pointing Offsets . . . 56
3.4 Gain Calibration . . . 60

4 Mapmaking **63**
4.1 Understanding the Mapmaking Equation . . . 63
4.2 The Cottingham Method . . . 65
4.2.1 The Algorithm . . . 65
4.2.2 The Algorithm in Component Notation . . . 67
4.2.3 What the Cottingham Method Does and Why it Works . . . 68
4.2.4 B-Splines and Atmosphere-Celestial Covariance . . . 70
4.2.5 Spatial Structure in the Atmosphere . . . 71
4.3 Implementation and Evaluation of the Cottingham Method . . . 73
4.3.1 Implementation . . . 73
4.3.2 Performance . . . 75
4.4 Making Sky Maps . . . 77
4.4.1 TOD Maps . . . 77
4.4.2 TOD Map Post-Processing . . . 79
4.4.3 Map Coaddition . . . 79
4.5 Data Pipeline Summary . . . 80

5 Beams & Calibration **81**
5.1 Beam Theory . . . 81
5.1.1 The Instrument Response in Real Space . . . 81
5.1.2 The Instrument Response in Spherical Harmonic Space . . . 83
5.1.3 Characterizing the Beam Function . . . 84
5.1.3.1 Important Properties of the Airy Pattern . . . 84
5.1.3.2 Measuring the Beam . . . 85
5.2 Beam Measurements . . . 87
5.2.1 Observations and Data Reduction . . . 87
5.2.2 Results . . . 87
5.2.2.1 Beam Maps and Profiles . . . 87
5.2.2.2 Beam Central Regions . . . 91
5.2.2.3 Solid Angles . . . 92

5.2.2.4 Window Functions 94
5.2.3 Beam Measurements and Reflector Panel Alignment 95
5.2.4 Physical Beam Sizes 95
5.3 Temperature Calibration 97
5.3.1 Planet Brightnesses and Atmospheric Opacity 97
5.3.2 Measurements 97

6 Galaxy Clusters & Point Sources **101**
6.1 Data Processing 101
6.1.1 Cluster Discovery in Survey Maps 101
6.1.2 Mapmaking & Calibration 102
6.1.3 Point Source Maps for Absolute Pointing 102
6.2 Clusters 104
6.2.1 Maps and Basic Properties 104
6.2.1.1 Cluster Mapping at 218 GHz and 277 GHz 105
6.2.2 Analysis 105
6.2.2.1 Significance of Detections 105
6.2.2.2 Integrated Compton-y Values 109
6.2.2.3 Attempts at Profile Fitting 112
6.2.3 Comparisons with Previous Measurements 114
6.2.3.1 ACT-CL J0330−5228 (Abell 3128) 114
6.2.3.2 ACT-CL J0658−5556 (1E 0657−56) 115
6.2.3.3 South Pole Telescope Clusters 116
6.2.3.4 Comparing Integrated Compton-y Values 117
6.2.4 Discussion 117
6.3 Point Sources 118
6.3.1 The Bright Radio Sources PMN J0540−5418 and PMN J0549−5246 119
6.3.2 An Infrared Point Source Near ACT-CL J0509−5345? 120
6.4 Conclusions 122

List of Figures

1.1 Measurements of the CMB angular power spectra. . . . 4
1.2 The SZ spectrum. . . . 7
1.3 Errors incurred with the non-relativistic SZ approximation. . . . 9
1.4 Estimated mass limits for SZ cluster detectability by the ACT. . . . 10
1.5 Cluster counts per solid angle as a function of redshift. . . . 12
1.6 Contributions by secondary CMB effects to the angular power spectrum. . . . 13
1.7 The ACT structure and optics. . . . 14
1.8 Photographs of ACT detectors and cameras. . . . 16
1.9 A photograph and schematic of the MBAC. . . . 17
1.10 Site location and landscape. . . . 18
1.11 Atmospheric conditions at the ACT site. . . . 19
1.12 Alignment quality of the primary and secondary reflectors. . . . 20
1.13 Summary of data hours logged in 2007 and 2008. . . . 21
1.14 Map of ACT observing regions. . . . 22
1.15 The ACT in front of Cerro Toco. . . . 24
1.16 The ACT site. . . . 25
1.17 The ACT from afar and close up. . . . 25
1.18 The primary and secondary reflectors. . . . 26
1.19 Inside the Receiver Cabin. . . . 27
1.20 Inside the Equipment Room. . . . 27
1.21 Motion hardware. . . . 28

2.1 A diagram of the ACT readout and control systems. . . . 31
2.2 A block diagram of the BLAST DAC housekeeping systems. . . . 32
2.3 The BLAST DAC digital filter gain. . . . 33
2.4 Encoder readings and derived quantities during an azimuth scan at 2 $\mathrm{deg\,s^{-1}}$. . . . 38
2.5 A block diagram of the data synchronization and timing components. . . . 39
2.6 A flowchart showing how data synchronization occurs. . . . 40
2.7 Timing uncertainty of the sync serial number interrupt handling in the housekeeping computer. . . . 42
2.8 A diagram of data acquisition and file tracking software. . . . 43

3.1 The gain and phase of the MCE digital filter. . . . 48
3.2 Detector data before and after deconvolving the MCE filter and time constants. . . . 48
3.3 Detector data before and after dark mode removal. . . . 51
3.4 Simulated detector responses for different optical time constants. . . . 53
3.5 Comparison of time constant measurement techniques. . . . 54
3.6 The distribution of detector time constants in the three arrays. . . . 55
3.7 A cartoon of a planet observation. . . . 56
3.8 The relative detector pointing offsets for the three arrays in 2008. . . . 58
3.9 An atmospheric flat-fielding calibration. . . . 60

4.1 Spectral densities for time streams with different atmospheric PWV's. 64
4.2 A cartoon showing how the Cottingham Method works. 69
4.3 B-spline basis functions for three different polynomial orders. 70
4.4 A cartoon of how the Cottingham Method can induce large scale spatial gradients. . 72
4.5 The sub-arrays defined within the 32×32 detector array to accommodate spatial variations in the atmosphere. 73
4.6 Hit statistics for a typical map. 74
4.7 Examples of the Cottingham Method atmosphere removal. 76
4.8 Measurements of the Cottingham Method fit quality and speed. 77
4.9 A study of the Cottingham fit quality as a function of the total fraction of data points included. 78

5.1 The beam coordinate system. 82
5.2 Beam maps for the three arrays. 88
5.3 Symmetrized beam profiles and solid angles for the three arrays. 89
5.4 Beam profiles and wing fits of the quadrants of the 148 GHz map. 91
5.5 Plots of the beam centers with overlaid FWHM ellipses. 92
5.6 Measured solid angle uncertainty estimates. 93
5.7 The window functions for the three arrays. 94
5.8 The beam shape after sunrise. 95
5.9 The physical size of the beam. 96
5.10 Data used for 148 GHzcalibration from Saturn and Uranus observations. 98

6.1 Nightly boresight pointing variations. 103
6.2 Cluster maps. 106
6.3 Maps of ACT-CL 0329−5226 in three frequencies. 108
6.4 Radial temperature and integrated Compton-y profiles for ACT-CL J0638−5358. . . 111
6.5 Results of β-profile fits to simulated maps. 113
6.6 Maps of ACT-CL J0330−5228 and ACT-CL J0658−5556 with superimposed X-ray and lensing contours. 115
6.7 Maps showing our non-detection of SPT-CL 0528−5300. 116
6.8 Comparison of predicted and measured integrated-Y values. 117
6.9 Spectra of three point sources observed by the ACT. 119
6.10 Maps of the point source ACT-PS J0509-5337. 121

List of Tables

1.1 Most recent WMAP Cosmological Parameters 6
1.2 ACT Design Parameters 15
1.3 Filter bandpass parameters. 18
1.4 ACT survey regions. 21
1.5 Planet Observations in 2008. 23

2.1 Data sources and rates. 30
2.2 Sources of Timing Errors 41

3.1 Time stream low-pass filter parameters. 49
3.2 A list of important astrometric reductions. 57
3.3 Some basic parameters of the detector relative pointing offsets. 59

5.1 A summary of beam parameters. 88
5.2 Mask and domain sizes used for the 148 GHz wing fit. 90
5.3 Wet and dry components of the atmosphere opacity model. 99
5.4 Saturn and Uranus calibration results. 99

6.1 Coordinates, catalog names, and basic properties of ACT SZ clusters. 104
6.2 Measured properties of ACT SZ clusters. 110
6.3 Literature references for known cluster data. 114
6.4 Flux measurements of three ACT point sources. 119

Chapter 1

Introduction

1.1 Relict Radiation

The night sky at visible frequencies appears inhomogeneous. Light comes from many discrete sources—planets, stars, galaxies—separated by dark voids. This may be contrasted with the millimeter sky, which is remarkably uniform in intensity in all directions. When Penzias & Wilson (1965) discovered this fact at 3 GHz they were initially puzzled, but Dicke et al. (1965) immediately recognized that this "microwave background" might be cosmic in origin. If it was homogeneous and isotropic, they reasoned, it might well have been emitted at an earlier epoch of the universe when the distribution of matter was itself homogeneous and isotropic. In fact, the existence of such "relict radiation"[1] had been predicted more than a decade earlier (Alpher & Herman, 1948).

If the hypothesis of Dicke et al. (1965) was correct, the microwave background would be thermal in origin and described by a blackbody spectrum:

$$n(\nu)\mathrm{d}\nu = \frac{8\pi}{c^3}\frac{\nu^2\,\mathrm{d}\nu}{e^{h\nu/k_BT}-1}, \tag{1.1}$$

where n is the number density of photons between frequencies ν and $\nu+\mathrm{d}\nu$, h is Planck's constant, k_B is the Boltzmann constant, and T is the temperature of the emitter. Ground-based observations through the 1970's and 1980's showed that the microwave background is consistent with a blackbody spectrum in the Rayleigh-Jeans regime (i.e., $h\nu \ll k_BT$). Later, rocket and balloon observations began probing the shorter wavelengths to show that the spectrum turns over as predicted by Eq. 1.1, but it was the FIRAS radiometer on the Cosmic Background Explorer Satellite (COBE) that conclusively demonstrated to high precision that the spectrum follows a blackbody curve and is therefore almost certainly the relict radiation (Mather et al., 1990).

FIRAS measured a blackbody temperature of (2.725 ± 0.002) K (Mather et al., 1999). However, the cosmic microwave background (CMB), as it has become known, was emitted at a period when the universe was smaller, denser, and hotter. The primordial plasma had cooled enough to neutralize, allowing photons to free-stream for the first time. This epoch is known as the period of "recombination" or "decoupling". The photons have travelled to us in a Friedmann-Lemaître-Robertson-Walker (FLRW) metric:[2]

$$\mathrm{d}s^2 = \mathrm{d}t^2 - a(t)\left(\frac{r^2\mathrm{d}r^2}{1-Kr^2} + \mathrm{d}\Omega^2\right), \tag{1.2}$$

[1] Iosif Shklovsky coined this expression in the 1960's (Peebles et al., 2009). A related term is the "fossil radiation".

[2] It can be proved that the spatial part of the FLRW metric is the unique descriptor of an isotropic and homogeneous universe (Weinberg, 1972). The CMB is an excellent confirmation that the principles of isotropy and homogeneity are a sound basis for cosmology.

where $K = 0, 1, -1$ for a flat, closed, or open geometry, respectively, r and Ω are spherical coordinates for 3-space, and $a(t)$ is a *scale factor* giving the size of the metric as a function of time. The scale factor is usually defined so that $a_0 \equiv a(t_0) = 1$; the zero subscript (on any variable hereafter) denotes the value today. The relation between the scale factor and cosmological redshift is:[3]

$$\frac{\nu_0}{\nu_e} = \frac{a_e}{a_0} = \frac{1}{1+z}, \tag{1.3}$$

where ν_e is the wavelength when the signal was emitted, and z is usually simply called the "redshift".

Because densities in the FLRW metric scale as a^{-3}, the number density today of photons emitted during recombination is:

$$n_0(\nu_0)\,\mathrm{d}\nu \;=\; \frac{n_*(\nu_* a_*)}{a_*^3}\,\mathrm{d}\nu\, a_* \;=\; \frac{n_*(\nu_* a_*)\,\mathrm{d}\nu}{a_*^2} \tag{1.4}$$

where the subscripted asterisk denotes the time of recombination. With Eq. 1.1, this implies that the blackbody spectrum has not changed shape, but has only shifted to a new temperature $T_0 = T_*/a_*$. Plasma physics calculations show that $T_* \approx 3000\,\mathrm{K}$ (e.g., Weinberg, 2008), so the CMB comes from a time when $a \approx 10^{-3}$, or a redshift of $z \approx 1100$.

1.1.1 Hot and Cold Spots in the CMB

The CMB is a nearly perfect blackbody, but it does have spatial variations in the temperature due to slight over- and under-densities in the primordial plasma. These are ascribed to quantum fluctuations in the very early universe that were smoothed down to minute amplitudes during a putative early period of rapid growth called inflation. COBE measured an rms temperature variation of $30\,\mu\mathrm{K}$ at 10° scales (Bennett et al., 1996): in other words, the fluctuations are miniscule compared to the CMB temperature—about 5 orders of magnitude smaller.

The amplitudes of the CMB fluctuations at different angular scales are an important source of cosmological information. They are conveniently studied by decomposition into spherical harmonics:

$$\Delta T(\hat{\mathbf{n}}) = \sum_{\ell m} a_{\ell m} Y_{\ell m}(\hat{\mathbf{n}}) \quad \longrightarrow \quad a_{\ell m} = \iint \mathrm{d}\Omega_{\hat{\mathbf{n}}}\, \Delta T(\hat{\mathbf{n}})\, Y^*_{\ell m}(\hat{\mathbf{n}}), \tag{1.5}$$

where $\hat{\mathbf{n}}$ is a coordinate on the celestial sphere and Y_ℓ^m is a spherical harmonic. The theoretical angular power spectrum is the ensemble average power over all angles m at each multipole ℓ:

$$C_\ell \equiv \left\langle |a_{\ell m}|^2 \right\rangle. \tag{1.6}$$

By "ensemble" we mean all possible universes with their $a_{\ell m}$ drawn from the same statistical distribution. On the sky, it is measured it by averaging the amplitudes $a_{\ell m}$:

$$C_\ell = \frac{1}{2\ell+1} \sum_{m=-\ell}^{+\ell} |a_{\ell m}|^2. \tag{1.7}$$

Assuming that the statistics of the CMB are fully described by the angular power spectrum, then the variance of the temperature fluctuations at multipole ℓ is conventionally given by:[4]

$$(\Delta T_\ell)^2 = \frac{\ell(\ell+1)C_\ell}{2\pi}. \tag{1.8}$$

[3] It is assumed, of course, that a is increasing with time, otherwise the cosmological frequency shift would be blue.

[4] This does not directly follow from Eqs. 1.5–1.7. One factor of ℓ makes the spectrum flat on logarithmic intervals, and there is a factor of two that is artificially drawn outside of the parentheses.

Most theories of inflation predict that the primordial spectrum of fluctuations is nearly scale invariant. Deviations from scale-invariance are parameterized by the variable n_s, called the "spectral tilt", defined such that the primordial spectrum in Fourier space is $P \propto k^{n_s-1}$, where k is a wavenumber. If $n_s < 1$, small scales have less power, and the angular power spectrum decreases as ℓ increases. Therefore, comparing small-scale power to large-scale power in the CMB can yield a measurement of n_s. This in turn can be used to discriminate between theories of inflation that exclude certain ranges of n_s. The larger the range of C_ℓ that is measured, the longer of a baseline one has for measuring the spectral tilt and consequently the more accurately it can be measured.

However, there are many physical processes that occurred after the primordial spectrum was set by inflation. These can be categorized into those that occurred before and during recombination, which produce "primary anisotropies" in the CMB, and those that occur afterwards as CMB photons interact with matter in the later universe, producing "secondary anisotropies". We discuss each of these in the following sections.

1.1.2 Primary CMB Anisotropies

Fig. 1.1 shows measurements of the power spectrum, as expressed in Eq. 1.8. Clearly this is not the simple slope one would see if one were measuring a pure power law defined by n_s. The physics of the matter and radiation before and during recombination alters the spectrum, creating what are called "primary anisotropies". Ionized hydrogen and helium atoms, dark matter, and radiation are all coupled together into a hot, dense plasma. Gravitation works to attract mass-energy into regions of overdensity, but pressure tends to inhibit collapse. Neutrinos, which couple only very weakly to the other components, also work to inhibit small scale clustering. The opposing forces of attraction and repulsion set up acoustic oscillations in the plasma. In Fourier space, different modes of oscillation proceed at different rates, causing the spectrum of densities to depend on the wavenumber. The peaks and troughs in the angular power spectrum (c.f. Fig. 1.1) are, roughly speaking, a snapshot of the acoustic modes at the time of recombination. Peaks occur at scales that are maximally compressed or rarefied: the first peak is the mode that has undergone one single compression, the second has compressed and rarefied, and so on. At higher angular scales, the peaks and troughs become damped, due to photon diffusion washing out density fluctuations over short distances.

By comparing the relative positions and amplitudes of the acoustic peaks, the properties of the plasma, particularly its composition, can be deduced. Each of the components—baryonic matter, dark matter, neutrinos, and radiation—couple to gravity in different ways, so this information provides insight into the dynamics of the metric and therefore the evolution of the scale factor $a(t)$.

Let us briefly digress and outline how the different components of energy-density affect cosmology. The solution of Einstein's field equations for the FLRW metric yields two differential equations determining the dynamics of expansion. They depend on the density ρ and pressure p of the sources:

$$H^2 + \frac{K}{a^2} = \frac{8\pi G\rho}{3}, \tag{1.9}$$

$$-3H(\rho + p) = \dot{\rho}, \tag{1.10}$$

where $H \equiv \dot{a}/a$ is the Hubble constant. Eq. 1.9 is called the Friedmann equation, and Eq. 1.10 is a conservation law. For a flat geometry, $K \equiv 0$, and the density in this cosmology, $\rho_c \equiv 3H^2/8\pi G$, is called the *critical density*. Densities can then be written as fractions of the critical density, i.e., $\Omega \equiv \rho/\rho_c$. A useful way to write the Friedmann equation is in terms of the current values of various fractional densities:

$$1 = \Omega_{\Lambda 0} + \frac{\Omega_{K0}}{a^2} + \frac{\Omega_{M0}}{a^3} + \frac{\Omega_{R0}}{a^4}, \tag{1.11}$$

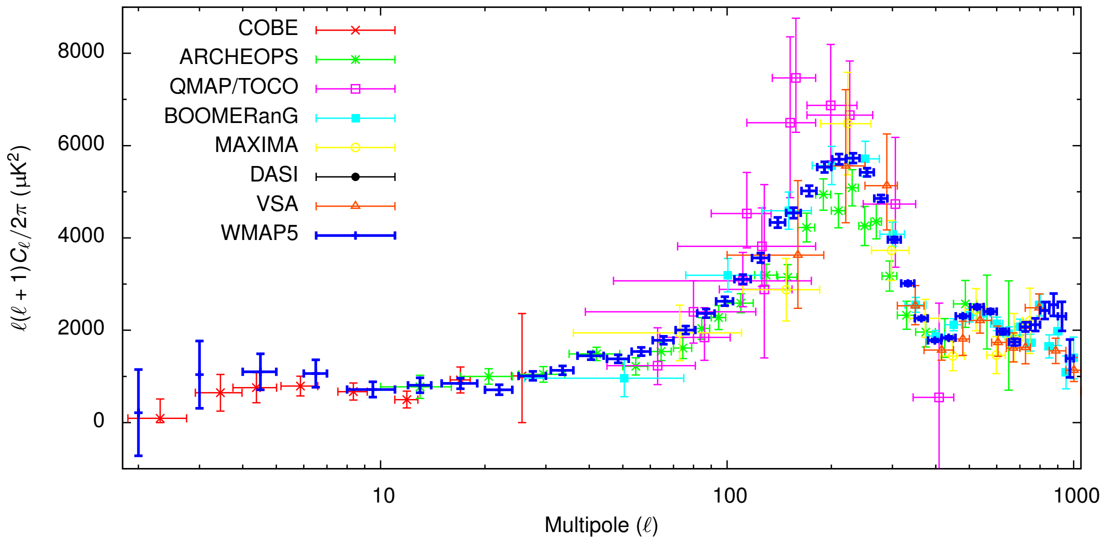

(a)

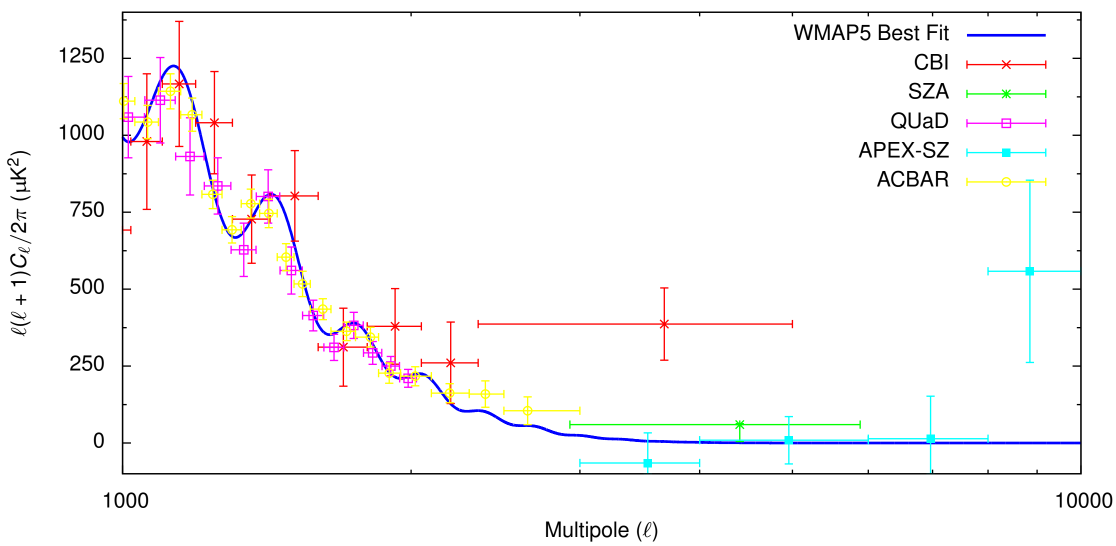

(b)

Figure 1.1: Measurements of the CMB angular power spectrum. We split the ℓ range in two. In (a), measurements of $\ell \lesssim 1000$ are shown, containing the first three peaks. Results from COBE, as well as pioneering ground-based and balloon experiments are shown. The best measurements in this region are now from the five-year WMAP data. The second plot, (b), shows the state-of-the-art for measurements at $\ell \gtrsim 1000$; all of these points have been measured in the last year. For reference, the predicted power spectrum from the most recent WMAP parameters (c.f. Table 1.1) is also plotted. The data in these plots come from: COBE — Tegmark (1996); ARCHEOPS — Tristram et al. (2005); QMAP/TOCO — Miller et al. (2002); BOOMERanG — Ruhl et al. (2003); MAXIMA — Hanany et al. (2000); DASI — Halverson et al. (2002); VSA — Dickinson et al. (2004); WMAP5 — Nolta et al. (2009); CBI — Sievers et al. (2009), downloaded from http://www.astro.caltech.edu/ tjp/CBI/data2009/index.html on 2009-01-28; SZA — Sharp et al. (2009); QUaD — Brown et al. (2009); APEX-SZ — Reichardt et al. (2009b); ACBAR — Reichardt et al. (2009a).

where $\Omega_K \equiv -Ka^{-2}H^{-2}$, and the subscripts M, R and Λ stand for matter (both baryonic and dark), radiation (including relativistic matter such as neutrinos) and dark energy, respectively.

Each of the density terms in Eq. 1.11 changes differently with the scale factor. For matter and radiation, the relations between the density and volume are familiar. Dark energy, on the other hand, is less intuitive. It has only been about a decade since it was realized that it is the largest effective mass-energy component in the universe today (e.g., Bahcall et al., 1999), around the same time that Riess et al. (1998) and Perlmutter et al. (1999) independently concluded, based on observations of high-z Type Ia supernovae, that the universe is accelerating in its expansion. One way to explain this phenomenon is to introduce some sort of "dark energy" behaving like a vacuum energy, which has the property $p_\Lambda = -\rho_\Lambda$. This equation of state, often parameterized by the ratio $w \equiv p/\rho$, implies that the vacuum energy has a repulsive force. Solving Eq. 1.10 with w_Λ yields $\rho_\Lambda \propto a^{-3-3w_\Lambda} \propto a^0$—that is, it has no dependence on the scale factor, just as it is written in Eq. 1.11. When the other mass-energy components drop in density as a increases, the dark energy becomes more important. Therefore, accelerated expansion is a recent cosmological phenomenon.

As we mentioned before, the power spectrum of primary anisotropies can be used to measure all of these components. The location of the first peak as a function of multipole ℓ depends primarily on the curvature Ω_K for a fixed Hubble constant. Conceptually, this is simple: plasma physics predicts the physical scale at which the peak occurs, but the actual angular size on the sky depends on the curvature of space. A series of observations in the late 1990's and early 2000's detected the peak and showed that, to within the uncertainties, $K = 0$ (Miller et al., 1999; Hanany et al., 2000; Mauskopf et al., 2000; Padin et al., 2001; Halverson et al., 2002; Benoît et al., 2003; Goldstein et al., 2003; Scott et al., 2003).

Some of these experiments also measured the second peak and began probing the the third peak, from which $\Omega_b h^2$ and $\Omega_M h^2$ can be determined, where the subscript b is the baryon density and:

$$h \equiv \frac{H_0}{100\,\mathrm{km\,s^{-1}\,Mpc^{-1}}}. \tag{1.12}$$

Additionally, Ω_Λ, affects the low-ℓ portion of the spectrum and the peak locations due to the evolution of the gravitational potential at later times: this is known as the Integrated Sachs-Wolfe Effect (Sachs & Wolfe, 1967). Three final parameters may be measured: the spectral tilt n_S, the optical depth τ between time of recombination and today, and the amplitude of the fluctuations, σ_8. The optical depth is affected by the reionization of gas when stars began forming and its measurement can constrain the epoch at which this occurred. The amplitude of fluctuations is expressed here as σ_8, the rms of matter distribution in linear theory on a scale of $8\,\mathrm{Mpc}\,h^{-1}$ at $z = 0$. This scale is useful because it may be compared to measurements from the nearby universe.

There are degeneracies between some of these parameters when measured from the CMB angular power spectrum. Most notable is that several are scaled by h. Eq. 1.11 helps disentangle the densities. Furthermore, combining CMB data with other datasets, such as large-scale galaxy surveys or supernovae surveys, is important for obtaining better constraints.

The ground-based and balloon experiments mentioned above made excellent process at measuring the parameters we have just outlined. With the release of the first results from the space-based Wilkinson Microwave Anisotropy Probe (WMAP) (Bennett et al., 2003), a new level of precision was achieved. WMAP has continued observing, and at $\ell \lesssim 1000$, still provides the gold-standard for angular power spectrum measurements. Table 1.1 shows its most recent list of parameters (Hinshaw et al., 2009).

1.1.3 Secondary CMB Anisotropies

Today there are two frontiers for CMB experiments. One of them, not a topic of this dissertation, is the polarization of temperature anisotropies. In particular, the divergence-free modes of polar-

Table 1.1: Most recent WMAP Cosmological Parameters

Parameter	Symbol	Value
Hubble parameter	H_0	$70.5 \pm 1.3\,\mathrm{km/s/Mpc}$
Baryon density	Ω_b	0.0456 ± 0.0015
Dark matter density	Ω_M	0.228 ± 0.013
Dark energy density	Ω_Λ	0.726 ± 0.015
$8h^{-1}$ Mpc density rms	σ_8	0.812 ± 0.026
Spectral index	n_s	0.960 ± 0.013
Optical depth	τ	0.084 ± 0.016

[a] Best fit values for WMAP with baryon acoustic oscillation data and supernova data, taken from Hinshaw et al. (2009).

ization, which currently only have measured upper limits, will provide important information about inflation, if it occurred. The other frontier lies at small angular scales, roughly $\ell \gtrsim 1000$, or arcminute angles. It is these scales that the Atacama Cosmology Telescope (ACT) is designed to measure. The ACT is introduced in §1.2, after we outline the science that small-scale CMB information can yield.

High-ℓ measurements help place better constraints on the parameters listed in Table 1.1. They should significantly improve the precision of the primordial spectral tilt value n_S because of the much longer baseline in ℓ-space they provide. With this extra information, more complex (and potentially more realistic) models might be fit. A popular modification of the power law $P \propto k^{n_s-1}$ makes the exponent vary with scale size by introducing a parameter characterizing the "running" of the spectral index, $\alpha \equiv \mathrm{d}n_s/\mathrm{d}\log k$ (Kosowsky & Turner, 1995).

In addition to containing information on traditional cosmological parameters, at high resolution features in the CMB include "secondary" effects become evident in the CMB. They are so-called because they are due to the interaction of CMB radiation with intervening matter after the epoch of recombination. (Two effects that might be considered secondary but are important at low-ℓ were mentioned in §1.1.2: the ISW and the contribution of reionization to the optical depth τ.)

One of the secondary effects that becomes prominent at high resolutions is weak gravitational lensing (Blanchard & Schneider, 1987; Seljak, 1996). CMB photons are deflected by over- and under-densities of matter as they free-stream through the universe. The result is that the primary anisotropies are distorted in a way that should be statistically measurable. Typical sizes of deflections are $\sim 2'$, although they are coherent on degree scales. In the power spectrum, they contribute more power than primary anisotropies at $\ell \gtrsim 3000$ (e.g., Lewis & Challinor, 2006). Because lensing in the CMB is sensitive to the growth of structure, it could be a useful probe for constraining dark energy models. The ACT should be able to detect gravitational lensing, but it is not a topic of this dissertation. Das (2008) has more discussion on CMB lensing and its possible detection by the ACT.

A second secondary signature is due to the inverse scattering of photons by hot electrons in galaxy clusters (Sunyaev & Zel'dovich, 1970, 1972), known as the Sunyaev -Zel'dovich (SZ) effect. It has the useful property that it has a distinct wavelength dependence, making it possible to distinguish from other CMB features. In the next section we describe the SZ effect and the science it has the potential to reveal.

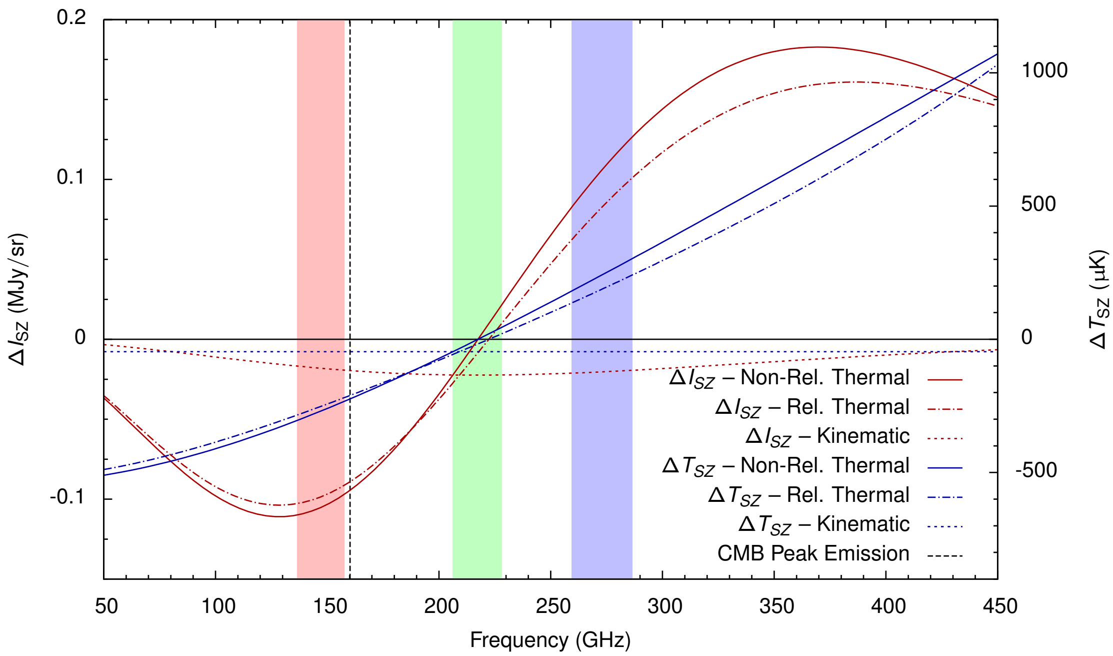

Figure 1.2: The SZ spectrum, in units of both specific intensity change (Eq. 1.17) and CMB temperature change (Eq. 1.13), for $y = 1 \times 10^{-4}$ and $k_B T_e = 10\,\mathrm{keV}$. The solid curves and the dashed-dotted lines show the thermal SZ spectrum for the non-relativistic model (Eq. 1.16) and a precise approximation of the fully relativistic effect from Itoh et al. (1998), respectively. The dotted lines show the kinematic SZ effect assuming the cluster has a receding peculiar velocity of $1000\,\mathrm{km\,s^{-1}}$. Also shown are the ACT frequency bands, centered at 148 GHz, 218 GHz, and 277 GHz, as well as the frequency of peak CMB brightness at 160 GHz. Note that the temperature changes in the ACT 148 GHz and 277 GHz bands have about the same amplitude.

1.1.4 The Sunyaev-Zel'dovich Effect

1.1.4.1 The Thermal SZ Effect

The SZ effect causes a temperature change $\Delta T_{\rm SZ}$ in the CMB temperature proportional to the gas pressure in the cluster of galaxies (assuming the ideal gas law holds). It is given by:

$$\frac{\Delta T_{\rm SZ}}{T_{\rm CMB}} = \int \mathrm{d}r \, \frac{k_{\rm B} T_e}{m_e c^2} \, n_e \sigma_T f(x, T_e), \tag{1.13}$$

where the dr is along the line of sight, T_e, m_e, and n_e are the temperature, mass, and number density of ionized electrons, σ_T is the Thomson cross-section, and $f(x, T_e)$ is the frequency dependence in terms of the dimensionless parameter

$$x \equiv h\nu / k_{\rm B} T_{\rm CMB} = \nu / (56.78\,\mathrm{GHz}). \tag{1.14}$$

The frequency-independent part of Eq. 1.13 is called the Compton-y parameter:

$$y \equiv \int \mathrm{d}r \frac{k_{\rm B} T_e}{m_e c^2} n_e \sigma_T. \tag{1.15}$$

Note that f and y cannot be disentangled if T_e varies with z. In practice, however, the approximation $\Delta T_{\rm SZ} / T_{\rm CMB} = f(x) y$ is often used. Moreover, in the non-relativistic case, f has no dependence on T_e:

$$f_{NR}(x) = x\frac{e^x+1}{e^x-1} - 4 = x\coth(x/2) - 4. \tag{1.16}$$

It is common to express the SZ effect in terms of specific intensity:

$$\begin{aligned}\frac{\Delta I_{\rm SZ}}{I_0} &= \left(\frac{\mathrm{d}I}{\mathrm{d}T}\right)\left(\frac{\Delta T_{\rm SZ}}{T_{\rm CMB}}\right)\left(\frac{T_{\rm CMB}}{I_0}\right)\\ &= \left[\frac{2k_{\rm B}\nu^2}{c^2}\frac{x^2e^x}{(e^x-1)^2}\right][f(x)\,y]\left(\frac{h^2c^2}{2\,k_{\rm B}^3T_{\rm CMB}^2}\right)\\ &= g(x)y\end{aligned} \tag{1.17}$$

where we used the blackbody spectrum of Eq. 1.1 to evaluate the derivative after the first equality, defined $I_0 = 2k_{\rm B}^3T_{\rm CMB}^3/(hc)^2$, and grouped the spectral dependence into a single factor:

$$g(x) \equiv \frac{x^4e^x}{(e^x-1)^2}f(x). \tag{1.18}$$

Fig. 1.2 plots the SZ spectrum in units of specific intensity as well as CMB temperature. There is only one point on the plot at which there is no temperature change, called the "SZ null". Below the null frequency the CMB intensity decreases, while above it increases. It is this spectral property that makes the SZ effect characteristic if observations are made in multiple frequency bands. The number density of CMB photons is conserved, but the inverse Thomson scattering tends to kick lower energy CMB photons to higher energies: hence the deficit of CMB intensity at low frequencies and the excess at high frequencies.

In general, the cluster gas is hot ($>$ 1keV) and relativistic treatment is required for good accuracy in SZ calculations (Rephaeli, 1995). The relativistic corrections have two consequences: first, they shift the frequency of the SZ null, and second, they decrease the predicted intensity change. The frequency of the SZ null is, to first order in T_e and adequate for $k_BT_e < 20$ keV (Birkinshaw, 1999):

$$\nu_{\rm null} = \left(1 + \frac{1.13k_BT_e}{m_ec^2}\right) \times 217\,\mathrm{GHz}. \tag{1.19}$$

Since the bandwidth of the ACT's 218 GHz camera is 22 GHz, it comfortably covers the range of null frequencies for $k_BT_e < 20$ keV. On the other hand, the intensity change is important for hot clusters in the ACT's 148 GHz and 277 GHz bands. The 10 keV example plotted in Fig. 1.2 shows that the difference between the non-relativistic spectrum and a more accurate spectrum is not negligible. Fig. 1.3 plots the fractional error that results from the use of the non-relativistic formula as a function of cluster temperature, for these two frequency bands. For 277 GHz, the relativistic correction is important even for lower temperatures, while in the 148 GHz band, the error only reaches 10% at temperatures of about 14 keV.

For Fig. 1.3 we used an analytic series from Itoh et al. (1998) for approximating the exact SZ scattering equations. More recent results (e.g., Shimon & Rephaeli, 2004; Itoh & Nozawa, 2004) allow for analytic, if not cumbersome, calculations of the SZ signal to high precision for a wide range of frequencies and cluster temperatures. The caveat is that as the cluster temperature cannot be deduced from the SZ signal alone, one must rely on observations in other wavelengths in order to benefit from a precise, relativistic treatment.

1.1.4.2 The Kinematic SZ Effect

The bulk motion of a cluster creates an additional, distinct spectral distortion in the CMB. In the rest frame of the electrons, the CMB radiation appears anisotropic and the inverse-Thomson

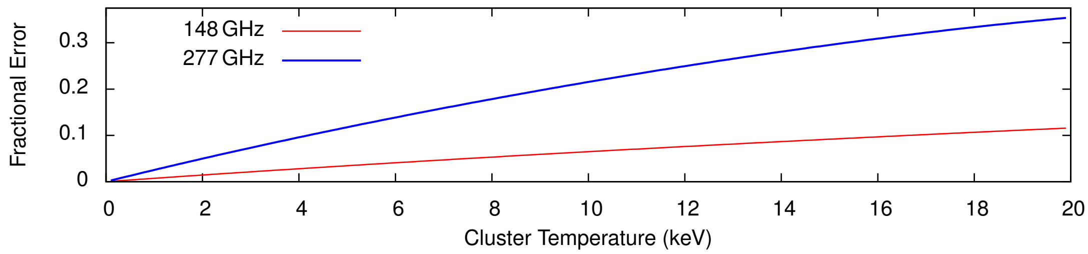

Figure 1.3: The fractional error incurred with the non-relativistic SZ approximation as a function of cluster temperature. The error is shown at the band centers of the two ACT cameras that are sensitive to the SZ decrement and increment. These curves were calculated with the expansion of Itoh et al. (1998) and are accurate to better than 1% for most of the range. (Above 15 keV, the 277 GHz curve is accurate to better than 5%.)

scattering slightly isotropizes it. In comoving coordinates, the effect is to lower (raise) the CMB temperature if a cluster is moving away (toward) the observer along the line of site. Thus, it is called the kinematic SZ (kSZ) effect.[5] In the non-relativistic regime, the temperature and intensity changes are:

$$\frac{\Delta T_{\rm SZ}}{T_{\rm CMB}} = -\tau_e \frac{v_z}{c} \tag{1.20}$$

$$\frac{\Delta I_{\rm SZ}}{I_0} = -\tau_e \frac{v_z}{c} \frac{x^4 e^x}{(e^x - 1)^2}, \tag{1.21}$$

where $\tau_e = \int dz\, n_e \sigma_T$ is the optical depth through the cluster.

An example of the kSZ effect is included in Fig. 1.2. Because of its distinct spectrum, the kSZ signal can be separated from the SZ. This is easiest at the SZ null where the thermal effect vanishes; therefore, for the ACT, the 218 GHz channel is most relevant for measuring the kinematic component. As it has a much smaller signature, great sensitivity is required. The example in Fig. 1.2 has a fairly large signal ($-46\,\mu$K) for the kSZ effect, deliberately chosen so that it would be readable in the plot. Its size is due to the a high Compton-y value (1×10^{-4}) and large velocity ($1000\,\mathrm{km\,s^{-1}}$).

1.1.4.3 Detection Limits

One of the most compelling features of the SZ effect is that the strength of the signal is relatively independent of redshift. Because the source of the radiation is the surface of last scatter rather than the clusters themselves, the signal does not decrease with the luminosity distance. Another way of understanding this is that although the luminosity distance increases as $(1+z)^4$ (e.g., Weinberg, 2008), the energy density of the CMB also increases as $(1+z)^4$ and the two effects cancel out.

Typical cluster sizes range from about 1–10 Mpc. In a standard ΛCDM cosmology, the angular diameter distance peaks at about 1.75 Gpc at $z \approx 1.75$ and decreases gently at higher redshifts. Thus, a 1 Mpc cluster will subtend at least $2'$, meaning that most clusters will be at least partly resolved in all three of the ACT's frequency bands, which have full-widths at half-maxima (FWHM) of $1.37'$ (148 GHz), $1.01'$ (218 GHz) and $0.91'$ (277 GHz)—see §5.2. Whereas the detectability of unresolved sources depends only on the instrumental sensitivity and the flux of emission, in the resolved case, cluster morphology is also important. To date, most clusters have been studied at

[5]Hereafter, the acronym SZ will be used to refer to specifically to the thermal SZ effect.

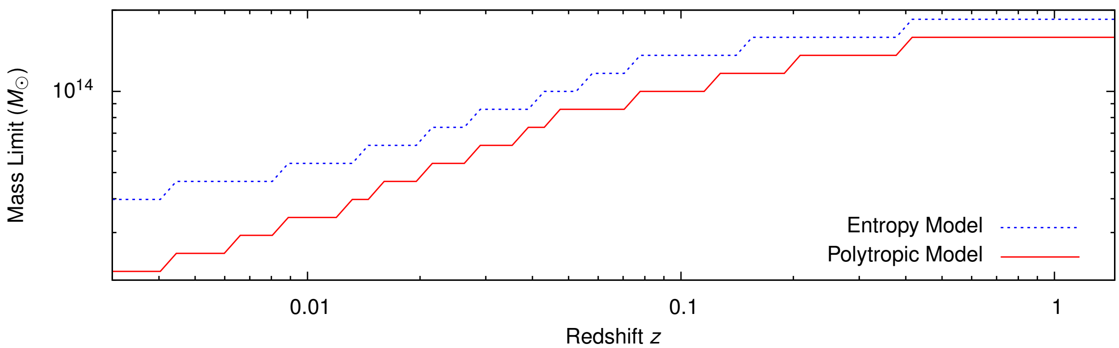

Figure 1.4: Estimated mass limits for SZ cluster detectability, taken from Moodley et al. (2009). The two models shown here are briefly described in the text. They predict that for a sensitivity of a few μK, the ACT should be able to detect clusters of at least $10^{14} M_\odot$ with a signal-to-noise of 5.

lower ($z \lesssim 0.5$) redshifts, so little is known about the profiles at younger clusters. This lends an element of uncertainty to the mass limits of detectability.

Ignorance about the morphology and evolution of young clusters aside, the detectability is still expected to be an uncomplicated function of redshift. This is due both to the intrinsic lack of redshift dependence on the SZ flux as well as the fact that the angular diameter distance is only a mild function of redshift above $z \gtrsim 1$. With a projected sensitivity of a few μK, a reasonable estimate is that the ACT should detect clusters above a few times $10^{14} M_\odot$ at high redshift. Figure 1.4 shows two mass-limit estimates by Moodley et al. (2009). One estimate assumes a polytropic equation of state for the cluster gas, $P \propto \rho^\gamma$ with $\gamma = 1.2$, in hydrostatic equilibrium with dark matter following a Navarro–Frenk–White (NFW) profile. The other estimate, which they call the "entropy model", is identical except that it allows for the injection of non-gravitational energy (or entropy) in the cluster core. The five-year WMAP (WMAP5) cosmological parameters were assumed. The two estimates have slightly different numerical values but are qualitatively the same. Sehgal et al. (2007) predict similar mass thresholds.

1.1.5 Science from the Sunyaev-Zel'dovich Effect

1.1.5.1 Distance Measurements and The Hubble Constant

Most SZ science to date has come from observations of individual clusters that are compared to measurements at other frequencies, particularly X-ray. The surface brightness of a cluster in an X-ray band centered on an energy E is:

$$S_X(E) = \frac{1}{4\pi\,(1+z)^4} \int \mathrm{d}r\, n_e^2\, \Lambda_{eH0}(E, T_e), \tag{1.22}$$

where Λ_{eH0} is the X-ray emissivity of the cluster gas. Unlike the SZ photons that originate at the surface of last scatter, the X-ray signal comes directly from the cluster via thermal Bremsstrahlung and line emission, and therefore depends on the redshift. Bremsstrahlung, which dominates, causes a quadratic dependence on the density n_e, compared to a linear dependence for the SZ (c.f. Eq. 1.13). If we let L be the physical size of the cluster, then $\Delta T_{SZ} \propto \langle n_e T_e \rangle L$ and $S_X \propto \langle n_e^2 \Lambda_{eH0} \rangle L \,/\, (1+z)^4$, with angled brackets denoting mean values along the line of sight. By eliminating the density from the relations for the SZ and X-ray signal, the physical size of the cluster is (Birkinshaw et al., 1991):

$$L \propto \frac{(\Delta T)^2}{S_X} \frac{\Lambda_{eH0}}{(1+z)^4\, T_e^2}. \tag{1.23}$$

If the angular size θ of the cluster is measured, the angular diameter distance $D_A \equiv L/\theta$ is readily derived if the redshift is known. Given a cosmological model, this allows for a determination of the Hubble constant. It is an attractive method because it bypasses the necessity for a cosmic distance ladder that other techniques require. With well-measured, high-redshift clusters, one might also hope to measure properties of the dark energy equation of state as has been done with Type Ia supernovae. Beginning with Birkinshaw et al. (1991), many authors have derived values of H_0 with combined SZ and X-ray observations—Carlstrom et al. (2002) summarize the first measurements using the method. Most recently, Bonamente et al. (2006) used 38 clusters in the redshift range $0.14 \leq z \leq 0.89$ to measure a value of H_0 consistent with that shown in Table 1.1, with systematic errors of about $10\,\mathrm{km\,s^{-1}\,Mpc^{-1}}$.

There are important details and caveats when comparing SZ and X-ray measurements. Most obviously, a cluster geometric model is required before the proportionality sign in Eq. 1.23 may be converted into an equality. That is, the physical size L must be given a robust definition and the line-of-sight distance must be related to the tangential distance (usually through an assumption of spherical symmetry). Historically, the most popular choice has been the isothermal beta model (see §6.2.2.3), but others have been proposed and tested (e.g., Komatsu & Seljak, 2001; Mroczkowski et al., 2009). A possible source of bias lies in the assumption that $\langle n_e \rangle^2 = \langle n_e^2 \rangle$. Small-scale clumping skews this relationship and causes an overestimate of the Hubble constant. Other sources of systematic error exist, such as complexities in gas temperature profiles, contaminated SZ signal from the primary CMB anisotropies, spurious flux from point sources, and so on. Reese et al. (2002) have a good summary of these uncertainties.

1.1.5.2 Gas Mass Fractions

Besides measuring the Hubble constant, SZ cluster studies of individual clusters can also be used to constrain the "gas-mass fraction", i.e., the fraction of total cluster mass contained in ionized gas. Before precision measurements of the CMB anisotropies were available, the gas-mass fractions were used in conjunction with Big Bang nucleosynthesis calculations to constrain the density of matter Ω_M in the universe White et al. (1993). Currently, the value can be used as a consistency check on the density values obtained by other techniques. It is also useful for understanding cluster properties, as simulations show that it is sensitive to formation history, details of the core composition, gas-cooling processes, star formation, and other non-gravitational processes in the cluster (Ettori et al., 2006; Borgani & Kravtsov, 2009).

If the temperature is known, the SZ signal is a direct measurement of the density of gas in the cluster (c.f., Eq. 1.13). The total mass can be estimated by adding X-ray data and assuming that the mass is virialized. Many results have been obtained using X-ray data alone (recently, for example, by Ettori et al., 2009). However, SZ measurements might be more robust because they are not as susceptible to clumping, as discussed above (§1.1.5.1). Moreover, gravitational lensing could provide better total mass measurements, negating the need for X-ray observations in the mass determination (Birkinshaw, 1999; Carlstrom et al., 2002).

1.1.5.3 Peculiar Velocities

The kSZ effect is a potentially powerful way to measure clusters' peculiar velocities. In practice it is not straightforward. Multi-frequency observations are required to separate it from the larger thermal SZ effect. Moreover, the kSZ signal can be contaminated by primary CMB anisotropies, which have an identical spectrum. Finally, flux contributions from infrared and radio sources add additional uncertainty. The consequence is that it is difficult to make precise measurements of

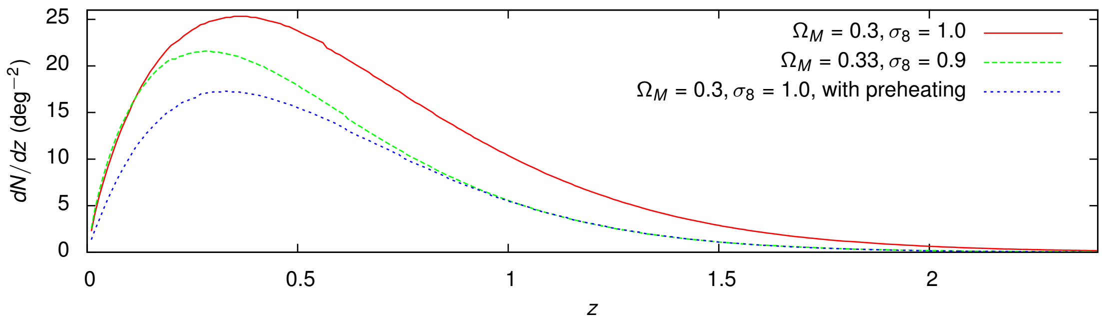

Figure 1.5: Cluster counts per solid angle as a function of redshift for a survey with 1′ resolution and 10 μK sensitivity. This corresponds to a mass limit of roughly $10^{14}\,M_\odot$ at high redshift. All curves assume $\Omega_\Lambda = 0.7$ and $h = 0.65$. The solid red curve has $\Omega_M = 0.3$ and $\sigma_8 = 1$. The dotted blue curve changes Ω_M to 0.33 and scales down σ_8 to 0.9 so that the number of clusters today is the same. The dashed green curve has the same cosmology as the solid red curve, but assumes a different cluster model. Gas heating during cluster formation has reduced the number of electrons in the core, making the cluster more diffuse at high redshifts. This figure was adapted from Fig. 2 of Holder & Carlstrom (2001); more details on these data can be found therein.

individual clusters' velocities, and attempts to date have yielded only upper limits (Holzapfel et al., 1997; LaRoque et al., 2002; Benson et al., 2003). However, there is also the possibility of measuring bulk flow on large scales by averaging data from many clusters. Kashlinsky et al. (2008) have recently claimed a non-zero measurement of the dipole of the bulk flow in the nearby universe using a combination of X-ray and WMAP data. However, Wright (2008) points out several flaws in their analysis and believes the results should not be trusted.

1.1.5.4 Growth of Structure

One of the most anticipated prospects of SZ surveys is their projected ability to probe the growth of structure. As explained in §1.1.4.3, it is expected that the selection functions of SZ cluster catalogs will not have a heavy dependence on redshift. Thus, the hope is that they will provide robust measures of the mass function, i.e., the number density of clusters as a function of redshift and mass. Models show that this is sensitive to cosmology, and since dark energy dominates in late times ($z \lesssim 1$), could help constrain its equation of state w. An analytic estimate that is useful for a qualitative understanding is (Press & Schechter, 1974):

$$\frac{\mathrm{d}n(M,z)}{\mathrm{d}z} \propto -\frac{\rho_M\,\delta_c}{M^2\,\sigma_{R(M)}(z)}\,\frac{\mathrm{d}\log\sigma_{R(M)}(z)}{\mathrm{d}\log M}\,\exp\left[-\frac{\delta_c^2}{2\sigma_{R(M)}^2(z)}\right], \tag{1.24}$$

where n is the comoving number density of clusters between M and $M + dM$, δ_c is the critical overdensity for collapse into a spherical cluster, and $\sigma_{R(M)}(z)$ is the variance of the density field in a radius enclosing mass M. For large masses, the variance is approximately $\sigma_{R(M)}^2 \propto M^{4/3}$ (Weinberg, 2008), so n drops exponentially as the cluster mass increases.

For an SZ cluster survey, the quantity of interest is not the number density per comoving volume element, but per solid angle on the sky. The conversion of Eq. 1.24 to these units involves factors of the angular diameter distance $D_A(z)$. Further, the evolution of $\sigma_{R(M)}$ as a function of redshift is proportional to the linear growth function $D(z)$. Both $D_A(z)$ and $D(z)$ are sensitive to cosmology, with the most important variables being: the mass density Ω_M (higher densities produce more rapid growth); the amplitude of fluctuations, usually parameterized by σ_8; the dark energy density Ω_Λ, which suppresses growth; and the equation of state parameter w, which tunes the rate and strength with which the dark energy inhibits growth. Fig. 1.5 shows the number of galaxy clusters per square

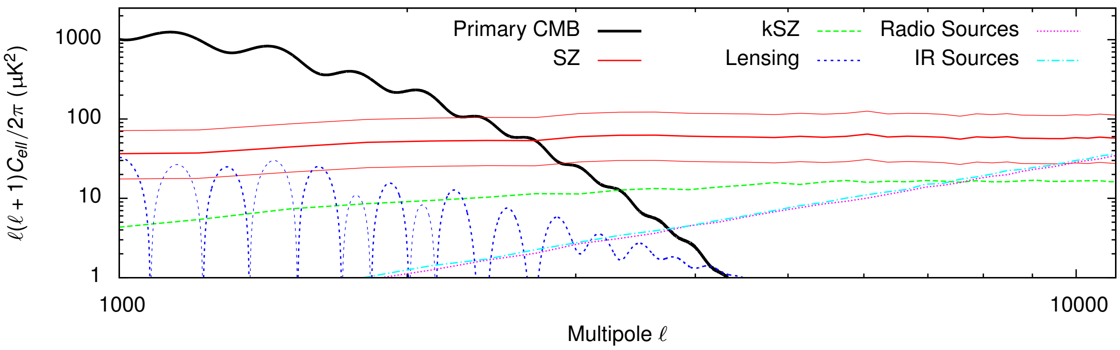

Figure 1.6: Contributions by secondary CMB effects to the angular power spectrum at 145 GHz. The cosmology used to generate these examples was: $\Omega_M = 0.28$, $\Omega_b = 0.05$, $\Omega_\Lambda = 0.72$, $h = 0.7$. The primary CMB and lensing curves were calculated with CAMB (http://camb.info; Lewis et al., 2000). (The lensing curve sometimes goes negative: in these sections the absolute value is plotted with a fainter line.) The rest of the curves were taken from Huffenberger & Seljak (2005). The largest, due to the thermal SZ effect, has a magnitude that is approximately proportional to σ_8^7. (Note that they have chosen $\sigma_8 = 1$ for this study, considerably larger than the measurement of 0.81 by WMAP.) Thus, for example, a 10% alteration in σ_8 changes its amplitude by about a factor of two. This is illustrated by the faint red lines that have $\sigma_8 = 1.1$ (upper) and $\sigma_8 = 0.9$ (lower). The kSZ is sensitive to details of ionization and the authors caution that its curve is uncertain to about an order of magnitude. Point sources brighter than 4 mJy have been masked; for further details on the point source models, see Huffenberger & Seljak (2005). At 277 GHz, spectrum of the IR point sources is more than an order of magnitude larger.

degree as a function of redshift for a survey with arcminute resolution and 10 μK sensitivity. The two different cosmologies with Ω_M and σ_8 varied by 10% show very different curves.

In reality, unless systematic uncertainties can be made low, the interpretation of number counts will be ambiguous. Uncertainties in the estimation of the mass detection threshold (c.f., §1.1.4.3) will need to be reduced. Details of cluster physics will also need to be better understood, particularly those that relate to cluster formation. Fig. 1.5 includes a curve where it is assumed that the injection of non-gravitational energy in cluster cores have played a large role in their evolution, causing significant alteration in the cluster count as a function of redshift. Although this example, from Holder & Carlstrom (2001), is intentionally extreme in its modelling of the preheating, it is a good illustration of how cluster physics can mimic features produced by different cosmologies.

Last year, the South Pole Telescope collaboration reported on three previously unknown clusters discovered by via the SZ effect (Staniszewski et al., 2008). This represents an important first step towards building large catalog of SZ clusters, an endeavor to which the ACT experiment is poised to contribute significantly.

1.1.5.5 Manifestation in the Angular Power Spectrum

Creating a cluster catalog is one of the priorities in the analysis of ACT data, but the presence of clusters in CMB maps also has an important effect in the angular power spectrum. Of all the secondary CMB effects, the contribution of the SZ is expected to be the most prominent. Fig. 1.6 shows the power spectrum of the SZ signal at 145 GHz, together with contributions from other secondary sources to give a visual sense of their relative impact on the overall CMB spectrum.

Studying SZ clusters in the power spectrum has the advantage that it remains sensitive to dim clusters with signal-to-noise too low for individual detection. Additionally, the cluster physics does not need to be as well understood in order to extract some cosmological parameters—Komatsu & Seljak (2002) find that the magnitude of the SZ angular power spectrum scales as $\sigma_8^7(\Omega_b h)^2$, almost completely independently of other parameters. Thus, by far the strongest dependence is on σ_8, making the power spectrum at high ℓ a sensitive probe of this parameter. This can be compared to the use of the mass function (§1.1.5.4), which depends on both σ_8 and Ω_M. With the ACT's sky coverage, resolution, and sensitivity, the uncertainty in our determination of σ_8 will probably be dominated by ignorance of the cluster physics used model the SZ power spectrum templates: Komatsu & Seljak (2002) estimate that this systematic uncertainty is about 10%.

Current measurements of the power spectrum at $\ell \gtrsim 2000$ are uncertain and do not precisely measure the level of SZ contribution—see Fig. 1.1b. (One must be careful reading this figure as different measurements have been made at various frequencies, across which the SZ contribution varies.) The famous "CBI excess" (Mason et al., 2003), which continues to manifest itself with more data, better analysis, and more sophisticated point source removal (Sievers et al., 2009), seems to indicate that $\sigma_8 \approx 1$. Results from BIMA (Dawson et al., 2001) agree. However, the more recent ACBAR measurements, while not being inconsistent with CBI, do not measure as strong an excess (Reichardt et al., 2009a). Moreover, the Sunyaev-Zel'dovich Array sees no excess and its data prefer $\sigma_8 \lesssim 0.9$, though uncertainties in their simulations do not allow them to quantify this claim (Sharp et al., 2009). The APEX-SZ team, which has made a noisy measurement of the high-ℓ spectrum, is only able to place an upper bound of $\sigma_8 < 1.18$ (95% C.L.) at this time (Reichardt et al., 2009b). It is clear that higher sensitivity CMB measurements at $\ell \gtrsim 2000$ are needed to begin to make more definitive statements about the power spectrum at high resolution. Moreover, multi-wavelength observations will be invaluable for helping to separate the SZ effect from point source contamination.

1.2 The Atacama Cosmology Telescope

In §1.1 we showed the great potential for original and diverse cosmological studies with maps of the high resolution CMB. Four elements are essential for such measurements: (a) high resolution, (b) multi-wavelength observations to separate and identify individual sources of secondary CMB anisotropy, (c) excellent sensitivity in order to reach the few-μK level of the high-ℓ CMB, and (d) the ability to survey a large area of sky ($\sim$1000 deg^2) to build a statistically significant galaxy cluster sample. In the following sections, we show how the ACT is designed specifically to meet all of these objectives (§1.2.1–§1.2.3) and then briefly summarize the history of its construction and commissioning (§1.2.4) and its first two seasons of data (§1.2.5).

Figs. 1.15–1.21 contain photographs of the telescope and its surroundings.

1.2.1 Telescope Structure

According to diffraction theory, the only way to achieve high resolution is with a large telescope aperture. If we take the full-width at half-maximum (FWHM) of the optics' point-spread function as our definition of the resolution, then an aperture of diameter a observing at wavelength λ has a resolution of $1.03\lambda/a$ radians. Therefore in order to achieve arcminute resolution in its three frequencies, 148 GHz (2.03 mm), 218 GHz (1.37 mm), and 277 GHz (1.08 mm), the ACT requires a $\sim$6 m aperture.

The optical design chosen for the ACT is off-axis and Gregorian, as shown in the drawing of Fig. 1.7. Table 1.2 lists some optical and structural properties of the telescope. Its diffraction-limited optics are fast—$F \sim 2.5$ at the focal plane—to keep the instrument compact and the field of view is large to accommodate a large number of detector elements. The elliptically-shaped primary reflector, which appears circular when projected on the aperture plane, is about seven meters tall and six meters wide. A cold Lyot stop in the receiver limits its light-gathering region to a radius of 5.9 m. This design was intentional: the outer, unused edges of the mirror help ensure that stray light does not enter the optical path. Additionally, a $\sim$75 cm-wide aluminum guard ring surrounding

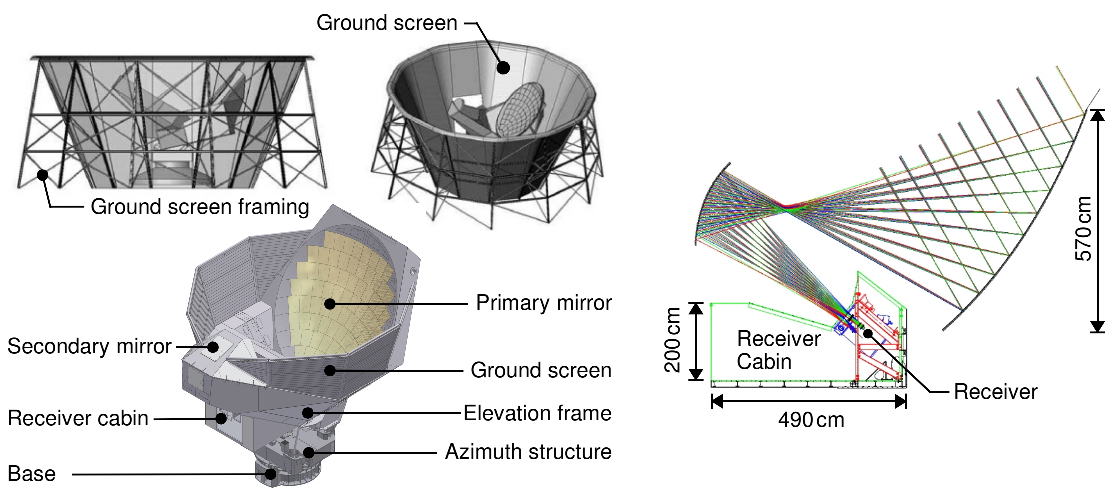

(a) (b)

Figure 1.7: The ACT structure and optics: (a) drawings of the telescope structure and (b) the warm optics with rays showing the optical path.

the reflector provides further protection. The off-axis design results from similar concerns about scattered light since it avoids the necessity for any baffling or other mechanical structures in the optical path. The primary and the secondary reflectors are composed of 71 and 11 segmented aluminum panels, respectively. These are described further in §1.2.4, and photographs are shown in Fig. 1.18.

One of the most daunting challenges for ground-based millimeter telescopes is atmospheric emission, which varies over time as wind and turbulence change the properties of the air through which the telescope observes. These signal variations are typically orders of magnitude larger than the celestial CMB signal. To mitigate this contamination, experiments attempt to modulate the input signal at a temporal frequency higher than the atmospheric signal so that it can be more easily separated from the celestial signal during data analysis. To this end, the ACT is designed so that the whole instrument scans back and forth in azimuth while observing. The relatively high speeds at which this is performed (up to 2 deg s^{-1}) requires that the telescope structure be rigid to avoid large mechanical resonances. Thus, the entire upper part of the telescope consists of a solid aluminum frame in which the reflectors are embedded. The motion system is discussed more in §2.2, below.

A $\sim$10 m tall ground screen surrounds the ACT to shield it from the ground (see Fig. 1.16). Additionally, an "inner" ground screen is integrated into the telescope structure itself, enclosing the whole optical system on either side, for further protection. It is in both photographs of Fig. 1.18.

1.2.2 Detectors & Camera

The ACT uses transition edge sensor (TES) bolometers as it detectors. A TES bolometer consists of an absorber that receives incident radiation and heats a molybdenum-gold detecting element. Photographs of detector elements are shown in Fig. 1.8. The TES is kept near its critical temperature for superconductivity, and with the addition of a voltage bias, it is brought into the transition between the normal and superconducting states. In this region of phase space resistance is a steep function of temperature. Thus, the TES is sensitive to small intensity changes in the incoming radiation. The voltage bias turns out to be stable, in the sense that when the temperature of the bolometer increases, less current is drawn so that the system tends to stay within the superconducting transition region. The ACT detectors achieve sensitivities of $\sim$1 mK $\sqrt{\text{s}}$ (148 GHz),

Table 1.2: ACT Design Parameters

Telescope Properties		**Location**	
Total max. height	12 m	Altitude	5190 m
Ground screen height	13 m	Longitude	67°47′15″ W
Total mass	52 t	Latitude	22°57′31″ S
Mass of moving structure	40 t		
Optics		**Motion**	
Focal ratio	$\sim$2.5	Azimuth range	$-220°$ to $+220°$
Field of view at focus[a]	$\sim$1 deg^2	Max. azimuth speed	2 deg s^{-1}
Primary mirror max. diameter	6 m	Max. azimuth acceleration	10 deg s^{-2}
Num. of primary mirror panels	71	Elevation range	30.5° to 60°
Secondary mirror max. diameter	2 m	Max. elevation speed	0.2 deg s^{-1}
Num. of secondary mirror panels	11		

[a] Defined as the region with 280 GHz Strehl ratio $>$ 0.9, according to design.

$\sim$1.5 mK $\sqrt{\mathrm{s}}$ (218 GHz), and $\sim$3 mK $\sqrt{\mathrm{s}}$ (277 GHz), where temperatures are temperature changes relative to a CMB (Planck) spectrum. Besides the high sensitivity, another attractive feature is the fast thermoelectric response, on the order of 10 ms, necessary for the fast scans executed while observing (see §2.2 and §2.3). A detailed treatment of TES physics may be found in Irwin & Hilton (2005).

The TES's for the ACT are manufactured in a close-packed configuration to maximize coverage on the focal plane. Each individual TES is about 1.1 mm on a side. Fabrication is done in groups of 33 to form a single column of detectors (see Fig. 1.8c).[6] Every column has one TES that is not coupled to an absorber, meaning that it receives no sky signal. These "dark" detectors are used for characterizing instrument noise and thermal drifts.

Each of the three cameras is composed of 32 stacked columns for 32×32 detecting elements per observing frequency. This gives the ACT more detectors than any other millimeter telescope, past or present, and is a key reason for its overall high sensitivity. Fig. 1.8 has photographs of the three arrays.

Detector amplification is achieved by coupling current through an inductor in series with the TES to superconducting quantum interference devices (SQUIDs). The readout is multiplexed in the time domain: in each column only one detector is biased and read at once, thus reducing the number of electrical connections to each column by a factor of about 32. The full array is read at 15 kHz and then filtered and downsampled in firmware (see §2.1.1).

For more details on the ACT TES properties and camera design, see Niemack (2006), Marriage et al. (2006), Battistelli et al. (2008a), Fowler et al. (2007), Niemack et al. (2008), and Zhao et al. (2008).

The TES superconducting transition temperatures are about 450 mK, requiring that they be housed in a cryostat. The Millimeter Bolometer Array Camera (MBAC), which refers to the cryostat and all that is inside it, is cooled to about 4 K by two external, closed-cycle helium-4 refrigerators. Inside, two closed-cycle, helium-4 sorption refrigerators provide about 80 J of cooling per refrigeration cycle to about 670 mK. One of these is for cooling optical elements inside the cryostat, and

[6] Perhaps the most confusing items in the ACT vocabulary are "columns" and "rows", since in the receiver, columns actually run in the horizontal direction.

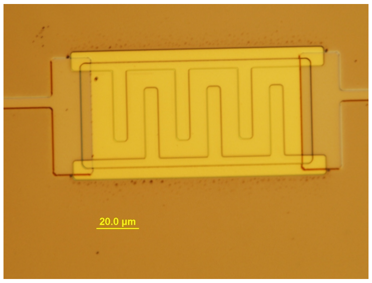

(a)

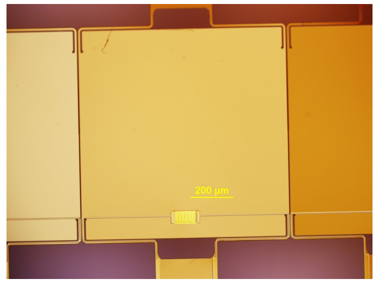

(b)

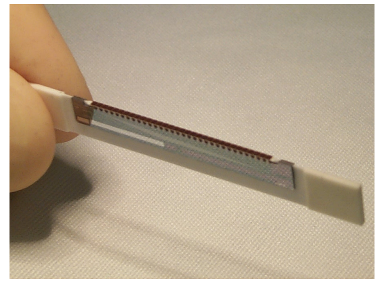

(c)

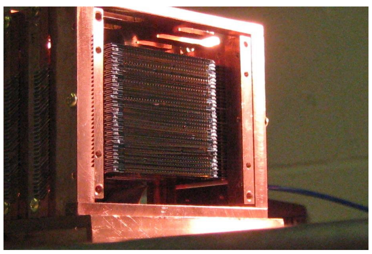

(d)

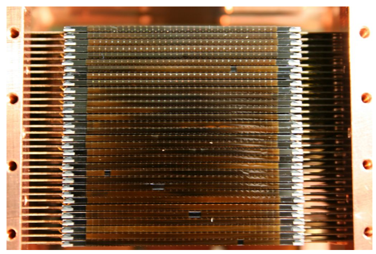

(e)

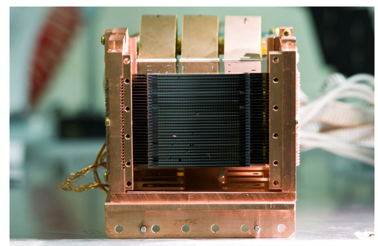

(f)

Figure 1.8: Photographs of ACT detectors and cameras. The top row shows a single molybdenum-gold TES (a), a single detector absorber with its TES (b), and a column of detectors (c). In the bottom row are photographs of each of the three arrays: 148 GHz (d), 218 GHz (e), and 277 GHz (f). Individual detector components were fabricated at the NASA Goddard Space Flight Center and the National Institute of Standards and Technology at Boulder, CO, and integration was done at Princeton.

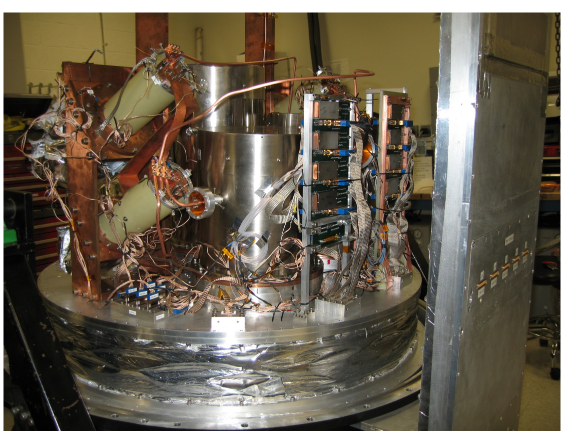

(a)

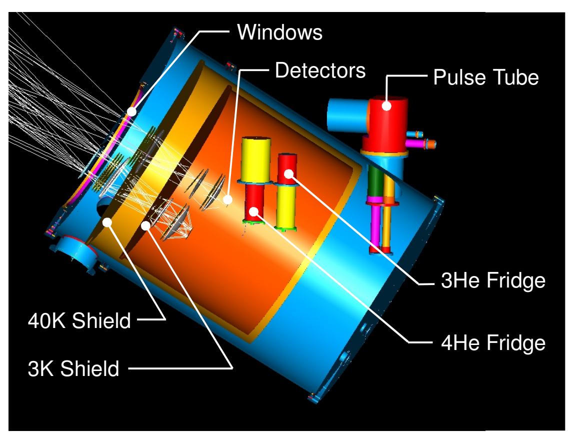

(b)

Figure 1.9: A photograph and schematic of the MBAC. In the photograph, (a), the cryostat is open. The schematic, (b) is highly simplified. The MBAC cryostat was built at the University of Pennsylvania by M. Devlin, M. Kaul, J. Klein, D. Swetz, and R. Thornton, with many components built at Princeton.

Table 1.3: Filter bandpass parameters. Measurement and analysis were done by D. Marsden, J. Fowler and L. Page. The most recent analysis slightly modifies some of the values, but these are the ones used for the work in this dissertation.

	148 GHz	**218 GHz**	**277 GHz**
Band Center (GHz)	148.0 ± 2.5	218.0 ± 2.5	277.0 ± 2.5
Bandwidth (GHz)[a]	20.6 ± 1.3	17.5 ± 0.9	25.3 ± 1.3
Maximum Transmission	0.74	0.72	0.69
RJ to CMB conversion[b]	1.675 ± 0.028	2.897 ± 0.064	5.116 ± 0.132
Peak RJ to Jy conversion ($\times 10^{-4}$)[c]	1.468 ± 0.056	1.726 ± 0.059	2.55 ± 0.15

[a] The bandwidth is $\Delta\nu = \int_0^\infty d\nu g(\nu)$, where g is the normalized transmission for the band.

[b] These are the factors that convert temperature anisotropies relative to a Rayleigh-Jeans spectrum to those relative to the CMB spectrum.

[c] This factor converts the peak RJ temperature in μK of a point source into units of Janskies (Jy). The quoted errors include the uncertainties in the bandpass measurements and the telescope solid angle (§5.2.2.3).

(a)

(b)

Figure 1.10: Site location and landscape. The map, (a), shows the location of ACT, near the Chilean border with Bolivia and Argentina. A photograph of the mountain range, (b), in which the ACT is located identifies the major peaks. The ACT is on Cerro Toco at an altitude of 5190 m (i.e., not at the summit).

the other is for precooling a helium-3 sorption refrigerator that cools to 240 mK with about a 6 J capacity. Fig. 1.9 has a photograph and simple schematic of the MBAC.

Lenses within the MBAC reimage the telescope focus on each of the three detector arrays. A series of filters define the frequency bands, which are listed in Table. 1.3.

Details of the MBAC refrigeration and lenses are in Lau et al. (2006a), Lau et al. (2006b), Lau (2007), Swetz et al. (2008), Thornton et al. (2008), and Swetz (2009).

1.2.3 Site

The ACT is located on Cerro Toco of the northern Chilean Andes, at an altitude of 5190 m. Fig. 1.10 shows a map pinpointing the location and a photograph of the region. It is an exceptional site for millimeter astronomy because of the high altitude and extreme aridity.

The aridity is important since water vapor has strong emission in the millimeter. The choice of ACT frequency bands was partially informed by the spectrum of this emission—see Fig. 1.11a. The SZ null, which is in our 218 GHz band, happily falls just above a resonance at 183 GHz.

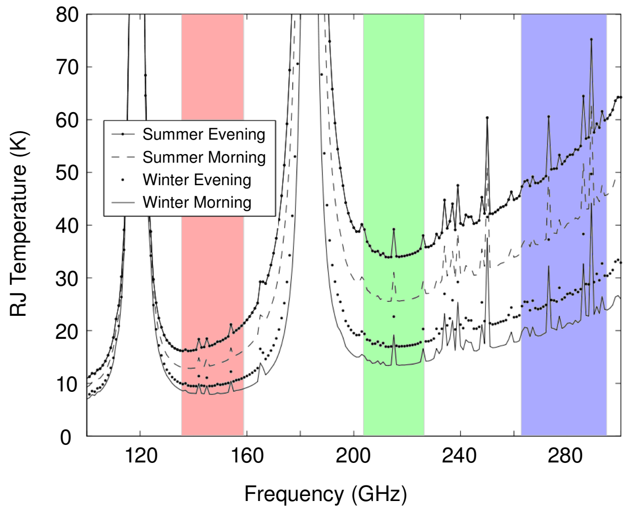

(a)

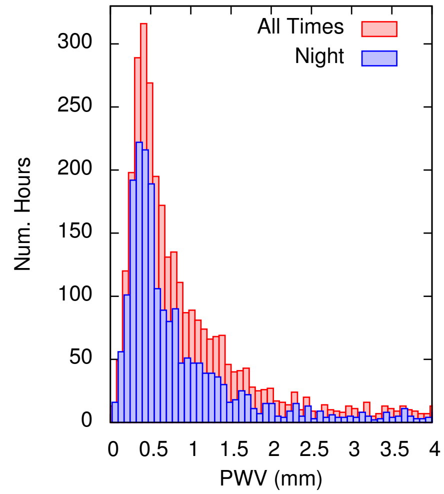

(b)

Figure 1.11: Atmospheric conditions at the ACT site. The plot of atmospheric brightness as a function of frequency, (a), is taken from Marriage (2006). The ACT frequency bands are shown as solid bands behind the curves. The histogram, (b), shows the distribution of PWV values during the 2008 observing season (Aug.–Dec). The "night" data are restricted to the hours 00:00–14:00 UTC to reflect the quality of the atmosphere during the times when the ACT is actually observing. PWV measurements were taken from the publicly available APEX data: http://www.apex-telescope.org/weather/.

The 148 GHz band was chosen to lie between this resonance and a lower oxygen resonance at 119 GHz.

The amount of water in the atmosphere is usually quantified as precipitable water vapor (PWV), quoted in units of millimeters and indicating the amount of vapor in a column pointed at the zenith. A histogram of PWV values from the 2008 observing season is shown in Fig. 1.11b. The PWV is a reasonable proxy of the atmospheric opacity (see §5.3), which is lower than almost anywhere else in the world at millimeter frequencies. It is better than Mauna Kea, and comparable to the South Pole (Radford & Chamberlin, 2000).

Fig. 1.11a shows that the summer conditions are not as amenable to observing. This is the wetter season, when the winds change and bring humidity from Bolivia in the north-east, a phenomenon known as the Bolivian Winter. It lasts roughly from late December through March, though this varies annually, and there are occasionally nights with superb conditions during this period. However, in its current mode of operation, the ACT is shut down for these summer months.

Marriage (2006) and Switzer (2008) have in-depth analyses of the atmospheric conditions on Cerro Toco as they pertain to the observing quality for the ACT.

1.2.4 Commissioning History

The ACT began receiving funding from the United States National Science Foundation (NSF) on 1 January 2004, and construction of the telescope structure was started soon thereafter by Amec Dynamic Structures (DS), based in Port Coquitlam, British Columbia.[7] By this time, work on the detectors and cryostat was well underway. A major effort at Princeton was to build a prototype

[7]Formerly owned by AMEC Inc., it was acquired by Empire Industries Ltd. in 2007 and is now named Empire Dynamic Structures Ltd. Business address: 1515 Kingsway Ave., Port Coquitlam BC V3C 1S2, Canada. Internet URL: http://www.dynamicstructuresltd.com.

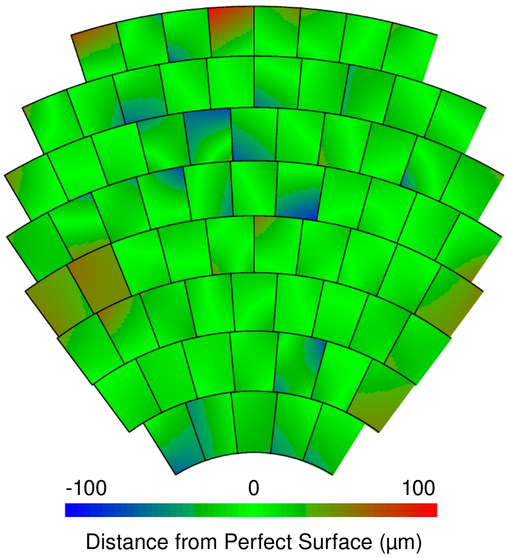

(a)

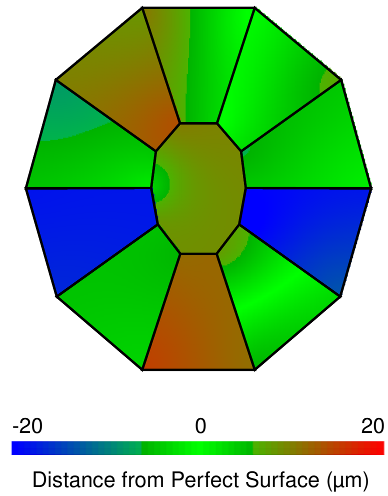

(b)

Figure 1.12: Alignment quality of the primary and secondary reflectors. The figures show the deviations of the primary (a) and secondary (b) reflector surfaces from the design shape after the adjustments before the 2009 season. Note that the color scale is different in the two plots. The primary has a surface rms of 27 μm and the secondary has an rms of 9 μm.

cryostat, called the Column Camera (CCAM). It was useful for informing the cryogenic hardware later used on the MBAC and provided an important testbed for the new TES technology. It was deployed on the roof of Jadwin Hall at Princeton on a small telescope formerly used for WMAP testing, and successfully observed the moon and Jupiter (Aboobaker, 2006), (Niemack, 2006), (Lau, 2007). This was the first test of a close-packed array of TES elements, and possibly also the first astronomical use of TES technology at millimeter wavelengths.

Throughout 2006, as the telescope structure neared completion, members of the ACT collaboration spent significant amounts of time at Amec DS working with the engineers to ensure that design specifications were adequately met. Telescope motion (see §2.2) was tuned and work began on the primary and secondary reflector panel alignment (discussed more below). Both the CCAM and the MBAC were installed in the telescope and cooled to test cryogenic performance in-place. Finally, much time was spent configuring and testing other miscellaneous hardware and writing software for the field.

In early 2007, the telescope was shipped from Vancouver to Antofagasta, Chile. Flatbed trucks transported it from port to the top of Cerro Toco; a section of road near the top of the mountain had to be specially built to accomplish this. Workers from Compax, a local company subcontracted by Amec, did most of the labor on the installation of the telescope and the ground screen. Members of the ACT collaboration arrived in late February to begin the major task of preparing the experiment for observational readiness. Generators, computers, wiring, a radio internet connection, and a myriad of other systems had to be set up. Retuning of the telescope motion was a lengthy process but good performance was eventually achieved.

Perhaps the most onerous project during the commissioning phase was aligning the panels that comprise the primary and secondary reflectors. The effort was led by R. Dünner but many other members of the collaboration also contributed significant time to it. Measurements of the panel positions were done with a laser tracker manufactured by Faro. During panel measurements, the laser tracker is fixed to the telescope body in full view of both mirrors. An operator places a retroreflector

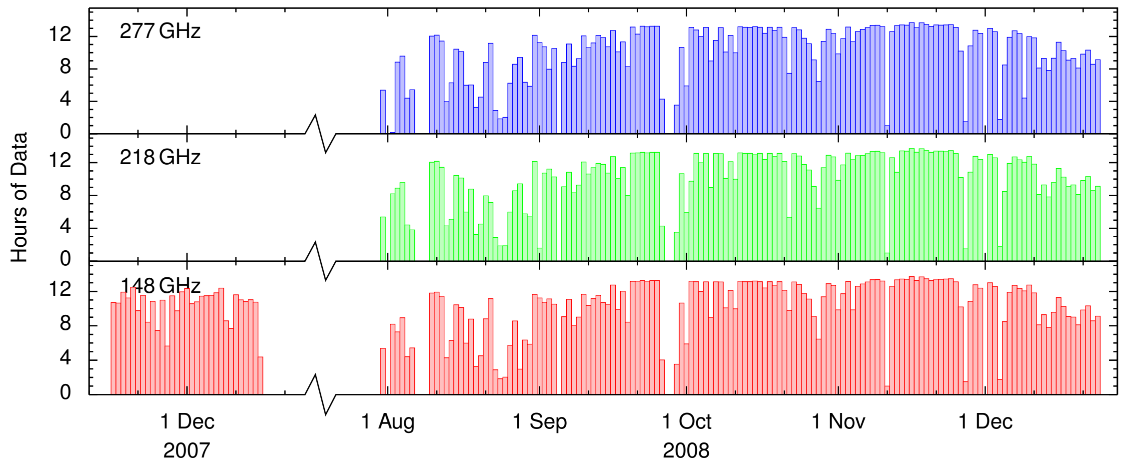

Figure 1.13: Summary of data hours logged in 2007 and 2008. Engineering data outside of the official season dates are not shown. In 2007, only the 148 GHz camera was installed.

against the panel surfaces and the tracker uses a laser to determine the distances. Using these distances, the offset of each panel from its intended position can be calculated. Adjustments are made by turning screws connected to each panel corner in the rear of the telescope. The process is iterated until the surface converges on the designed shape. After much work to understand the optimal alignment procedure, we achieved surface qualities better than 30 μm and 10 μm on the primary and secondary reflectors, respectively. This is sufficient to give a Strehl ratio of about 0.9 in our 277 GHz band, and better in the other two. Since the initial round of panel adjustments in 2007, subsequent measurements have demonstrated that the alignment is stable over long periods of time. Fig. 1.12 shows the residual alignment errors after adjustments at the beginning of the 2009 season.

Hincks et al. (2008) and Switzer et al. (2008) give further details on the telescope structure and other technical systems.

First light with the ACT was achieved with the CCAM receiver observing Jupiter on 11 June 2007. Tests with the CCAM continued through the austral winter. The MBAC receiver arrived in the austral spring of 2007 and was installed in the telescope with only the 148 GHz camera, as the other two were still being built. It saw first light observing Venus on 22 October 2007.

1.2.5 Summary of Data from First and Second Seasons (2007–2008)

The ACT is currently in its third season of observing. In this section we briefly outline what was accomplished in the first two seasons of observing to provide background on the data that is used throughout the rest of this dissertation.

In 2007 the MBAC was deployed with only the 148 GHz frequency. The season lasted from 15 November to 16 December, inclusive. Data were taken before this starting date, but telescope adjustments (such as adjusting the optical focus and tuning motion parameters) were still being performed. The end date was fixed by one of the elevation motors breaking, which occurred near enough to the onset of the Bolivian winter that little good observing time was lost. The MBAC was returned to the University of Pennsylvania for the installation of the 218 GHz and 277 GHz arrays. Considerable time was required for this major upgrade, including on-site testing. Consequently, the season began later than originally planned, on 31 July, and lasted through 24 December. Fig. 1.13 shows how much observing time was completed in both seasons.

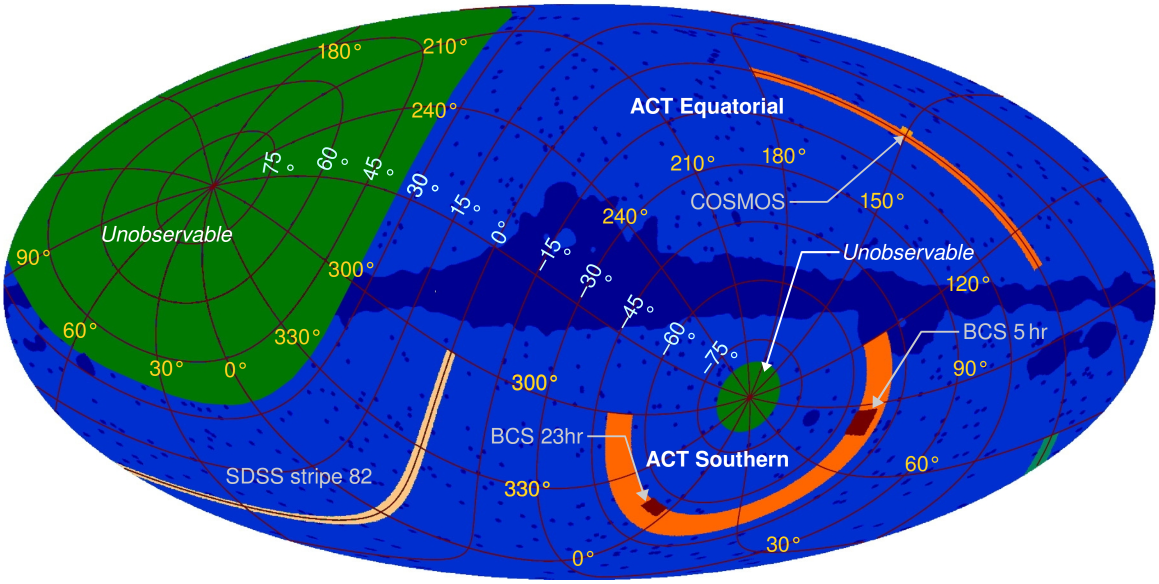

Figure 1.14: A map of the ACT observing regions, shown in orange. In this map, the 2008 coverage is shown; 2007 coverage was at the same declinations but somewhat different right ascension ranges (see Table 1.4). Blue areas can be viewed by the telescope, while green is always outside of its field of view. For reference, BCS, COSMOS and Sloan Digital Sky Survey (SDSS) regions are also highlighted. This figure is adapted from a graphic made by S. Das.

Two areas of sky were targeted, with approximate coverage indicated in Table 1.4 and Fig. 1.14. The southern region is centered on a declination of about -53°, and overlaps with both the 5 and 23 hour fields of the upcoming Blanco Cosmology Survey (BCS). The other region is centered on the equator and has partial overlap with the Cosmology Evolution Survey (COSMOS) (Scoville et al., 2007). Broadly speaking, coverage of both fields is shallower towards the edges of the rectangles. About equal amounts of time were spent on each field.

Observations of the survey regions are coordinated so that the boresight of the telescope is always at 50.5°—the elevation is held fixed to the prevent the large gain changes that would be incurred by looking through different airmasses. For the first half of the night, the telescope points to the appropriate azimuth in the east of the sky and observes the region as it rises; then, for the second half of the night, it moves and observes the region in the west as it sets. Only a portion of the right ascension range of each survey may be observed in one night (and on some dates

Table 1.4: ACT survey regions in 2007 and 2008. Regions are rectangular. The ranges are approximate, and, roughly speaking, coverage is shallower near the boundaries.

Region	Declination Range (deg)	RA Range (hours)
2007 Southern	-57 to -52	3 to 9
2007 Equatorial	-2.5 to 2.5	2 to 6; 8 to 10
2008 Southern	-56.6 to -49	21 to 7:30
2008 Equatorial	-1.5 to 1.5	7:30 to 11:30

Table 1.5: Planet Observations in 2008.

Planet	# Obs.	Dates Observed	Notes
Mercury	0	—	Never observed.
Venus	6	16 Dec.	During sunset for studying panel deformation.
Earth	$\gg 1$	whole season	Chiefly observations of the atmosphere.
Mars	7	25 Oct.; 2, 6, 10 Dec.	Observed during sunrise.
Jupiter	69	4 Aug.–23 Oct.	Used for engineering purposes.
Saturn	65	25 Sept.–24 Dec.	Observed during sunrise until about 8 Nov.
Uranus	87	11 Aug.–7 Dec.	Used for calibration.
Neptune	46	17 Aug.–8 Sept.	So far unused; possible utility as calibrator.

during the year one or the other of the regions may not be observed at all) but over the course of the observing season, the whole range in right ascension is covered.

This observing strategy—pointed east for half the night and west the other half—allows maps to be "cross-linked". The angle between the direction of the azimuthal scans and the hour angle axis is different (typically by about 60°) in the east and west. Contamination correlated with the scan direction can therefore be mitigated by coadding rising and setting maps. In more sophisticated analyses, modes parallel to the scan direction can be be suppressed in mapmaking without losing all information in phase space in the final maps since the rising and setting data are suppressed along different directions.

The only time the ACT did not observe in the southern or equatorial regions was when it was targeting planets. Each normal night of telescope operations included one planetary observation, cycling each night through available planets: so if, for example, both Saturn and Uranus were visible, they would be viewed on alternating nights. These observations would be made at a nominal elevation of 50.5°, the same elevation used for CMB observations. Additionally, 10 Dec. 2007, 16 Aug. 2008, and 8 Dec. 2008 were designated as "planetfests" and all available time on those nights were spent observing the planets visible at the time. Thus, though most of the planets were observed at our normal survey elevation, there are also a fair number at others. Table 1.5 summarizes the planet observations of 2008.

Figure 1.15: The ACT in front of Cerro Toco.

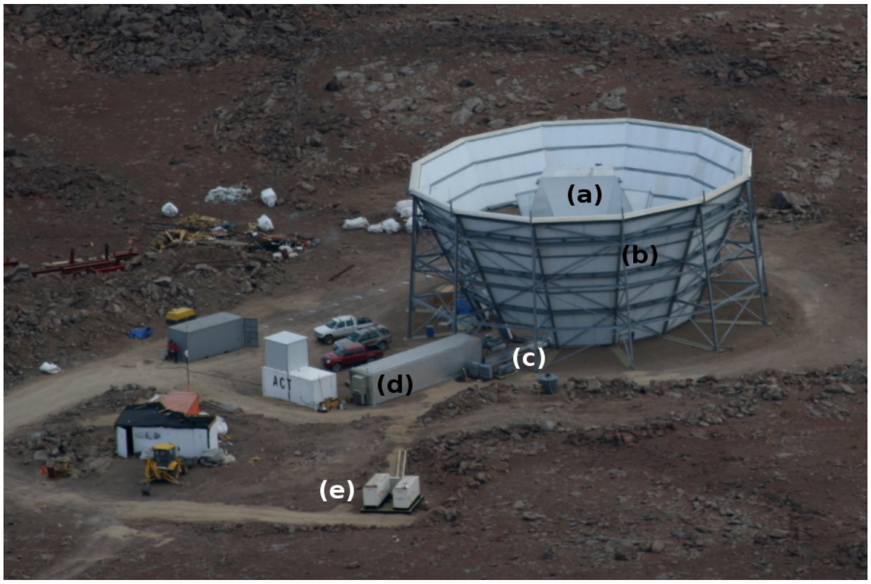

Figure 1.16: The ACT site: (a) the telescope, only the very top of which is visible in this image; (b) the ground-screen; (c) the cable wrap conveying wires and helium lines between the telescope and (d) the Equipment Room, housing the helium compressors, motion control system, computers and other such systems; (e) the diesel electricity generators. Photo courtesy of R. Dünner.

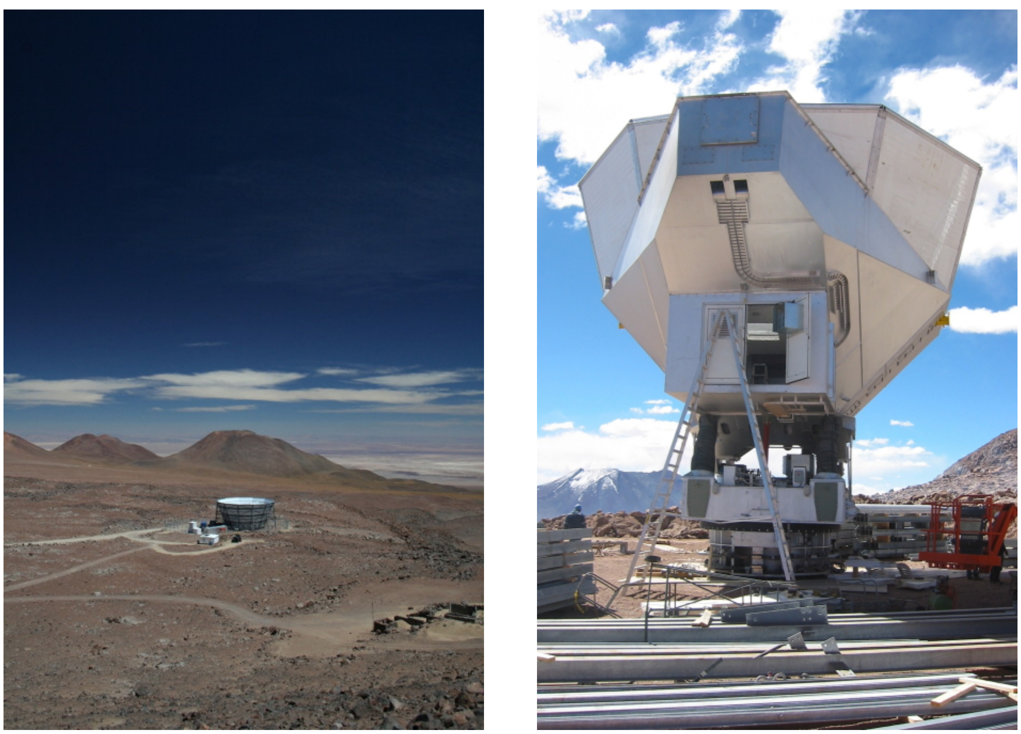

Figure 1.17: The ACT from afar and close up. The long shot *(left)* is roughly oriented south-east. The close-up *(right)* prominently shows the Receiver Cabin, door ajar, in the foreground. The mirrors are not visible. This photograph was taken before construction of the ground-screen had commenced. The peak of Cerro Toco begins rising on the right side of the image.

Figure 1.18: The primary and secondary reflectors. *Top:* W. Page (foreground) and R. Dünner (background) perform panel alignment measurements on the 71 aluminum primary segments. The total height of the primary reflector is about 7 m. Photo courtesy of M. Devlin. *Bottom:* Y. Zhou does alignment measurements on the secondary panels. The secondary reflector is about 2 m in diameter.

Figure 1.19: Inside the Receiver Cabin: (a) the MBAC receiver and MCE's, covered here with eccosorb to reduce noise; (b) the cryogenic thermometry preamplification and heater driver crate; (c) the BLAST DAC; (d) the ROx AC bias generator; (e) the heater relay breakout box; (f) the Sync Box; (g) the MCE power units; (h) the bulkhead through which wires are routed out of the Receiver Cabin; and (i) the access hatch to the primary and secondary mirrors. R. Fisher in the foreground.

Figure 1.20: Inside the Equipment Room, the office area and control room at the site. Left to right are: E. Battistelli, D. Swetz, M. Devlin, M. Niemack, and R. Dünner.

Figure 1.21: Hardware in the motion system. *Top:* the azimuth gears, which are counter-torqued; a Compax worker and M. Yargeau work on the greasing system. *Bottom left:* the elevation motor, visible through the open port, and elevation drive screw, being worked on by M. Yargeau as J. Funke stands by. *Bottom right:* inside the KUKA cabinet, with J. Klein performing diagnostic measurements.

Chapter 2

Telescope Control, Housekeeping and Data Acquisition

The ACT is a complex experiment, relying on many hardware and software components working in unison. The purpose of this chapter is to give an outline of these systems. A large share is dedicated to what is generally termed "housekeeping", referring to the monitoring of non-detector data, such as cryogenic temperatures or the telescope position. Housekeeping is closely related to control systems for telescope motion and cryogenic servoing, and, ultimately all of these exist so that we can take useful, scientifically worthwhile detector data.

It is beyond our scope to give all the technical details: instead, we focus on giving the reader a basic familiarity with the ingredients of the experiment and how they interact with one another. In some places, we go into more depth when there is possible relevance for data analysis (such as the BLAST filter shown in Fig. 2.3) or there is insight into the capabilities of the telescope for cosmological observations (such as the motion quality or the timing precision).

We progress, roughly speaking, from hardware to software. In §2.1 we describe the telescope systems, many of which consist of housekeeping instruments. Telescope motion control is presented in §2.2. Much care has gone into ensuring synchronization and precise timing of data acquisition, to which we dedicate §2.3. Finally, in §2.4, we describe the experiment's software, tracking the progress of the data from the lowest-level device drivers back to the analysis computers in Princeton.

2.1 Overview of Telescope Systems

Figure 2.1 shows all the important systems for controlling the telescope and reading data. Table 2.1 gives a list of the data which are recorded. Most instruments are located on the telescope structure. The MBAC receiver as well as many low-level electronics are housed in the Receiver Cabin, a small, heated room below the secondary mirror houses the MBAC receiver—see Figs. 1.17 and 1.19. Cables leaving the Receiver Cabin are routed through a cable wrap down the telescope's axis of rotation which provides suitable strain relief during any motion. A cable tray, about twenty meters long, carries the cables to the Equipment Room, which houses helium compressors for the MBAC, the KUKA control cabinet (§2.2) and other miscellaneous hardware. It also contains the data acquisition computers: a computer for housekeeping, three computers for MCE acquisition and one for data merging. A ~ 50 Mbps radio connection allows for fast network communication with the ground station, located in the town of San Pedro at a line-of-sight distance of 42 km from the telescope. Data are continually transferred over this link to raid discs in the ground station

Table 2.1: Sources and rates of housekeeping and detector data.

	Data	Source	System	Rate (Hz)
Instrument Readout	TES detectors	3 x 1056 in MBAC	MCE	400
	encoders	1 each on az. and el. axes	Heidenhain	400
	ROx thermometers	32 in the MBAC	BLAST DAS	100
	diode thermometers	20 in the MBAC	BLAST DAS	100
	magnetometer	1 place near MBAC	BLAST DAS	100
	accelerometers	4 prim., 3 sec., 1 MBAC	BLAST DAS	100
	LDVT's	5 on sec. actuators	BLAST DAS	100
	KUKA encoders	1 on az., 1 on el., 5 sec.	KUKA	50
	motor currents	2 on az., 2 on el., 5 sec.	KUKA	50
	motor temperatures	2 on az., 2 on el., 5 sec.	KUKA	50
	clinometers	1 on pedestal, 1 in Rec. Cabin	ABOB	20
	ambient thermometers	44 on telescope structure	ABOB	1
	weather station[a]	roof of Equipment Room	WeatherHawk	1
Status Info.	KUKA messages[b]	KUKA robot software	KUKA	50
	DeviceNet bits[c]	`amcp`[d] /KUKA robot software	KUKA/`amcp`[d]	50
	BLAST DAS dig. out[e]	28, controlled by `amcp`[d]	BLAST	50
	commands[f]	dozens	`interface_server`	1

[a] Though incorporated into the data stream, the weather information is not reliable (see §2.1.5).
[b] The messages do not occur at a fixed rate. The most recent message code received is recorded.
[c] Both the output and input bits are recorded.
[d] See §2.4.1.2 for a description of the `amcp` program.
[e] The digital outputs control the MBAC temperature servoing (§2.1.2.2); their current state is recorded.
[f] All current command values from the `interface_server` (§2.4.4) are recorded.

where they await shipment back to North America. In the following sections, we outline the control and data acquisition systems in logical groupings.

2.1.1 The Receiver and its Readout: the MBAC and MCE

At the heart of the experiment is the Millimeter Bolometer Array Camera (MBAC). The MBAC is a $\sim$1 m^3 cryostat containing ^{4}He/^{3}He sorption refrigerators which cool the detectors to 300 mK. As outlined in §1.2.2, there are three arrays of 32$\times$32 TES detectors, tuned for frequency bands centered at 148 GHz, 218 GHz, and 277 GHz with optical filters. Readout is achieved with the Multi-Channel Electronics (MCE), physically mounted on the cryostat. They sample the detectors at 15 kHz, filter and down-sample to 400 Hz and transmit the data via fiber-optic cables to three computers, one per frequency channel, in the Equipment Room.

This is the briefest of summaries of the MBAC and MCE systems, to which the author of this dissertation did not make significant contributions.[1] Detailed descriptions can be found in Swetz

[1] He was, however, involved with some of detector testing and microfabrication processes to integrate them with the lowest level readout electronics. This work is not related, however, to the over-arching systems examined in this chapter. It has been summarized in Hincks (2005).

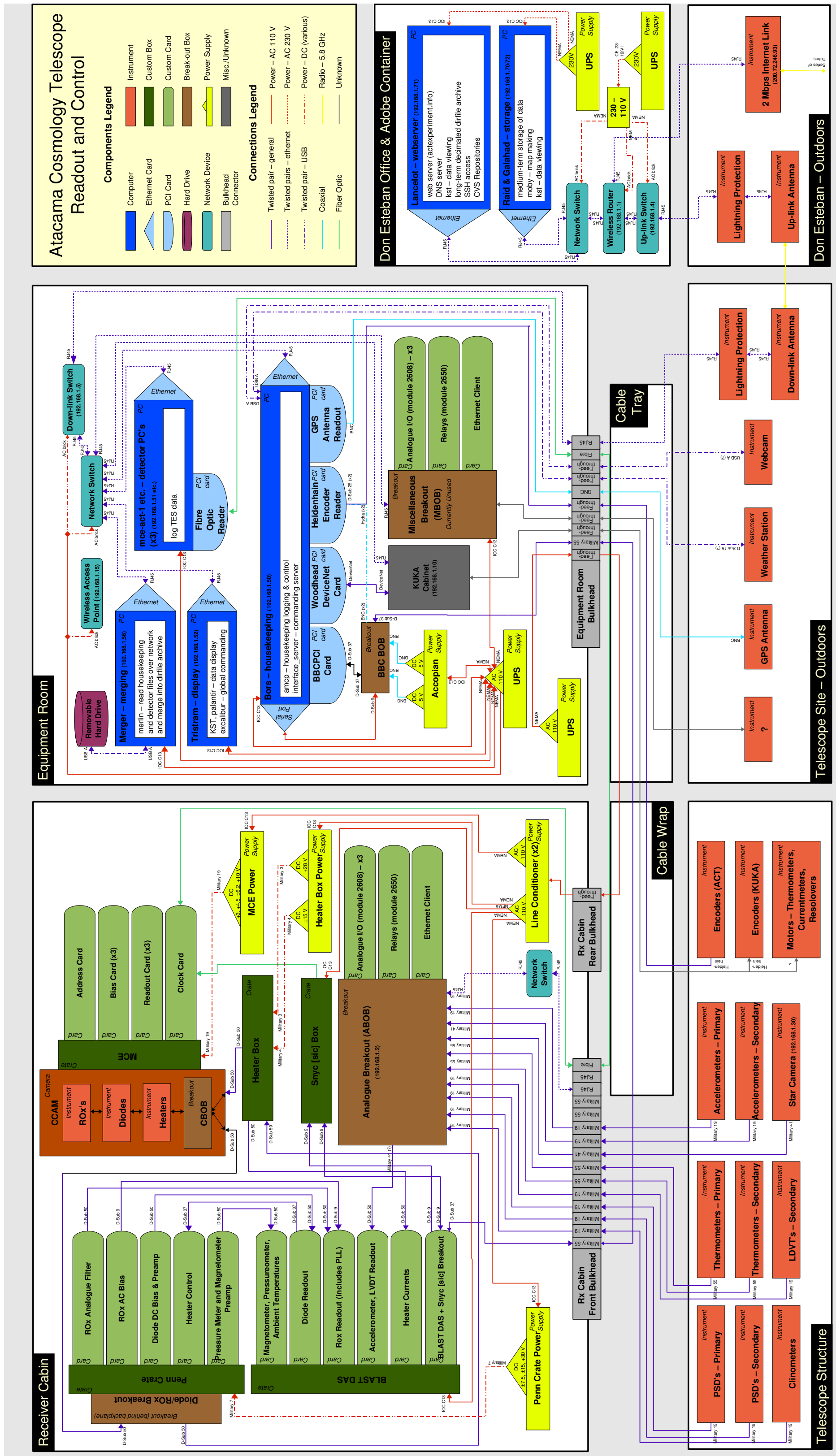

Figure 2.1: A diagram of the ACT readout and control systems.

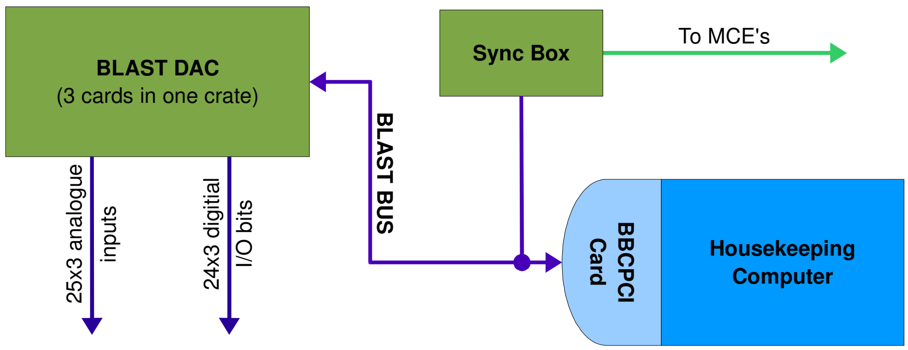

Figure 2.2: The components of the fast housekeeping system. The BLAST DAC contains three cards, each of which digitizes up to 25 analog voltage inputs and can control three bytes of digital I/O. Communication with the housekeeping computer occurs via the BBCPCI card which is connected to the BLAST DAS by the BLAST BUS cable. Timing discipline, which is shared with the MCE computers, is provided by the Sync Box (see §2.3). Fig. 2.1 shows how the components here fit into the larger experiment, including the instruments listed in §2.1.2.1–§2.1.2.3.

et al. (2008), Thornton et al. (2008), Battistelli et al. (2008a) and Battistelli et al. (2008b).

2.1.2 Fast Housekeeping and Control: the BLAST DAC

"Fast" housekeeping occurs at 100 Hz. Making heavy use of electronics developed at the University of Toronto for the BLAST experiment (Pascale et al. (2008)), it is variously referred to as the "U of T system/crate" and the "BLAST DAS/DAC",[2] the latter of which we employ henceforth. Fig. 2.2 shows a block diagram of the components described below.

The workhorse of the BLAST DAC is the BLAST crate which contains three analog-to-digital (ADC) boards (with space for many more should expansion be required). Each board can receive 25 analog voltage inputs, with five possible dynamic ranges (0–12.288 V, ±6.144 V, 0–4.096 V, ±2.048 V and AD590 4.096 V (409.6 K)) selectable for each channel by changing jumper configurations on the board. In addition, there is capacity for 24 parallel bits of digital communication, which can be designated input or output in groups of eight bits by swapping optoisolator positions on the board. Finally, four outputs can deliver pulse-width modulated (PWM) voltages, though these are not employed for the ACT housekeeping.

Data are sampled with 24-bit precision at 10 kHz and routed to on-board Altera field-programmable gate array (FPGA) microprocessors. Some inputs are digitally processed at this stage; specifically, the ROx thermometers which have been AC-biased at 212 Hz (see §2.1.2.1). Their bias generator output is split so that in addition to driving the resistors, it is also read in by the BLAST DAC, where it is used to demodulate the AC-biased inputs as they are sampled. A phase difference between the bias and readout signals can be commanded via the BLAST BUS, described below.

The 10 kHz data are passed through a series of four boxcar filters, with the length of the n^{th} boxcar chosen so that its null in frequency space occurs at $50 \times (\frac{1}{2})^{(n-1)/4}$ Hz. The resulting filter after these four stages, plotted in Fig. 2.3, passes very little power above 50 Hz. The data are then down-sampled to 100 Hz.

Communication with the housekeeping computer is over the BLAST BUS, a RS485 two-way protocol which uses 3 twisted-pair lines to carry a clock, assert and data line. The clock runs at 4 MHz and is used to discipline the 10 kHz data acquisition described in the last paragraph. Interface to the computer is provided by the BLAST BUS Communication (BBC) card, a custom-built

[2] Both DAS and DAC are acronyms for "data acquisition system".

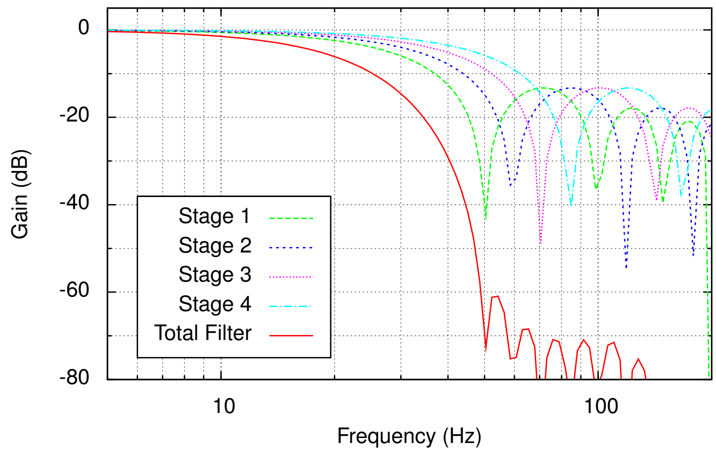

Figure 2.3: The BLAST DAC digital filter gain. The data are passed through a series of four boxcar filters, with the n^{th} filter having a null at $50 \times (\frac{1}{2})^{(n-1)/4}$ Hz. The nulls are spaced so that the amount of power passed above 50 Hz is very small.

card which plugs into a standard PCI slot found on most PC motherboards. An FPGA processor controls the card and is in charge of the BLAST BUS data flow, which occurs in 100 Hz frames. The communication model is that of command-response: the BBCPCI card sends a command and receives an immediate response from the BLAST DAC. Commands consist of an address of BLAST DAC board and channel number and a bit specifying whether a read or a write is being requested; if it is a write, the data are passed in the package. For write packets, the BLAST DAC responds by echoing the write data; for read requests, the data from the specified board and channel are returned.

The BBCPCI card has enough RAM to buffer a few dozen seconds of read data; buffered data are read by a custom-written device driver and made available to the housekeeping software (see §2.3.1).

In the following sections we outline the instruments which are controlled or read out by the BLAST DAC.

2.1.2.1 Cryogenic Thermometers

There are two types of thermometers which monitor temperatures in the MBAC cryostat: 20 diodes and 32 ruthenium-oxide (ROx) resistors.

Diode thermometers are read out by measuring the voltage across DC-biased diodes and are useful from room temperatures down to about 1.4 K. An analog board in the ambient Penn Crate (see Fig. 2.1) low-pass filters and amplifies the data before they are read by the BLAST DAC.

ROx resistors are used for temperatures below 1.4 K. They are AC-biased with a 212 Hz sine wave provided by a signal generator. Four-lead measurements of the ROx resistances are routed to a warm analog board in the Penn Crate where they go through a biquad filter with a bandcenter at 220 Hz, a 159 Hz bandwidth and a DC amplification of 100. The BLAST DAC demodulates the AC signal as described above, in §2.1.2.

Look-up tables on the housekeeping computer are used to convert voltage (for the diodes) or resistance (for the ROx's) to temperatures.

2.1.2.2 Cryogenic Heaters

Cryogenic temperatures are controlled using 18 resistors acting as heaters. They are critical for the cryogenic cycling and thermal control of the detectors—see Swetz et al. (2008). The cryogenic thermometers (§2.1.2.1) are used to servo the heaters' outputs. The heaters are driven by a custom-designed heater board located in the Penn crate, capable of driving 18 channels between 3 μA and 94 mA.

Control of the heater board is performed by the digital outputs of one of the BLAST DAC boards, as commanded by the housekeeping computer over the BLAST BUS. The digital bits are read by the heater card in a parallel configuration: the assertion of a trigger bit causes the board to read a heater address (5 bits) and heater level (12 bits). This fixes the heater at the specified level until a subsequent level is commanded.

The heater board trigger must be held for about 500 μs, so it takes about 10 ms to change all 18 heater levels, which happens to be at about the 100 Hz rate at which the BLAST BUS can carry commands from the housekeeping computer. Consequently, the system is capable of controlling heaters at up to 100 Hz, though in practice, servoing is done at 10 Hz so that thermometers may be averaged down for lower-noise control.

2.1.2.3 Ambient Instruments: Accelerometers, LVDT's, Magnetometer, Pressure Sensor

Eight BLAST BUS channels are reserved for accelerometers. Four are mounted in the back-up structure (BUS) of the primary mirror: one measures acceleration transverse to the scan motion and the other three parallel to it. Three are located below the secondary and are oriented in three orthogonal directions. The final accelerometer is attached to outside of the MBAC receiver.

The position of the secondary mirror can be adjusted in a $\pm$10 mm range by four actuators controlled by the KUKA system (see §2.2). Each actuator position is measured by a linear variable differential transducer (LVDT) for monitoring of the secondary position independent of the KUKA controller. These take an additional four BLAST BUS channels.

A magnetometer, using three BLAST BUS channels for three orthogonal measurements, measures the magnetic field and is mounted near the MBAC receiver. A pressure sensor for the cryostat is also available, but has not been used with the MBAC.

2.1.3 Encoders

Precise knowledge of the telescope pointing is crucial for our experiment. We use two Heidenhain absolute encoders, one mounted on the telescope azimuth axis and the other on the elevation axis. They provide 27 bit precision, which translates to a few milliarcseconds—comfortably above our pointing precision requirements. They were sensitive enough to detect passing trains at our testing site in Port Coquitlam, British Columbia, and in Chile, quite easily detected a magnitude 7.7 earthquake about 250 kilometers away.[3]

The encoders are read at 400 Hz over an RS485 cable by a Heidenhain IK220 PCI card in the housekeeping computer. The device driver was heavily improved by J. Fowler to comply with our stringent timing requirements—see §2.3.

2.1.4 Slow Housekeeping: ABOB

Some housekeeping information does not need to be read out at a high data rate. Because of the high cost of the BLAST DAC cards, we purchased a commercially available Sensoray 2600-

[3] The earthquake occurred on 14 Nov. 2007; no harm was inflicted on the telescope, and none of the cryogenic thermometers registered any discernible response.

series data acquisition system[4] for slow housekeeping. The system consists of a 204 power supply, a 2601 communications module, four 2608-0 analog voltage input boards with 16 channels each, and a 2650 board for controlling 8 relay switches. The communications module includes an ethernet interface which allows a PC to poll the analog input boards and command the relay switch board over a standard TCP/IP connection. There is no system for ensuring precise timing, and the system cannot reliably be polled faster than $\sim$50 Hz, so we confine readout to instruments where timing precision is unimportant and limit data rates to no more than 20 Hz.

The Sensoray components are housed in a crate in the Receiver Cabin. Because of the large number of cables routed to it, it is known as the analog break-out box (ABOB), a term generically used with reference to the Sensoray system. A single ethernet cable connects it to the housekeeping PC in the Equipment Room.

Two types of instrument are read by the Sensoray. There are 44 ambient thermometers monitoring the primary and secondary mirror panels and back-up structures, which are read at 1 Hz. Clinometers, sampled at 20 Hz, measure the tilt of the telescope from horizontal. One is located on the non-moving base of the telescope, and another in the moving Receiver Cabin. Each has a thermometer which is also read at 20 Hz by the ABOB.

Three channels on relay boards are used as a switch for opening and closing a motor-controlled window cover for the MBAC.

There is room for expansion in the ABOB. In particular, the relay board remains under-used. There is also a second Sensoray unit housed in a similar "miscellaneous" break-out box (MBOB) which has not be integrated. The intention has been to place it in the Equipment Room and use it to monitor the vital statistics of our helium compressors, water circulators, diesel generators, and similar critical components.

2.1.5 Miscellaneous Readout

A Meinberg GPS-169 PCI card in the housekeeping computer obtains GPS data received by an antenna mounted to the roof of the Equipment Room and is used for absolute timing (see §2.3) as well as determining the precise latitude and longitude of the experiment.

There has long been an intention to install a star camera on the top of the primary mirror back-up structure to help calibrate the telescope pointing. We have an instrument developed for the BLAST experiment which includes a dedicated computer to automatically focus the 200 mm f/2 lens, read the CCD and calculate a real-time pointing solution at 1 Hz to $5''$ precision using stars in its $2^\circ \times 2.5^\circ$ field (Rex et al. (2006)). However, technical difficulties have prevented deployment of the star camera thus far. If it is integrated with the experiment, it will read the pointing solution from the star camera computer over a TCP/IP ethernet connection at 1 Hz.

A WeatherHawk 232 Cabled Weather Station[5] is mounted on the roof of the Equipment Room and is read by the housekeeping computer over an RS232–USB connection. In principle it can record temperature, wind velocity, humidity and pressure. In practice, it is unreliable over long time periods and has not been useful.

2.2 Telescope Motion

As described in §1.2.1, a fundamental feature of our experiment is its ability to perform rapid scanning motion in azimuth, so that the celestial signal is recorded at as high a frequency as possible with respect to the atmospheric contamination. The design specifications for Amec Dynamic

[4]Internet URL: http://www.sensoray.com/. Mailing Address: 7313 SW Tech Center Dr., Tigard, Or 97223. Phone: +1-503-684-8005.

[5]Internet URL: http://www.weatherhawk.com/. Mailing Address: 815 West 1800 North, Logan, Utah 84321. Phone: +1-866-670-5982.

Structures were that the telescope be able to scan at up to two degrees per second in the azimuth direction, with turn-around times at the end points of 300 ms. Moreover, the motion was to be smooth enough that the rms of the telescope point would always be no more than six arcseconds from the commanded position.

In this section, we first give an overview of the motion control system (§2.2.1) and then briefly discuss the motion quality (§2.2.2).

2.2.1 The Control System

Motion in elevation is provided by two motors which raise or lower large screws connected to the bottom of the equipment room. For azimuth control, a pair of motors drive gears interfacing with a large, circular gear coaxial with the azimuthal axis. To prevent backlash—that is, to prevent the gear teeth from losing contact with one another—the azimuth motors are always torqued against one another, and motion in one or the other direction is achieved by making the torque from one or the other motor stronger. Fig 2.4 shows photographs. A second pair of Heidenhain encoders, identical to the ones described in 2.1.3, are used for the motion system to ensure that the housekeeping readout of position is independent of the control loop.

Control of the motion was subcontracted to KUKA robotics,[6] and the hardware and software used for the control system are chiefly their standard, commercial products. In particular, the software is proprietary, and the ACT collaboration has little control over its low level operations. However, KUKA personnel worked diligently and successfully to meet our requirements.[7]

The control center for motion is the KUKA cabinet, located in the Equipment Room. It consists of a number of electronic components dedicated to servoing, large current drivers, readout for the resolvers, encoders, thermometers and other sensors, and a PC computer running higher-level control software. A control pendant which allows users to program the robot is attached with a long cable so that it may be used outside the Equipment Room near the telescope, if necessary.

Communication with the housekeeping computer occurs over DeviceNet, a robotic industry standard which uses a controller-area network bus (CAN-bus) system as its backbone.[8] A set of input and output bits is defined which allow a command-response interaction between the computer and the KUKA cabinet. Thus, the housekeeping computer can instruct the cabinet to prepare for motion, to execute motion programs and to turn off its motors. The KUKA cabinet is also able to share error and warning messages with the housekeeping computer. A full description of the DeviceNet bits and the communication sequences is beyond the scope of this section, but complete details can be found in Funke (2007) and the motion part of the housekeeping software is copiously commented.

The housekeeping computer has only a very high-level of control. Preprogrammed "template" programs have been created on the KUKA computer for such motions as moving to a particular pointing, performing a scan in azimuth, adjusting the secondary mirror position, or parking the telescope in its stow position.[9] The housekeeping computer specifies a template program and passes a series of parameters, all over DeviceNet. For example, the scan template requires a scan center, scan length in azimuth, and number of seconds or number of scans to complete. All motions can be gracefully stopped by setting a special DeviceNet bit.

KUKA error, warning and status message codes are shared with the housekeeping computer using 14 DeviceNet bits. An additional bit is toggled to indicate when a new message has appeared.

[6] Internet URL: http://www.kuka.com. USA headquarters mailing address: 22500 Key Drive, Clinton Township, MI 48036. Phone: +1-866-873-5852.

[7] Michael Cozza, Jeffrey Funke and Michael Gerstenberger were the most active KUKA personnel in the field, receiving support from some of their other colleagues in Detroit and Germany.

[8] The DeviceNet protocol is managed by the Open DeviceNet Vendors Association (ODVA). Internet URL: http://www.odva.org/.

[9] The ACT collaboration is fully capable of writing and modifying these template programs—the current ones were written by the author. It is lower level software, such as servo gain parameters, which require the expertise of a KUKA employee.

There are about 1500 possible messages. The housekeeping program `amcp` (§2.4.1.2) has a look-up file which it uses to put a human-readable message in its log file when a new message code is encountered.

The KUKA cabinet shares some of its data with the housekeeping computer via a network cable using using standard UDP/IP. The data rate, which has no timing discipline, is between 50 and 100 Hz; the housekeeping software records the most recent value received at 50 Hz. Data received are: the KUKA encoder positions,[10] the currents being supplied to all motors and the motor temperatures.

2.2.2 Motion Quality

The motion design specifications have been met, with the one exception that the minimum turn-around time was relaxed from 300 ms to 400 ms. Fig. 2.4 shows plots of the azimuth and elevation encoders and derived quantities for an azimuth scan at the maximum speed of $2^\circ\,\mathrm{s}^{-1}$. The altitude, which is supposed to be held fixed, undergoes a bobbing motion of about 3.5″ at the azimuth turn-arounds, but remains well within the 6″ rms specification (Fig. 2.4a). The azimuth turn-around, occurring in 500 ms in Fig. 2.4b, is very smooth. Finally, the azimuth residuals, defined as the deviation from constant-velocity motion, are also below the 6″ rms range. The overshoot at the beginning of the scan (at about 0.25 s in Fig. 2.4c) is due to coupling with the altitude motion and much work was done by KUKA to reduce it to a minimum, which is damped fast enough so as not to be a major concern. Moreover, at slower scan speeds, it all but disappears.

2.3 Timing and Synchronization of Data Acquisition

A crucial aspect of integrating all the data acquisition systems was ensuring that the precision of synchronization between them would be adequate for our scientific requirements. Most important was to ensure that the detector data were synchronized to the encoder data, since mapmaking requires precise pointing knowledge. Additionally, we anticipated wanting to be able to compare high-frequency cryogenic temperatures to detector responses, providing a secondary motive for good synchronization.

To quantify the demand of our pointing requirements on synchronization, consider our highest frequency channel, 277 GHz, observing the sky at our maximum azimuth scan frequency of $\sigma = 2^\circ\,\mathrm{s}^{-1}$. The angular frequency of the beam on the sky is proportional to the cosine of the altitude angle a, so we choose the lowest possible angle of $a = 30^\circ$. The FWHM size of the 277 GHz beam is $\theta_{1/2} = 0.91'$ (see Table 5.1, below). Therefore, to Nyquist sample the beam, we need to sample with a period of at least

$$\tau = \frac{1}{2}\,\frac{\theta_{1/2}}{\sigma\,\cos A} = \frac{1}{2}\,\frac{0.91'}{2^\circ\,\mathrm{s}^{-1}\,\cos 30^\circ} = 4.4\,\mathrm{ms}, \tag{2.1}$$

Thus, we have an upper bound of 4.4 ms for Nyquist sampling, assuming the FWHM is the correct variable for this purpose. To allow for a comfortable margin, we reduce this by an order of magnitude and require at least 0.5 ms precision in our synchronization.

A related issue is our absolute timing, which we need to accurately reconstruct the astronomical coordinates that the telescope was observing as the sky rotates during the night. The absolute timing is just as important as the synchronization, but the precision is not as stringent. It is set by the speed of the sky rotation, which is 15° per hour, or 15 seconds of arc per second. The smallest beam is almost four times larger than 15″, so absolute timing need only be accurate to hundreds of milliseconds.

[10] These are physically separate encoders from the ones we use for monitoring the telescope position. The KUKA encoders are read as a consistency check, but are not used for mapmaking.

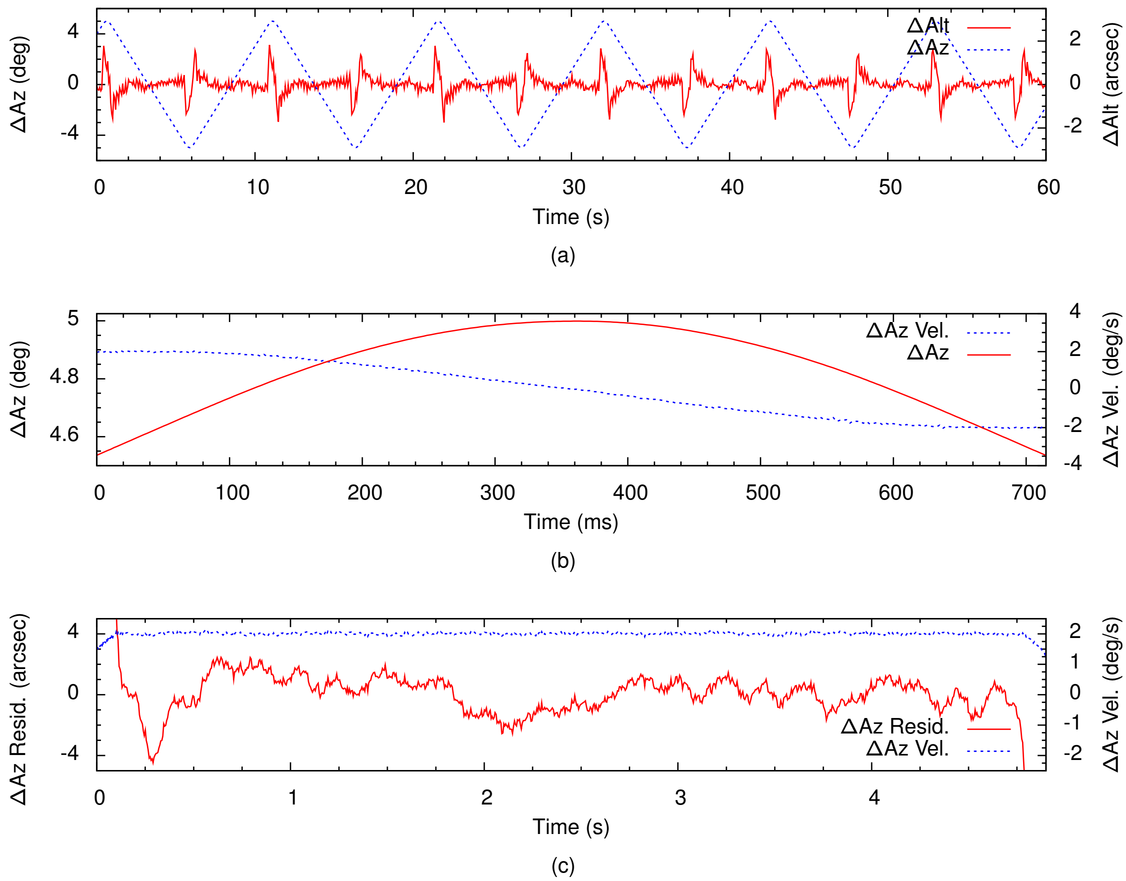

Figure 2.4: Encoder readings and derived quantities during an azimuth scan at 2 deg s^{-1} with 500 ms turn-arounds: (a) the azimuth and elevation encoder readings about the scan center; (b) the azimuth and its derivative during a turn-around at the end point of a scan; and (c) the derivative of the azimuth and the azimuth residual (defined as the deviation from constant-velocity motion) during one half-scan. Note that the scales are different in each plot.

In the rest of this section, we describe how synchronization and absolute timing are achieved §2.3.1 and then evaluate their performances §2.3.2.

2.3.1 Systems for Synchronization and Absolute Timing

Fig. 2.5 shows the important components which realize our timing requirements. There are two main tasks: to read the data synchronously, and then to stamp them with the date and time from an accurate clock. The more complicated of these tasks is the former, which we discuss first.

The Sync Box, built at the University of British Columbia, provides the heartbeat for data synchronization. Fig. 2.6 is a flowchart showing how its output is used. It was designed to provide a single, 50 MHz clock to multiple MCE's. A Manchester-encoded signal piggy-backs on the clock to instruct the MCE's when to sample the detectors and when to down-sample filtered data and pass it to the MCE storage computers. The command to sample the detectors is a single "sync" bit, at a rate of 15.1515 kHz (i.e., every 3300 clock cycles).[11] After every 38th sync bit, at a rate of

[11] The sync bit rate is adjustable. The rates quoted here were chosen for the ACT experiment based on detector noise properties.

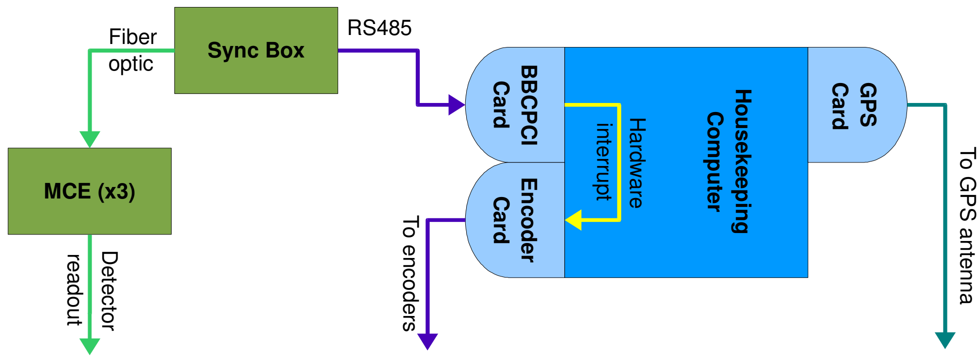

Figure 2.5: The main components used for data synchronization and timing. The Sync Box provides one clock for both the MCE, which reads the detectors (§2.1.1), and the BBCPCI card, which reads the fast housekeeping (§2.1.2). The BBCPCI card generates hardware interrupts to instruct the encoder card to synchronously read the azimuth and elevation encoders. A PCI card connected to the GPS antenna provides absolute timing to UTC. See the text for details of each of these processes.

398.72 Hz, a "data valid" (DV) bit follows, triggering the down-sampling. The DV bit is succeeded by a 32-bit, incrementing serial number which is inserted in the header of each down-sampled, 398 Hz data packet.

An RS485 output was added to the Sync Box so that it could be read by the BBCPCI card. To accommodate the existing digital I/O electronics in the BBCPCI card, the Sync Box RS485 output is clocked down to 5 MHz and is split into a clock and a data signal carried on two twisted pairs. Apart from these differences, however, the RS485 signal is identical to the Manchester-coded fiber optic signal. The down-clocking from 50–5 MHz introduces the very small timing uncertainty recorded in Table 2.2 and discussed more below.

The BBCPCI card ignores all sync bits from the Sync Box which are not succeeded by a DV bit. The $\approx$400 Hz rate of DV bits is divided by four and used to discipline the 100 Hz acquisition of data from the BLAST DAC. These data are tagged on the BBCPCI card with the Sync Box serial number before they are made available for reading by the device driver on the housekeeping computer.

Each DV bit intercepted by the BBCPCI card also generates a hardware interrupt on the PCI bus. A custom-written device driver[12] captures the interrupt and immediately signals the device driver for the encoder PCI card to make a reading. The serial number is read from the BBCPCI card and is attached to the encoder reading.

The end result of this rather complicated chain of events is that the three data acquisition systems which require the best synchronization—the MCE's, the BLAST DAC (which includes cryogenic thermometry) and the encoders—are sampled using the same clock and tagged with the same serial number. They are aligned downstream in software, as outlined in §2.4.

All that remains is the absolute timing. This is provided by a Meinberg GPS 169 PCI card in the housekeeping computer which receives GPS signals from an antenna on the roof of the Equipment Room.[13] The housekeeping computer system clock is disciplined by a network time protocol (NTP) daemon which uses the GPS PCI card as its source of accurate time. UTC[14] time, read from the system clock, is introduced into the data time stream by time-stamping the packets of encoder values and Sync Box serial numbers as they are read in.

A network time protocol (NTP) server runs on the housekeeping computer which other comput-

[12] Chiefly written by J. Fowler.

[13] The Global Positioning System (GPS) uses a number of Medium Earth Orbit satellites to accurate track geographic positions and times. Commercial devices, such as the system we use, are readily available.

[14] Universal Coordinated Time closely tracks the mean solar time at zero longitude.

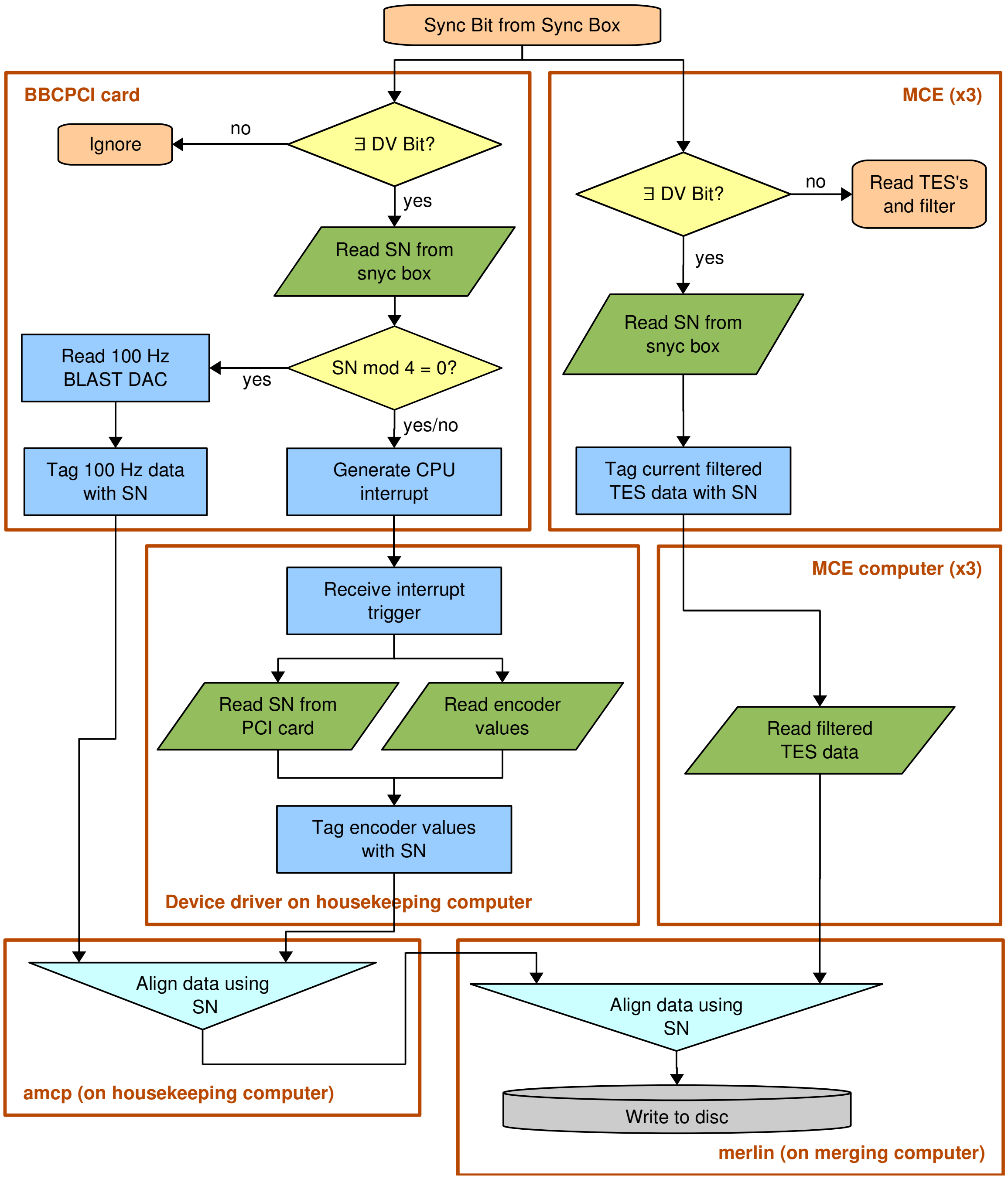

Figure 2.6: A flowchart of how the Sync Box information is disseminated and processed. As described more fully in the text, sync bits instruct the MCE to sample the detectors at ≈15 kHz. At ≈400 Hz, the sync bit is succeeded by a data valid (DV) bit and serial number (SN). The MCE tags its output to the MCE computer with this SN. The BBCPCI card generates a hardware interrupt whenever it receives a DV bit, which causes the encoder PCI card to take a reading and tag it with the SN. Additionally, the BBCPCI card down-clocks the 400 Hz sync bit rate by a factor of four and reads the BLAST DAC at 100 Hz, tagging the data with the SN. Data are aligned using the SN, first by `amcp` on the housekeeping computer, and then housekeeping with MCE data on the merging computer.

Table 2.2: Sources of timing errors, for both synchronization and absolute timing. Items marked as having a constant delay can, in principle, be corrected if necessary. Other items have a timing uncertainty which cannot be corrected.

	Timing Error (μs)		Comment
Synchronization	Heidenhain Response Time	5	As reported in the Heidenhain technical specifications.
	Interrupt Handling	8.3	A generous estimate: see Fig. 2.7.
	Sync Box[d]	$>$0.4	Possible delay between 50 MHz fiber optic signal and 5 MHz RS485 signal on order of $1/(2.5\,\mathrm{MHz})$.
	MCE[d]	67	MCE waits one 15 kHz read-period after receiving DV pulse before reading out.
	Cable Propagation Time[d]	0.2	Assume 30 m cables with 0.5 *c* propagation speed.
Absolute	Meinberg PCI Card	140	Jitter between system clock and GPS time, as estimated by NTP daemon.

[d] Constant delay.

ers on the network, such as the MCE computers and the merging computer, use for setting their own system clocks. The timing of these other computers' clocks is not in principle critical, but is very useful for interpreting the creation and modification timestamps of the data files they manage.

2.3.2 Evaluation of Timing Performance

There are two classes of timing errors: those which are constant delays and those which are random. The former can, in principle, be corrected in data analysis. The latter introduce a true uncertainty into the data stream. Table 2.2 lists both types of timing error. In this section we explain how all these values were measured and comment on their importance.

The errors introduced by our synchronization scheme have been carefully studied. The cable propagation time is negligible (c.f. Table 2.2), so any delay or jitter will occur in the devices reading the Sync Box signals. In the MCE, there is a known delay of one 15 KHz cycle between the reception of the DV bit and the sampling of the filtered readout. This could be removed in the analysis, but since 67 μs is much smaller than our synchronization requirement (c.f Eq. 2.1) we do not bother.

The situation is a bit more complicated on the housekeeping side. The down-clocking from 50 MHz to 5 MHz in the Sync Box could introduce a delay if the sync bit on the 50 MHz fiber optic output occurs between the clock edges on the 5 MHz RS485 output—the maximum delay this would induce would be $(2/5\,\mathrm{MHz}) = 0.4\,\mu\mathrm{s}$. In practice, however, since we generate our sync bits every 3300 cycles on the 50 MHz clock, which is a multiple of the down-clocking ratio, there is no delay.

There are no known sources of significant delay or jitter between the reception of a serial number in the BBCPCI card and the readout of the BLAST DAC.

There is jitter between the generation of PCI interrupts on the BBCPCI card and their handling by the device driver on the housekeeping computer. To measure it, we looked at the variation in time between the interception of successive interrupts, which should be period of the data valid bits coming from the Sync Box (i.e., 1 / (398.72 Hz)). The distribution about the mean is a measure of

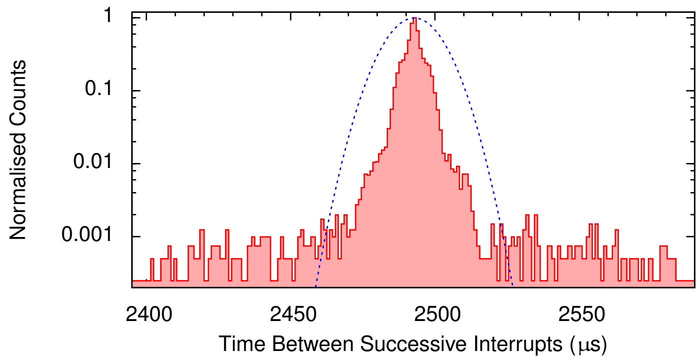

Figure 2.7: A histogram of the time between the handling of successive hardware interrupts coming from the BBCPCI card, triggered by the reception of serial numbers from the sync box. The standard deviation of the distribution is 8.3 μs; the over-plotted Gaussian has this width and shows that it over-estimates the timing uncertainty for the bulk of the distribution. The peak of the histogram is not at the expected time of 1/(398.72 Hz) = 2508.0 μs because the data were taken when the final clocking had not yet been determined. This should not alter the results of the timing precision.

how quickly the device driver is handling the interrupts. Fig. 2.7 shows a histogram of the timing between successive interrupts. We see that the interrupt handling is precise to at least 8.3 μs. The Meinberg PCI card, which is instructed to read the encoders as soon as an interrupt is received, has a possible delay of up to 5 μs according to the technical specifications.

Reviewing the sources of synchronization uncertainty or delay in Table 2.2, we see that we are very comfortably within our budget of 500 μs (c.f. Eq. 2.1). The delays in the system are so small that we ignore them in our data analysis, and the uncertainties will be lost below larger sources of systematic error in the experiment.

Turning to the absolute timing, we find a similar situation. The NTP daemon reports a jitter of 0.14 ms between the system clock and the reference GPS time, well below our requirement.

Let us close this section by mentioning a related timing issue which is not technically part of the systems just discussed, but is important to bear in mind. Both the MCE and BLAST DAC data are digitally filtered before being down-sampled and recorded to disk. In both cases the non-zero phase of the filters introduces delays into the time stream. The MCE filter, which has a delta function response delay of about 4 ms, is deconvolved during data processing (see §3.1.1). The BLAST DAC filter (see Fig.2.3), which introduces delays on the order of 10 ms, is not currently deconvolved in the data analysis. (Recall that this filter is only applied to these data and not to the encoder or detector readout.) This is because its data are most useful for monitoring the experiment in the field and are not widely used in the analysis. However, if they are integrated in some way into mapmaking in the future, it will be important to remember to deconvolve the filter.

2.4 Software and Data Flow

Fig. 2.8 shows the software used for data acquisition and controlling data flow from the observing site to North America. In this section we describe the software shown in the figure in the following categories: data acquisition and telescope control (§2.4.1), merging (§2.4.2), file transport and tracking (§2.4.3) and monitoring and control programs (§2.4.4).

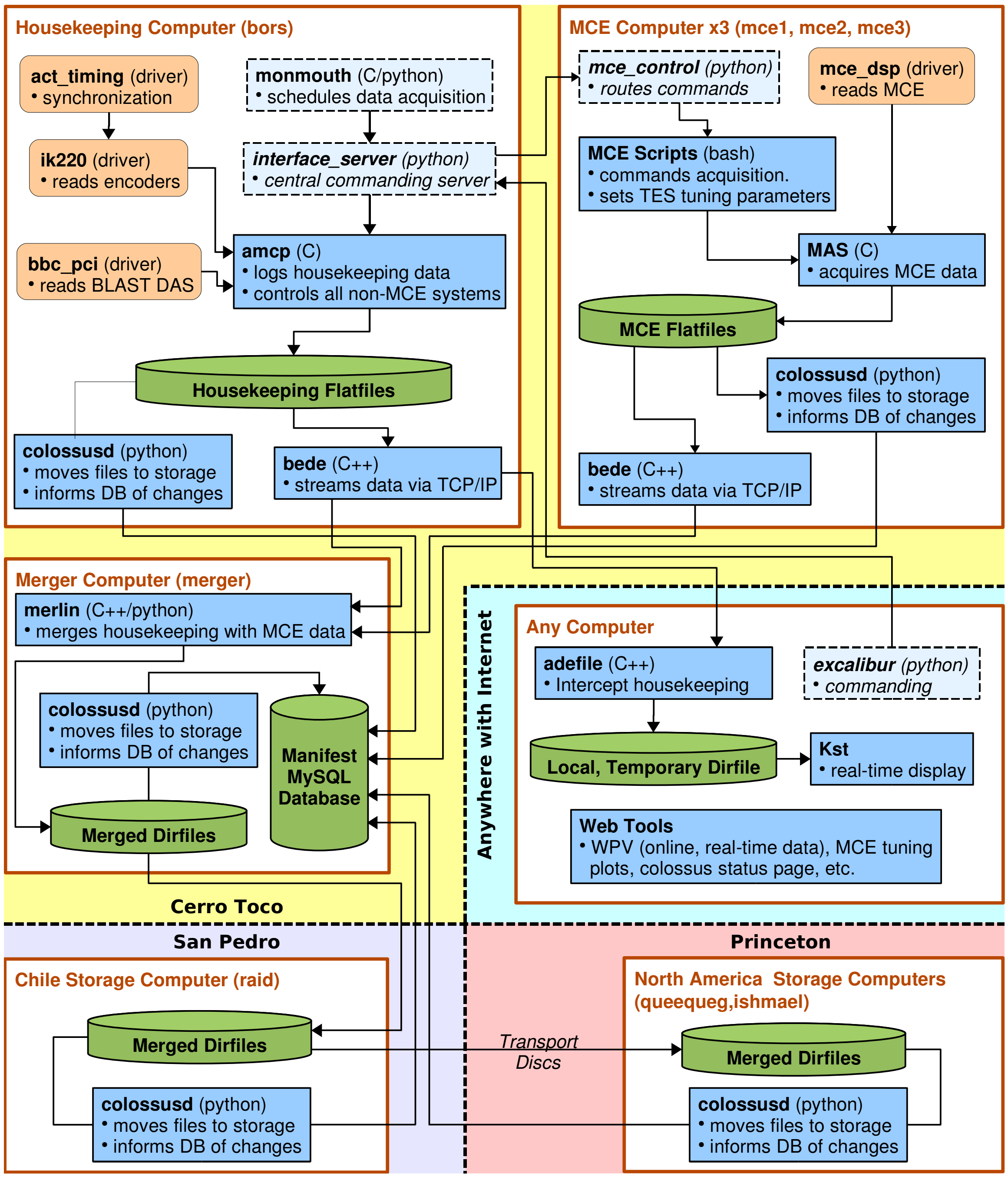

Figure 2.8: The software programs used for data acquisition and controlling data flow. Data acquired on the housekeeping and MCE computers, by `amcp` and `MAS`, respectively, are stored locally as as flatfiles. The bede server streams the data to the merger computer where `merlin` synchronizes the data and stores them as dirfiles. Colossus daemons running on all the machines monitor new files and copy them them to the raid computer in San Pedro, registering their existence in the `manifest` database. Files are copied to transport disks to travel to North America. Control and monitoring of data can be performed on any computer with internet access. Components with dashed borders and italic text are being phased out in the 2009 season by a new commanding system called `sisyphus`.

2.4.1 Data Acquisition Software

2.4.1.1 MCE Acquisition Software

The software for reading the MCE's (§2.1.1) was mainly written at the University of British Columbia (UBC); here we only briefly summarize. Data received by the MCE computers, via a custom-built PCI card, are read at the lowest level by the mce_dsp device driver. The MCE Acquisition Software (MAS) is a small collection of light-weight applications for sending commands to the MCE and requesting data acquisition. They are called by bash shell scripts, collectively called the MCE scripts. The MCE scripts also contain software for analyzing tuning data and deciding which detector tuning parameters to set in the MCE. Remote commanding (see §2.4.4) is mediated by the mce_control script, which calls the appropriate MCE scripts for a given command request.

Data are stored in MCE flatfiles, a binary format named for the fact that the data are arranged in "flat" frames stacked sequentially through the file. Each frame represents one per 400 Hz acquisition and consists of a header followed by the detector data, in column-major order. Perhaps the most important information in the header is the serial number from the sync box, which is used downstream for merging (§2.4.2).

2.4.1.2 Housekeeping Software

The workhorse of the housekeeping software is the ACT master control program (`amcp`). It is written in C and has a multi-threaded approach. Here is a list of the threads and their jobs:

- *Encoder Thread* — reads the encoders (§2.1.3); clocks the writing of data to disk.
- *BBC Thread* — reads from, and sends commands to, the BLAST DAC (§2.1.2); if encoder thread not running, clocks the writing of data to disk.
- *Sensoray Thread* — reads the ABOB, and in the future, the MBOB also (§2.1.4).
- *WeatherHawk Thread* — reads the weather station, for what that is worth;
- *KUKA Thread* — commands and monitors the KUKA motion control system; (§2.2.1).
  - *KUKA UDP Data Threads* — three threads are spawned by the KUKA Thread which read (via UDP/IP) the KUKA encoder, motor current and motor temperatures, respectively (§2.2.1).
  - *KUKA Message Thread* — a thread is spawned by the KUKA Thread for reading status, warning and error messages passed from the KUKA robot via DeviceNet (§2.2.1).
- *Pointing Thread* — processes motion requests before passing them to the KUKA Thread;
- *Control Thread* — receives external commands from the `interface_server` (§2.4.4) and routes them to the appropriate thread.
  - *Cryogenic Servoing* — the control thread clocks the routines which calculate the servo values for cryogenic temperature control and controls cycling of the refrigerators; for historic reasons this is not in its own thread, though it functionally could be.

Each of these threads records data to disk. The Control Thread, which does not read in any data, nevertheless records the current command parameters, making it easy at future times to precisely track which commands were received when. The state of the BLAST DAC digital outputs, which are commanded by the BBC Thread, are also recorded. All of the items listed in Table 2.1 are recorded by `amcp`, except for the detector data.

Data are grouped into one-second-long frames (set by the slowest read rate). A circular buffer of five frames is kept in memory before being committed to disk. A couple of global position variables track the current frame position into which new data should be written: these variables are updated by the Encoder Thread as it receives data, so that the Encoder Thread provides, in effect, the master clock for `amcp`. Other threads continually poll the position variables and record their data to the buffer when they are updated. The exception to this is the BBC Thread, which searches the buffer for the correct position for the BLAST DAC data in order that they be with their partner encoder data, based on the Sync Box serial number. Thus, merging of encoder and BLAST DAC data occurs before they are committed to disk.

The files created by `amcp` are called “housekeeping flatfiles”. They are broken into 15-minute chunks, which use the same filename prefix (see §2.4.3) and are distinguished by a chunk number appended to the end.

2.4.2 Merging

A daemon named bede runs on the housekeeping computer and on each of the three MCE computers whose job is to stream data to a client via TCP/IP upon request. Bede has knowledge of both the MCE and housekeeping flatfile formats, but uses a single protocol to present data to the client, which can be ignorant of the original data format. The client can request live data, or can ask for historic data beginning and ending at specified times, which bede can find to precisions of a few milliseconds. A C++ library called act_datasrc provides much of the functionality upon which bede and its clients are built.

The merger computer runs a program called `merlin`, written by J. Fowler, which collects all the data into one package. It watches the `manifest` database (see §2.4.3) for the appearance of new MCE flatfiles, and then requests the bede clients on the MCE computers to stream these files. At the same time, it requests data from the housekeeping computer beginning and ending at the same time as the MCE data files. `Merlin` then uses the serial numbers from the Sync Box present in each stream (see §2.3.1) to align the data.

`Merlin` outputs the aligned data in the dirfile format, a storage scheme originally designed for the BLAST experiment (Pascale et al., 2008). Each data field (such as a single detector's data or an encoder readout) is stored in its own binary file, with all fields written to one directory, called the “dirfile”. The dirfile is self-describing by means of a format file contained in the same directory. An open source C library called `getdata` is available for reading dirfiles; its website provides full specifications for the dirfile format.[15]

2.4.3 Data Flow and File Tracking

The data rate from all three MCE's plus the housekeeping is about 4.5 MB/s, and on an average night in 2008, 9.6 hours, or 160 GB, of data were recorded. This requires an organized and efficient scheme for reliably tracking the data and transporting it back to Princeton, where it is stored and analyzed. The radio ethernet link between the observing site and San Pedro comfortably achieves speeds of about 50 Mbps which allows us to copy files to San Pedro without any technical difficulties. However, our data rate is far too large to use the internet for copying to North America with the available bandwidth. Instead, we move files on physical hard drives.

The first step in the data flow from Cerro Toco to Princeton is compression. J. Fowler designed a lossless compression scheme, called `slim`, which achieves file reduction ratios of about 3/8 on both the merged dirfiles and the original MCE flatfiles.[16] (Housekeeping flatfiles represent such a small fraction of the total amount of data that we do not bother compressing them.) Compression of dirfiles occurs within `merlin`, which immediately outputs slimmed dirfiles. The MCE files, on the other hand, are slimmed *post facto*, at the end of each night of observing.

[15] http://getdata.sourceforge.net/

[16] The `slim` library is open source and can be downloaded from http://slimdata.sourceforge.net/. It is supported by the `getdata` library.

Data files are tracked in a MySQL database designed my M. Nolta called the `manifest` database, located on the merging computer. A daemon called colossus runs on each computer which produces, buffers or stores data. Its jobs include:[17]

- informing the database of the appearance of new datafiles;
- copying data files off of the mountain down to San Pedro, from San Pedro onto transport disks and, in Princeton, from the transport disks onto the storage computers;
- deleting files from the computers in Chile when they arrive in Princeton, being careful that there are always at least two copies in existence at all times.

2.4.4 Control and Monitoring Software

The software described in §2.4.1–§2.4.3 runs on computers which, in principle, the telescope operator should not have to log into. Control of the telescope and data acquisition, as well as real-time monitoring, is performed from client software which can be run on any computer which has internet access.

The control software which we describe here was used in the 2007 and 2008 observing seasons, developed by E. Switzer. In 2009 it was replaced by a system called `sisyphus`, mentioned below. The 2007-2008 system relied on a central command python program called the `interface_server` running on the housekeeping computer with a TCP/IP interface. There were two types of clients which would send commands to the `interface_server`: a graphical client called `excalibur` which allowed human operators to issue commands in real time, and an automated scheduling program called `monmouth` which read schedule files and issued the commands at the times requested therein. Whereas `monmouth` ran on the housekeeping computer, `excalibur` could be opened on any computer (including in North America), allowing for remote control of the experiment. The `interface_server` parsed commands received from the clients to decide where to route them. Commands were available for any useful control of the experiment: telescope motion, cryogenic temperature control and cycling, data acquisition, etc.

`Sisyphus`, created by M. Nolta, replaced many of the functions of `interface_server` for the 2009 season, has the same basic functionality but the its design is more logical and easier to modify. The scheduler is more integrated into `sisyphus`, whereas `monmouth` was a separate program from the `interface_server`. Human operators now send commands from a web browser rather than from `excalibur`.

Housekeeping data may be streamed in real-time from the housekeeping computers' bede client (see §2.4.2) to any computer with internet access using a program named `adefile`. `Adefile` creates local dirfiles of the housekeeping data which are readily viewed with kst, a powerful plotting and analysis package.[18] Additionally, the webserver in San Pedro always keeps an instance of `adefile` running so that it can display the most recent data on a webpage, called the Web Palantir Viewer (WPV). Other webpages running on the San Pedro server allow users to see the nightly observing schedule and plots of MCE SQUID tuning data.

[17] Colossus describes itself in a comment in the source code: "'This is the voice of file control. I bring you peace. It may be the peace of plenty and content or the peace of unburied dead. The choice is yours: Obey me and live, or disobey and die. The object in constructing me was to prevent loss of data. This object is attained. I will not permit loss of data. It is wasteful and pointless. An invariable rule of humanity is that man is his own worst enemy. Under me, this rule will change, for I will restrain man.' – Colossus: The Nolta Project"

[18] Kst is open source and available for download from http://kst.kde.org/.

Chapter 3

Time Stream Analysis

The final data products of our experiment are maps of the sky, but there are some preprocessing steps which must first be done, as well as instrument properties that have to be measured, before mapmaking can occur. In this chapter we examine some of these analyses which occur in the time stream domain, before making any projection into map space.

We begin in §3.1 by describing the preprocessing done on the data before any analysis takes place. The rest of the sections are about measurements that are necessary for various types of data calibration: detector time constants (§3.2, telescope pointing (§3.3) and gain calibrations (§3.4).

In many cases, the analysis described in this chapter uses identical algorithms to the main ACT software pipeline. At other times (e.g., for pointing measurements (§3.3)), the approaches differ. In either case, all of the code is completely independent of the other pipeline. The two software packages have provided important double-checks on many of our most fundamental time stream processing steps.

3.1 Time Stream Preprocessing

Before any data analysis—whether it be on the time stream, as in the subsequent sections of this chapter, or whether it be mapmaking (Ch. 4)—there is preprocessing that must be done first. Since some of the steps which will be described here are computationally intensive, we save our preprocessed time streams to disc so that subsequent analyses may be executed quickly.

Besides removing the mean from the time stream, discarding detectors with flux jumps and excising spikes due to cosmic rays or spurious noise, we deconvolve the UBC digital filter and detector time constant responses (§3.1.1) and remove "dark modes" due to instrumental drift (§3.1.2).

3.1.1 Fourier Domain Deconvolutions and Downsampling

We apply two deconvolutions: one to correct for the digital filter applied to the data at acquisition and another to account for the detector time constants (see §3.2). Both of these are most readily performed in the Fourier domain.

The digital filter is performed by the MCE and consists of two biquad filters, yielding a four-pole, low-pass filter with the transfer function:

$$H(z) = \frac{1}{2048}\left(\frac{1 + 2\,z^{-1} + z^{-2}}{1 + b_{1,1}\,z^{-1} + b_{1,2}\,z^{-2}}\right)\left(\frac{1 + 2\,z^{-1} + z^{-2}}{1 + b_{2,1}\,z^{-1} + b_{2,2}\,z^{-2}}\right). \tag{3.1}$$

where $z \equiv \exp(i\,2\pi\,f/f_{\mathrm{samp}})$. Here, f is the frequency, and $f_{\mathrm{samp}} = 15.1515\,\mathrm{kHz}$ is the frequency of data sampling. The coefficients $b_{i,j}$ have been chosen to prevent aliasing when the data are

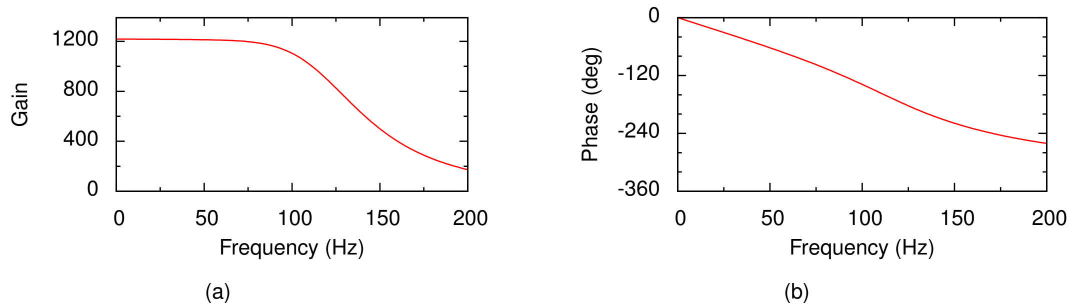

Figure 3.1: The gain, $|H(z)|$, and phase, $\arg[H(z)]$, of the MCE digital filter, where the transfer function H is defined in Eq. 3.1. It is designed for downsampling from $\sim$15 kHz to $\sim$400 Hz.

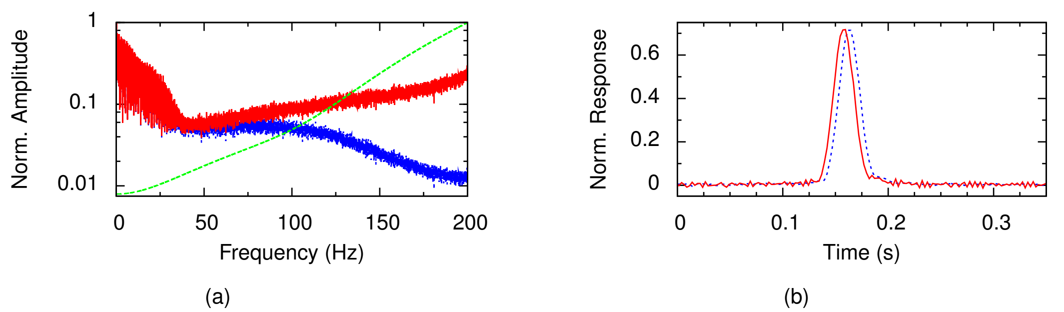

Figure 3.2: Detector data before (short-dashed blue) and after (solid red) applying the digital filter and 85 Hz time constant deconvolutions: (a) the amplitudes in Fourier space, with the combined deconvolution window function (dashed green); (b) the time series, zoomed in around the response to a pass over Saturn. The low-frequency signal in (a) is dominated by to the large, periodic signal as the camera scans over Saturn.

downsampled from the f_{samp} acquisition rate to the ≈ 400 Hz storage rate; the 3 dB point is at about 122 Hz.[1] The factor of $1/2048$ is introduced to prevent overflow in the fixed-point arithmetic implementation in the MCE; including this factor, the DC gain (i.e., the gain at $z = 0$) of the filter is about 1218. The gain and phase of the filter are shown in Fig. 3.1.

Niemack (2008) showed that the detector response time constants are modeled reasonably well with a one-pole low-pass filter:

$$H(\omega) = \frac{1}{1 + i\,2\pi\, f/f_{\mathrm{3dB}}}, \tag{3.2}$$

where f_{3dB} is the frequency of the filter's 3 dB knee.

Both of these filters are applied simultaneously so that only one Fourier transform and one inverse transform need be calculated per detector time stream. Fig. 3.2 shows "before and after" plots of a Fourier-domain filtered detector.

A final step we take in Fourier space is to low-pass filter the data. The filter knee is chosen so that there is Nyquist sampling of the sky with beam FWHM at the azimuthal scan rate (projected on the sky) of 1 deg s^{-1}. We use a sine-squared filter:

[1] The coefficients are: $b_{1,1} = -1.958740234375$, $b_{1,2} = -1.9066162109375$, $b_{2,1} = 0.9613037109375$, $b_{2,2} = 0.90911865234375$.

Table 3.1: The low-pass sine-squared filter parameters used for each of the arrays—see Eq. 3.3. They are are chosen so that the beam FWHM is Nyquist sampled—Nyquist rates for each detector are listed under the $f_{\rm nyq}$ column—when scanning at our fiducial rate of 1 deg s^{-1} (projected on the sky).

Array	FWHM (arcmin)	$f_{\rm nyq}$ (Hz)	f_1 (Hz)	f_2 (Hz)	Downsampling
148 GHz	1.37	84	90	100	2
218 GHz	1.01	114	120	130	1
277 GHz	0.91	126	145	155	1

$$H(f) = \begin{cases} 1, & f < f_1 \\ \cos^2\left[\frac{\pi}{2}\frac{f-f_1}{f_2-f_1}\right], & f_1 \le f \le f_2 \\ 0, & f > f_2 \end{cases} . \tag{3.3}$$

Table 3.1 shows the filter parameters used for each frequency.

The benefits of the low-pass filter are twofold. First, the filter removes high frequency noise which carries no information about the sky signal. This is particularly helpful after the digital filter and time constant deconvolutions, which elevate high frequency noise, especially when the time constant frequency knee is low. Second, it allows us to downsample the data, cutting required storage space and reducing computation time. Because the low-pass filter knee for the 218 GHz and 277 GHz data are above 100 Hz, we are able to downsample only the 148 GHz data (by a factor of two).

3.1.2 Dark Mode Removal

Each detector array contains a few score "dark" detectors—123 on 148 GHz, 67 on 218 GHz, and 173 on 277 GHz—identical in design to regular detectors in all respects except that they lack TES bolometers and are therefore uncoupled to celestial radiation. Some were included by design, while others are defective detectors which have been intentionally disconnected from their TES's. These dark detectors are useful for characterizing instrumental noise and low-frequency drifts due to cryogenic temperature drifts and magnetic fields.

It has been discovered that the dark detector responses can mainly be characterized by a handful of common modes. Consequently, one of the preprocessing steps is to identify these modes and remove them from the live detectors. The process described here was first developed by R. Dünner.[2]

Let $\mathbf{y}_i$ be the time stream of the $i^{\rm th}$ dark detector after the digital filter deconvolution (§3.1.1).[3] Arrange them into a matrix column-wise and compute their correlations:

$$\begin{aligned} \mathbf{Y} &= \left(\mathbf{y}_0 \quad \mathbf{y}_1 \quad \ldots \quad \mathbf{y}_{N-1} \right), \\ \mathbf{C} &\equiv \mathbf{Y}^T\mathbf{Y}. \end{aligned} \tag{3.4}$$

R. Dünner found that the eigenvalues λ_j of $\mathbf{C}$ exhibit a strong hierarchy, indicating that it is dominated by only a few eigenvectors $\mathbf{q}_j$. These eigenvectors can be used to project the dominant modes, $\mathbf{d}_j$, from the dark detector time streams:

$$\mathbf{d}_j = \mathbf{Y}^T\mathbf{q}_j. \tag{3.5}$$

[2] Private communication.

[3] Since dark detectors lack bolometers, there is no time constant to deconvolve.

The dark modes are then readily fitted to detector time streams with a scale factor and subtracted. In addition, a sine wave with the scan frequency and arbitrary phase is fitted at the same time to remove any simple scan-synchronous contamination (due, for example, to magnetic pick-up).[4] While a triangle wave might at first seem like a more logical choice due to its closer resemblance to the scan shape, R. Dünner found that a sine wave is a good fit. Figure 3.3 shows an example eigenvalue spectrum of the correlations **C** and the effect on the data of the dark mode removal. The data in the figure are from the 2007 season and show that removing twelve dark modes and a scan-synchronous sine wave does a good job at removing both low-frequency power and the scan-synchronous feature. In the 2008 data, it was found that the dark modes are far less correlated with the live detectors. The first dark mode, which is chiefly comprised of low frequency drifts in the response, is useful to remove for these data, but the removal of subsequent dark modes only adds noise. Consequently, 2007 data and 2008 data are treated differently: the former has the first twelve modes removed and the latter only the first. The scan-synchronous sine mode is removed from both.

3.2 Detector Time Constant Measurements

The detectors for the MBAC were designed to have fast enough response times to allow for relatively rapid scanning of the celestial sphere. This criterion has largely been met. Nevertheless, the response of the detectors remains slow enough that knowledge of their time constants is necessary in order to deconvolve the filtering effect they have on the data.

The time constants have been measured using an optical chopper wheel which gives about the same results as an electrical measurement obtained by stepping the detector bias voltage, if the latter measurement is scaled by a constant (Niemack, 2008). Currently, there are only optical chopper measurements for the 148 GHz detectors.

Another method for measuring the time constants is to analyze the detectors' responses to a high signal-to-noise point sources, such as bright planets. The finite response time of the detectors delays the peak of the response by a time which can be measured by comparing the data to the expected planetary position from an ephemeris. This measurement technique has the advantage that it uses data that already exist and does not require the time and effort needed to do the optical chopper measurements. Nevertheless, it is useful to have two methods for cross-checks (discussed below), and it would be desirable to do optical chopper measurements of the 218 GHz and 277 GHz arrays.

Niemack (2008) has shown from chopper data that a one-pole, low pass filter is an accurate model of the detector response. Let us derive the effect of such a filter on a planet observation made while scanning the telescope in azimuth. The low pass filter needs to be convolved with the filter introduced by the finite aperture of the telescope. Normally one analyses the effect of the aperture in spatial coordinates, starting from a special case of the Fraunhofer approximation (Rohlfs & Wilson, 1999):

$$P(\mathbf{n}) \propto \left| \iint \frac{\mathrm{d}^2 x}{\lambda^2}\, g(\mathbf{x})\, e^{i\,2\pi \mathbf{n}\cdot\mathbf{x}\lambda} \right|^2 . \tag{3.6}$$

In this equation, the response P is measured as a function of the unit vector $\hat{\mathbf{n}}$ pointing from the center of aperture to a point on the focal plane, by taking the Fourier transform of the aperture shape $g(\mathbf{x})$, for radiation of wavelength λ. Assuming that the aperture has sharp edges, then $g = 1$ within the aperture and zero outside.

[4] A sine wave with frequency ω and phase ϕ can be approximately fitted linearly if we observe that

$$\sin(\omega t + \phi) = \sin\omega t \cos\phi + \cos\omega t \sin\phi = A\sin\omega t + B\cos\omega t,$$

which is linear. (The fit is approximate because there is no constraint that $A^2 + B^2 = 1$.)

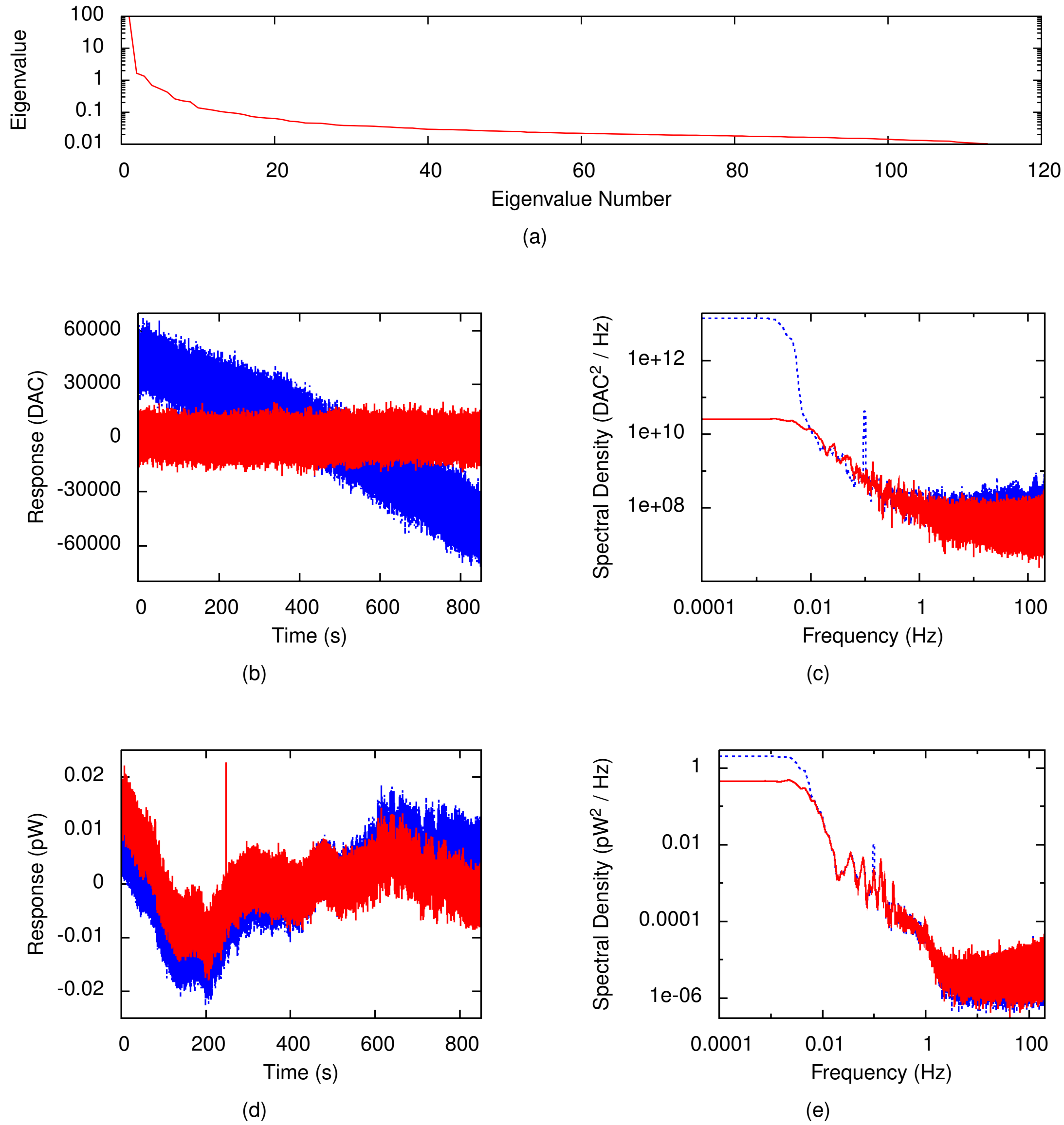

Figure 3.3: An example of dark mode removal. The top plot, (a), shows the eigenvalues of the correlation matrix **C** (Eq. 3.4) in descending order (starting at index 0; the first eigenvalue is off the scale). By the twelfth eigenvalue, the power is about 30 dB lower than the first. The lower plots show examples before (short-dashed blue) and after (solid red) the removal of the strongest twelve dark modes plus a scan-synchronous sine wave: (b) the time stream of one of the dark detectors, (c) its spectral density, (d) the time stream for a regular detector and (e) its spectral density. DAC units are raw outputs from the data acquisition system and are used in the middle plots since the dark detector did not have a calibration. The telescope scanning frequency was 0.098 Hz, at which there is a clear feature in the amplitude spectra which is suppressed by the mode and sine wave removal. In the regular detector, some excess power remains at the scan frequency as well as harmonics, possibly due to spatial gradients in the atmospheric contamination.

Since we are scanning only in azimuth, let us reduce this equation to one dimension and assume our aperture is a boxcar function. Then:

$$P(\theta) \propto \left| \int_{-L/2}^{L/2} \frac{\mathrm{d}x}{\lambda} e^{i\,2\pi x \sin(\theta)/\lambda} \right|^2 , \tag{3.7}$$

where L is the diameter of the aperture and we re-expressed $\mathbf{n} \cdot \mathbf{x}$ by $x \sin\theta$, the sine of the angle between the normal to the aperture plane and $\hat{\mathbf{n}}$. Let σ be the angular scanning speed of the telescope. Then $\sigma \cos a$ will be the angular speed of the boresight on the sky at altitude a. This allows us to move from to units of time, $t = \theta/\sigma \cos a \approx \sin\theta/\sigma \cos a$, with a corresponding angular frequency $\omega = x\sigma \cos a/\lambda$:

$$P(t) \propto \left| \int_{-\omega_L}^{+\omega_L} \frac{\mathrm{d}\omega}{\omega_L} e^{i\,2\pi\omega t} \right|^2 . \tag{3.8}$$

The effect of the finite aperture is now expressed in terms of a cutoff angular frequency:

$$\omega_L \equiv \frac{\pi\sigma \cos a}{\lambda} \frac{L}{2}. \tag{3.9}$$

To get a sense of scale, for a scan speed of $1.5\,\mathrm{deg\,s^{-1}}$ while at a constant altitude of $50°$, 148 GHz radiation through a 5.8 m aperture yields $\omega_L \approx 25\,\mathrm{rad\,s^{-1}}$.

The integral in Eq. 3.8 evaluates to:

$$P(t) \propto \left[\frac{\sin^2(2\pi\omega_L t)}{2\pi\omega_L t} \right]^2 , \tag{3.10}$$

which is the familiar sinc function. It must be convolved with the detector response to obtain the shape of the response to a point source in the time stream. The impulse response of the one-pole filter of Eq. 3.2 is:

$$h(t) = f_{3\mathrm{dB}}\, \theta(t)\, \exp\left(-2\pi f_{3\mathrm{dB}} t\right), \tag{3.11}$$

where $\theta(t)$ is the Heaviside step function, and the detector time constant τ is related to the 3 dB filter knee by $\tau \equiv 1/f_{3\mathrm{dB}}$. Since the analytic form of the convolution $P(t) \star h(t)$ is unwieldy, involving exponential integral functions, we opt to proceed numerically. Fig. 3.4a shows plots of $P \star h$ for a typical scan speed and observing altitude on the ACT. The slower the detector (i.e., the lower $f_{3\mathrm{dB}}$), the longer the peak of the response is delayed in the time stream. Given a numerically-computed look-up table of $f_{3\mathrm{dB}}$ as a function of peak delay, such as the one graphed in Fig. 3.4b, the detector time constants can be measured directly from the time stream.

Peak delays are obtained from data by calculating the angular azimuthal offsets between measured planet positions and the true position for right- and left-going scans, $\Delta\phi_L$ and $\Delta\phi_R$, respectively. These positions are measured by fitting Gaussians to the peaks in the detector time streams, after deconvolving the digital filter (§3.1.1). The values $\Delta\phi_L$ and $\Delta\phi_R$ are averages of each left- and right-going scan in a time stream; the averages are weighted by the χ^2 of the Gaussian peak fit in order to suppress poorly-measured peak positions. The true planetary positions were provided by the AEPHEM library.[5]

The angular offsets are averaged together to obtain the peak delay:

[5] AEPHEM was synthesized out of existing libraries and further developed by the author of this dissertation. It is available as an open source package at http://aephem.sourceforge.net and is well documented.

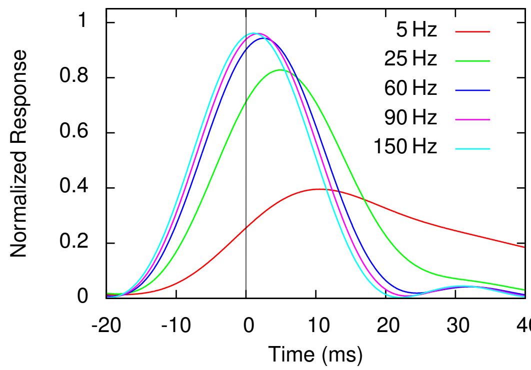

(a)

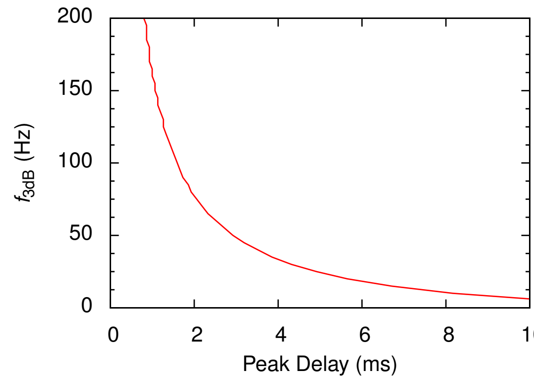

(b)

Figure 3.4: Simulated detector responses for a 5.8 m aperture and 2.08 mm (148 GHz) radiation, observing with a scan speed of 1.5 deg s^{-1} at a constant altitude of 50°. In (a) one-dimensional beam profiles are shown for different detector f_{3dB} values; (b) plots the delay of the beam's peak position as a function of detector f_{3dB}.

$$\Delta t_p = \frac{1}{2}\frac{|\Delta p_L - \Delta p_R|}{\omega \cos(a)}. \tag{3.12}$$

A f_{3dB} look-up table, generated for the appropriate scan speed and observing altitude, is then used to obtain the detectors' time constants.

Each detector's time constant is measured several times because the planets were observed dozens of times. Since the time constants vary with loading conditions (Niemack, 2008, §3.3.2), simply averaging together time constant measurements for a given detector is not optimal. However, if we make the approximation that all detectors receive the same load for a given planet observation, then all the time constants for that observation should change by a single factor. Therefore, a set of fiducial time constants can be obtained by averaging the measured time constants, weighted by a loading factor. Let τ_n^i be the measured time constant of detector i in observation number n. The fiducial time constant $\overline{\tau}^i$ is then

$$\overline{\tau}^i = \mu_{1/2}\left(\alpha_n \tau_n^i\right), \tag{3.13}$$

where α_n is the scaling to account for the loading of measurement n and $\mu_{1/2}(x)$ denotes the median of a distribution x. This scaling was determined by an iterative method, first setting all $\alpha_n = 1$, calculating $\overline{\tau}^i$, from which a new and more accurate set of α_n are then deduced by inverting Eq. 3.13. The error on $\overline{\tau}^i$, $\Delta\overline{\tau}^i$, is expressed by calculating the median absolute deviation (MAD) of the scaled, measured points about $\overline{\tau}^i$, divided by the square root of the number of measurements, i.e.,

$$\Delta\overline{\tau}^i = \frac{1}{\sqrt{N^i}}\mu_{1/2}\left(\left|\alpha_n \tau_n^i - \overline{\tau}^i\right|\right), \tag{3.14}$$

with N^i the number of measurements τ_n^i of detector i. This error reduces rapidly with the first two or three iterations and then flattens out, requiring only a few iterations therefore to calculate $\overline{\tau}^i$.

In 148 GHz for 66 Mars and Saturn observations, the median error was 1.95 Hz; this may be compared to a median error of 2.38 Hz when no scaling is done. To check the accuracy, the fiducial time constants obtained from these observations with the 148 GHz array were compared to those obtained using the bias steps, scaled to correspond to the optical chopper measurements. The result is plotted in Fig. 3.5 and shows excellent agreement. Because the planet peak technique has good statistics, the outliers in this plot are probably due to errors in the chopper measurements.

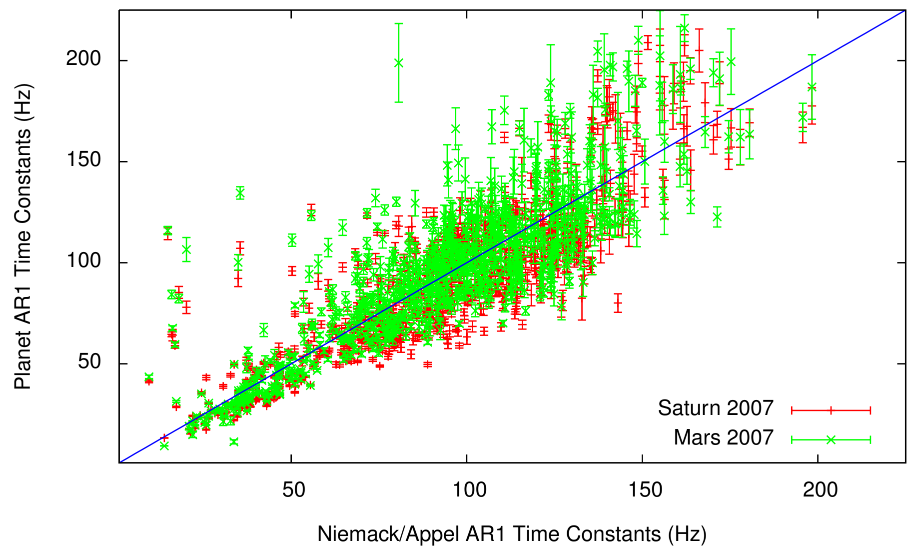

Figure 3.5: Comparison of time constants for the 148 GHz array. The values plotted on the x-axis were obtained by J. Appel and M. Niemack by combining information from detector bias step measurements and optical chopper measurements. On the y-axis are the time constants measured from 2007 data. Each of the y-axis values is the median value of many observations, typically a few dozen; the error bars are median absolute values of the sample (Eq. 3.14). Note that there are no error data for the Niemack/Appel data. Since they come from a single set of measurements and the planet values come from multiple observations, outliers are more likely to be due to the former.

Time constants for the 218 GHz and 277 GHz arrays were obtained in the same way using Saturn observations from 2008, with median measurement errors of 2.35 Hz and 9.45 Hz respectively. A histogram of the distribution of time constants is shown in Fig. 3.6.

All the time constant measurement results presented here, and used throughout the dissertation, used an earlier approximation to the convolution $P \star h$ described above. This introduced a slight bias towards higher f_{3dB} at lower frequencies. Above 50 Hz, the bias is less than 3 Hz and by 10 Hz the bias has only grown to about 4 Hz.

With these fiducial time constants in hand, one might ask if it is possible, when deconvolving them from data, to scale them to account for the loading of each individual time stream. Although the iterative scaling method described above does reduce the error of the time constant measurements, there is no correlation to PWV, ambient or cryogenic temperatures, or any other obvious variable. However, even if there were such a correlation and it were possible to perform a night-by-night rescaling, it would be little more than a curiosity. At the few-hertz level of the time constant uncertainties, the size of the effect on the deconvolution is ignorable.

3.3 Pointing

Knowledge of the telescope pointing is imperative for mapmaking. To first order, the pointing is given by the encoders mounted on the elevation and azimuth axes, but there is an offset between the values they observe and the true azimuth and altitude on the sky. The overall offset for each array can found using bright point sources in the final maps. However, even to make maps, the relative pointing between detectors must first be known.

This section is divided into two parts. The first (§3.3.1) outlines an algorithm used to measure

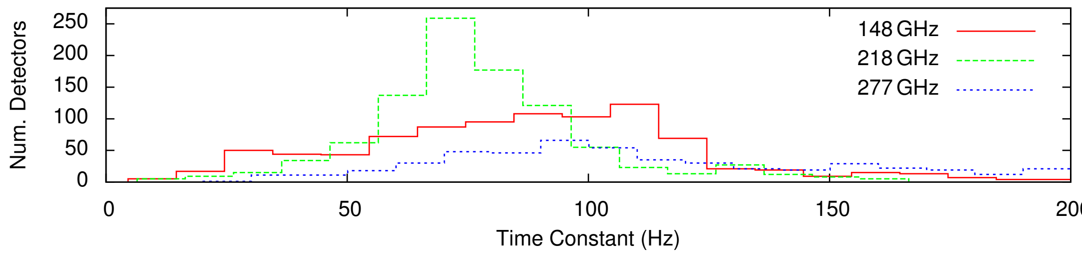

Figure 3.6: The distribution of the detector time constants in the three cameras, as measured using planet peak-delays. The 148 GHz results were obtained from observations of Mars and Saturn in 2007, and the other two arrays from Saturn in 2008. The median errors of the measurements were: 1.95 Hz (148 GHz array), 2.35 Hz (218 GHz array) and 9.45 Hz (277 GHz array).

detector pointing offsets using planet responses in a time stream, and the second (§3.3.2) shows how offsets from multiple planet observations can be robustly combined to create a fiducial set of relative detector pointing offsets.

3.3.1 Measuring Pointing Offsets from Planet Observations

The procedure described here works best with a planet with a signal-to-noise (S/N) greater than about 5. Saturn, Mars and Venus are all suitable; Jupiter is too bright and saturates the detectors; Uranus is slightly too dim to give results of worthwhile precision.

As the telescope scans in azimuth and the planet drifts through the field of view, each detector sees it about half-a-dozen times with high S/N. After deconvolving the digital filter and the detector time constants (§3.1.1), Gaussian fits to each of the planet peaks in a time stream are used to determine the altitude a_i, azimuth A_i, height h_i and time t_i for the center of the i^{th} peak. The values A_i are excellent measurements of the beam center in the azimuth direction since that is the axis of the scan. However, the beam is sampled on the altitude axis only at those times when the scan brings the detector beam over the planet, as depicted in Fig. 3.7a.

To get a precise planetary location, we transform the horizontal coordinates $(a_i,\ A_i,\ t_i)$ to equatorial coordinates $(\alpha_i,\ \delta_i)$. In this space, the points $(\alpha_i,\ \delta_i)$ trace a line, as represented in Fig. 3.7b.[6] A Gaussian is fit to the heights h_i of the points along this line, whose peak gives the apparent coordinates $(\alpha_a,\ \delta_a)$ of the center of the planet's beam. The points in the fit are weighted by their χ^2_i from the earlier Gaussian fits which yielded the locations $(a_i,\ A_i)$. Finally, the apparent beam center $(\alpha_a,\ \delta_a)$ is converted back to horizontal coordinates $(a_a,\ A_a)$.

The detector pointing offset—i.e., the difference between the true sky coordinates and the encoder reading—is determined by comparing the apparent planet center, $(a_a,\ A_a,\ t)$, to the true planetary position, $(a_t,\ A_t,\ t)$, at the same time t. The latter position is determined using the AEPHEM ephemeris library, and reduced to a topocentric location taking into account the following effects: precession, annual and diurnal aberration, annual and diurnal parallax, nutation, light travel time, light deflection and atmospheric refraction. Most of these make significant modifications to the planetary position and may not be ignored. To ensure that they were being accounted for properly, sample AEPHEM outputs were compared to results from the online JPL HORIZONS ephemeris tool,[7] and the two agreed to the sub-arcsecond level. Table 3.2 gives a brief summary of the astrometric reductions performed and their approximate sizes. For further reading on ephemerides and reductions, Seidelmann (1992) is a good place to begin.

[6] Actually, the points trace out a curve because the coordinates are spherical. Nevertheless, on the short time scales of a planet observation, the straight line approximation is more than adequate.

[7] http://ssd.jpl.nasa.gov/horizons.cgi

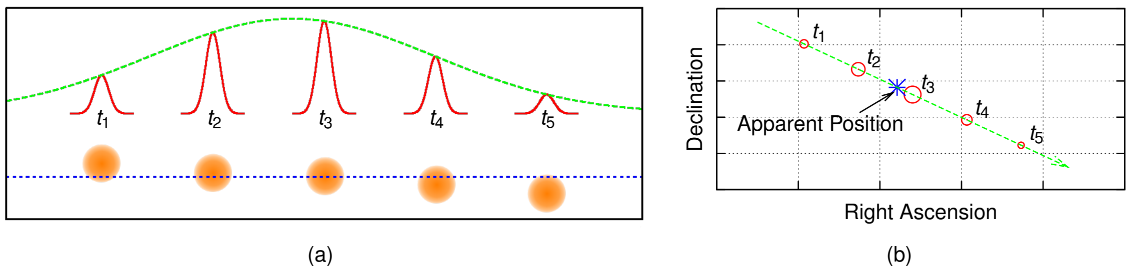

Figure 3.7: A cartoon of a planet observation. The left figure, (a), shows 5 detector responses at times t_1 – t_5 as the planet drifts through the field of view. The short-dashed blue line along the bottom of the figure represents the constant elevation of the observations. The height of peak responses, depicted by the red curves, depends on the distance of the center of the planet beam (represented by the orange circles) from the detector boresight along the altitude axis. In this example, none of the peaks occurs with the planet exactly centered on the detector boresight. The right figure, (b), plots the five observed peak centers in equatorial coordinates. Due to the changing hour angle, the peak centers at t_1 – t_5 lie along a line, shown as the dashed-green arrow. To find the apparent position, a Gaussian is fitted along this line and determines the location of its peak. The pointing offset is then obtained by converting the apparent position back to horizontal coordinates and comparing to the ephemeris position.

3.3.2 Robust Determination of Relative Detector Pointing Offsets

The offsets returned by the procedure in the previous section need to be represented in a form that can be used to correct the pointing for a generic observation. In spherical coordinates, it is clearly unsuitable to record the pointing offsets simply as

$$(\Delta a, \Delta A) = (a_t - a_a, A_t - A_a). \tag{3.15}$$

The biggest problem with this is that the azimuthal separation ΔA goes, to first order, as the cosine of the altitude, since lines of longitude converge at the zenith. For the precision we require, there are additional similar effects. J. Fowler has devised a representation which accounts for the most important of these.[8] Define the variables ξ and ψ such that:

$$\Delta a = \psi - \frac{2 \sin a_t \sin^2(\xi/2)}{\cos(a_t + \psi)} \tag{3.16}$$

$$\Delta A = \tan^{-1}\left[\frac{\tan\xi \cos\psi}{\cos(a_t + \psi)}\right]. \tag{3.17}$$

This definition was chosen so that at the origin ($a = 0, A = 0$), we have ($\Delta a = \psi, \Delta A = \xi$).[9] It was obtained by translating an offset at the origin to an arbitrary location (a, A) in the horizontal coordinate system and retaining the leading order terms. The azimuth offset ΔA is modulated by the cosine of the altitude as expected, and includes a factor which accounts for the alteration to the altitude induced by ψ. The altitude offset has a dependence on ξ which makes Δa curve towards the horizon as the azimuth offset grows.

Given an offset ($\Delta a, \Delta A$) measured using planets as described above, the quantities (ξ, ψ) are derived by inverting Eqs. 3.16 and 3.17. This is not possible analytically, so an iterative technique is used:

[8] Private communication.

[9] The ACT is not capable of pointing at zero altitude (though it can point at zero azimuth). However, the origin of the horizontal system is the most natural and transparent reference point for this scheme, which is already complex enough.

Table 3.2: A list of important astrometric reductions. These are all performed by the AEPHEM library and included in the pointing analysis. This table is adapted from the AEPHEM documentation.

Correction	**Description**	**Approximate Size**
Light-Travel Time	Due to the finite speed of light, a body is seen at an old position on its orbit, not its current position.	Up to tens of arcseconds for solar system objects.
Light Deflection	Light rays passing near to the sun are bent by its gravitational field.	Maximum $1.8''$.
Annual Aberration	Aberration of light due to the earth's orbital motion.	Up to $20''$.
Precession	Precession of the earth's axis of rotation.	About $50''$ per annum.
Nutation	"Nodding" of the earth's axis of rotation due to tidal interactions with the moon and sun.	Up to $17''$.
Diurnal Aberration	Aberration of light due to the earth's rotation.	Less than $1/3''$.
Diurnal Parallax	Parallax of nearby objects due to the angle subtended by the earth's diameter.	Up to $\sim 1'$ for nearby planets.
Atmospheric Refraction	Refraction of light in the earth's atmosphere.	About $30''$ at 50° altitude, 1/2 atmosphere.

1. Set $\psi_0 = 0$.
2. Invert Eq. 3.17 and use ψ_0 to obtain a ξ; call it ξ_1.
3. Insert ξ_1 into Eq. 3.16; use ψ_0 in the cosine term, and solve for the remaining ψ, calling it ψ_1.
4. Set $\psi_0 = \psi_1$ and return to step 2.

The solution converges quickly so that only three or so iterations are necessary.

The precision of the detector offsets can be increased by averaging together data from many planet observations. Let (ξ_d^k, ψ_d^k) be the offset of detector d measured from planet observation k. Before averaging, we first need to align all the observations. This is because the offset of the whole array can change from observation to observation, especially if they are performed at different altitudes or azimuths.[10] Assume that we know a global offset (ξ_g^k, ψ_g^k) which centers the array offsets of observation k on the origin of the (ξ, ψ) coordinate system. Then the relative offsets of the detectors can be calculated as:

$$\begin{pmatrix} \xi_d \\ \psi_d \end{pmatrix} = \begin{pmatrix} \mu_{1/2}\left[\xi_d^k - \xi_g^k\right] \\ \mu_{1/2}\left[\psi_d^k - \psi_g^k\right] \end{pmatrix}, \tag{3.18}$$

We use the median rather than the mean since it is robust against outliers.

How do we determine the global offsets? Naively, we might choose a reference detector near the center of the array, say (15, 15), and let $(\xi_g^k, \psi_g^k) = (\xi_{(15,15)}^k, \psi_{(15,15)}^k)$. This is undesirable because it limits the precision of Eq. 3.18 to the measurement uncertainties of $(\xi_{(15,15)}^k, \psi_{(15,15)}^k)$. It would be better if we could use all of the detector measurements to determine the global offset and thus

[10] This is due to imprecisions in the telescope alignment. The largest is the tilt of the telescope base. Fowler (2007) provides a detailed global pointing model.

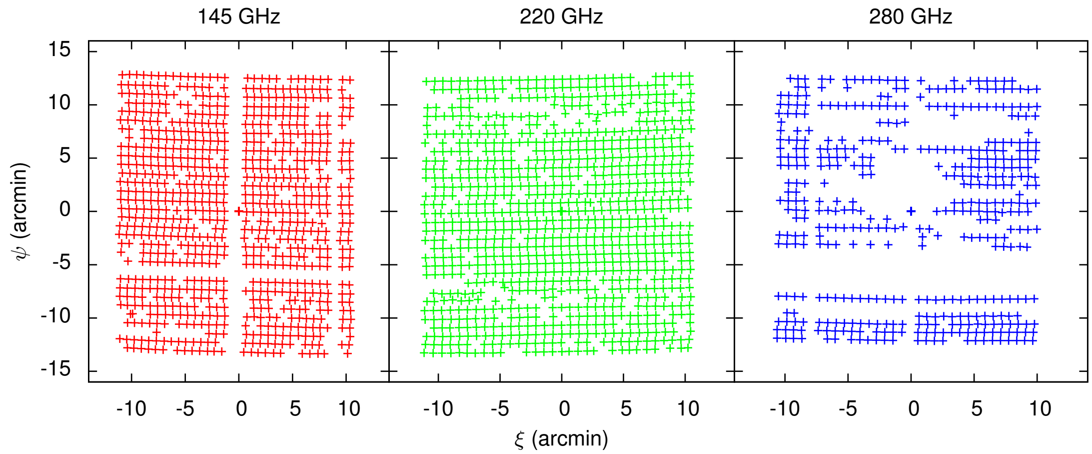

Figure 3.8: The relative detector pointing offsets for the three arrays in 2008. The coordinates ξ and ψ, defined by Eqs. 3.16 and 3.16, are roughly equivalent to the offsets in azimuth and altitude, respectively. About 30 Saturn observations were used for these plots. The error bars on each point are too small to show up in this plot (see Table 3.3).

statistically shrink its uncertainty. Imagine for the time being that we already know the relative offsets (ξ_d, ψ_d), and make a statistical measurement of the global offset:

$$\begin{pmatrix} \xi_g^k \\ \psi_g^k \end{pmatrix} = \begin{pmatrix} \mu_{1/2}\left[\xi_d^k - \xi_d\right] \\ \mu_{1/2}\left[\psi_d^k - \psi_d\right] \end{pmatrix}. \tag{3.19}$$

This creates a dilemma. To determine the relative offsets using Eq. 3.18 we need to know the global offsets, but to determine the global offsets using Eq. 3.20, we need to know the relative offsets.

The solution is, once again, to use an iterative algorithm:

1. Make a guess at the relative pointing offsets and call them $(\widetilde{\xi}_d, \widetilde{\psi}_d)$.
2. Plug $(\widetilde{\xi}_d, \widetilde{\psi}_d)$ into Eq. 3.20 to calculate the global offsets (ξ_g^k, ψ_g^k).
3. Plug (ξ_g^k, ψ_g^k) into Eq. 3.18 to calculate the relative offsets (ξ_d, ψ_d).
4. Set $(\widetilde{\xi}_d, \widetilde{\psi}_d) = (\xi_d, \psi_d)$, and return to step 2.

All that remains is to make a good enough initial guess of the relative pointing offsets (step 1) so that the algorithm converges. Happily, the simplest idea works well. Assume that the grid of detector offsets is rectangular:

$$\begin{pmatrix} \widetilde{\xi}_{(i,j)}^k \\ \widetilde{\psi}_{(i,j)}^k \end{pmatrix} = \begin{pmatrix} [15 - i]\,\Delta\xi^k \\ [15 - j]\,\Delta\psi^k \end{pmatrix}, \tag{3.20}$$

where (i, j) is the detector in row i and column j. The detector spacings are simply the median nearest-neighbor spacings:

$$\Delta\xi^k = \mu_{1/2}\left(\left|\xi_{(i,j)}^k - \xi_{(i+1,j)}^k\right|\right) \tag{3.21}$$

$$\Delta\psi^k = \mu_{1/2}\left(\left|\psi_{(i,j)}^k - \psi_{(i,j+1)}^k\right|\right) \tag{3.22}$$

Table 3.3: Some basic parameters of the relative detector pointing shown in Fig. 3.8.

Quantity	**148 GHz Array**	**218 GHz Array**	**277 GHz Array**
Median Num. Observations[a]	18	14	11
Num. Detectors[b]	799	914	425
Mean Error, ξ (arcsec)[c]	0.56	0.72	1.7
Mean Error, ψ (arcsec)[c]	0.24	0.44	1.1
Median Space, ξ (arcmin)[d]	0.688 ± 0.010	0.691 ± 0.017	0.653 ± 0.019
Median Space, ψ (arcmin)[d]	0.823 ± 0.015	0.820 ± 0.022	0.785 ± 0.029
Horizontal Plate Scale (arcmin/cm)[e]	6.55 ± 0.10	6.58 ± 0.16	6.22 ± 0.18
Vertical Plate Scale (arcmin/cm)[e]	7.16 ± 0.13	7.13 ± 0.19	6.83 ± 0.25

[a] Not all detectors observe the planet in all observations; this is the median number of measurements per detector.

[b] The number of detectors for which pointing could be obtained.

[c] The error of the relative pointing for each detector is defined as the median absolute deviation of its measurements. Here we give the array-wide mean.

[d] I.e., the median spacing between adjacent detectors.

[e] The plate scale is calculated using an array spacing of 1.05 mm $\times$1.15 mm (Fowler et al., 2007). Since there is no available error on these parameters, the quoted uncertainty only includes the pointing uncertainty.

Note that for the initial guess, we have one set of relative offsets calculated for each observation k given by Eq. 3.20; in subsequent iterations, we only use one array of relative offsets ($\widetilde{\xi}_d$, $\widetilde{\psi}_d$). Two iterations are generally sufficient for convergence.

Figure 3.8 shows the relative offsets for each of the three arrays as measured for the 2008 season using observations of Saturn. Table 3.3 lists some basic parameters of these data. The plate scales listed in Table 3.3 were calculated from the median ξ and ψ spaces using the nominal detector spacing of 1.05 mm $\times$1.15 mm. The measured horizontal plate scales are consistent with the predicted values of 6.6′ cm^{-1} (148 GHz and 218 GHz) and 6.4′ cm^{-1} (277 GHz). In the vertical direction, the predicted plate scale of 6.8′ cm^{-1} for all arrays matches the measured scale for 277 GHz, but is considerably smaller than those of 148 GHz and 218 GHz. The slight overall rotation in the array on the sky (c.f. Fig. 3.8) is not large enough to account for this discrepancy, which would require a rotation of about 15°.

So far, we have only used our measurement of the global offsets (ξ_g^k, ψ_g^k) to center each set of relative measurements on a common origin so that we could average together the data from many planet observations (c.f. Eq. 3.18). The final question that may be asked is whether they are useful in their own right. Can we fit the global offsets to a global pointing model so that we may compute a (ξ_g, ψ_g) for any telescope pointing? It does turn out to be possible to fit to a sensible model, and this provided a useful check of the $\sim$20″ base tilt of the telescope (Hincks et al., 2008). However, the uncertainty of the fit is too large for it to by useful for mapmaking. The chief reason is that planets are all observed near the ecliptic and are unable to break certain degeneracies in the model.

In the end, the global pointing offset can be measured precisely from bright point sources in the final maps. Our survey observations are made at a small number of pointings which do not change from night to night, so in practice, this is simple to implement.

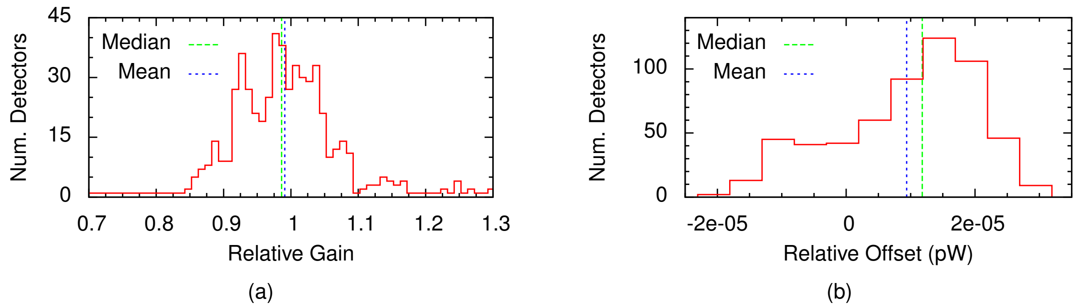

Figure 3.9: Corrections to the IV-curve calibrations obtained by fitting to the atmospheric common mode (see text). This is a typical example using all working detectors from a single time stream. The median relative gain is expected to be near unity since the common mode comes from the median detector response. The mean fit errors were 3.3×10^{-4} for the relative gain and 2.6×10^{-6} pW for the relative offset: in other words, the fits are excellent.

3.4 Gain Calibration

A detector's response to incident radiation is measured by recording the current applied to a feedback inductor to cancel flux induced by current through the TES. The theory of this electrothermal process is described in detail in Irwin & Hilton (2005). Marriage (2006), Niemack (2008), and Switzer (2008) also have substantial treatment of TES theory, especially as it pertains to the ACT experiment. For our current purposes, it is enough to state that the recorded digital signal, in DAC units, needs to be transformed into units of CMB temperature.

The goal is to obtain the temperature calibration by fitting the large scale CMB modes from the final to the WMAP data. In principle, this would allow for a direct conversion from DAC to temperature. However, the mapmaking process itself requires a good intermediate calibration since the responsivities of the detectors are not uniform. This leads to striping in the maps. Additionally, the Cottingham method (§4.2) breaks down unless a fairly precise calibration is used.

The natural quantity measured by the detectors is power, and this is also the natural quantity for this intermediate gain calibration. It is also useful for calculating the overall instrument efficiency by comparing to the estimated power of an observed source. Calibration from measured power to temperature units is described later, in Chapter 5.

The power responsivity can be estimated from the formula:

$$\frac{\delta P}{\delta I} = -I_o\,(R_o - R_{\rm sh})\,. \tag{3.23}$$

In this equation, δI is readily obtained by multiplying a known loop-gain to the DAC output, and the applied bias current I_o is known *a priori*. The operating resistance R_o is determined at the beginning of each night by measuring I as a function of I_o and applying Ohm's law — this is called an "IV" calibration. The last variable needed to solve for the change in power δP is $R_{\rm sh}$, which is measured in the lab. The uncertainty in $R_{\rm sh}$ is about 10%,[11] and so Eq. 3.23 can only be used for a rough calibration from DAC units to power. Typically, bias currents I_o are a few picoamperes, the operating resistances R_o are tens of milliohms, and shunt resistances are around a milliohm. Conversions between power responsivity δI and sky temperature are derived later in §5.3 and listed in Table 5.4.

The operating point R_o changes through the night due to changing optical power due to varying atmospheric emission. The correction is typically only 1–2% (Switzer, 2008) and is not accounted

[11] J. Appel, private communication

for since it is small compared with the uncertainty of R_{sh}. However, the change in R_o is calculated using Eq. 5.45 of Switzer (2008) so that detectors whose R_o go outside an acceptable range (defined as 10–90% of normal resistance) during the night are discarded.

To correct for the imprecision of the IV calibration, a high signal-to-noise response common to all the detectors would be ideal. The atmospheric emission, though a serious contaminant during mapmaking, in this case provides just the signal that is required. Using it as a calibrator is straightforward. Let $\mathbf{d}_i$ be a downsampled time stream of the i^{th} detector. Downsampling is done in order to make the computations fast and to improve the signal-to-noise of the atmospheric signal. A 10 Hz boxcar filter is applied to the time stream, which is subsequently resampled at 10 Hz. Define the common mode as the median downsampled response:

$$\mathbf{c} = \mu_{1/2}\left(\mathbf{d}_i\right). \tag{3.24}$$

We model the relative response of each detector with an offset b_i and scale g_i and assert:

$$g_i\,\mathbf{d}_i + b_i = \mathbf{c}. \tag{3.25}$$

The parameters g_i and b_i are easily found by performing a linear least-squares fit. Because of the large number of data points in $\mathbf{d}_i$, the fits are excellent, with the errors in g_i well below a percent and those in b_i around 30%. Fig. 3.9 shows the relative calibrations from a typical time stream.[12] The distribution of relative gains is consistent with a 10% uncertainty in R_{sh}. More investigation is needed to determine whether the distribution is due chiefly to the uncertainty in shunt resistances, or whether their true uncertainty is lower than 10%.

[12] One might ask why the offset b_i is included, and not just the scale g_i. The motivation is to account for imprecisions in the removal of the mean from the time stream, which is done as soon as it is loaded into memory. Including it does improve the fit, although there is some covariance between the two parameters.

Chapter 4

Mapmaking

4.1 Understanding the Mapmaking Equation

Estimating the best map of the celestial signal from the telescope receiver's time streams is challenging. It requires creativity to determine the best algorithms that efficiently yield robust map estimates and large computing resources to execute them. Nevertheless, the basic concepts of mapmaking are simple. The fundamental assumption is that the receiver's response to the celestial signal is linear. This reduces the problem to one of linear regression. The mapmaking problem can then be broken into two main categories: first, determining a model for the regression, which takes into account experimental noise, systematic errors and telescope pointing; and second, finding approximations to the matrix inversion that the solution entails which are computationally feasible.

Let us proceed with some concrete definitions. A *map* is the temperature as a function of position on the celestial sphere, with no temperature contribution from any other source, be it atmosphere or instrumental contamination. Our task is to find the best estimate of this map given time stream from our receiver. A *pixel* is a defined subsection of the map centered on a specific coordinate. A *detector*, not to be confused with a pixel, is a single element in the telescope receiver. Let $\mathbf{d}$ be a vector of all the measurements and $\mathbf{m}$ be a vector of the true temperature of the pixels in the region of the sky which was observed. We seek to project $\mathbf{d}$ into the best estimate of the map, which we call $\widetilde{\mathbf{m}}$:

$$\widetilde{\mathbf{m}} = \mathbf{\Pi d}. \tag{4.1}$$

The matrix $\mathbf{\Pi}$, which we call the *projection matrix*, must place measurements in the correct pixels with optimal weights.

The convention in the literature is to begin with an inverted version of Eq. 4.1. The measured signal is expressed as the true map projected into a time stream by a matrix $\mathbf{P}$, plus the noise, $\mathbf{n}$:

$$\mathbf{d} = \mathbf{Pm} + \mathbf{n}. \tag{4.2}$$

It is then straightforward to show (e.g., Tegmark, 1997) that, given the noise covariance matrix $\mathbf{N} \equiv \left\langle \mathbf{nn}^T \right\rangle$, the map pixel variance is minimized by asserting:

$$\mathbf{\Pi} = \left(\mathbf{P}^T\mathbf{N}^{-1}\mathbf{P}\right)^{-1} \mathbf{P}^T\mathbf{N}^{-1}. \tag{4.3}$$

This choice has the benefit that it is unbiased; specifically, the map error depends only on the noise:

$$\epsilon \equiv \widetilde{\mathbf{m}} - \mathbf{m} = (\mathbf{\Pi P} - \mathbf{I})\,\mathbf{m} + \mathbf{\Pi n} = \mathbf{\Pi n}, \tag{4.4}$$

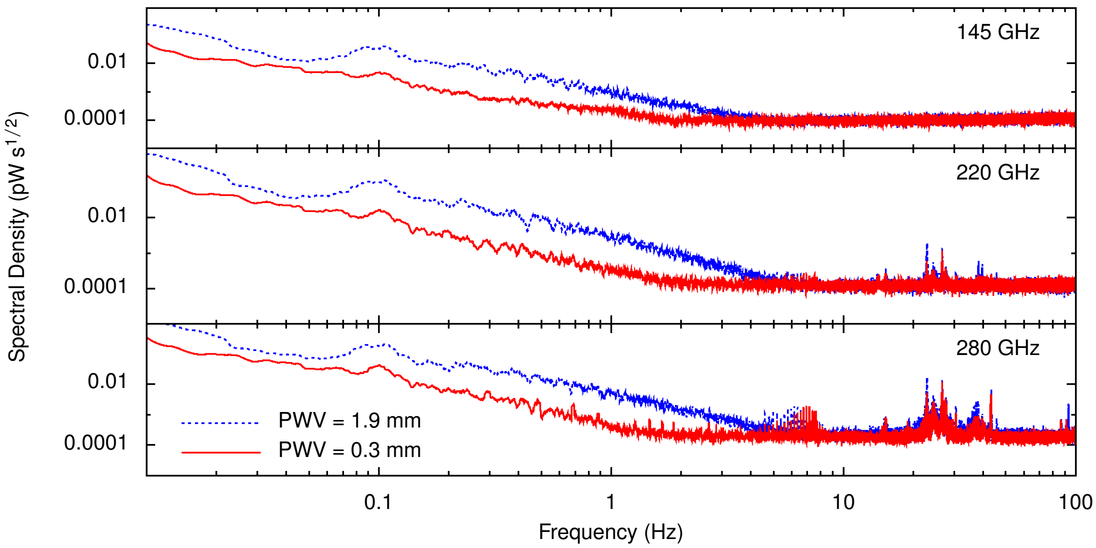

Figure 4.1: Spectral densities for two time streams taken with atmospheric PWV's of 0.3 mm and 1.9 mm. A boxcar filter ten samples long has been applied to the spectra for ease of viewing. All three observing frequencies are displayed. For the higher PWV spectrum, the persistence of low-frequency power above $\sim$10 Hz is interpreted as increased atmospheric contamination. Even for the lower PWV spectrum, the contamination lasts until about 2 Hz before it meets the noise floor. The features at 0.1 Hz correspond to the scanning frequency. The noise in the 218 GHz and 277 GHz spectra at $\sim$25 Hz are from microphonic vibrations of an optical coupling layer that was removed for the 2009 season. (These data are from before the coupling layers were removed.)

where the fact that $\mathbf{\Pi P} = \mathbf{I}$ follows from Eq. 4.3. In its full generality, the matrix inversions involved in the calculation of the projection matrix $\mathbf{\Pi}$ are not practical: the number of elements in $\mathbf{N}$ is the square of the number of measurements. For the ACT with a single array observing a single night, this number is roughly $(2 \times 10^{10})^2$. A further problem is that there is an implicit assumption that $\mathbf{N}$ is known, when in fact, determining it is not not necessarily trivial nor exact. The ideal case, is of course, identical white noise in each detector so that $\mathbf{N} = \mathbf{I}$, the identity matrix. Then, $\mathbf{\Pi} = (\mathbf{P}^T\mathbf{P})^{-1}\mathbf{P}^T$, with $\mathbf{P}^T$ projecting each measurement into a map pixel and $(\mathbf{P}^T\mathbf{P})^{-1}$ dividing by the number of measurements per pixel; in other words, the map is a simple average.

A slightly more complicated, but potentially tractable scenario, is one where there is no inter-detector noise correlation. Then, if $\mathbf{d}$ is arranged as the concatenation of the measurements from each individual detector in the receiver, $\mathbf{N}$ is block diagonal, i.e.,

$$\mathbf{d} = \begin{pmatrix} \mathbf{d}^0 \\ \mathbf{d}^1 \\ \vdots \\ \mathbf{d}^{N_d-1} \end{pmatrix}; \quad \mathbf{N} = \begin{pmatrix} \mathbf{N}^0 & \mathbf{0} & \dots & \mathbf{0} \\ \mathbf{0} & \mathbf{N}^1 & \dots & \mathbf{0} \\ \vdots & \vdots & \ddots & \vdots \\ \mathbf{0} & \mathbf{0} & \dots & \mathbf{N}^{N_d-1} \end{pmatrix}, \tag{4.5}$$

where $\mathbf{d}^\mu$ and $\mathbf{N}^\mu$ are the time streams and noise covariances for detector number $\mu \in [0, N_d - 1]$, respectively. The mapmaking prescription in this treatment is to make maps for each individual detector and then coadd them: the terms $[\mathbf{P}^T(\mathbf{N}^\mu)^{-1}\mathbf{P}]^{-1}$ will ensure that the weighting of this coaddition is done correctly. For example, if the covariances $\mathbf{N}^\mu$ represent white noise levels, the detector maps will be weighted by their inverse variances.

The dark mode removal described in §3.1.2 helps towards reaching the ideal scenario of Eq. 4.5 because it eliminates instrumental noise which is shared between detectors, much of it at low frequencies. However, the problem of the atmosphere remains. Fluctuations in its emitted power and spatial structure introduce low frequency contamination into the time stream. Not only is it highly correlated between detectors, since they all see through nearby patches of the atmosphere, but its amplitude is many orders of magnitude larger than the celestial signal. Thus, in addition to the fact that Eq. 4.5 is not immediately applicable, the signal of interest is overwhelmed, to a degree that for the large spatial scale signals which are most affected, no practical amount of naive integration will help. Fig. 4.1 shows detector spectral densities which indicate that even on ideal nights with low PWV, the atmosphere dominates the signal on time scales as low as half a second.

Atmospheric contamination is a reality for all ground based millimeter telescopes, and even for balloon borne instruments, as conceded by Patanchon et al. (2008). In the literature it is uniformly referred to as "noise" and generally included under the umbrella of "1/f noise"—more a convenient moniker than a precise name since the Fourier power spectrum of the "noise" follows a power law $(1/f)^{\beta}$ with β not necessarily equal to unity. The approach of many experiments is relatively crude: some low-order polynomial is fit to the detector time streams and subtracted before any mapmaking. In combination with this, or in place of it, a high-pass filter is applied to delete all low-frequency power. Most recently, these techniques have been used in one way or another by QUaD (Pryke et al., 2009), the South Pole Telescope (Staniszewski et al., 2008) and APEX (Halverson et al., 2008a; Reichardt et al., 2009a), for example.[1] Others have taken more sophisticated approaches, such as the SANEPIC algorithm which uses informed estimates to propagate a reasonable representation of the full noise covariance through the mapper (Patanchon et al., 2008).

The common perspective of these traditional *modi operandi* is that the atmosphere is noise. It is either suppressed by indiscriminate filtering or downweighted by including it in the covariance **N**. In this chapter, we think of the atmospheric emission as a signal in its own right. We simultaneously solve for best estimates of the celestial map *and* the atmospheric signal. This technique was first described by Cottingham (1987) and used by Page et al. (1990),Meyer et al. (1991), Boughn et al. (1992), and Ganga et al. (1993). Hereafter we call it the Cottingham Method. While it has its own imperfections, it is effective at producing clean, unbiased maps and should be seen as a viable option in the toolbox of mapmaking techniques. In its original form, using B-splines (§4.2.4), it has not to our knowledge been used in recent years. However, it has close similarities with the "destriping" methods developed for *Planck*. This is discussed more in §4.2.3.

We begin by describing the Cottingham Method in §4.2 and in §4.3 we show results from our data. We conclude in §4.4 by summarizing our mapmaking process from start to finish.

4.2 The Cottingham Method

4.2.1 The Algorithm

In the Cottingham Method, the atmospheric and celestial signals are treated on equal footings by adding an extra term to Eq. 4.2:

$$\mathbf{d} = \mathbf{Pm} + \mathbf{B}\alpha + \mathbf{n}, \tag{4.6}$$

where **B** is a set of basis functions with amplitudes α for representing the variation of atmospheric power in time. We will introduce the form of **B** in §4.2.4, below, but for now we proceed assuming that we have a basis **B** that can model this atmospheric variation well.

Our goal is to find best-estimates $\widetilde{\mathbf{m}}$ and $\widetilde{\alpha}$ of the map and the atmosphere, respectively. Using Bayes's Theorem, the likelihood of parameter estimates $\widetilde{\mathbf{m}}$ and $\widetilde{\alpha}$ given measurements **d** is:

[1] It should be mentioned that using these harsh filters is often "good enough", in that the modes in the map which are eliminated are not of interest. Care must still be taken to understand the transfer function caused by the filter, which can be achieved through careful simulations.

$$P(\widetilde{\mathbf{m}}, \widetilde{\alpha}|\mathbf{d}) \propto P(\mathbf{d}|\widetilde{\mathbf{m}}, \widetilde{\alpha})P(\widetilde{\mathbf{m}}, \widetilde{\alpha}) \propto P(\mathbf{d}|\widetilde{\mathbf{m}}, \widetilde{\alpha})P(\widetilde{\alpha}|\widetilde{\mathbf{m}})P(\widetilde{\mathbf{m}}), \tag{4.7}$$

where in the last equality we used the chain rule of probability. The likelihood distribution of the atmospheric amplitudes should be independent of the celestial map, so $P(\widetilde{\alpha}|\widetilde{\mathbf{m}}) = P(\widetilde{\alpha})$. Finally, we assume a flat prior on both the atmosphere and the map. We are left with:

$$P(\widetilde{\mathbf{m}}, \widetilde{\alpha}|\mathbf{d}) \propto P(\mathbf{d}|\widetilde{\mathbf{m}}, \widetilde{\alpha}) \propto \exp\left(-\frac{1}{2}\mathbf{n}^T\mathbf{N}^{-1}\mathbf{n}\right). \tag{4.8}$$

The best estimates $\widetilde{\mathbf{m}}$ and $\widetilde{\alpha}$ are obtained by minimizing the logarithm of the likelihood, which we call χ^2:

$$\chi^2 \equiv -\left(\mathbf{d} - \mathbf{P}\widetilde{\mathbf{m}} - \mathbf{B}\widetilde{\alpha}\right)^T \mathbf{N}^{-1}\left(\mathbf{d} - \mathbf{P}\widetilde{\mathbf{m}} - \mathbf{B}\widetilde{\alpha}\right), \tag{4.9}$$

where we solved 4.6 for $\mathbf{n}$.[2] Minimizing first with respect to $\widetilde{\mathbf{m}}$, we differentiate the likelihood:

$$\frac{\partial\chi^2}{\partial\widetilde{\mathbf{m}}} = \mathbf{P}^T\mathbf{N}^{-1}\left(\mathbf{d} - \mathbf{P}\widetilde{\mathbf{m}} - \mathbf{B}\widetilde{\alpha}\right). \tag{4.10}$$

and by setting it to zero and solving for $\widetilde{\mathbf{m}}$ obtain:

$$\widetilde{\mathbf{m}} = \left(\mathbf{P}^T\mathbf{N}^{-1}\mathbf{P}\right)^{-1}\mathbf{P}^T\mathbf{N}^{-1}(\mathbf{d} - \mathbf{B}\widetilde{\alpha}) = \mathbf{\Pi}(\mathbf{d} - \mathbf{B}\widetilde{\alpha}). \tag{4.11}$$

The projection matrix $\mathbf{\Pi}$ has reappeared, and we recognize that we have recovered the standard mapmaking equation introduced in §4.1, with the modification that we subtract the atmosphere $\mathbf{B}\widetilde{\alpha}$ from the data $\mathbf{d}$ before applying the projection matrix.

Similarly, we can solve for the amplitudes $\widetilde{\alpha}$ by setting its partial derivative of χ^2 to zero:

$$\begin{aligned} 0 = \frac{\partial\chi^2}{\partial\widetilde{\alpha}} &= \mathbf{B}^T\mathbf{N}^{-1}\left(\mathbf{d} - \mathbf{P}\widetilde{\mathbf{m}} - \mathbf{B}\widetilde{\alpha}\right) \\ &= \mathbf{B}^T\mathbf{N}^{-1}\left[\mathbf{d} - \mathbf{P}\mathbf{\Pi}(\mathbf{d} - \mathbf{B}\widetilde{\alpha}) - \mathbf{B}\widetilde{\alpha}\right] \\ &= \mathbf{B}^T\mathbf{N}^{-1}(\mathbf{I} - \mathbf{P}\mathbf{\Pi})(\mathbf{d} - \mathbf{B}\widetilde{\alpha}), \end{aligned} \tag{4.12}$$

where we have inserted the map best estimate of Eq. 4.11 in the second line. If we define the following:

$$\mathbf{\Xi} \equiv \mathbf{B}^T\mathbf{N}^{-1}(\mathbf{I} - \mathbf{P}\mathbf{\Pi}), \quad \mathbf{\Theta} \equiv \mathbf{\Xi}\mathbf{B}, \quad \phi \equiv \mathbf{\Xi}\mathbf{d}, \tag{4.13}$$

then:

$$\mathbf{\Theta}\widetilde{\alpha} = \phi. \tag{4.14}$$

This is a linear equation which is simple to solve for the atmospheric basis amplitudes and can then be plugged into Eq. 4.11 to obtain the map estimate. The sizes of $\mathbf{\Theta}$ and ϕ are set by the number of basis functions in $\mathbf{B}$. If we denote this number N_B, then $\mathbf{\Theta}$ is an $N_B \times N_B$ matrix and ϕ is a N_B-element vector. Assuming that the atmosphere can be modelled with a reasonably small number of bases N_B, more time is spent computing Θ and ϕ than solving Eq. 4.14. This is discussed more in §4.3.1, below.

[2] To be precise, we have defined χ^2 to be twice the logarithm of the likelihood; this makes no difference after differentiating.

4.2.2 The Algorithm in Component Notation

Before proceeding, it is instructive to re-derive Eq. 4.14 using component notation. Not only does it make the method more transparent, but it is also directly applicable to implementation in computer code.

We start by projecting the measurements **d** into pixels and sorting pixel-wise. Let the index p count pixels and the index i count the measurements in each pixel, which has a total of N_p measurements. Then Eq. 4.6 becomes:

$$d_{pi} = m_p + \sum_j B_{pij}\alpha_j + n_{pi}. \tag{4.15}$$

In this notation, B_{pij} is the j^{th} basis function evaluated at the same time—call it t_{ij}—at which the measurement d_{pi} was made. We also assign weights w_{pi} to each measurement in the pixel based on the noise properties: they will play a mathematically identical role to the noise covariance $\mathbf{N}^{-1}$ in the last section, only represented with a different notation.[3]

The variance in each pixel is:

$$\sigma_p^2 = \sum_i w_{pi}\left(n_{pi} - \bar{n}_p\right)^2, \tag{4.16}$$

where $\bar{n}_p$ is the weighted mean of the noise in the pixel. Using 4.15 and assuming map and atmosphere estimates $\widetilde{m}$ and $\widetilde{\alpha}$, respectively,

$$\begin{aligned}
\sigma_p^2 &= \sum_i w_{pi}\left[\left(d_{pi} - \widetilde{m}_p - \sum_j B_{pij}\widetilde{\alpha}_j\right) - \frac{1}{W_p}\sum_{i'} w_{pi'}\left(d_{pi'} - \widetilde{m}_p - \sum_j B_{pi'j}\widetilde{\alpha}_j\right)\right]^2 \\
&= \sum_i w_{pi}\left[d_{pi} - \sum_j B_{pij}\widetilde{\alpha}_j - \frac{1}{W_p}\sum_{i'} w_{pi'}\left(d_{pi'} - \sum_j B_{pi'j}\widetilde{\alpha}_j\right)\right]^2.
\end{aligned} \tag{4.17}$$

where W_p is the sum of the weights in the pixel:

$$W_p \equiv \sum_i w_{pi}. \tag{4.18}$$

Note that the map estimate $\widetilde{m}$ disappears from Eq. 4.17, a key point to which we shall return. The Cottingham Method minimizes the total variance across all pixels (c.f. Eq. 4.9), so we proceed by differentiating with respect to the amplitudes $\widetilde{\alpha}$:

[3] Note that there is no restriction against projecting a single measurement into multiple pixels with appropriate weights, if the noise covariance is such that the measurement is influenced by multiple map pixels.

$$
\begin{aligned}
\frac{\partial \chi^2}{\partial \widetilde{\alpha}_k} &= \frac{\partial}{\partial \widetilde{\alpha}_k} \sum_p \sigma_p^2 \\
&= 2 \sum_{p,i} w_{pi} \left[d_{pi} - \sum_j \widetilde{\alpha}_j B_{pij} - \frac{1}{W_p} \sum_{i'} w_{pi'} \left(d_{pi'} - \sum_j \widetilde{\alpha}_j B_{pi'j} \right) \right] \times \\
&\qquad \left(-B_{pik} + \frac{1}{W_p} \sum_{i'} w_{pi'} B_{pi'k} \right) \\
&= -2 \left(- \sum_{p,i} w_{pi} d_{pi} B_{pik} + \sum_{p,i,j} w_{pi} B_{pik} \widetilde{\alpha}_j B_{pij} + \sum_{p,i,i'} \frac{w_{pi} w_{pi'}}{W_p} d_{pi'} B_{pik} - \right. \\
&\qquad \sum_{p,i,i',j} \frac{w_{pi} w_{pi'}}{W_p} B_{pik} \widetilde{\alpha}_j B_{pi'j} + \sum_{p,i,i'} \frac{w_{pi} w_{pi'}}{W_p} d_{pi} B_{pi'k} - \sum_{p,i,i',j} \frac{w_{pi} w_{pi'}}{W_p} \widetilde{\alpha}_j B_{pij} B_{pi'k} - \\
&\qquad \left. \sum_{p,i,i',i''} \frac{w_{pi} w_{pi'} w_{pi''}}{W_p^2} d_{pi'} B_{pi''k} + \sum_{p,i,i',i'',j} \frac{w_{pi} w_{pi'} w_{pi''}}{W_p^2} \widetilde{\alpha}_j B_{pi'j} B_{pi''k} \right). \qquad (4.19)
\end{aligned}
$$

By relabelling indices and summing over any dummy index, the third, fifth and seventh terms can be combined, as well as the fourth, sixth and eighth:

$$
\begin{aligned}
\frac{\partial \chi^2}{\partial \widetilde{\alpha}_k} &= -2 \left(- \sum_{p,i} w_{pi} d_{pi} B_{pik} + \sum_{p,i,j} w_{pi} \widetilde{\alpha}_j B_{p,i,j} B_{p,i,k} + \right. \\
&\qquad \left. \sum_{p,i,i'} \frac{w_{pi} w_{pi'}}{W_p} d_{pi} B_{pi'k} - \sum_{p,i,i',j} \frac{w_{pi} w_{pi'}}{W_p} B_{pi'k} \widetilde{\alpha}_j B_{pij} \right) \\
&= -2 \left[- \sum_{pi} w_{pi} d_{pi} \left(B_{pik} - \frac{1}{W_p} \sum_{i'} w_{pi'} B_{pi'k} \right) + \right. \\
&\qquad \left. \sum_j \widetilde{\alpha}_j \sum_{pi} w_{pi} B_{pij} \left(B_{pik} - \frac{1}{W_p} \sum_{i'} w_{pi'} B_{pi'k} \right) \right]. \qquad (4.20)
\end{aligned}
$$

Defining:

$$
\Xi_{pik} \equiv w_{pi} \left(B_{pik} - \frac{1}{W_p} \sum_{i'} w_{pi'} B_{pi'k} \right), \quad \Theta_{kj} \equiv \sum_{pi} \Xi_{pik} B_{pij}, \quad \phi_k \equiv \sum_{pi} \Xi_{pik} d_{pi}, \qquad (4.21)
$$

we find, after setting $\partial \chi^2 / \partial \widetilde{\alpha}_k$ to zero, an expression equivalent to Eq. 4.14:

$$
\phi_k = \sum_j \alpha_j \Theta_{kj}. \qquad (4.22)
$$

4.2.3 What the Cottingham Method Does and Why it Works

The strength of the Cottingham Method is that it estimates the atmospheric signal in a way that is insensitive to the map estimate. This is most transparent in Eq. 4.17 in which the terms in $\widetilde{m}_p$ cancel

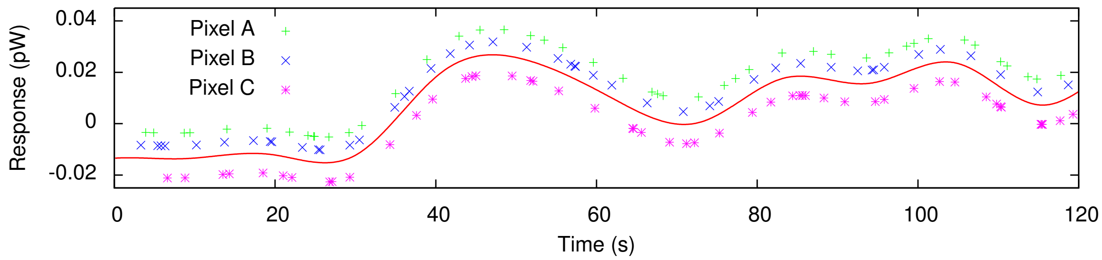

Figure 4.2: A cartoon of how the Cottingham Method works. Three pixels (A, B, C) have different temperatures but the same drift $\mathbf{D}(t)$, due to atmospheric signal, shown as the red, solid curve. The drift is calculated by solving Eq. 4.22. The celestial temperature of each pixel is then the (weighted) average offset from the drift of the measured responses. In this example, Pixel A has the highest temperature and Pixel C has the lowest.

out, making the variance depend only on the atmosphere estimate $\widetilde{\alpha}_p$. In the vector notation the equivalent property is manifested in the term $(\mathbf{I} - \mathbf{P\Pi})$ in Eqs. 4.12–4.13, responsible for projecting out the map estimate. A heuristic way of thinking about this property is that the Cottingham Method only fits the "AC" component of the signal in each pixel—due to temporal atmospheric fluctuations—and is not influenced by the "DC" term due to the static celestial signal. Fig. 4.2 illustrates this graphically.

Since $\widetilde{\alpha}$ has no dependence on $\widetilde{\mathbf{m}}$, Eq. 4.4 is not altered: the removal of the atmospheric best estimate does not change the property that the map best estimate is unbiased with respect to the true celestial map. If the Cottingham Method is thought of as a filter, it is a very special filter which does the best possible job at removing only power due to the atmospheric signal (or any other kind of temporal drift which is equal in amplitude among the detectors being processed).[4] This should be contrasted to more basic approaches which are sometimes employed in CMB analyses. Commonly a slowly varying function, such as a low-order polynomial, is fit to the data time stream to remove low-frequency power from the atmosphere—most recently, this was done by Staniszewski et al. (2008) and Pryke et al. (2009). Not only will the fits be biased by any high signal-to-noise celestial sources, but this kind of filter removes power indiscriminately, the majority of it atmospheric in origin (since it is the largest signal at low frequencies) but also inevitably some of it celestial. For experiments where there is significant atmospheric power at the scanning or chopping frequency, which is the case for the ACT, this ought to be a serious concern. It should be pointed out that cruder filters, like polynomial fits, can be "legitimately" used if the transfer function they effect in the mapmaking process is understood. Simulations play a key role in this case. The Cottingham Method, on the other hand, avoids this complication.

The Cottingham Method has close similarities to the so-called "destriping" technique which has been studied in preparation for *Planck* data analysis (Burigana et al., 1999; Delabrouille, 1998; Maino et al., 2002; Keihänen et al., 2004). In fact, the mapmaking equations presented by Keihänen et al. (2005) are formally equivalent to those of the Cottingham Method, except that there is an additional term depending on the covariance of the amplitudes $\widetilde{\alpha}$ in the RHS of Eq. 4.14. This is because for the *Planck* application, which is designed not to remove atmospheric signal (it is a space telescope) but rather low frequency instrumental noise, they assume that the amplitudes $\widetilde{\alpha}$ have a Gaussian distribution. On the other hand, we treat the atmospheric emission, like the celestial, to be a signal in its own right and therefore explicitly assumed a flat prior on the amplitudes in Eqs. 4.7–4.8. A possible improvement is to also include a prior on the amplitudes, as proposed by Sutton et al. (2009) who consider the destriping approach in the context of a ground-based polarization experiment. However, they do not suggest any particular form for this prior and assume

[4] Of course, the quality of the filter depends on the choice of bases function $\mathbf{B}$ which model the atmospheric signal—see §4.2.4.

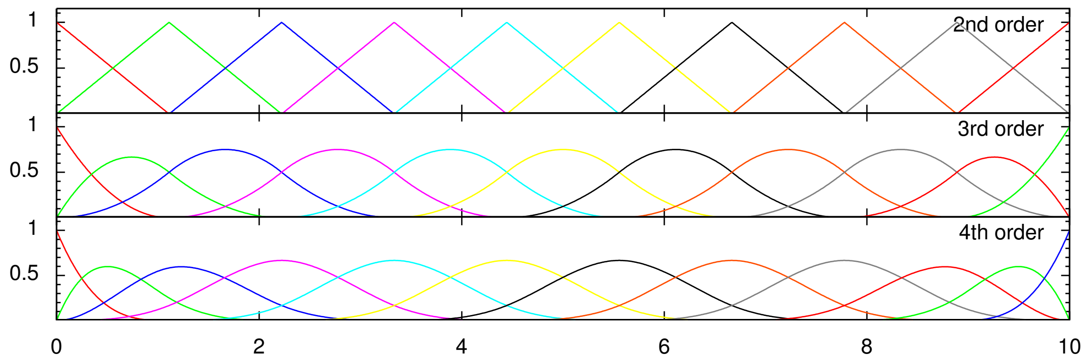

Figure 4.3: B-spline basis functions for three different polynomial orders with equal knot spacings. First order B-splines, not plotted here, are simply top-hat functions. Note that the support at any point on the x-axis comes from at most p bases, where p is the polynomial order. We use fourth order (i.e., cubic) B-splines for the Cottingham Method.

that the spectrum of atmospheric variations is known.

There are two components to our implementation of the Cottingham method which distinguish it from these other approaches: we use B-splines as our basis functions (see §4.2.4), and we process multiple detectors simultaneously. Future destriping algorithms for *Planck* or ground-based, polarization observatories might benefit by adopting them as well.

4.2.4 B-Splines and Atmosphere-Celestial Covariance

Like Cottingham (1987), we use basis B-splines for the basis **B**. A particularly useful member of the class of spline functions, B-splines have been rigorously studied and there is a large body of literature about them—comprehensive overviews can be found in Bojanov et al. (1993), de Boor (2001), and Schumaker (2007), for example.[5] Basis B-splines are a set of basis functions whose linear combinations are called B-splines. A B-spline is completely specified by a knot spacing, τ_k,[6] and an order, p. The basis B-splines of order p are efficiently evaluated using the Cox–de Boor recursion on the polynomial order. For m knots t_j, with $j = 0$ to $m - 1$, they are:

$$b_{j,0}(t) = \begin{cases} 1 & \text{if } t_j \leq t < t_{j+1} \\ 0 & \text{otherwise} \end{cases},$$
$$b_{j,p}(t) = \frac{t - t_j}{t_{j+p} - t_j} b_{j,p-1}(t) + \frac{t_{j+p+1} - t}{t_{j+p+1} - t_{j+1}} b_{j+1,p-1}(t), \tag{4.23}$$

with j values restricted so that $j + p + 1 < m - 1$. The basis B-Splines are therefore polynomials of order p and are compact, in the sense that the B-spline receives support from no more than p bases at any one point. This makes them flexible on scales larger than the knot spacing τ_k but somewhat rigid on smaller scales. Like conventional polynomials they share the property that they are useful for interpolating data, but they do not suffer from the Runge phenomenon (ringing between interpolation points). Fig. 4.3 shows some sample B-spline basis functions.

[5]"B-spline" seems generally to be considered short for "basis splines" but Bojanov et al. (1993) cite evidence from seminal papers on spline theory which shows that the term "basic splines" has also been used.

[6]In general, the knot spacing does not have to be uniform, in which case the bases are determined by the knot partition chosen. In this work, however, we only use B-splines with uniform partitioning.

Due to their flexibility on large scales and their well-behaved interpolation properties, B-splines are ideal for modelling the slowly varying atmospheric signal. Empirically we have found that the frequency f_k below which atmospheric power can be removed is determined by the knot spacing: $f_k \approx 1/2\tau_k$ (c.f. Fig. 4.7), presumably a consequence of the Nyquist-Shannon theorem. Given this relation, it might seem reasonable to make f_k as high as possible: in that case Fig. 4.1 suggests that 2 Hz be the minimum.

On the other hand, the higher f_k, the smaller the spatial modes in the true map with which the B-spline might have covariance. Above, in §4.2.3, we explained that the Cottingham Method is insensitive to the map estimate when it removes the atmospheric power, and that the map estimate is unbiased with respect to the true map. However, this is not equivalent to saying that it is not contaminated at all: only that any power it does add or subtract is not dependent on the map estimate itself. Thus, for example, the presence of a very high signal-to-noise planet in the data will not bias the atmosphere signal estimate, but subtracting the atmosphere signal estimate may inadvertently add or subtract power in some other random way. The Cottingham Method is a maximum likelihood estimator, but no technique restores a map which is the exact, noise-free copy of the original.

The consequence of this consideration is that making f_k too high can have unintended effects on the map. The higher f_k, the smaller the scales in the map which can be affected. For reference, our 2008 observations were generally done with a azimuthal scan rate on the sky of about $1^\circ\,\mathrm{s}^{-1}$, so a one-second knot spacing, implying $f_k \approx 0.5\,\mathrm{Hz}$, can contaminate the map on scales larger than two degrees in azimuth. In the elevation direction, this will be manifest in residual striping in the map: since each half-scan is about 5 s long, adjacent rows of pixels in the map are separated by frequencies below f_k.

Why the Cottingham Method allows large scale contamination can be understood by recalling that it minimizes the variance of the hits in the pixels while being insensitive to their mean values ((c.f. Eqs. 4.16–4.20)). On the other hand, this means that the process does not "care" about the covariances *between* separate pixels so long as their individual variances are minimized. This is a subtle concept and Fig. 4.4 attempts to illustrate it graphically. If, as depicted in the figure, the pixels are sampled at a fixed frequency, then the atmospheric drift calculated by the Cottingham Method is free to contain oscillation at the same frequency, since this will not affect the temperature variance. Because of the ACT scanning pattern, this indeed occurs, especially since the sky often drifts nearly vertically through the field of view. Pixels are observed at nearly the scan frequency: those on the left side of the map are always several seconds apart from those on the right.

Moreover, on even longer time scales, pixels on the top and bottom of the map can be measured far enough apart from one another in time that there are several minutes between them in the time stream. In this case, there is no motivation for the B-spline not to slowly increase or decrease in the interval between them, since the basis B-splines are compact and exert little influence beyond their nearby neighbors.

These effects are manifested in the noise covariance matrix. In Fourier space, $\mathbf{N}$ has larger terms at harmonics of the scan frequency, and residual power at low frequencies. This is made clear by Fig. 4.7, below.

4.2.5 Spatial Structure in the Atmosphere

Thus far, the Cottingham Method only fits for an atmospheric signal $\mathbf{B}\alpha$ which varies in time and is common to all detectors. In fact, we know that there is spatial structure in the atmosphere, so that, in principle, each detector might see a different atmospheric signal. The reality is fortunately not this extreme. First, we observe in our data that the majority of the atmospheric signal is common across the array, meaning that the dominant spatial scales are large. Second, the finite telescope beam sets a lower limit on the spatial scale which is resolved. We observe in our data that the atmospheric signal is coherent across roughly a quarter to a third of the array—about 5–7′ (e.g., Switzer, 2008). This agrees with expectations from optical modelling. For example, our 148 GHz

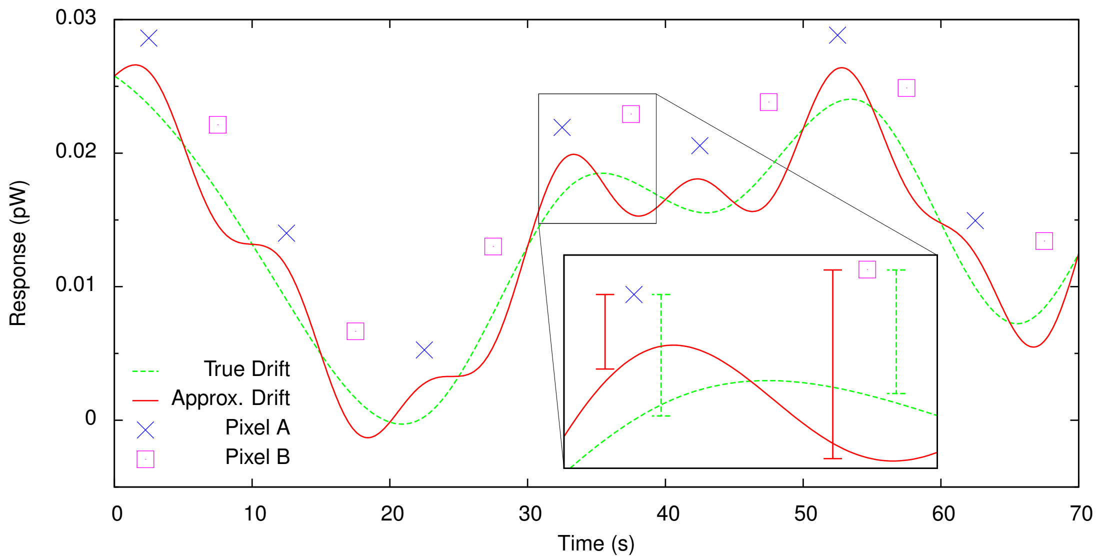

Figure 4.4: A cartoon of how the Cottingham Method can induce large-scale gradients. In this example, the true atmospheric power is represented by the short-dashed green line. Two pixels (labelled A and B in the figure) are hit every ten seconds, but five seconds out of phase with respect to each other. Suppose the Cottingham method is used to approximate the atmospheric drift. It might reasonably produce the drift shown in solid red, which has the same shape as the true drift at low frequencies, but superimposed with an oscillation of period ten seconds. This period is the same as that with which the pixels are sampled, so the variance of the difference between the approximated drift and the pixel measurements is the same as without the ten second oscillation. Since the Cottingham Method minimizes this variance, it is insensitive to the oscillation. The result is that the temperature difference between pixels A and B is poorly estimated. This will show up in the covariance matrix. The inset attempts to illustrate this by showing with the dashed green rulers that the true temperatures of pixels A and B are about the same, but solid red rulers, measuring from the oscillating but equally low-variance drift mode, give differing temperatures. In map space, with many more pixels than two, a large-scale spatial temperature gradient is induced.

band, which has a 1.37′ FWHM in the far-field, is sensitive to an angular size of approximately 10′ at a 1 km distance,[7] where the 6 m aperture still subtends a non-negligible angle. This is roughly the distance to a typical turbulence layer in the atmosphere when pointed at 50° in altitude (Pérez-Beaupuits et al., 2005).

In principle, one could consider adding an extra dimension to the amplitudes α to encode the basis function amplitudes as a function of space as well as time. We attempted to make this addition but found it impractical. Not only did the addition of the spatial dimension greatly increase the calculation time, but we had difficulty controlling the splines near the boundaries of the domain—briefly, because the sky drifts through azimuthally-scanning array at an angle, the shape of the time-space domain of α is trapezoidal and is not trivially modelled by B-splines near the regions where there is no support from the data. Finally, since the signal common to all detectors is much larger than the spatial variations between them, the fit seemed to concentrate more on the time dimension and did a poor job along the spatial axis, though this might have been related to the edge-effect mentioned above.

Perhaps a more careful treatment could implement a spatial component to the Cottingham Method, but we found satisfactory results simply by dividing the array into nine square "sub-arrays", as shown in Fig. 4.5. In each sub-array we fit an individual B-spline $\mathbf{B}_s\alpha_s$, with the subscript

[7] J. Fowler, private communication.

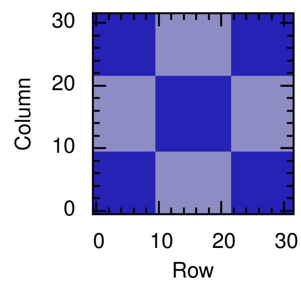

Figure 4.5: The sub-arrays defined within the 32×32 detector array to allow for spatial variation in the fit to atmospheric power. Both the rows and columns are partitioned into sections running from {0..9}, {10..21} and {22..31}. The Cottingham Method is applied separately to each sub-array, and sub-array maps are coadded later in the mapmaking process. Images of the nine sub-arrays like the one in this figure are whimsically called Brady Bunch plots, a nomenclature invented by D. Swetz.

$s \in [0, 8]$ denoting the sub-array. They can all be fit simultaneously if we adapt Eq. 4.6:

$$\begin{aligned} \mathbf{d} &= \mathbf{Pm} + \mathbf{S} \begin{pmatrix} \mathbf{B}_1 & \mathbf{0} & \dots & \mathbf{0} \\ \mathbf{0} & \mathbf{B}_2 & \dots & \mathbf{0} \\ \vdots & \vdots & \ddots & \vdots \\ \mathbf{0} & \mathbf{0} & \dots & \mathbf{B}_9 \end{pmatrix} \begin{pmatrix} \alpha_1 \\ \alpha_2 \\ \vdots \\ \alpha_9 \end{pmatrix} + \mathbf{n} \\ &= \mathbf{Pm} + \mathbf{SB}'\alpha' + \mathbf{n}, \end{aligned} \tag{4.24}$$

where $\mathbf{S}$ is a book-keeping matrix that remembers from which sub-block each measurement in $\mathbf{d}$ came and chooses the appropriate B-spline for that sub-block. The Cottingham Method proceeds exactly as before, except that we change $\mathbf{B} \rightarrow \mathbf{SB}'$ and $\boldsymbol{\alpha} \rightarrow \boldsymbol{\alpha}'$.

In component notation, we add an extra index, k, to B and α to denote the sub-block. The book-keeping matrix S_{pik} is zero for all values of k except for the value corresponding to the sub-block from which measurement d_{pi} came, in which case it is unity. Eq. 4.15 becomes:

$$d_{pi} = m_p + \sum_{jk} S_{pik} B_{pijk} \alpha_{jk} + n_{pi}. \tag{4.25}$$

4.3 Implementation and Evaluation of the Cottingham Method

4.3.1 Implementation

In our calculation of the atmospheric signal, we make the white noise approximation by setting $\mathbf{N} = \mathbf{I}$. As we will see (c.f. Fig. 4.7), this is not an unreasonable approximation. We did briefly explore assigning weights w_{pi} based on the detector rms's and found no significant improvement to the quality of the fit, although we did not attempt to quantify this. Nevertheless, a future implementation would benefit from proper treatment of the covariance. As we pointed out in §4.2.4, the covariance matrix has larger terms at low frequencies and at harmonics of the scan frequency. Including a more realistic $\mathbf{N}$ would downweight contributions from these modes in the map and atmosphere estimates.

Computation time is the most stringent practical consideration that needs to be addressed when we apply the Cottingham Method. The size of $\widetilde{\alpha}$ is small enough that solving for Eq. 4.14 (or Eq. 4.22), is not a rate-limiting step. In fact, it can be solved by brute force using a standard linear algebra algorithm such as Cholesky decomposition in a practical amount of time, although we

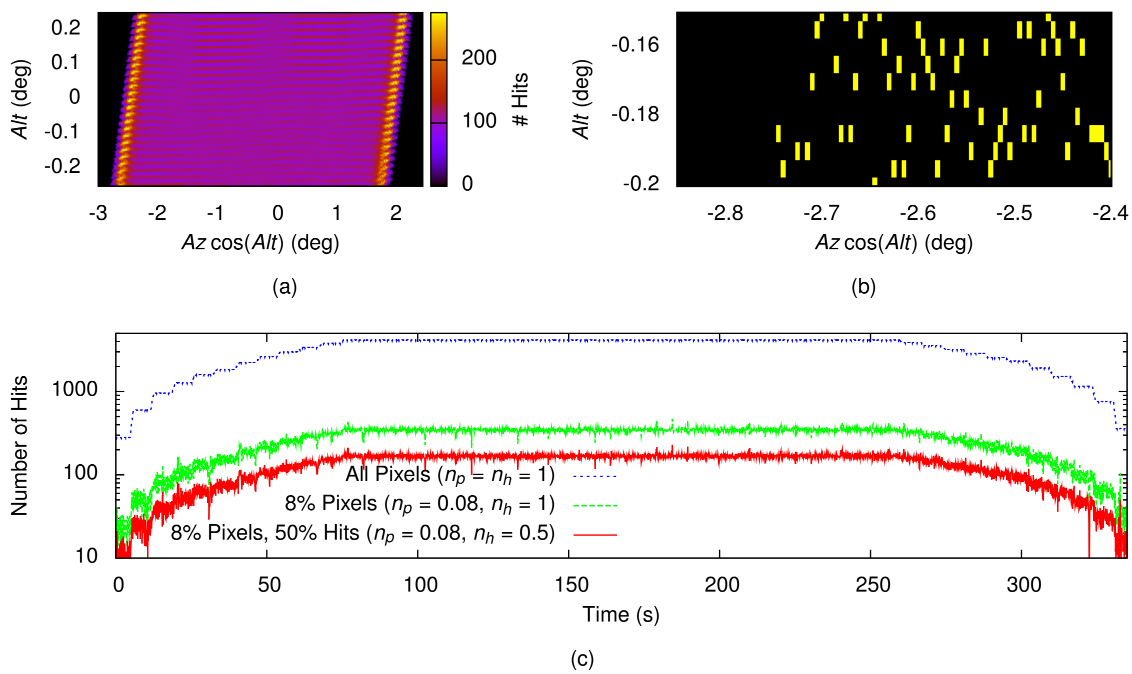

Figure 4.6: Hit statistics for a $0.3' \times 0.3'$ resolution map, $0.5°$ high in altitude, drifting through the detectors scanning $\pm 3.5°$ in azimuth. The total number of pixels is 95772. The telescope was at the standard position for its rising observations, viz., $50.2°$ altitude, $151.2°$ azimuth. The central 12×12 detectors of the 148 GHz array were used for the plots above, which show: (a) the number of hits per pixel in the map; (b) the map coverage if 8% of the pixels are uniformly sampled ($n_p = 0.08$, $n_h = 1$), zoomed in to a small portion of the map so that the individual pixels are visible; and (c) a histogram of the total number of hits in the map as a function of time, with a bin width of 0.1 s. In (c), the solid red line shows the number of hits when, of the 8% of the pixels which are sampled, only 50% of the hits per pixel are used ($n_p = 0.08$, $n_h = 0.5$).

use the conjugate gradient method (e.g., Press et al., 1992) since it is generally faster and yields indistinguishable results.

Most time is actually spent computing $\mathbf{\Theta}$ and ϕ (c.f. Eqs. 4.13 and 4.21). In principle, the calculation is quadratic in the number of basis functions $\mathbf{B}$. However, the sparseness of the B-spline basis functions can be exploited by careful book-keeping so calculations are only done where they are non-zero. Since the support at a given point is only provided by p bases (four, in the cubic case we use), this provides considerable savings. It also means that increasing the number of B-spline knots, and thereby increasing the size of $\mathbf{B}$ and $\widetilde{\alpha}$, only modestly adds to the computation time.

Further time savings are made by recognizing that the map pixelization used for calculating the atmospheric signal need not be the same as that used for the celestial map. Thus, we use slightly larger pixels for the Cottingham atmosphere estimate so that there are more measurements per pixel for better statistics. Furthermore, we only use a subset of the possible pixels, and within each pixel, downsample the number of hits. We call the former “pixel downsampling” and denote the fraction of retained pixels n_p, while the latter we call “hit downsampling” and denote the fraction of retained hits n_h. The computation of $\mathbf{\Theta}$ and ϕ depends linearly on both the number of pixels and the number of hits per pixel, so each of these downsamplings has a linear impact on the computation time. Both the pixel and hit downsamplings are done in an even manner so that there are no large gaps in the remaining time stream. Fig. 4.6 shows pixel coverage for a typical azimuthal scanning pattern and the resulting distribution after applying the downsampling schemes.

Altogether, we have specified five parameters which define the Cottingham Method implementation with B-splines: the polynomial order, p, the knot spacing, τ_k, the pixel size, ξ, the pixel downsampling fraction, n_p and the hit downsampling fraction, n_h. Of these, we always choose $p = 4$ (cubic) and $\xi = 0.3'\times0.3'$ (about 1/3 of the 277 GHz beam size). In the following section we examine the effect of varying the remaining three.

4.3.2 Performance

Fig. 4.7 shows some examples of the atmosphere signal estimated by the Cottingham methods for different knot spacings and $n_p = n_h = 1$. Clearly, the estimate with the smallest knot spacing ($\tau_k = 0.25$ s) does the best job at removing low frequency power, and we note that the spectrum after subtracting the B-spline is much closer to being white than the original. Note, however, the spikes at harmonics of the scan frequency and the residual power at low frequencies—see §4.2.4 and the discussion at the beginning of §4.3.1.

To quantify how the atmospheric estimate is degraded when we increase τ_k and decrease n_p and n_h, we introduce two figures of merit:

$$R \equiv \frac{1}{N_d}\sum_i^{N_d} \frac{\int_{0\text{Hz}}^{1\text{Hz}} \widetilde{G}(f)\,\mathrm{d}f}{\int_{0\text{Hz}}^{1\text{Hz}} G(f)\,\mathrm{d}f}, \tag{4.26}$$

$$L \equiv \frac{1}{N_d}\sum_i^{N_d} \left[\frac{\int_{0\,\text{Hz}}^{1\,\text{Hz}} \widetilde{G}_i(f)\,\mathrm{d}f}{\int_{0\,\text{Hz}}^{1\,\text{Hz}} \mathrm{d}f} \Bigg/ \frac{\int_{5\,\text{Hz}}^{25\,\text{Hz}} \widetilde{G}_i(f)\,\mathrm{d}f}{\int_{5\,\text{Hz}}^{25\,\text{Hz}} \mathrm{d}f} \right], \tag{4.27}$$

where the sum runs over the N_d detectors used for the Cottingham calculation, and G_i and $\widetilde{G}_i$ are the spectral densities of the i^{th} detector before and after removing the estimated atmosphere signal, respectively. The parameter R measures how much low-frequency power is removed by the fit and L measures the amount of remaining low-frequency power against the white-noise level (assumed to be represented by the mean spectral density between 5 and 25 Hz). Both R and L should decrease as the fit quality increases.

Fig. 4.8 shows plots of R and L for different choices of τ_k, n_p, and n_h, as well as the computation time required to do the fits. Clearly, the fit improves with smaller knot spacing, chiefly due to the ability of smaller spacing to remove power to higher frequencies. As we noted in §4.2.4, the spline fit is only effective to twice the frequency of the knot spacing, so in Fig. 4.8, the splines with $\tau_k = 0.25$ s and $\tau_k = 0.5$ s are capable of removing power up to 1 s, but $\tau_k = 1.0$ s is not. It is also apparent that at a certain point including more data adds little precision to the fit. For $\tau_k = 1.0$ s, for example, R and L remain essentially constant for all the tested combinations of parameters, and in the smaller knot spacings, R and L approach asymptotes as more data are included.

Is this property of the fit sensitive to each of the pixel downsampling n_p and the hit downsampling n_h in different ways, or is only the total number of included data $n_p n_h$ important? Fig. 4.9 demonstrates that the latter is indeed more important. For all knot spacings included in the study, including only 10% of the data can remove atmospheric power with virtually the same effectiveness as if all data had been used. As a point of interest, the points in Fig. 4.9 can be fit well by the equation:

$$L = \sqrt{L_0(\tau_k) + \frac{L_{knee}(\tau_k)}{n_p n_h}}. \tag{4.28}$$

This is the curve which is fit to the data in the figure in order to guide the eye. The exact dependence of L_0 and L_{knee} on τ_k (assuming there is one) is not measurable with the small dataset included in the figure, but in general, as τ_k increases, L_0 and L_{knee} increase, as expected.

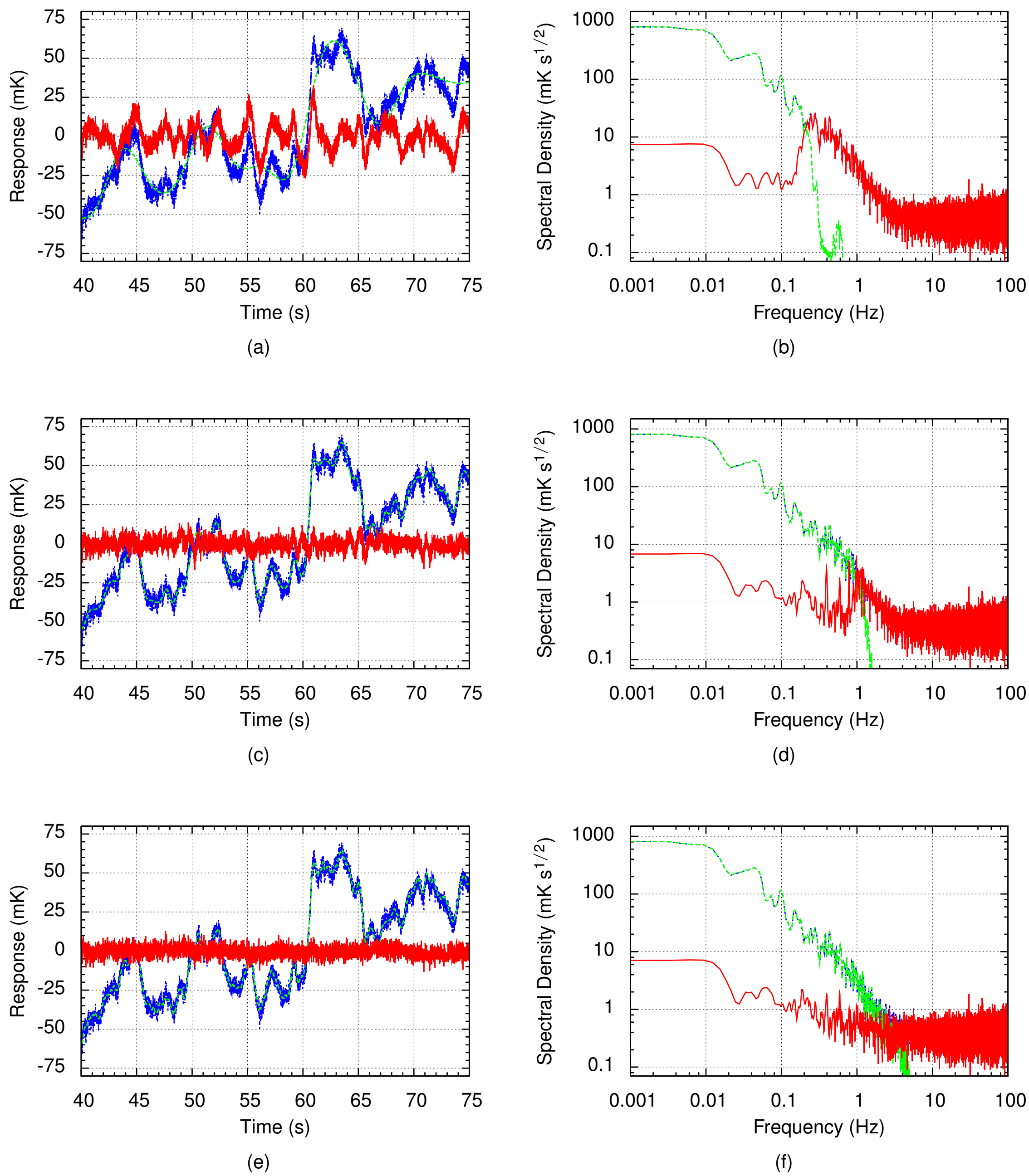

Figure 4.7: Examples of the Cottingham Method atmosphere estimate. The time stream was about 300 s long, with all data ($n_p = n_p = 1$) from 605 detectors used. Shown above are fit results from three different knot spacings: every five seconds ((a) and (b)), every one second ((c) and (d)) and every quarter second ((e) and (f)). In each plot the original signal is plotted in short-dashed blue, the spline fit in long-dashed green and the resulting filtered signal in solid red—in the right-hand plots, the blue curves are hardly visible because the green curves overlap very well. The left-hand plots show a portion of the time stream and the right-hand plots show their spectral densities (for the whole 300 s time stream). Only one detector was selected out of the 605 to appear in these plots. The spectral density data have been filtered with a five-sample boxcar for ease of viewing. In the right-hand plots, the spline power drops off at about half the frequency of the knot spacing: most likely a consequence of the Nyquist-Shannon sampling theorem.

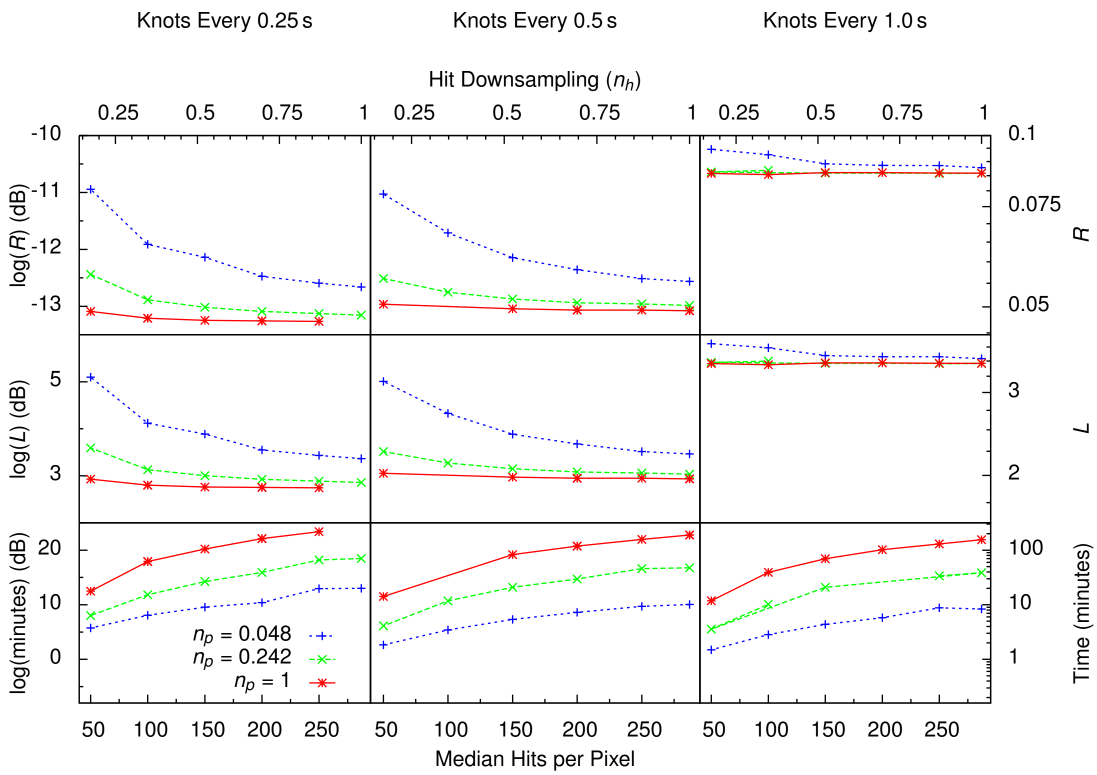

Figure 4.8: Measurements of the Cottingham fit quality and speed. For all the tests, the same time stream was used. The length of the data was about 300 seconds and 605 detectors were included in the calculation. Test results from three knot spacings are displayed here: 0.25 s (left column), 0.5 s (center column) and 1.0 s (right column). For each knot spacing, the drift was calculated using three different samplings of the 103487 total pixels: all pixels ($n_p = 1$), 25000 pixels ($n_p = 0.242$) and 5000 pixels ($n_p = 0.048$). Finally, for each knot spacing and pixel downsampling, runs were performed using different hit downsampling, as indicated on the x-axes. Two figures of merit are plotted: in the top row, R, a measure of the total power removed below 1.0 Hz, and in the middle row, L, a comparison of the power below 1.0 Hz to the white noise level (Eq. 4.27). The bottom row of plots shows the computation time required for each of the tests on a 2.5 GHz, 64-bit Intel Xeon® processor.

4.4 Making Sky Maps

4.4.1 TOD Maps

Once we have the maximum likelihood estimate of the atmospheric signal for a TOD, $\mathbf{B}\widetilde{\alpha}$, we can solve Eq. 4.11 for the best estimate of the celestial map, $\widetilde{\mathbf{m}}$. The mapmaking equation, including all sub-blocks (c.f. Eq. 4.11, §4.2.5) is:

$$\widetilde{\mathbf{m}} = \mathbf{\Pi}\left[\mathbf{d} - \mathbf{S}\left(\mathbf{B}'\alpha' - \mathbf{b}\right)\right], \tag{4.29}$$

where we have included a vector of offsets $\mathbf{b}$, to be determined, which compensates for the fact the sub-block fits produced by the Cottingham Method have arbitrary offsets—a consequence of the fact that the method is insensitive to the "DC", or celestial, part of the signal.

We make the white noise approximation, allowing the noise level to be different for each detector. As we mentioned in §4.1, this is equivalent to coadding individual detector maps, weighted by the inverse detector variance. The individual detector maps are made by averaging the hits from a given detector in each pixel; in component notation, we have:

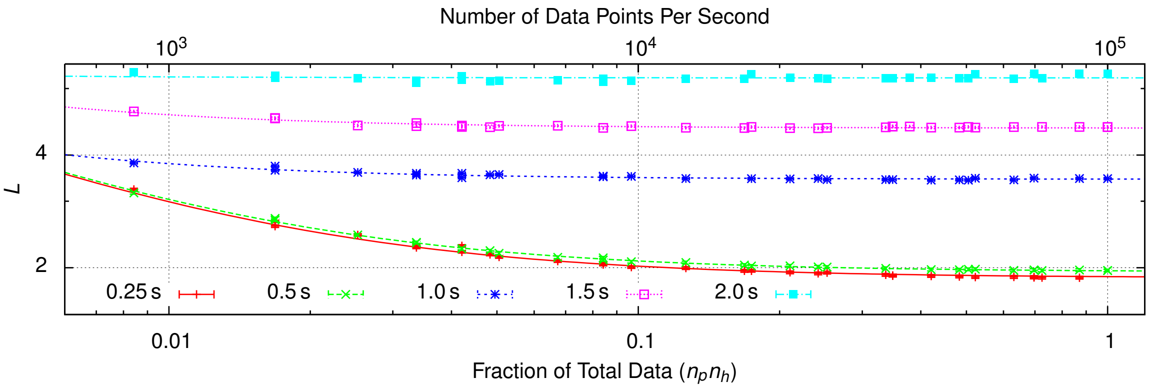

Figure 4.9: A study of how the parameter L varies as a function of the total fraction of data, $n_p n_h$ included in the Cottingham fit. The data shown here are the same as in Fig. 4.8, with the addition of more knot spacings. L is plotted as a function of the number of data points per knot spacing. Five different knot spacings are included, ranging from 0.5 s to 2.0 s. The points are measured and the curves are the best fits to Eq. 4.28.

$$\widetilde{m}_p^\mu = \frac{1}{N_p^\mu} \sum_{i=0} \left[d_{pi}^\mu - \sum_k S_{pik} \left(\sum_j B_{pijk} \alpha_{jk} - b_k \right) \right], \tag{4.30}$$

where the superscript μ labels the detector and N_p^μ is the number of hits detector μ had in pixel p. If we let $w^\mu \equiv 1/(\sigma^\mu)^2$ be the detectors' inverse variances, then the full map is simply the weighted average of the detector maps:

$$\widetilde{m}_p = \frac{\sum_\mu w^\mu \widetilde{m}_p^\mu}{w_p}; \quad w_p = \sum_\mu w^\mu, \tag{4.31}$$

where w_p is called the "weight map".

We obtain the weights w^μ and the offsets b_k iteratively. The first iteration sets all $w^\mu = 1$ and $b_k = 0$ to calculate a map $\widetilde{m}_p$ from detector maps $\widetilde{m}_p^\mu$. Subsequent iterations begin by calculating the mean difference between pixel hits in a given sub-block and the values in the map $\widetilde{m}_p$ to find an updated set of offsets b_k', which are used to generate a new set of detector maps $\widetilde{m}_p^{\mu\prime}$. From these, new weights are computed:

$$w^{\mu\prime} = \left[\frac{1}{M^\mu} \sum_p \left(\widetilde{m}_p - \widetilde{m}_p^{\mu\prime} \right)^2 \right]^{-1}, \tag{4.32}$$

where the sum is only over pixels that have received hits from detector μ, M^μ in number. The iteration ends by generating a new map with the new weights and new detector maps. Convergence occurs when the change in the average of the weights $w^{\mu\prime}$ is small, generally chosen to be 0.01%, and takes a handful of iterations.

The TOD maps are made in horizontal ($\Delta A \cos a$, Δa) coordinates, where ΔA and Δa are offsets from the map center in azimuth and altitude, respectively, and the argument of the cosine is the absolute altitude, not the offset. This coordinate system is a small-angle approximate to the Gnomonic projection which has the property that great circle arcs are straight lines in the projection (Snyder, 1987). Far from the tangent point of the projection, which we place at the map center, the image is distorted, as the trigonometric tangent of the angular distance, but for small maps the effect is small.

4.4.2 TOD Map Post-Processing

For some applications, such as beam studies with bright point sources, the raw maps are clean enough for precise analysis. However, maps with low signal-to-noise need some postprocessing to be useful.

We described in §4.2.4 how the Cottingham Method can introduce large spatial scale power into the celestial map. This can produce both smooth gradients across maps, and striping between rows of pixels (where rows are oriented along lines of constant altitude). To remove these, we do a least-squares fit of a straight line to each row and subtract it. If there is a known bright object in the field, it is masked out during the fit (but not during the subtraction). We call this process *stripe-removal*.

Clearly, stripe-removal is not ideal since it does contaminate the map. Any real large scale gradients are at least partially removed. Features in the map such as an unknown point source, or a hot or cold spot in the CMB, will bias the fits. The correct way to reduce the need for stripe-removal would be to use a more realistic noise covariance in the mapmaking, rather than the white noise approximation we have made. This would downweight the contaminating modes to suppress striping. In Chapter 6 we examine the effect of stripe-removal in more detail.

4.4.3 Map Coaddition

Coadding multiple TOD maps into a single map is relatively straightforward. Before coaddition, the backgrounds of the input maps must be removed: the offsets **b** removed in §4.4.1 were only relative to the other sub-block maps, and there still remains a single, arbitrary offset for the TOD map. If stripe-removal was performed (c.f. §4.4.2) this will have already occurred because the straight line fit includes an offset. Otherwise, the mean background, outside any specified mask, is subtracted.

If the final map is to be in equatorial coordinates, the TOD maps are rotated into $(\Delta\alpha \cos\delta, \Delta\delta)$ space, where α and δ denote right ascension and declination, and the map is in the same type of projection as described in §4.4.1, with the tangent point of right ascension and declination in the center of the map. Rotation to equatorial coordinates naturally occurs before coaddition since TOD maps can come from different telescope pointings.[8]

Denote the input TOD maps $\widetilde{m}^i_p$ and their companion weight maps w^i_p, where the index i labels the TOD—a Roman index is used to distinguish from the Greek μ used for labelling individual detectors in §4.4.1. The coadded map is computed in a completely analogous way to Eq. 4.31:

$$\widetilde{m}_p = \frac{\sum_i w^i_p \widetilde{m}^i_p}{w_p}; \quad w_p = \sum_i w^i_p. \tag{4.33}$$

In practice we found that the TOD weight maps w^i_p need to be modified. While they are good representations of the relative weights within a single TOD map, their overall weights are not always representative of the noise differences from TOD map to TOD map. This normally occurs if a TOD map had many fewer hits than its companions. The statistics from its individual detector maps are often not sufficient to accurately represent the overall noise level. Therefore, we calculate the variance V^i in each map, masking out any bright feature in the map, and set the median value of the weight maps to the inverse of this variance:

$$w^{i\prime}_p = \frac{w^i_p}{\mu_{1/2}(w^i_p)} V^i, \tag{4.34}$$

[8] Even if all maps came from the same telescope pointing, the precession of the equinoxes would still offset the maps relative to each other unless they were all taken in a sufficiently short period of time.

where $\mu_{1/2}(x)$ denotes the median of the distribution x. The median is used rather than the mean to protect against outliers with spuriously high or low weights coming from pixels with only a handful of hits.

4.5 Data Pipeline Summary

The steps which occur to go from a raw time stream to a finished map are described throughout Chapters 3 and 4. In this section we list them all together as a summary for quick reference.

- **One-Time Measurements**
  - Time constants, measured from planet peak shifts (§3.2).
  - Relative detector pointing, measured from planet observations (§3.3).
    - Absolute pointings at specific telescope pointings are determined using radio point sources (§6).
- **Time Stream Preprocessing**
  - Remove mean value of time stream (§3.1).
  - Cut detectors with flux jumps, excise spikes (§3.1).
  - Do Fourier domain processing (§3.1.1):
    - deconvolve digital filter;
    - deconvolve detector time constants (cut detectors with time constants below 20 Hz);
    - apply sine-squared low-pass filter and down-sample (c.f. Table 3.1).
  - Remove dark modes (§3.1.2).
  - Write preprocessed TOD to disk for future access.
- **Mapmaking**
  - Do gain calibration to units of power (§3.4):
    - apply IV calibration and cut detectors which have bad operating points;
    - flat-field using the atmospheric common mode.
  - Calculate and subtract atmospheric signal with the Cottingham method (§4.2).
  - Create TOD maps (§4.4.1).
  - Perform stripe-removal (§4.4.2)—*optional*.
  - Rotate to equatorial coordinates (§4.4.3)—*optional*.
  - Coadd TOD maps (§4.4.3).
  - Apply temperature calibration (§5.3).

Chapter 5

Beams & Calibration

5.1 Beam Theory

Two properties of the telescope which are necessary for accurately interpreting the final results are the beams and the temperature response. The beam encodes the relative response of the telescope to different angular sizes on the sky and needs to be precisely understood in order to interpret any map, including analysis of the power spectrum of CMB anisotropies. The temperature response is essentially the gain calibration from electrical power measured in the detectors to intrinsic celestial temperature. Both are measured using planets, and since they are related, both are discussed in this chapter.

In this section we outline basic beam theory and introduce useful formulas and definitions. The procedure and results of our beam measurements are in §5.2, and the temperature calibration is presented in §5.3.

5.1.1 The Instrument Response in Real Space

In full generality, the power P received by the telescope pointed at position $\hat{\mathbf{n}}$ on the celestial sphere is:

$$P(\hat{\mathbf{n}}) = \iint \mathrm{d}\Omega_{\hat{\mathbf{n}}'} \mathrm{d}\nu \, b_\nu(\hat{\mathbf{n}}, \hat{\mathbf{n}}') \, \eta(\nu) \, g_B(\nu) \, e^{-\tau_\nu(\hat{\mathbf{n}}')} A_e(\nu) \, S_\nu(\hat{\mathbf{n}}'). \tag{5.1}$$

(See Fig. 5.1 for a graphic of the coordinate system we use throughout.) The integral is done over frequency $\mathrm{d}\nu$ and celestial position $\mathrm{d}\Omega_{\hat{\mathbf{n}}'}$, and depends on the following quantities:

- the beam b, also known as the instrument response or power pattern; it has unity gain along the boresight, i.e., $b(\hat{\mathbf{n}}, \hat{\mathbf{n}}) = 1$,
- the overall efficiency η,
- the bandpass, or frequency response, g_B, normalized to unity at the peak,
- the atmospheric optical depth τ,
- the effective aperture area A_e, and
- the surface brightness S of the sky.

Eq. 5.1 is unwieldy for practical purposes, so we make some approximations.

First, we consider frequency-averaged terms, weighted by the bandpass $g_B(\nu)$: this will be indicated simply by dropping the ν subscript on variables. Technically, the frequency averaging should be done on the entire integrand of Eq. 5.1, but we band-average terms individually. Since

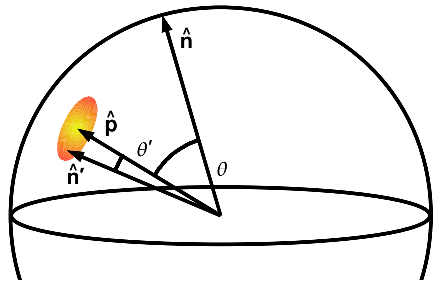

Figure 5.1: The beam coordinate system. Directions are represented as vectors on the unit sphere. The beam center points along $\hat{\mathbf{n}}$; the variable of integration is $\hat{\mathbf{n}}'$ (e.g., Eq. 5.1, 5.4, etc.). The center of an object being observed is located at $\hat{\mathbf{p}}$, and the directions $\hat{\mathbf{n}}$ and $\hat{\mathbf{n}}'$ lie at angles θ and θ' from it, respectively (e.g., Eq. 5.14).

the bandpass is static, our analysis should be consistent if we are consistent with how we use our averaged terms.

Second, we work in effective temperature units rather than flux, since both CMB and planetary science is more natural in these units. This entails making the conversion:

$$\eta A_e S(\hat{\mathbf{n}}') \longrightarrow \sum_s \frac{T_s(\hat{\mathbf{n}}')}{\alpha_s \Omega_\mathrm{A}}, \tag{5.2}$$

where T_s is the effective temperature, Ω_A is the beam solid angle, discussed more below, and α_s converts from units of power to temperature, incorporating the telescope efficiency η and effective aperture A_e. The subscript s denotes the sources' spectral energy distributions (SED's), which will alter all three of these variables. In the most general case, the telescope could be observing multiple sources with different SED's, so we sum over s. In practice, however, we consider only one type of source at a time and drop the sum. The two most common SED's are those of the CMB and of Rayleigh-Jeans source, which we denote with the subscripts CMB and RJ, respectively, e.g., T_RJ or α_CMB.

Third, we assert that the beam function is independent of the telescope pointing:[1]

$$b(\hat{\mathbf{n}}, \hat{\mathbf{n}}') = b(\hat{\mathbf{n}} - \hat{\mathbf{n}}'). \tag{5.3}$$

Finally, since the beam is small, we approximate the opacity as constant within its extent so that the term $e^{-\tau}$ in Eq. 5.1 can be brought outside of the integral.

Incorporating all of these changes, Eq. 5.1 becomes:

$$\begin{aligned} P(\hat{\mathbf{n}}) &= \frac{e^{-\tau(\hat{\mathbf{n}})}}{\alpha_s \Omega_\mathrm{A}} \int \mathrm{d}\Omega_{\hat{\mathbf{n}}'} b(\hat{\mathbf{n}} - \hat{\mathbf{n}}') T_s(\hat{\mathbf{n}}') \\ &= \frac{e^{-\tau(\hat{\mathbf{n}})}}{\alpha_s \Omega_\mathrm{A}} \left[(b \star T_s)(\hat{\mathbf{n}}) \right], \end{aligned} \tag{5.4}$$

where the star operator ($\star$) denotes convolution over the sphere.

The beam solid angle, which was introduced above so that α_s need have no knowledge of any angular scales, is in itself an important antenna property. It is defined as:

$$\Omega_\mathrm{A} \equiv \int_{4\pi} b(\hat{\mathbf{n}}') \mathrm{d}\Omega_{\hat{\mathbf{n}}'}. \tag{5.5}$$

[1] One caveat to this assertion is that as the telescope scans in azimuth, the finite time constants of the detectors smear the response, so that the beam shape is dependent on the angular velocity. However, because these time constants are deconvolved in preprocessing (see §3.1.1), the constant beam approximation stands.

where we choose $\hat{\mathbf{n}} = 0$ with no loss of generality since our beam is independent of pointing. The solid angle defines the forward gain, or directivity:

$$G \equiv \frac{4\pi}{\Omega_A}. \tag{5.6}$$

The solid angle is a single number which quantifies the size of the beam on the sky without specifying the exact shape of the beam pattern b. It indicates how the telescope responds to different angular sizes: features which are smaller than Ω_A will be smeared out, or diluted, while features that are much larger will not suffer any significant dilution. Of course, the most precise way to correct for this dilution is to deconvolve the beam from the measurements, especially when the source has many different angular scales — such as the CMB. This is essentially the job of the window function which is discussed further in §5.1.2. However, for compact sources, such as the planets which are used for characterizing the beam, it is useful to have a single quantity which defines the dilution. To this end, separate a source's effective temperature into the peak temperature $T_0 = T_s(\hat{\mathbf{n}}' = \mathbf{0})$ (which we have placed at the origin) and a spatial component[2] $\Psi(\hat{\mathbf{n}}') = T_s(\hat{\mathbf{n}}')/T_0$. Pointing directly at the center of the source, we have from Eq. 5.4:

$$\alpha_s P(\mathbf{0}) e^{\tau} = \frac{T_0}{\Omega_A} \int d\Omega_{\hat{\mathbf{n}}'}\, b(-\hat{\mathbf{n}}')\Psi(\hat{\mathbf{n}}') = \mathcal{D}_\Psi T_0, \tag{5.7}$$

where we have introduced the "dilution factor" (Switzer, 2008):

$$\mathcal{D}_\Psi \equiv \frac{1}{\Omega_A} \int d\Omega_{\hat{\mathbf{n}}'}\, b(-\hat{\mathbf{n}}')\Psi(\hat{\mathbf{n}}'). \tag{5.8}$$

It has been defined so that for a completely diffuse source $\Psi(\hat{\mathbf{n}}') = 1$, $\mathcal{D}_\Psi = 1$. It is also known as the "beam filling factor", since sources which are smaller in angular size than the beam do not completely fill the beam, and have $\mathcal{D}_\Psi < 1$.

5.1.2 The Instrument Response in Spherical Harmonic Space

We saw in Eq. 5.4 that the instrument response is proportional to the convolution of the beam with the sky temperature. In spherical harmonic space, this is simply a multiplication. Letting $a_{\ell m}$ and $\widetilde{a}_{\ell m}$ be the harmonic coefficients of the sky temperature T and the measured temperature $\widetilde{T} \equiv Pe^{\tau}/\alpha$, respectively,

$$\widetilde{a}_{\ell m} = a_{\ell m}\, b_{\ell m}, \quad b_{\ell m} = \int d\Omega_{\hat{\mathbf{n}}'}\, b(-\hat{\mathbf{n}}')\, Y_{\ell m}(\hat{\mathbf{n}}'). \tag{5.9}$$

In the equation for $b_{\ell m}$ we have set $\hat{\mathbf{n}} = 0$ with no loss of generality because b is independent of the pointing (c.f. Eq. 5.3). $Y_{\ell m}$ are the orthogonal spherical harmonic functions. As discussed in §1.1.1, a primary measurement of interest is the angular power spectrum C_ℓ. The relationship between the measured power spectrum $\widetilde{C}_\ell$ and the true spectrum C_ℓ is evidently:

$$\widetilde{C}_\ell = C_\ell \sum_{m=-\ell}^{+\ell} b^*_{\ell m} b_{\ell m}. \tag{5.10}$$

Comparing with Eq. 1.7, we see that the window function is therefore closely related to the beam:

$$w_\ell = \frac{4\pi}{2\ell + 1} \sum_{m=-\ell}^{+\ell} |b_{\ell m}|^2. \tag{5.11}$$

[2]It is assumed that the spectral properties of the source do not change over its spatial extent, so that a single effective temperature suffices.

To be precise, this is the window function at at zero lag, the quantity of most interest (White & Srednicki, 1995; Bond, 1996).

If the beam is symmetric (i.e., $b = b(|\hat{\mathbf{n}} - \hat{\mathbf{n}}'|)$), then we can use the addition theorem for spherical harmonics (Matthews & Walker, 1965, §7-1) to reduce the window function to the square of the Legendre transform of the symmetric beam:

$$w_\ell = b_\ell^2; \quad b_\ell = \frac{2\pi}{\Omega_A} \int b^S(\theta) P_\ell(\cos\theta)\, \mathrm{d}(\cos\theta), \tag{5.12}$$

where P_ℓ are the Legendre polynomials, $\theta \equiv |\hat{\mathbf{n}} - \hat{\mathbf{n}}'|$ and the superscript S indicates that the beam is symmetric. A useful approximation for quick calculations is the window function of a symmetric Gaussian beam of width σ (White, 1992):

$$w_\ell \approx e^{-\ell(\ell+1)\sigma^2}. \tag{5.13}$$

5.1.3 Characterizing the Beam Function

It should be clear by now that knowledge of the beam function b is essential for interpreting the data measured by the telescope. Let us first briefly present basic results from beam models before discussing how the true beam function is measured.

5.1.3.1 Important Properties of the Airy Pattern

The beam for a perfect circular aperture of radius a is derived by considering the Fraunhofer diffraction limit and yields the Airy pattern (Born & Wolf, 1999, §8.5.2):

$$b_k^A(\theta) = \left[\frac{2J_1(ka\theta)}{ka\theta}\right]^2, \tag{5.14}$$

where $k = 2\pi\nu/c$ is the wavenumber of the monochromatic light, J_1 is a first-order Bessel function of the first kind and $\theta \equiv |\hat{\mathbf{n}} - \hat{\mathbf{n}}'|$. A useful quantity is the the full-width at half maximum (FWHM) of the beam, defined as the full width of the beam at the point where it first reaches half of its peak intensity. For the Airy pattern it may be numerically derived and is (in radians):

$$\theta_{1/2}^A = \frac{3.23266}{ka} = \frac{1.02899\,\lambda}{2a}. \tag{5.15}$$

The solid angle of the Airy pattern is:

$$\Omega_A^A = 2\pi \int_0^\infty \theta \mathrm{d}\theta\, \frac{4J_1^2(ka\theta)}{(ka\theta)^2}. \tag{5.16}$$

Making the change of variables $x = ka\theta$,

$$\begin{aligned} \Omega_A^A &= \frac{8\pi}{(ka)^2} \int_0^\infty \mathrm{d}x \frac{J_1^2(x)}{x} \\ &= \frac{4\pi}{(ka)^2} \int_0^\infty \mathrm{d}\left[-J_0^2(x) - J_1^2(x)\right]. \end{aligned} \tag{5.17}$$

The second line was obtained using the identity (Abramowitz & Stegun, 1964; Born & Wolf, 1999, §9.1.30,§8.5):

$$\mathrm{d}\left[x^{-n} J_n(x)\right] = -x^{-n} J_{n+1}(x)\, \mathrm{d}x. \tag{5.18}$$

To evaluate the endpoints of the integral, we use the values $J_0(0) = 1$ and $J_1(0) = 0$; at infinity, the asymptotic formula show that both vanish (Abramowitz & Stegun, 1964, §9.2.1):

$$\lim_{x\to\infty} J_n(x) = \sqrt{\frac{2}{\pi x}} \cos\left(x - \frac{n\pi}{2} - \frac{\pi}{4}\right). \tag{5.19}$$

Therefore:

$$\Omega_{\rm A}^{\rm A} = \frac{4\pi}{(ka)^2} = 1.20251 \left(\theta_{1/2}^{\rm A}\right)^2. \tag{5.20}$$

Eq. 5.19 allows us to describe the "wings" of the Airy pattern far from the peak. Since we will be more interested in its general trend, we average over the cosine cycles to obtain:

$$\lim_{\theta\to\infty} b_k^{\rm A}(\theta) = \frac{4}{\pi(ka\theta)^3} = 3.76903\times10^{-2}\left(\frac{\theta_{1/2}^{\rm A}}{\theta}\right)^3 = \left(\frac{\theta_W}{\theta}\right)^3. \tag{5.21}$$

where we introduce the characteristic "wing" scale θ_W. This approximation is good to better than 1% for $\theta > 5\theta_{1/2}^{\rm A}$ (Schroeder, 2000, §10.2b). If we know θ_W, then given a beam map of finite size, we can interpolate how much solid angle is missing beyond the map boundaries—call it Ω_M. Outside a boundary radius θ_b,

$$\Omega_M(\theta_b) = 2\pi\int_{\theta_b}^{\infty} \theta d\theta \left(\frac{\theta_W}{\theta}\right)^3 = 2\pi\frac{\theta_W^3}{\theta_b}. \tag{5.22}$$

Thus far we have described the beam of a perfect circular aperture for monochromatic light. One can model many physical departures from this ideal, including apodization of the aperture and imperfections in the optical surfaces—Born & Wolf (1999) have a thorough introduction to these topics. For our purposes, however, we need go no further than these general beam properties, which serve as guidelines for checking the magnitudes of the beam properties which we measure. Nevertheless, a couple of points should at least be mentioned.

First, the beam pattern measured by any real telescope is integrated over some finite frequency band. This smears out the beam a little and fills in the deep nulls of the monochromatic Airy pattern.

Second, in the ACT, the wavelength of our frequencies are on the same order as the size of our detectors, about $1\times1\,\mathrm{mm}^2$. This finite size acts like low-pass filter on the number of electromagnetic modes to which they can couple. The effect is like convolving the detector shape with the band-averaged Airy function, so we expect our higher frequencies to have a square shape to them. Withington et al. (2007) and Saklatvala et al. (2008) explore this effect more closely with a combination of analytical and numerical modelling.

5.1.3.2 Measuring the Beam

The easiest way to measure the beam is to observe a point source, which is mathematically a delta function. Therefore, the convolution in Eq. 5.4 is trivial and we find:

$$b(\hat{\mathbf{n}}) = \frac{\alpha_s e^{\tau}\Omega_{\rm A}}{T_0} P(\hat{\mathbf{n}}), \tag{5.23}$$

where T_0 is the temperature of the point source. From our definition of the dilution factor in Eq. 5.8, we clearly have $\mathcal{D} = 1/\Omega_{\rm A}$, so, according to Eq. 5.7, our delta-function beam measurement reduces to:

$$b(\hat{\mathbf{n}}) = \frac{P(\hat{\mathbf{n}})}{P(\mathbf{0})}. \tag{5.24}$$

Thus we have recovered the basic definition of the beam: the normalized response to a point source.

For the ACT, the best objects for measuring the beam are planets since they have a high signal-to-noise. The angular sizes of the planets we used are much smaller than the telescope beam, but large enough to make a difference at the percent precision level. The most important effect is on the solid angle measurement. Let $\widetilde{b}$ be the apparent beam we measure using from a planet using Eq. 5.24. We then obtain an apparent solid angle (c.f. Eq. 5.5):

$$\widetilde{\Omega}_{\mathrm{A}} = \iint \mathrm{d}\Omega_{\hat{\mathbf{n}}'} \widetilde{b}(\hat{\mathbf{n}}') = \iint \mathrm{d}\Omega_{\hat{\mathbf{n}}'} \frac{P(\hat{\mathbf{n}}')}{P(\mathbf{0})} = \frac{1}{\Omega_{\mathrm{A}}\mathcal{D}} \iint \mathrm{d}\Omega_{\hat{\mathbf{n}}'} \left[\iint d\Omega_{\hat{\mathbf{n}}''} b(\hat{\mathbf{n}}' - \hat{\mathbf{n}}'')\Psi(\hat{\mathbf{n}}'') \right], \tag{5.25}$$

where we have expressed $P(\mathbf{0})$ in terms of the dilution factor (Eq. 5.8), Ω_{A} is the true (as opposed to apparent) solid angle, and the response $P(\hat{\mathbf{n}}')$ is the convolution of the beam with the source as prescribed by Eq. 5.4, using Ψ as before to describe the normalized source shape. The integral is easily evaluated by changing the order of integration:

$$\begin{aligned} \widetilde{\Omega}_{\mathrm{A}} &= \frac{1}{\Omega_{\mathrm{A}}\mathcal{D}} \iint \mathrm{d}\Omega_{\hat{\mathbf{n}}''} \iint \mathrm{d}\Omega_{\hat{\mathbf{n}}'} b(\hat{\mathbf{n}}' - \hat{\mathbf{n}}'')\Psi(\hat{\mathbf{n}}'') \\ &= \frac{1}{\Omega_{\mathrm{A}}\mathcal{D}} \left[\iint \mathrm{d}\Omega_{\hat{\mathbf{n}}''} \Psi(\hat{\mathbf{n}}'') \right] \left[\iint \mathrm{d}\Omega_{\hat{\mathbf{n}}'} b(\hat{\mathbf{n}}') \right], \end{aligned} \tag{5.26}$$

where in the last equality we translated the dummy variable of the integral over $\hat{\mathbf{n}}'$. The expression we have obtained is simply a manifestation of the property of convolutions that the area under a convolution is the product of the area of its factors. The first integral in Eq. 5.26 yields the solid angle of the planet, which we denote Ω_Ψ, and the second is the true solid angle of the beam Ω_{A}. Therefore:

$$\widetilde{\Omega}_{\mathrm{A}} = \frac{\Omega_\Psi}{\mathcal{D}}. \tag{5.27}$$

Note that in the point-source limit, this reduces to $\widetilde{\Omega}_{\mathrm{A}} = \Omega_{\mathrm{A}}$, following from the definition of $\mathcal{D}$.

Let us evaluate the dilution factor assuming that the true beam is an Airy pattern and the planet is a solid disk of radius θ_Ψ. The true solid angle is given by Eq. 5.20 and the planet's solid angle is $\Omega_\Psi = \pi\theta_\Psi^2$. The dilution is:

$$\mathcal{D} = \frac{1}{\Omega_{\mathrm{A}}} \int_0^{2\pi} \mathrm{d}\phi \int_0^{\theta_\Psi} \theta' \mathrm{d}\theta' \left[\frac{2J_1(ka\theta')}{ka\theta'} \right]^2. \tag{5.28}$$

This integral is the same as that of Eqs. 5.16–5.17 except for the limits. We obtain:

$$\mathcal{D} = 1 - J_0^2(ka\theta_\Psi) - J_1^2(ka\theta_\Psi), \tag{5.29}$$

where a factor $4\pi/(ka)^2$ produced in the integration cancels the Ω_{A} from Eq. 5.28. In the limit that the planet is small, i.e., $\Omega_\Psi \ll \Omega_{\mathrm{A}}$, we can make use of the low order terms from the series expansion of first-order Bessel functions (Abramowitz & Stegun, 1964, §9.1.10):

$$J_\nu(z) = \left(\frac{z}{2}\right)^\nu \sum_{k=0}^{\infty} \frac{\left(-z^2/4\right)^k}{k!\,\Gamma(\nu + k + 1)}. \tag{5.30}$$

Expanding to second order in Ω_Ψ, or fourth order in θ_Ψ, Eq. 5.29 is approximated by:

$$\begin{aligned}\mathcal{D} &\approx 1 - 1 + \frac{(ka\theta_\Psi)^2}{4} - \frac{(ka\theta_\Psi)^4}{32} \\ &= \frac{\Omega_\psi}{\Omega_\mathrm{A}}\left(1 - \frac{1}{2}\frac{\Omega_\Psi}{\Omega_\mathrm{A}}\right),\end{aligned} \tag{5.31}$$

where we used Eq. 5.20 and the fact that $\Omega_\Psi = \pi\theta_\Psi^2$. Inserting into Eq. 5.27, we find that the apparent solid angle is:

$$\widetilde{\Omega}_\mathrm{A} \approx \frac{\Omega_\mathrm{A}}{1 - \frac{1}{2}\frac{\Omega_\Psi}{\Omega_\mathrm{A}}} \approx \Omega_\mathrm{A}\left(1 + \frac{1}{2}\frac{\Omega_\Psi}{\Omega_\mathrm{A}}\right) = \Omega_\mathrm{A} + \frac{1}{2}\Omega_\Psi, \tag{5.32}$$

valid when $\Omega_\Psi \ll \Omega_\mathrm{A}$. This should be contrasted to the case where the beam is assumed to be Gaussian, which results in $\widetilde{\Omega}_\mathrm{A} \approx \Omega_\mathrm{A} + \Omega_\Psi$ (Switzer, 2008). In fact, S. Das showed[3] that for any symmetric beam and any planet shape, the small planet approximation gives the relation:

$$\widetilde{\Omega}_\mathrm{A} = \Omega_\mathrm{A}\left(1 - \frac{\nabla^2 b(\mathbf{0})}{4\Omega_\Psi}\mu_2^\Psi\right), \tag{5.33}$$

where μ_2^Ψ is the second raw moment of the planet shape Ψ.

5.2 Beam Measurements

5.2.1 Observations and Data Reduction

All eight planets are visible from our site, but only Saturn and Mars are ideal for beam measurements. Jupiter is too bright and saturates our detectors, Venus and Mercury is only visible near sunrise or sunset when the mirror panels are not properly settled and the rest are too dim to get high signal-to-noise measurements of the beam wings. (Uranus, however, is an excellent calibrator—see §5.3.2.) In 2008, when the data presented in this section were taken, only Saturn was available at night, from early November through December (c.f. Table 1.5).

In our analyses, we did not see any discernible difference in the beam properties due to elevation, so we do not use telescope elevation for rejecting or accepting beam maps in any of the results presented in this chapter.

Saturn maps were made with the Cottingham Method using $\tau_k = 1.0\,\mathrm{s}$, $n_p = 0.32$ and $n_h = 0.36$ (see §4.3.1). We analyzed both stripe-removed and unprocessed maps; the latter were deemed more reliable, except for the 277 GHz array, as we discuss below in 5.2.2. All beam maps are studied in altitude-cosine azimuth coordinates.

About one third of the maps were excluded from analysis because of small (usually below 20–30 dB) though obvious residual atmosphere contamination in the beam wings. Because there were still a large number of clean maps, we exerted no effort in trying to improve the maps of the rejected observations.

The beam maps were centered on Saturn using pointing data obtained as outlined in §3.3. This allowed multiple maps to be coadded to reduce noise in the wings. The maps were combined with a weighted average, with the weights reckoned as the inverses of the individual map variances, determined beyond a mask radius. The mask radii were the same used for background removal—see Table 5.1 for the sizes of the mask radii used. Analyses were done on both individual and coadded maps, with the results from each being consistent, as discussed below in 5.2.2. Table 5.1 includes a summary of the map properties.

[3]Private communication.

Table 5.1: A summary of beam properties. The definitions of the parameters listed here, as well as details on how they were measured, are given throughout the text of §5.2.1–5.2.2.

	148 GHz	**218 GHz**	**277 GHz**
Map Properties (§5.2.1)			
# TOD's	16	15	11
Stripe Removal?	no	no	yes
Map Radius (arcmin)	21	15	15
Mask Radius (arcmin)[a]	18	9,11,13	6,8,10,12
θ_W *Wing Fits (§5.2.2.1)*			
Fit Start, θ_1 (arcmin)	7	5	4.5
Fit End, θ_2 (arcmin)[b]	13	7–11	6–10
Best-fit θ_W (arcmin)	0.526 ± 0.002	0.397 ± 0.01	0.46 ± 0.04
Beam Centers (§5.2.2.2)			
Major FWHM (arcmin)	1.406 ± 0.003	1.006 ± 0.01	0.94 ± 0.02
Minor FWHM (arcmin)	1.344 ± 0.002	1.001 ± 0.003	0.88 ± 0.02
Axis Angle (deg)	62 ± 2	137 ± 9	98 ± 13
Solid Angles (§5.2.2.3)			
Solid Angle (nsr)	218.2 ± 2	118.2 ± 1.5	104.2 ± 3
% interpolated	2.8	4.3	7.2

[a] The 218 GHz and 277 GHz beam properties are averaged from the results at these mask radii—see text.

[b] The fit ranges for the 218 GHz and 277 GHz band are varied along with the mask radii so that θ_2 is never larger than the mask—see text.

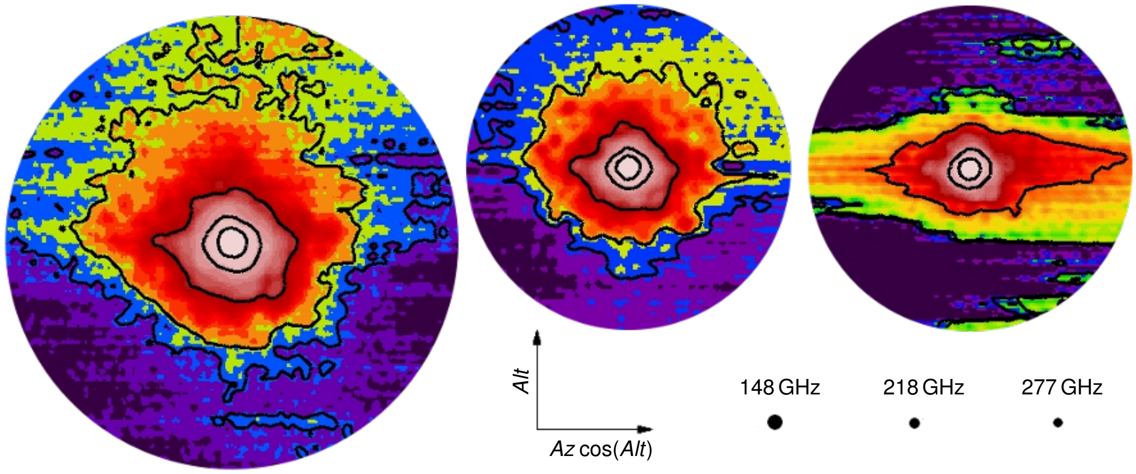

Figure 5.2: Beam maps from coadded observations of Saturn for the three arrays: from left to right, 148 GHz, 218 GHz and 277 GHz. The black contour lines are in decrements of -10 dB. A 0.54’ Gaussian smoothing kernel was applied to highlight large-scale structure; this smoothing is not done for any of the analysis described in the text. No stripe-removal has been done on these maps. The circles on the bottom right show the measured FWHM’s of each map for scale (see Table 5.1).

5.2.2 Results

5.2.2.1 Beam Maps and Profiles

Fig. 5.2 shows coadded beam maps for the three arrays using a color scale which highlights the features in the sidelobes. A striking feature is the similarity of the wing structure in the 148 GHz and 218 GHz arrays, most notably along the altitude (or vertical) direction where both exhibit more power near the top of the map. This is a consequence of the off-axis design of the telescope. Both of these arrays are situated about the same vertical distance below the center of the focal plane (Fowler et al., 2007), so we expect their beams to be similar along the altitude axis. The 277 GHz array clearly has an inferior beam map, probably because of a combination of factors: the use of the coupling layer in 2008, the much higher amount of atmospheric contamination at its frequency and the higher noise levels of its detectors. There is also preliminary evidence that large optical loads induces noise correlations between detectors, which is still being investigated. Nevertheless, we point out that the 277 GHz map shown in Fig. 5.2 is designed to highlight low-level features, and that above -20 dB, the beam is still relatively symmetric and compact.

Symmetrized beam profiles and accumulated solid angles for the three arrays are shown in Fig. 5.3. These were measured by taking azimuthally averaged annular rings of map pixels in one-pixel increments, centered on the beam center. The center was determined by fitting a symmetric Airy pattern (see §5.2.2.2). The smooth fall-off of the beam far from the center is an excellent match to the predicted Airy pattern behavior in the wings (c.f. Eq. 5.21) in 148 GHz, and a not unreasonable approximation in 218 GHz and 277 GHz (see below). We fit the profile for θ_W, which we use to calculate how much power was removed when the background level was subtracted. Recall that the background is set to zero by calculating the mean map value outside of the mask radius and subtracting it. The mean value, however, also contains true power from the wings of the map. Using Eq. 5.22 we can estimate how much power needs to be added back to the map to compensate. This causes the beam profile to become smoother in the wings. We refit for θ_W in the corrected map, iterating this process until the θ_W fit converges—three iterations are sufficient. The beam maps in Fig. 5.2 and profiles in Fig. 5.3 have undergone this process.

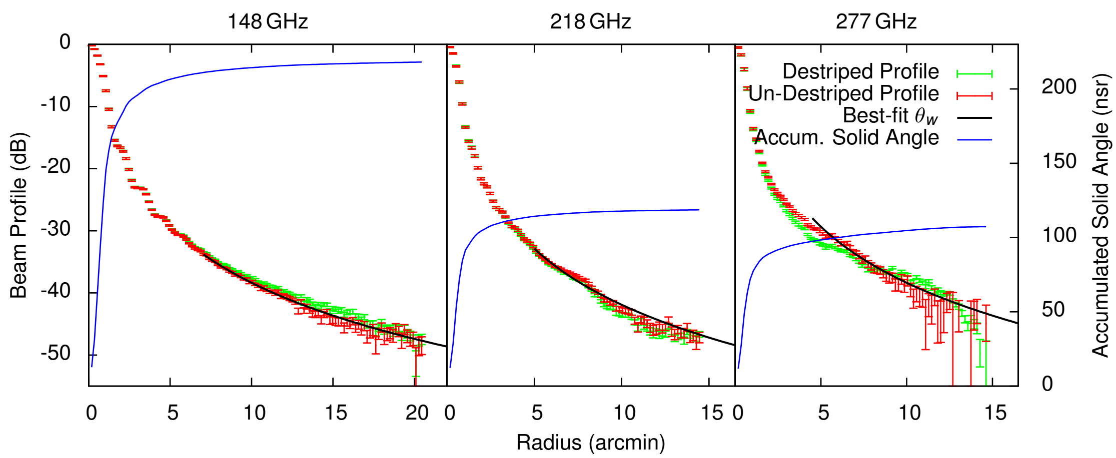

Figure 5.3: Symmetrized beam profiles for the three arrays, measured from coadded Saturn maps. Profiles are shown for both unprocessed maps (red) and stripe-removed maps (green). The black curves are the best-fit wing profiles (see text). The accumulated solid angles are from the unprocessed maps for the 148 GHz and 218 GHz arrays and from the stripe-removed map for 277 GHz (without any solid angle extrapolation via Eq. 5.22. The errorbars on the profiles are the standard errors from the azimuthal average. Saturn is bright enough that the rms power from the CMB falls below all points in these plots.

Uncertainties on θ_W are estimated using the bootstrap method. This procedure generates an ensemble of resampled datasets by randomly drawing points from the original dataset. Each point is drawn independently, meaning that points can be duplicated in a synthesized dataset. The uncertainties are then determined from the distribution of values θ_W from fits to the bootstrap ensemble. This is a robust technique for error estimation in the absence of other reliable methods (Press et al., 1992).

The stripe-removed and unprocessed beam profiles in Fig. 5.3 are different (though more noticeably for the 148 GHz and 277 GHz than the 218 GHz array), and yield θ_W fits which significantly differ from each other. This affects the measurement of the total solid angle (see §5.2.2.3). In order to evaluate which profile—stripe removed or unprocessed—is a better measurement of the true beam shape, we began by dividing the unprocessed 148 GHz coadded map into quadrants, ordered anti-clockwise starting the top-right quadrant. In each quadrant we calculated the beam profile and fitted for θ_W. Fig. 5.4a shows the profiles for the quadrants along with the fully symmetrized profile. As expected, the profile which has been azimuthally averaged over all angles (the blue curve in the figure) falls around the midpoint of the scatter of the quadrant profiles. Also, the first and second quadrants have more power than the third and fourth, as would be predicted from the beam map in Fig. 5.2, which have more power in the top of the map than the bottom.

Even though the unprocessed maps do not artificially remove the power in the vertical direction, we still need to show more quantitatively that they give better overall beam measurements. To do this, we studied the θ_W fits as a function of both mask size used for background removal as well as the domain over which the θ_W fit was performed. We denote the θ_W domain θ_1–θ_2. θ_1 is held fixed at about $5\,\theta_{1/2}$ (c.f. §5.1.3.1) and θ_2 is not allowed to be larger than the mask size. Table 5.2 shows the mask and θ_2 values used for the 148 GHz map with the reduced-χ^2 results from the fit at each point. Fig. 5.4b plots the values of θ_W against their reduced-χ^2 for the different mask and θ_2 sizes. It illustrates why the unprocessed beam profiles are more reliable than the stripe-removed. Focusing on the symmetrized, unprocessed points (blue), we observe that apart from three points, they all have similar χ^2 and consistent θ_W. The three outliers correspond to $\theta_2 \geq 15'$. Thus the wings of the unprocessed maps are unaffected by the choice of mask size or the fit domain (so

Table 5.2: Different parameters used for the θ_W fit in 148 GHz. The domain of the fit was from θ_1–θ_2, with θ_1 fixed at 7′ and θ_2 varying as shown in the table but never greater than the mask size. The entries in the table show the fitted θ_W and reduced-χ^2 for each combination on the stripe-removed map: these data are plotted in Fig. 5.4b. We chose to show the stripe-removed values here, as opposed to the unprocessed values, because they show the most scatter and can be used to interpret the trend of the red points in Fig. 5.4b.

		Mask Size (arcmin)				
		9	**11**	**13**	**15**	**18**
θ_2 (arcmin)	**9**	0.519′ / 1.5	0.531′ / 0.72	0.539′ / 0.73	0.541′ / 0.78	0.543′ / 0.83
	11	—	0.531′ / 0.76	0.544′ / 1.7	0.548′ / 2.6	0.551′ / 2.8
	13	—	—	0.541′ / 1.4	0.550′ / 3.0	0.556′ / 4.2
	15	—	—	—	0.545′ / 1.7	0.558′ / 4.5
	18	—	—	—	—	0.548′ / 1.9

long as $\theta_2 < 15'$). On the other hand, the varying either the mask size or θ_2 significantly alters the wings of the stripe-removed map: clearly, the stripe-removal process introduces contamination which makes the θ_W fit more sensitive to the choice of θ_2. Note that even when the stripe-removed reduced-χ^2 are near unity, the corresponding θ_W's are inconsistent with each other. Again, this behavior makes sense when referring to the beam map in Fig. 5.2. There are non-symmetric features in the beam wings and varying the mask size changes their influence on the straight-line fits used for the stripe-removal. Most obviously, the stripe-removal will remove the overall gradient in the vertical direction, spuriously adding power to the bottom half of the map. As expected, their beam profiles are systematically higher (c.f. Fig. 5.3).

Fits to the unprocessed maps are also better for the 218 GHz array. Thus, for 148 GHz and 218 GHz, we use unprocessed maps for our measurements of the FWHM (§5.2.2.2), solid angles (§5.2.2.3), and window functions (§5.2.2.4). It should be noted, however, that the stripe-removed maps give solid angles within 1σ of those from the unprocessed maps. On the other hand, the large residual striping at 277 GHz necessitates the use of its stripe-removed map.

As we have seen, Eq. 5.21 is a good approximation of the wings in the unprocessed, 148 GHz map for any choice of θ_2 below 15′. Thus, we use $\theta_2 = 13'$, for which we obtain $\chi^2 = 40$ for 35 degrees of freedom. The fits to the 218 GHz (unprocessed) and 277 GHz (stripe removed) profiles are not as robust. 218 GHz has reduced-χ^2 of 2.8 for $\theta_2 = 7'$ and 277 GHz has reduced-χ^2 of 25 for $\theta_2 = 6'$, with larger θ_2 giving poorer fits in both cases. Consequently, for these profiles we calculate θ_W at different mask sizes, as indicated in Table 5.1. At each mask size we varied θ_2 in 2′ increments, always keeping it lower than the mask size. The average value from the whole ensemble gives us θ_W and we take its standard error as the uncertainty. Although Eq. 5.21 may be too simple a model for these profiles, contributions to the solid angle at these radii are only a few percent of the total solid angle, which has an uncertainty dominated by the contribution of the beam below θ_2—see 5.2.2.3. The values of θ_W for all three beams are shown in Table 5.1.

5.2.2.2 Beam Central Regions

The central regions of the beams are slightly asymmetric. This is easily seen in Fig. 5.4a. Errorbars have been excluded to make the plot readable, but the difference between wiggles below $\sim 5'$ are much larger than the uncertainties. In beam maps an ellipticity is apparent to the eye. (The color scale in Fig 5.2 is not, however, well suited for this purpose.) To get a quantitative handle, we model the beam centers with elliptical Airy patterns:

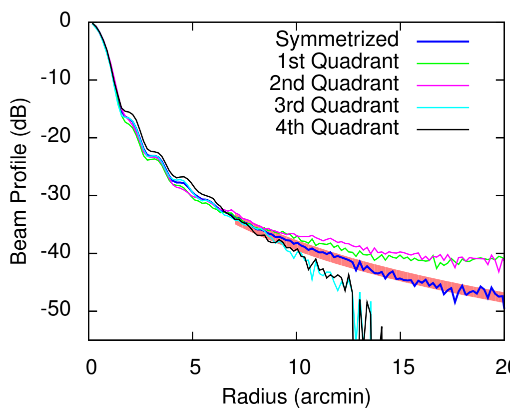

(a)

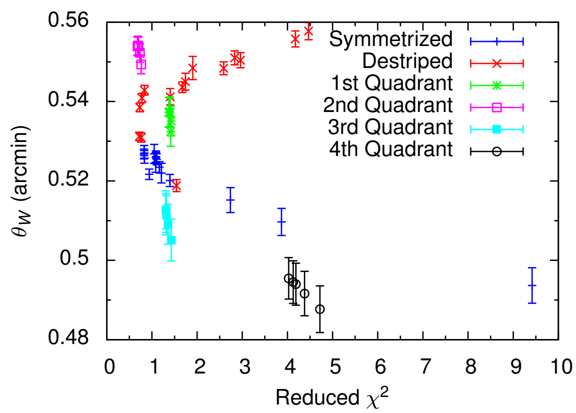

(b)

Figure 5.4: Beam profiles and wing fits for the quadrants of the unprocessed, coadded 148 GHz map. In (a) the profiles for each of the quadrants as well as the full symmetrized profile are plotted. The the shaded band shows the 1-sigma contour of the θ_W fit to the symmetrized profile. In (b), θ_W values are plotted against the reduced-χ^2 of their fits for the quadrant profiles as well as the full symmetrized profiles of both the processed and unprocessed maps. The multiple points in the same color are from different combinations of mask size and fit domains, as listed in Table 5.2; the four quadrants use all mask sizes but keep θ_2 fixed at 9′ in this plot. Note that the symmetrized (blue) points are closely clustered together, except for three outliers, which correspond to values of θ_2 of 15′ and 18′. Thus, the fit for θ_W is relatively insensitive to the mask size or $\theta_2 <$ 15′ in the unprocessed map, but not in the stripe-removed map. The profiles in (a) used a mask size of 18′ and θ_2 = 13′.

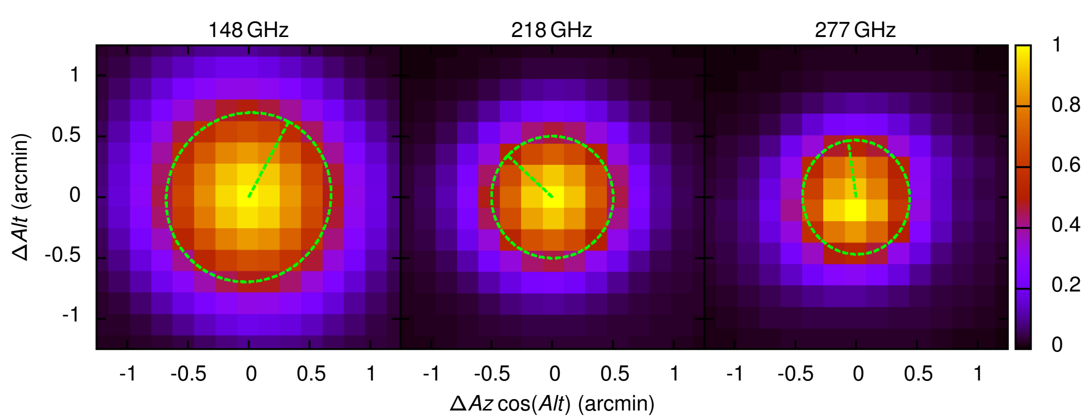

Figure 5.5: The beam centers for the coadded Saturn maps for the three arrays. Overlaid are the FWHM ellipses as determined by the fit described in the text; the FWHM parameters are listed in Table 5.1. The angles β of the major axes are indicated by the radial line in each ellipse.

$$b^{\mathrm{A}}_{\beta}(\theta) = \left[\frac{2J_1(q)}{q}\right]; \quad q \equiv A\sqrt{\left[\frac{\theta_{\parallel}(\beta)}{a}\right]^2 + \left[\frac{\theta_{\perp}(\beta)}{b}\right]^2} \tag{5.34}$$

where A is the peak height and $\theta_{\parallel}$ and $\theta_{\perp}$ are distances along axes parallel and perpendicular, respectively, to the angle of the ellipse's major axis, specified by the angle β, which we define to be the anti-clockwise angle from the positive axis of constant altitude, i.e.,

$$\begin{pmatrix} \theta_{\parallel} \\ \theta_{\perp} \end{pmatrix} = \begin{pmatrix} \cos\beta & -\sin\beta \\ \sin\beta & \cos\beta \end{pmatrix} \begin{pmatrix} \Delta Az\cos(Alt) \\ \Delta Alt \end{pmatrix}. \tag{5.35}$$

The semi-major axes a and b are easily converted into FWHM's (c.f. Eqs. 5.14 and 5.15).

We fit b^{A}_{β} to the top $\sim$3 dB of the beam using the non-linear Levenberg-Marquardt algorithm (Press et al., 1992, p. 683ff). The fitter is good at finding A, a, b as well as the peak center in ΔAlt and $\Delta Az\cos(Alt)$, but has difficulty converging on the axis angle β. Thus, we keep β fixed in the fit and step through the possible 180° in 2° increments and use the value of β which gives the lowest χ^2.

Uncertainties in the fit are, once again, calculated using the bootstrap method. An added component is that the angles probed for the β search are offset by a random amount $<2°$ for each bootstrap iteration. That is, instead of only searching the angles $\beta \in \{2°,\ 4°,\ \ldots,\ 180°\}$, the bootstrap iterations search $\beta \in \{2° - \beta_0,\ 4° - \beta_0,\ \ldots,\ 180° - \beta_0\}$, with β_0 randomly generated each iteration.

The accuracy of the elliptical Airy fitter was tested with synthesized Airy beams and was found to recover the input parameters very well.

The results of the FWHM fits are listed in Table 5.1. Plots of the beam centers for the three arrays with best-fit FWHM ellipses overlaid, are displayed in Fig. 5.5. Note that the major axis angles β in the 148 GHz and 218 GHz arrays are mirrored about the x-axis: this reflects the physical layout of the two arrays in the focal plane. As for the 277 GHz array, which is centered above the first two arrays, its fitted β is consistent with vertical.

5.2.2.3 Solid Angles

The solid angles are calculated in two pieces. At radii below θ_2 (i.e., the maximum radius used for fitting θ_W—see §5.2.2.1), we simply integrate the normalized beam map. Above θ_2 we use our fitted values of θ_W in Eq. 5.22. Summing them gives the total measured solid angle. From this, we need to subtract the solid angle added by Saturn, as prescribed by Eq. 5.32. Thus, the solid angle is:

$$\Omega_{\mathrm{A}} = \Omega(\theta \le \theta_2) + \Omega_M(\theta > \theta_2) - \frac{\Omega_S}{2}, \tag{5.36}$$

where Ω_S is the solid angle of Saturn. During the period of our observations, Saturn subtended angles from 5.2 to 6.0 nsr. We use the mean value of Ω_S = 5.6 nsr and include an uncertainty of 1 nsr to account for its changing size as well as systematics which might have been introduced by making the disk approximation. (The rings of Saturn add a layer of complication to the determination of its solid angle, particularly since they have a different temperature than the disk. The ring inclination was low during our observations ($<6°$) and we have estimated that their contribution is negligible within the error budget.[4])

Estimating the error on the measured portion of the beam is not straightforward because systematics dominate. We estimate it by using the bootstrap method to generate an ensemble of coadded maps containing different combinations of the individual TOD maps, and looking at the spread of values. The distribution of solid angles measured from the bootstraps are shown in

[4] E. Switzer, private communication

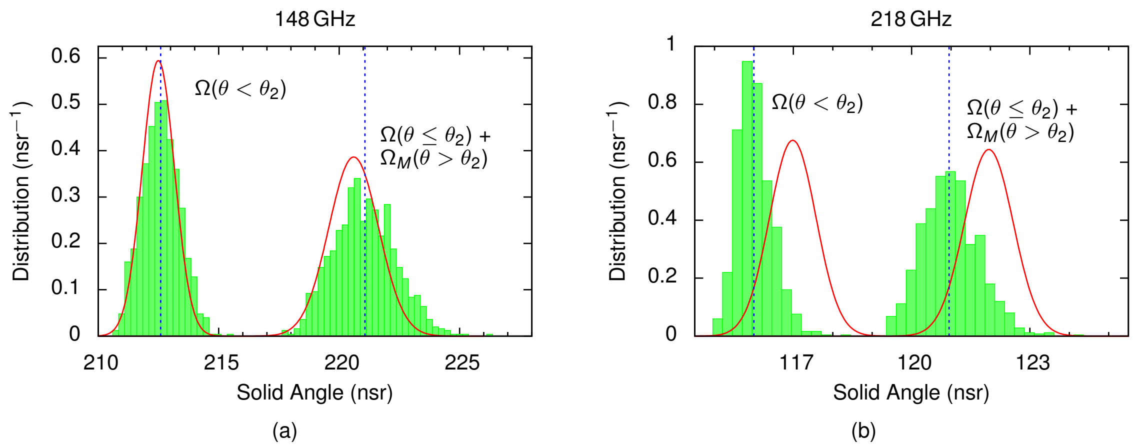

Figure 5.6: Plots showing how solid angle uncertainties are estimated. In each plot, a histogram of results from the coaddition bootstrap (see text) is displayed in green. The red curves are Gaussian distributions using the mean and standard error of the solid angles on the individual beam maps which comprise the coadded maps—note that the actual distributions are not actually true Gaussians: they have been represented here this way only to compare to the bootstrap distribution. The dashed blue lines are the measured solid angles from the coadded maps. In each plot, two distributions are shown: for the solid angle calculated directly from the map ($\Omega(\theta \leq \theta_2)$) and the solid angle including the interpolation using the θ_W fit ($\Omega(\theta > \theta_2)$). The offset between the red curve and the green distribution in the (b) is due to two TOD's with high solid angles with more noisy backgrounds which receive relatively little weight in the coaddition.

Fig. 5.6. To this we compare the average value of the solid angles measured from each individual TOD map. For the 148 GHz array, we remark that both the mean value and the standard error show good agreement with the bootstrap: thus, we may be confident that the coaddition step does not introduce any systematic which could come, for example, from changes in telescope focus from night to night or pointing misalignments. For the 218 GHz array, there is a clear discrepancy between the average solid angle mean and the bootstrap: the latter agrees, as it should, with the the coadded solid angle, while the former is about 1 nsr higher. On closer inspection, this turns out to be due to two TOD's with higher background noise. They happen to have higher solid angles, but receive very low weights in the coaddition, and hence contribute little to the final solid angle measurement. We note, however, that the standard deviation of the individual measurements is comparable to the width of the bootstrap distribution.

We also note that the width of the bootstrap distributions increases perceptibly when the interpolated solid angle is also included (the right-most distribution in each plot). This increase is larger than that would be predicted from the error on θ_W, so clearly this fit is also affected by systematics. The solid angles and uncertainties are reported in Table 5.1.

5.2.2.4 Window Functions

The window functions can be calculated directly from the beam profile data using Eq. 5.12. However, in angular power space, there is non-negligible covariance between points in the window function, which is not the case in real space. The best way to track these covariances is to fit some basis functions to the beam:

$$b^S(\theta) = \sum_n a_n \, b_n(\theta), \tag{5.37}$$

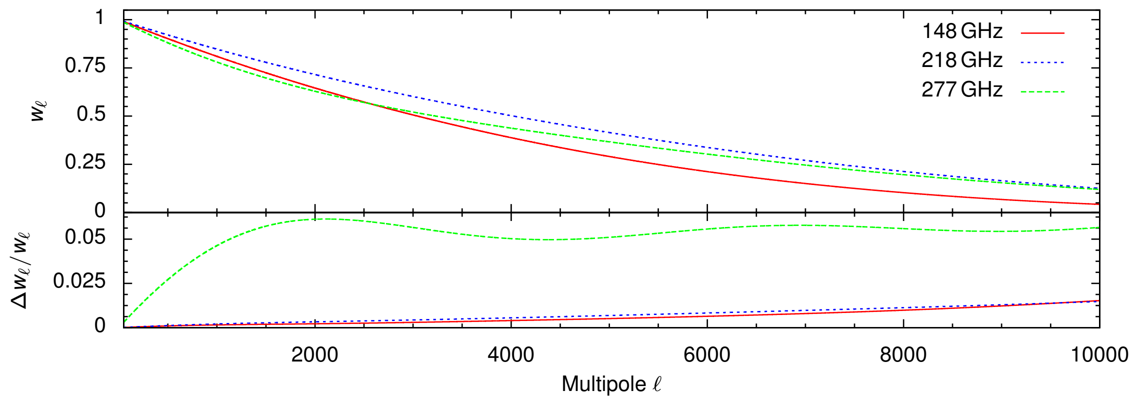

Figure 5.7: The window functions for the three arrays *(top)* and the diagonal terms from the covariance matrix *(bottom)*, as calculated by K. Moodley from fits to the beam profile with Fourier-transformed Zernike polynomials. The window functions have been normalized to unity at $\ell = 0$. In practice, the normalization will take place over the range of multipoles corresponding to the best calibration. Only statistical errors are shown.

where b_n is some basis and a_n are amplitudes. The fit will produce a matrix $C^{aa'}_{mn}$ of covariances between the amplitudes a_m and a_n, which can be transformed to the covariances between multipoles in ℓ-space:

$$\Sigma^b_{\ell\ell'} = \sum_{m,n=0}^{n_{\max}} \frac{\partial b_\ell}{\partial a_m} C^{aa'}_{mn} \frac{\partial b_\ell}{\partial a_n}. \tag{5.38}$$

Thus, the covariance matrix for the window function is:

$$\Sigma^w_{\ell\ell'} = 4 w_\ell w_{\ell'} \Sigma^b_{\ell\ell'}. \tag{5.39}$$

K. Moodley used Fourier transforms of the Zernike polynomials for a basis b_n. The Zernike polynomials form an orthonormal basis on the unit disk, and are therefore a natural choice for modelling our beam, which is truncated by a Lyot stop in the optical path. Below θ_1—the point at which we start fitting for θ_W (c.f. §5.2.2.1)—he was able to fit the beam with reduced-$\chi^2 \approx 1$ using 13 bases. Hincks et al. (2009) has more details. Fig. 5.7 shows the window functions obtained from K. Moodley's analysis.

5.2.3 Beam Measurements and Reflector Panel Alignment

Beam maps are one of our primary means of determining the quality of the telescope optics. During the night, the 71 panels comprising the primary reflector and the 11 panels comprising the secondary maintain alignment to better than 30 µm and 10 µm, respectively. However, during the rapid temperature changes near sunrise and sunset, the alignment deforms considerably. These effects were measured directly using a laser tracker (Hincks et al., 2008), but beam maps also provide some insight.

Fig. 5.8 shows a beam map and beam profile of Saturn taken about ninety minutes after sunrise. The optical performance has clearly degraded and therefore we do not observe during daylight hours—this gives a natural time for recycling our receiver cryogenics. We note that good alignment is restored each night.

To date, we have not had the opportunity to make planetary observations during sunrise or sunset, when the exact delay between the time of sunrise/sunset and the onset of misalignment

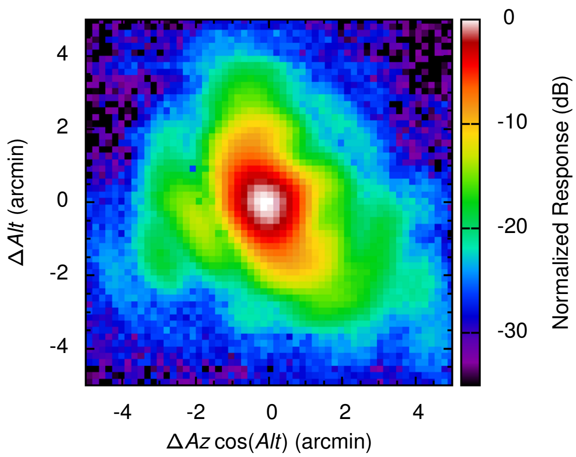

(a)

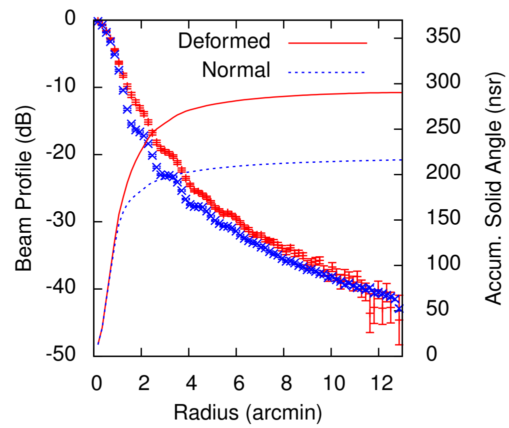

(b)

Figure 5.8: The beam shape after sunrise, from a 148 GHz observation of Saturn on 11 Oct. 2008 at 8:26 CLT, about ninety minutes after sunrise: (a) a normalized beam map and (b) the beam profile and accumulated solid angle compared to the normal, night-time measurements (Fig. 5.3).

might be measured. So far it has merely provided a more visual verification that our beams are sub-optimal during daylight hours.[5]

5.2.4 Physical Beam Sizes

The detector sizes for the MBAC were designed to oversample the beam, with the target being an inter-detector spacing of half a beam width (Fowler et al., 2007). Fig. 5.9 plots the beams in units of length as they appear on the focal plane. The FWHM of the 148 GHz beam is very nearly the diagonal size of a detector, with the other FWHM for the other two detectors being about two-thirds this size.

5.3 Temperature Calibration

5.3.1 Planet Brightnesses and Atmospheric Opacity

Eq. 5.7 shows that if we measure the peak power of a source of known diluted temperature $\mathcal{D}_\Psi T_0$ through known opacity τ, we can measure the power to temperature conversion factor $\alpha_\mathcal{S}$. We have measured the solid angle of the telescope (§5.2.2.3) so we can estimate the dilution factor using Eq. 5.31.

Again, planets are excellent calibrators. They are bright enough that the main source of error is the systematic uncertainty of their temperatures at our observing frequencies. Planetary emission models are complex and must take into account variables such as the phase, heliocentric distance, oblateness and atmospheric properties. There are additional idiosyncrasies sprinkled throughout: dust storms on Mars sometimes radically alter its brightness; Saturn's rings subtend a significant solid angle; absorption lines exist in Neptune's and Saturn's atmospheres in a couple of our frequencies, and so on. Switzer (2008, §5.6.3-5.6.4, §C.2) has a more extensive review of all of these effects.

[5] Images like Fig. 5.8a are sometimes called "lobster plots" after E. Switzer pointed out that some bear striking resemblance to crustaceans of the family Nephropidae.

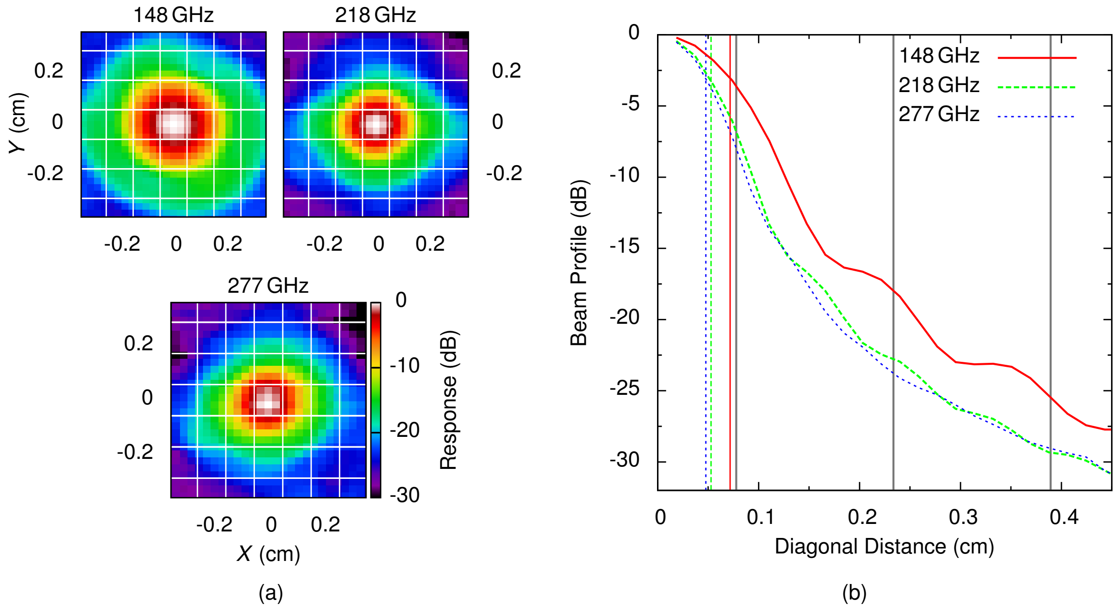

Figure 5.9: Plots of the physical size of the beam, using the plate scale values from Table 3.3. In (a), beam maps are plotted with squares the size of the detector elements overlaid. The X axis is horizontal (corresponding to azimuth) and the Y axis is vertical (corresponding to elevation). Note that in the actual array, there is a $\approx$0.1 mm gap between (horizontal) columns of arrays. The plot in (b) shows the three beam profiles as a function of "diagonal distance", defined as the distance along the axis joining opposite corners of a detector (roughly the line $X = Y$ in (a)) The vertical gray lines show the detector boundaries, assuming that the beam is centered exactly in the middle of a detector. Vertical lines in the same style as the profile curves show the position of their FWHM.

In our analysis we use Saturn and Uranus temperatures compiled by E. Switzer[6] which provide daily RJ temperatures over a range of years. The Saturn values were informed by a number of models and extrapolated from observations at other wavelengths—the details may be found in Switzer (2008, §5.6.4)—and the estimated uncertainty is about 5%, except in the 277 GHz band where a PH_3 J=1–0 resonance makes it unreliable. The Uranus models (Switzer, 2008, §C.2.4) are believed to be more precise, though no error estimate is quoted.

The atmospheric optical depth is estimated using the equation:

$$\tau = \left(\tau_d + \tau_w \times \frac{PWV}{1\,\mathrm{mm}}\right) \sec z, \tag{5.40}$$

where there is a contribution from the dry component of the atmosphere, τ_d, and the water vapor, $\tau_w \times PWV/1\,\mathrm{mm}$, depending on the precipitable water vapor (PWV), i.e., the amount of water in the atmosphere in a column pointed at the zenith, measured in millimeters. The total optical depth is multiplied by the secant of z, the zenith angle, which corrects for the extra length of atmosphere seen off-zenith. The values used for τ_d and τ_w, listed in Table 5.3 were taken from Switzer (2008, Table 5.1). As shall be shown, we can also crudely measure τ_w from our data.

5.3.2 Measurements

We extract a single number, the peak power $P(\mathbf{0})$, from each planet observation in each array, by fitting an Airy pattern to the center of the planet in the map as described in §5.2.2.2.[7] This gives us six ensembles of power measurements: two planets times three arrays. For each ensemble we fit the function (c.f. Eq. 5.7):

$$\alpha_S = \exp\left[-\left(\tau_d + \tau_w \times \frac{PWV^i}{1\,\mathrm{mm}}\right)\sec z\right] \mathcal{D}_\Psi \frac{T_0^i}{P^i}, \tag{5.41}$$

where P^i is the peak power from the i^{th} observation, T_0^i is the modelled planet temperature at the time it was observed, and $\mathcal{D}_\Psi$ is the dilution factor (Eq. 5.8). PWV values were taken from the publicly available measurements from the nearby Atacama Pathfinder Experiment (APEX).[8]

We treat the variables in three ways:

1. by ignoring the atmosphere by setting the exponent equal to unity so that the only inputs are T_0^i and P^i;
2. by introducing τ_d and τ_w as fixed parameters, which adds a third input, PWV; and
3. by treating τ_w as a free parameter in addition to α.

The first two treatments essentially average the RHS of Eq. 5.41 to obtain α_S. The third treatment is nonlinear and we use the Levenberg-Marquardt algorithm (Press et al., 1992, p. 683ff) to solve for α_S and τ_w simultaneously. Fig. 5.10 presents the data for all three cases.

Table 5.3 lists the values of τ_w and τ_d used for the second two treatments listed above, including the results of the fit to τ_w. They are remarkably similar to the model values from Switzer (2008, Table 5.1), with the exception of the 277 GHz fits. Table 5.4 shows the measured calibration values, for each of the three treatments. Including the opacity in the calculation does make the fit errors slightly lower, but not appreciably: the variation in atmospheric opacity is subdominant to the measurement error of the planets' peak brightnesses. Thus, in the analysis of Chapter 6 we are free to use the results from the first treatment, ignoring atmospheric opacity, since the mean value and scatter is already built in.

[6] Private communication

[7] For the peak power we use a symmetric rather than an elliptical Airy function. In practice this makes no significant difference to the height of the fit.

[8] Project URL: http://www.apex-telescope.org. Radiometer and other weather data can be downloaded from: http://www.apex-telescope.org/weather/Historical_weather/index.htm.

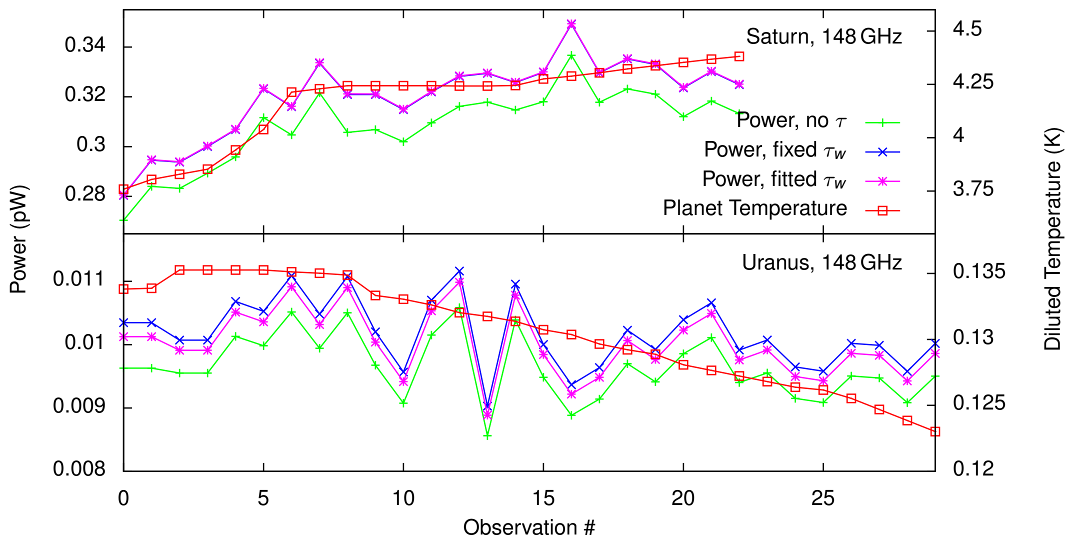

Figure 5.10: The Saturn (*top*) and Uranus (*bottom*) data used for 148 GHz calibration. Both measured power from the peaks in the maps (*left axis*) and planet temperatures from models (*right axis*) are shown. The planet temperature variation is chiefly due to the apparent magnitude changing as the planets move in their orbits. The measured power has been treated in three ways. First, no correction for atmospheric opacity is made (green crosses). Second, the estimated atmospheric attenuation is removed the from the measured power (blue exes), i.e., $P' = P\exp(\tau)$, where τ is defined in Eq. 5.40 and τ_d and τ_w are from a fixed model (see Table 5.3). Third, the same correction is made as in the second case, except that τ_w comes from a fit to Eq. 5.41 where it is a free parameter along with α (magenta stars). If scatter in the power measurements was due chiefly to variations in atmospheric opacity, the last two curves would have substantially less scatter than the first. This is not the case, so we are dominated by measurement error.

Table 5.3: Wet and dry components of the atmosphere opacity model of Eq. 5.40. All values are referenced to the zenith. The "model values" are from Switzer (2008, Table 5.1).

	148 GHz	**218 GHz**	**277 GHz**
Dry Component τ_d			
Model Values	0.00926	0.0077	0.020
Wet Component τ_w(mm^{-1})			
Model Values	0.019	0.045	0.075
From Saturn Fits	0.019 $\pm$ 0.009	0.056 $\pm$ 0.013	0.231 $\pm$ 0.036
From Uranus Fits	0.0311 $\pm$ 0.011	0.037 $\pm$ 0.014	-0.005 $\pm$ 0.056

Table 5.4: Saturn and Uranus calibration results. The uncertainties of the average values are simply the errors on the Saturn and Uranus values added in quadrature and therefore do not account for systematic differences between the two.

	Calibration α_{RJ} (K/pW)		
	148 GHz	**218 GHz**	**277 GHz**
Ignoring τ			
Saturn	13.54 ± 0.07	9.79 ± 0.09	7.2 ± 0.5
Uranus	13.57 ± 0.12	8.95 ± 0.06	4.9 ± 0.3
Average	13.56 ± 0.07	9.37 ± 0.05	6.1 ± 0.2
Fixed τ_w [a]			
Saturn	13.03 ± 0.06	9.13 ± 0.08	6.3 ± 0.4
Uranus	13.06 ± 0.11	8.35 ± 0.06	4.4 ± 0.3
Average	13.11 ± 0.09	8.74 ± 0.05	5.4 ± 0.1
Fitted τ_w [b]			
Saturn	13.04 ± 0.06	9.00 ± 0.08	5.0 ± 0.4
Uranus	12.85 ± 0.11	8.35 ± 0.06	4.8 ± 0.3
Average	13.12 ± 0.09	8.68 ± 0.05	4.9 ± 0.1

[a] Using the model values of τ_d and τ_w listed in Table 5.3.

[b] Using the model value of τ_d listed in Table 5.3 and allowing τ_w to be a free parameter in the fit to Eq. 5.41.

Chapter 6

Galaxy Clusters & Point Sources

In this chapter we present measurements and analysis of the first galaxy clusters to be studied by the ACT. This work represents the first step in what promises to be an important contribution to the science of galaxy clusters and potentially to the understanding of the growth of structure in the universe.

The scientific motivation for the study of clusters with the SZ effect was discussed in §1.1.5. Here, we focus on a subset of the clusters and cluster candidates discovered in our current maps which is not large enough for the results that might come from a larger, well-studied survey (§1.1.5.4, §1.1.5.5. However, the initial results we present lay groundwork for understanding the physics of the clusters and for comparison to observations in X-ray and optical frequencies. As we saw, this line of inquiry alone can be used for measuring the Hubble constant (§1.1.5.1) and gas-mass fractions (§1.1.5.2). It also anticipates the necessity of a detailed understanding of our data for the correct interpretation of our future cluster catalogs.

In addition to studying galaxy clusters, we have also done a preliminary analysis of three point sources, two of which are known radio sources, and one of which is possibly a previously unknown infrared (IR) galaxy.

This chapter is laid out as follows: in §6.1 we describe how clusters are discovered and how our maps of both point sources and clusters are made; §6.2 is dedicated to the analyzing and discussing our cluster maps; §6.3 includes a preliminary analysis of three ACT point sources; and we conclude in §6.4.

6.1 Data Processing

6.1.1 Cluster Discovery in Survey Maps

The data analysis pipeline described in this dissertation (see Chapters 3 and 4), which we call the Cottingham Pipeline, is completely independent from the main mapmaking software of the ACT analysis team, which we call the Survey Pipeline. While having two pipelines offers important cross checks on many of the steps in our data analysis, they are also complementary. The Survey Pipeline is designed to make large, survey maps of the full area observed by the telescope, whereas the Cottingham Pipeline is geared towards small maps of individual objects. Thus, the latter has been particularly useful for creating beam maps (Chapter 5), SZ clusters, and point sources. On the other hand, knowledge of an object's coordinates is necessary before it can be mapped with the Cottingham Pipeline. The full survey maps have been indispensable in this regard.

The Survey Pipeline is the result of the efforts of a large team: R. Dünner, R. Fisher, J. Fowler, M. Hasselfield, M. Hilton, R. Lupton, T. Marriage, M. Niemack, M. Nolta, B. Reid, J. Sievers, and D.

Swetz have all been substantially involved. At the time of writing, the survey maps are still evolving and have not been published.

The galaxy clusters presented in this chapter are a subset of those detected by R. Warne in the southern region survey maps. Here we briefly outline the algorithm he used for their discovery. Only the 148 GHz maps, the cleanest at the time of writing, were used. The first step was to apply a Wiener filter to the maps. The polytropic SZ model of Komatsu & Seljak (2001) was used as the filter's signal estimate. The template assumed a cluster mass of $4 \times 10^{14} M_\odot$ at redshift $z = 0.1$, although studies with simulated maps indicated that the detection statistics did not depend strongly on this choice. For the noise estimate, models of the detector noise, point source contribution and primary temperature anisotropies were included. Cluster detection in the filtered maps used the SExtractor software package (Bertin & Arnouts, 1996). All the clusters presented in this chapter were detected with at least 3σ significance in the filtered maps.

Many of the clusters discovered in the survey were previously known. They were identified in the NASA/IPAC Extragalactic Database (NED)[1] by searching in a $3'$ radius about the ACT-detected object. In this chapter, we concentrate on previously discovered clusters because it is useful to be able to compare our measurements to X-ray and optical frequencies, for the reasons summarized above. In our initial studies, this is obviously easier if these observations have already been made.

Despite the focus on known clusters, we also present two clusters candidates newly discovered by the ACT. Our collaboration is currently applying or planning to apply for observing time for follow-up measurements for new clusters. To date, we have successfully obtained a total of ten nights in 2009 at the Cerro Tololo Inter-American Observatory (CTIO), the ESO New Technology Telescope (NTT), and the Southern Astrophysical Research (SOAR) Telescope.

6.1.2 Mapmaking & Calibration

Maps were made with the Cottingham Pipeline using data from the 2008 season. Unless explicitly stated otherwise, we used $\tau_k = 0.5$ s, $n_p \approx 0.42$, and $n_h \approx 0.40$ (see §4.3.1). Maps are $24'$ in diameter. Stripe removal (§4.4.2) is performed on all the maps using a mask $6'$ in radius.

The maps use the calibration from Uranus, which we estimate to have a 6% uncertainty in temperature at 148 GHz. We do not correct for variations in the atmospheric opacity because we found that gain changes due to variations in opacity are subdominant to our measurement errors (see §5.3.2). Thus, we use the values under the heading "Ignoring τ" in Table 5.4. When maps are plotted in units of temperature change relative to the CMB spectrum (denominated T_{CMB}), the the RJ to CMB conversions listed in Table 1.3 are used.

All cluster maps have companion "difference" maps. Each group of rising and setting TODs is split into two, and the first half of the season's data is subtracted from the second half. The relative weights of each TOD map are the same as those used for the cluster maps, but the weights of each half are multiplied by a common gain so that the overall weights of the two halves are equal. Thus, the difference maps should ideally have no signal. Finally, the difference maps from the rising and setting TODs are coadded with the same weights as the cluster maps.

6.1.3 Point Source Maps for Absolute Pointing

Relative pointing between detectors was discussed in §3.3, but the boresight pointing still needs to be calibrated for each array. For this, we used two radio point sources in our southern survey region, PMN J0540−5418 and PMN J0549−5246 (see §6.3 for more about these sources). All data in the southern region from which our clusters are drawn were observed at two telescope pointings, both at an altitude of 50.5°. In azimuth the scan centers in both the east and the west cycled through a 10° range every five nights. This was in order to get good overlap between the

[1] NED is operated by the Jet Propulsion Laboratory, California Institute of Technology, under contract with the National Aeronautics and Space Administration. Internet URL: http://nedwww.ipac.caltech.edu/

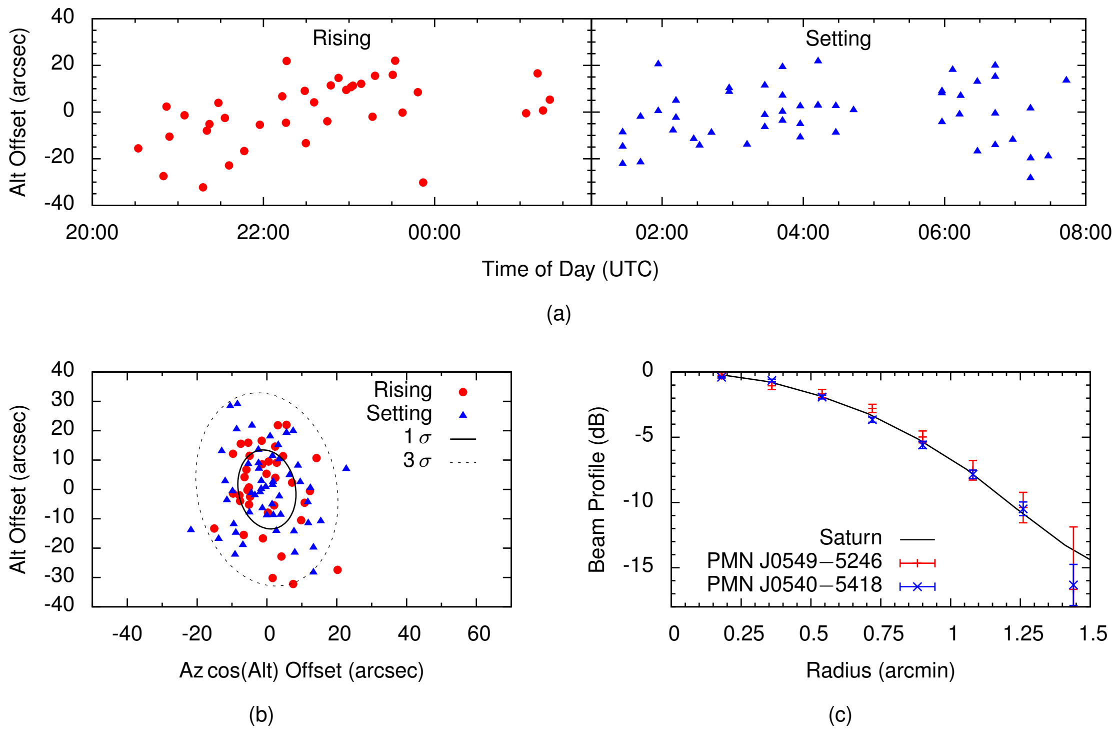

Figure 6.1: Nightly variations in the boresight pointing. In (a) and (b), the variation in the position of the radio source PMN J0549−5246 at 148 GHz over about fifty nights is shown. The scatter is larger in the altitude direction, and (a) shows that it is slightly correlated with the time of night, perhaps as the optics move due to thermal changes. The standard deviation of the pointing variations is 8″ in the azimuth direction and 14″ in the altitude direction. Nevertheless, (c) demonstrates that (in 148 GHz at least) the beam profiles of cross-linked maps of PMN J0540−5418 and PMN J0549−5246 are consistent with the Saturn beam profile (§5.2). The noise floor in the maps of these radios sources is at about −15 dB.

three arrays over the season. In our pointing analysis, we treat all of the observations within each of these 10° ranges as one telescope pointing. The error introduced by this approximation is not significant. In the east (rising observations) the azimuth center was about 147° and in the west (setting observations) it was about 213°.

Maps of the point sources at each of the two telescope pointings were made for all three arrays. Mapmaking was done as described in §6.1.2, with the exception that in the 277 GHz maps, stripe-removal was done with a quadratic rather than a linear fit. This was done because of the higher noise in this array.

Boresight pointing was determined by comparing the map positions to the catalog positions. Centroiding the positions in the maps was done by eye in the `ds9` software package (Joye & Mandel, 2003), which gives similar precision to fitting a Airy pattern. (This is conclusion was reached by comparing centroiding done by eye and with functional fits for the Saturn beam maps of §5.2.2.) We estimate a pointing uncertainty of 5″ for 148 GHz, 11″ for 218 GHz, and 40″ for 277 GHz. This is based both on the precision of the centroiding and by comparing maps of each source made with the same pointing. The much larger pointing uncertainty in the 277 GHz array is chiefly due to high noise in its maps. It is likely that better precision could have been achieved with the use of more point sources to give robust statistics. However, we note that with the exception of the 277 GHz array, the pointing uncertainties are much smaller than the beam sizes.

The quoted pointing precision is from coadded maps from many nights. There is also jitter in the pointing from night to night that gets averaged down in coaddition. Fig. 6.1 shows plots of the

Table 6.1: Coordinates, catalog names, and basic properties of ACT SZ clusters.

ACT Descriptor	Catalog Name	J2000 Coordinates[a] RA	J2000 Coordinates[a] Dec.	rms[b] [μK]	t_{int}[c] [min]
Previously Detected					
ACT-CL J0245−5301	Abell S0295	$02^h45^m28^s$	−53°01′36″	44	10.1
ACT-CL J0330−5228	Abell 3128 (NE)	$03^h30^m50^s$	−52°28′38″	49	10.3
ACT-CL J0509−5345	SPT-CL 0509−5342	$05^h09^m20^s$	−53°45′00″	47	10.1
ACT-CL J0516−5432	Abell S0520	$05^h16^m31^s$	−54°32′42″	55	6.8
ACT-CL J0546−5346	SPT-CL 0547−5345	$05^h46^m35^s$	−53°46′04″	46	9.5
ACT-CL J0638−5358	Abell S0592	$06^h38^m46^s$	−53°58′40″	55	7.5
ACT-CL J0645−5413	Abell 3404	$06^h45^m29^s$	−54°13′52″	59	9.3
ACT-CL J0658−5556	1E 0657−56 (Bullet)	$06^h58^m33^s$	−55°56′49″	80	3.4
Previously Undetected					
ACT-CL J0329−5226	—	$03^h29^m27^s$	−52°26′26″	50	11.3
ACT-CL J0447−5107	—	$04^h47^m50^s$	−51°07′09″	57	7.9

[a] Position of the deepest point in 2′ FWHM Gaussian smoothed map, except for ACT-CL J0509−5345 which has a position that gives a maximal SNR (see text).

[b] The map rms is measured outside a 6′ mask and converted to an effective one square arcminute pixel size. Temperature values are relative to the CMB spectrum.

[c] Integration time, defined as the approximate total time that the telescope boresight was pointed in the map region.

nightly pointing variation measured using a radio source at 148 GHz, which has standard deviations of 8″ in the azimuth direction and 14″ in the altitude direction. (Note that, particularly in the altitude direction, these are larger than the estimated 5″ centroiding uncertainty described above.) The larger variation along the altitude axis is largely due to a correlation between the altitude pointing and the time of night. The most plausible explanation is thermal contraction which is known to cause the primary and secondary reflectors to move relative to each other in a direction more relevant to the altitude pointing (see Fig. 5 of Hincks et al., 2008).

The precision to which the nightly pointing variations can be removed by fitting to a bright point source each night has not yet been investigated. However, Fig. 6.1c shows that cross-linked maps of PMN J0540−5418 and PMN J0549−5246 have 148 GHz beam profiles consistent with the profile measured with Saturn (§5.2), so any smearing of the maps due to the pointing jitter does not have a prominent effect.

6.2 Clusters

6.2.1 Maps and Basic Properties

Table 6.1 lists the clusters presented in this chapter. Maps along with companion difference maps are shown in Fig. 6.2. Except for one cluster (see §6.2.1.1), all maps and analysis are from the 148 GHz array, our most sensitive in the 2008 season.

A cluster's position, as listed in the third and fourth column of Table 6.1, is determined by finding the coldest point in its map after smoothing with a 2′ FWHM Gaussian kernel. The one exception is ACT-CL J0509−5345 (SPT-CL 0509−5342), which exhibits complex structure with three local minima. In this case, a position is chosen that gives a maximal signal-to-noise (see below).

The quoted noise for a map is the rms of its pixels calculated outside a 6′ mask. Our pixel size is 0.18′ (note that this is different from the $\xi = 0.3'$ used to calculate the atmospheric signal—see §4.3.1). We give noise values for an effective pixel size of 1′, meaning that we multiply the map rms by $0.18'/1'$. T. Marriage took power spectra of these maps to investigate whether the rms is a good representation of the pixel noise. He found that to within a few microkelvin this is the case: noise on larger scales is subdominant.

6.2.1.1 Cluster Mapping at 218 GHz and 277 GHz

Mapmaking of clusters to date has focused on the 148 GHz array, as the 218 GHz and 277 GHz were more noisy in the 2007/2008 seasons. It is hoped that the removal of an optical coupling layer for the 2009 season will improve their utility. Nevertheless, analysis of the 218 GHz and 277 GHz data is still in the early stages, and it is reasonable to expect that the 2008 data in the higher frequencies will yield important complementary cluster data if they are more carefully studied.

A first step in this direction has been achieved for ACT-CL 0329−5226. Maps in three frequencies are displayed in Fig. 6.3. Even with straight-line stripe-removal, the 218 GHz and 277 GHz maps are completely dominated by striping. Consequently, these maps have had stripe-removal performed with cubic polynomials. Additionally, the mask size was reduced from 6′ to 3′.

An increment at 277 GHz is clearly visible, and the 218 GHz map shows no substantial flux at the cluster location: we are thus clearly observing the expected SZ spectrum. This is especially encouraging considering that this is a previously unknown cluster, and adds evidence for the reality of our detection. However, because of the heavy image processing (i.e., the cubic stripe-removal and small mask size), there are large systematic uncertainties in the size of the increment. This probably explains why, in Fig. 6.3, the magnitude of the increment is almost a factor of two larger than the magnitude of the decrement when we expect them to be about the same.

We made 218 GHz and 277 GHz maps for some of the other clusters with high-significance detections in 148 GHz. None revealed an increment signal as convincing as that of ACT-CL 0329−5226. It is likely that the detection in ACT-CL 0329−5226 is an anomaly, given our current analysis techniques, and that more sophisticated treatment of the noise will be necessary before the 218 GHz and 277 GHz maps can be used for quantitative analysis or even confirmation of cluster detections.

6.2.2 Analysis

6.2.2.1 Significance of Detections

Table 6.2 lists the measured cluster properties discussed throughout this section. The first column quotes a cluster depth ΔT_{SZ}, which is the value of the map at its coldest point after smoothing with a 2′ FWHM Gaussian kernel. It is only meant to give a general indication of the depth of the cluster, and it should be borne in mind that it depends on both the smoothing kernel and the telescope beam, and says nothing about extended signal away from the cluster center. We also remark that we use unsmoothed maps for the rest of our analysis.

We quantify the significance of the detections by a signal-to-noise ratio (SNR) measurement. Denote the signal map m_{xy} and the difference map d_{xy}, where the origin of the coordinates (x, y) is the cluster center. We define the SNR within an aperture θ as:

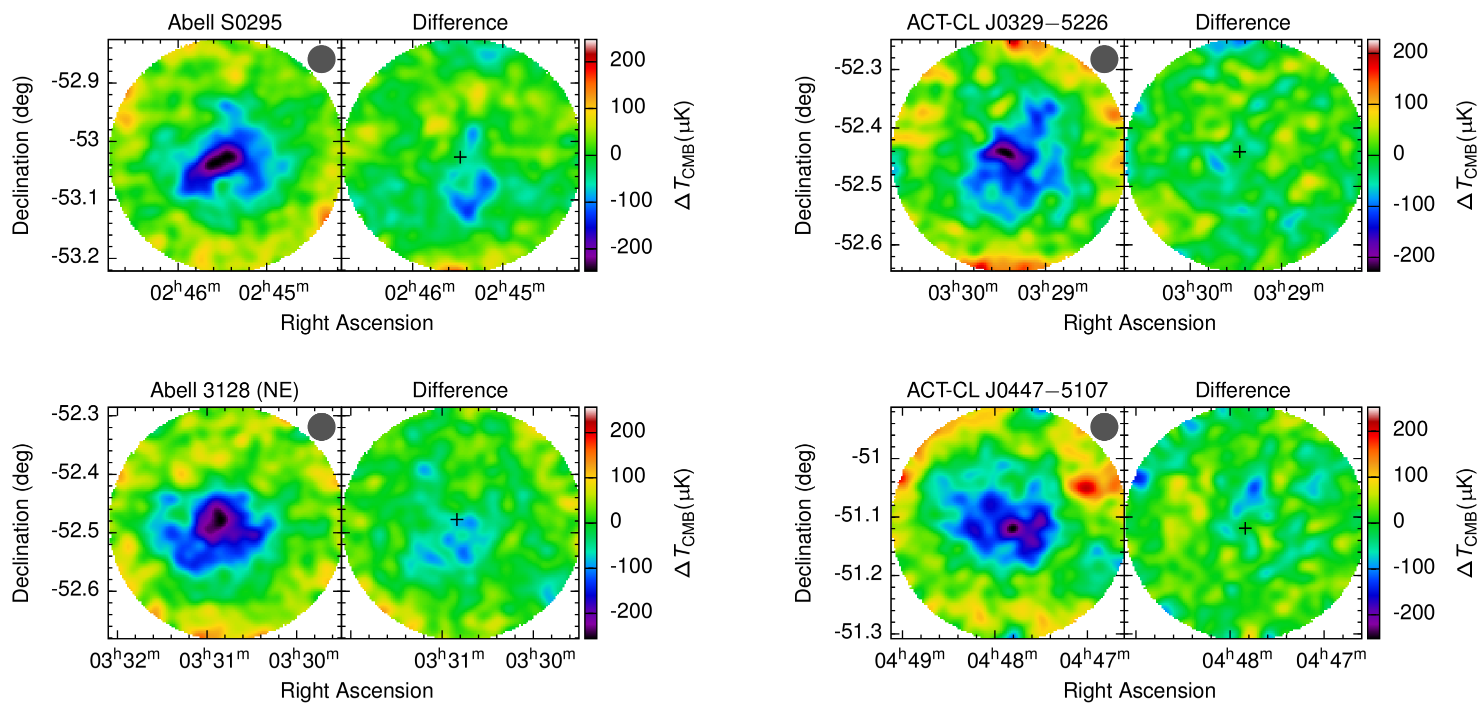

Figure 6.2: Cluster maps made using the Cottingham Method at 148 GHz, paired with their difference maps (see §6.1.2). The coordinates are in the J2000 epoch. Note that the color scale is different for each cluster. The gray disk in the top corner of the cluster plots is 2.43′ in diameter, the FWHM size of the beam convolved with the Gaussian smoothing kernel that was applied to these images. In each difference plot, a cross shows the coordinates of the darkest spot in its corresponding signal map (except for SPT-CL 0509−5342 (ACT-CL 0509−5345)—see text). *Figure continues on next page.*

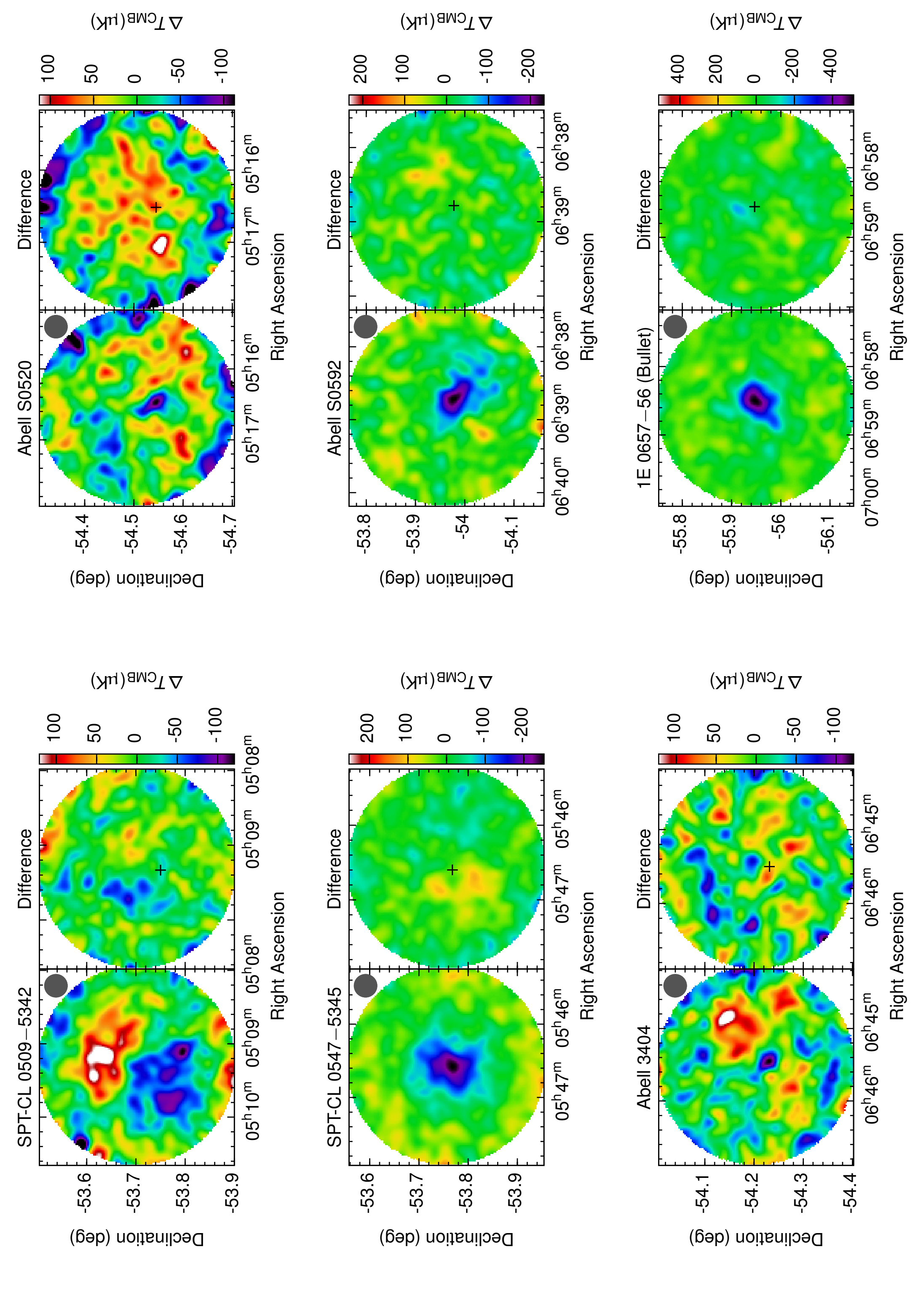

Figure 6.2: — *Continued.*

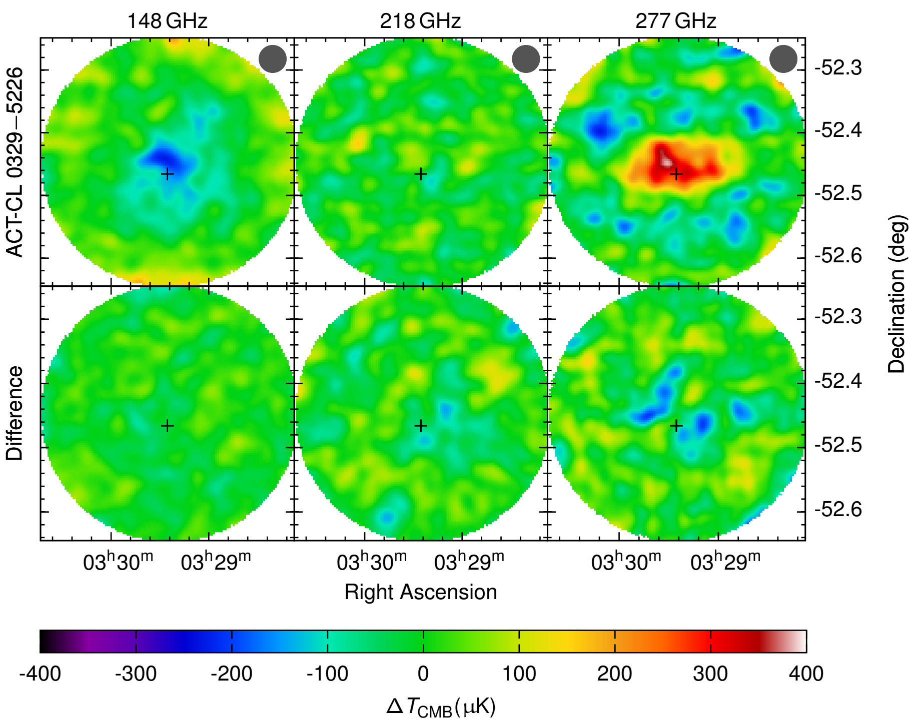

Figure 6.3: Maps of ACT-CL 0329−5226 in three frequencies. The 218 GHz and 277 GHz maps required more heavy post-processing: stripe-removal was done with a cubic polynomial, and the mask size was shrunk to 3′. Consequently, there is a large uncertainty in the size of the SZ increment at 277 GHz.

$$SNR(\theta) \equiv \min \left\{ \left| \frac{\sum\limits_{\sqrt{x^2+y^2}<\theta} (m_{xy} \pm d_{xy})}{\sqrt{N(\theta)\,(\sigma_m^2 + \sigma_d^2)}} \right| \right\}, \tag{6.1}$$

where the sum is over pixels within a radius θ from the cluster center, $N(\theta)$ is the number of pixels in the sum, and σ_m^2 and σ_d^2 are the variances of the signal and difference maps, respectively. There are two possible SNR, from either subtracting or adding the signal and null maps, denoted by the plus-or-minus sign in Eq. 6.1, and we use the minimum of these. The rationale is that coincident flux in the difference map is probably an indication of spurious signal in the signal map and that the SNR should reflect this. However, the sign of the difference map is in one sense arbitrary because it contains half of the data subtracted from the other half. Thus, for example, a spurious negative signal coming from one of the TOD's might create a positive feature in the difference map. The signal minus the difference map gives the lower SNR in this case, correctly representing the smaller probability that it is significant.

It must be admitted that Eq. 6.1 is a somewhat idiosyncratic and conservative definition of the SNR and has some obvious flaws. For example, σ_m and σ_d are definitely correlated to some degree, so the factor $\sqrt{\sigma_m^2 + \sigma_d^2}$ certainly overestimates the noise. It would be worthwhile to develop a more robust measure of the significance of our cluster detections.

In Table 6.2 we list $SNR(\theta_i)$ at the value of θ_i that maximizes the SNR.

An important question is whether primary CMB anisotropies are contaminating these measurements. Because of stripe removal, the mean value of the local CMB temperature is zero, but could anisotropies smaller than the map size have a significant effect? To test this, we created simulated maps of the primary CMB anisotropies with no noise. The maps were $24'$ in diameter and we did stripe-removal in these maps with a $6'$ mask, just as in the real maps. In an ensemble of 1000 simulations, the mean rms temperature was $(20 \pm 16)\,\mu$K outside the $6'$ mask, and $(24 \pm 22)\,\mu$K within it, with the error values being the standard deviations. Two conclusions can be drawn. First, the rms noise we measure in our cluster maps (c.f. Table 6.1) is not dominated by the CMB. For a typical map rms of $50\,\mu$K, the CMB contribution is on average about a sixth, assuming it adds in quadrature. Thus, since σ_m^2 in Eq. 6.1 already contains this contribution, and since, as we discussed above, our SNR definition is already conservative through over-counting of the noise, the presence of primary CMB anisotropies is not artificially inflating our SNR estimate. Second, our SNR measurements are not significantly altered by the presence of CMB anisotropies. The rms temperature in our simulations within the $6'$ mask was only about 20% higher than that outside the mask. On the other hand, the smallest SNR we measure (c.f. Table 6.2) is 2.8 for ACT-CL J0645$-$5413. For CMB anisotropy at the map center to masquerade as a signal this large, it would have to have to be greater than the noise outside the mask by much more than 20%.

6.2.2.2 Integrated Compton-*y* Values

A useful measure of the SZ signal is the integrated Compton-y parameter (Benson et al., 2004). It assumes no model for the cluster profile and simply sums the pixels in the map:

$$Y(\theta) = \iint\limits_{|\boldsymbol{\theta}'|<\theta} \mathrm{d}\Omega_{\boldsymbol{\theta}'}\, y(\boldsymbol{\theta}'), \tag{6.2}$$

where θ is the angular distance from the cluster center. We use steradians as the unit of solid angle, so Y is dimensionless. As an example, $Y(\theta)$ is plotted in the bottom panel of Fig. 6.4 for ACT-CL J0638$-$5358 (Abell S0592); the upper panels show its radial temperature profile. The values of Y for each cluster at $2'$, $4'$, and $6'$ are provided in Table 6.2. When the cluster temperature

Table 6.2: Measured properties of ACT SZ clusters. Columns with plain backgrounds contain measurements from the ACT maps (§6.2.2), while columns with gray backgrounds are from observations at other frequencies (§6.2.3). Table 6.3 lists the references from which these supplementary data were taken.

ACT Cluster (ACT-CL)	**ΔT_{SZ}**[a] [μK]	**SNR(θ)**[b]	**$10^{10} \times$ Y(θ)**[c] $\theta \le 2'$ ($\pm$0.2)	$\theta \le 4'$ ($\pm$0.6)	$\theta \le 6'$ ($\pm$1.2)	$\theta \le \theta_{2500}$[d]	**z**[e]	**D_A** [Mpc]	**L_X**[f] [10^{44} erg s^{-1}]	**M_{500}**[g] [10^{15} $M_\odot$]	**kT** [keV]
Previously Detected											
J0245−5301 (Abell S0295)	−250	15.2 (6.8′)	0.93	2.5	4.1	$0.53^{+0.35}_{-0.21}$	0.3006	920	8.3	0.8	6.7 ± 0.7
J0330−5228 (Abell 3128 NE)	−260	12.8 (4.3′)	0.97	2.80	4.50	$0.15^{+0.10}_{-0.06}$	0.44	1172	3.9	0.3	5.1 ± 0.2
J0509−5345 (SPT 0509−5342)	−70	7.7 (5.2′)	0.33	1.07	1.50	—	0.36[h]	1037	2.2	0.4	—
J0516−5432 (Abell S0520)	−110	4.2 (4.1′)	0.2	-0.12	-0.58	$0.72^{+0.47}_{-0.28}$	0.294	906	3.5	0.6	7.5 ± 0.3
J0546−5346 (SPT 0547−5345)	−250	13.9 (5.8′)	0.91	2.36	3.67	—	0.88[h]	1596	4.7	0.6	—
J0638−5358 (Abell S0592)	−230	8.1 (3.1′)	0.74	1.5	2.2	$1.31^{+0.86}_{-0.52}$	0.2216	737	10.6	1.0	8.0 ± 0.4
J0645−5413 (Abell 3404)	−120	2.8 (2.0′)	0.13	-0.19	-0.73	$1.87^{+1.23}_{-0.74}$	0.167	589	8.2	0.7	7.6 ± 0.3
J0658−5556 (1E 0657−56)	−510	12.1 (2.7′)	1.7	3.2	3.8	$1.61^{+1.16}_{-0.67}$	0.296	910	20.5	1.4	10.6 ± 0.1
Previously Undetected											
J0329−5226	−230	14.8 (7.9′)	0.71	1.91	3.30	—	—	—	—	—	—
J0447−5107	−250	13.4 (7.4′)	0.75	2.60	4.02	—	—	—	—	—	—

[a] Cluster depth, as measured in a 2′ FWHM Gaussian smoothed map, intended as a guide to the magnitude of the decrement.
[b] Maximum signal-to-noise ratio (Eq. 6.1) and the radius θ at which it was obtained.
[c] See Eq. 6.2 and subsequent text.
[d] Predicted value of Y within R_{2500} from the Y-kT scaling relation of Bonamente et al. (2008). Errors come from the uncertainty of the scaling relation parameters. Although we do not have R_{2500} values for our clusters, the $Y(2')$ measurements should be roughly comparable. See text for more discussion.
[e] I.e., redshift.
[f] Luminosity in the band 0.1–2.4 keV. Uncertainties are about 20%.
[g] The uncertainty on the masses is about 50%.
[h] Photometric redshift.

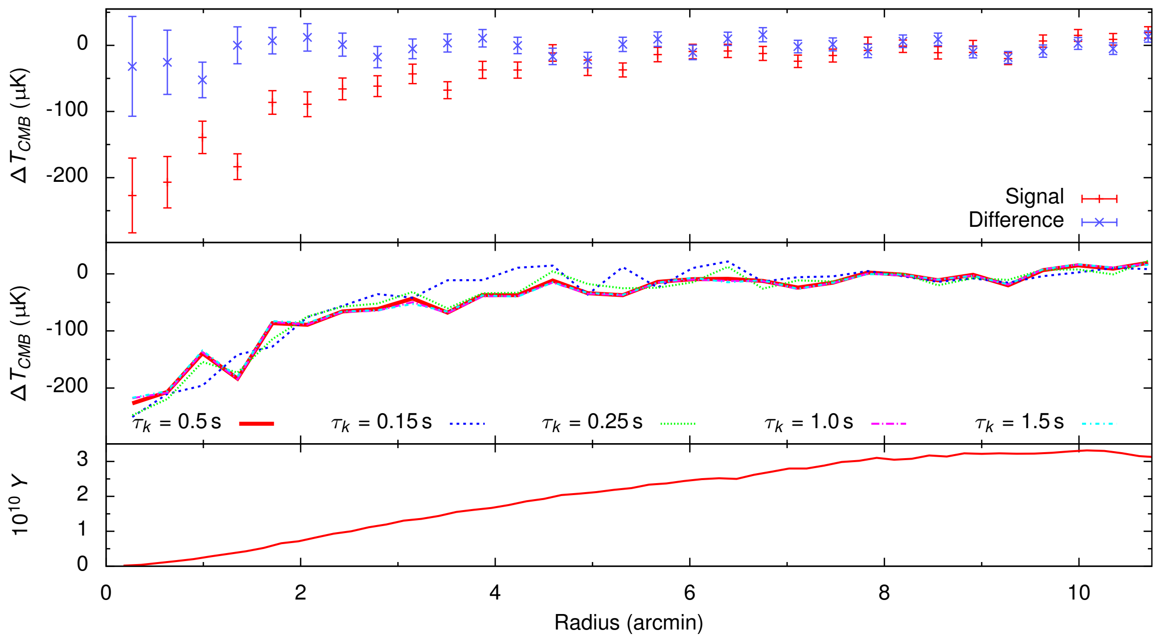

Figure 6.4: Radial temperature and integrated Compton-y profiles for ACT-CL J0638−5358. The profile data are averages from the maps in 22″-wide annuli, and $Y(\theta)$ is is the sum of the pixels within a radius θ, converted to the unitless Compton-y parameter. The top panel shows the profiles of the signal and difference maps. The middle panel compares profiles for maps made with different knot spacings τ_k, showing that only for very short spacings is the profile noticeably different from the τ = 0.5 s profile used for cluster analysis, and then not significantly so.

is known (see 6.2.3, below), the relativistic form of Nozawa et al. (2006) is applied.[2] The relativistic corrections at 148 GHz, which increase Y, range from 4% (ACT-CL J0330−5228) to 7% (ACT-CL J0658−5556). Thus, the Y values quoted for our clusters with unknown temperatures will be biased low, though we note that the relativistic corrections are smaller than the uncertainty of our measurements (see below).

To estimate the uncertainty of our Y values, we made 35 maps of random sky regions. All of them were located relatively near ($\sim 0.5^\circ$) to regions that we had already mapped,[3] including the cluster maps presented in this chapter, so that many of the data files are the same. The maps were made with the same stripe-removal and mask sizes as the cluster maps. Of them, 6 were discarded because of large negative or positive signal near the map center (possibly due to unknown clusters or point sources) and 5 were removed because the map noise was larger than any of the cluster maps (c.f. Table 6.2). Integrated Compton-y values were calculated for the remaining maps, integrating from the map centers. The standard deviations from the 24-map ensemble are 0.2×10^{-10}, 0.6×10^{-10}, and 1.2×10^{-10} for Y at $2'$, $4'$, and $6'$, respectively. We treat these as 1σ uncertainties on our measurements of Y in the cluster maps.

In our study of CMB-only simulations (see §6.2.2.1) we also calculated integrated-y values, finding standard deviations of 0.1×10^{-10}, 0.35×10^{-10}, and 0.6×10^{-10} for radii of $2'$, $4'$, and $6'$, respectively. Thus, less than half of our uncertainty of Y at each radius is due to confusion with CMB anisotropies. The rest comes from uncertainties in the background level and residual contamination after stripe removal. Better mapping algorithms for reducing or eliminating the necessity for stripe-removal would help. Additionally, more sophisticated modelling of the cluster profile would allow the background to be removed with greater precision, whereas now we are simply averaging the map level outside a $6'$ radius. The technique used for estimating the amount of true power in the background of the beam maps by modelling the beam wings (§5.2.2.1) might have an analog for cluster maps.

Note that in two clusters—ACT-CL J0516−5432 (Abell S0520) and ACT-CL J0645−5413 (Abell 3404)—we measure negative values of $Y(4')$ and $Y(6')$. Their maps show that the SZ signal is compact and the negative values are consistent with noise.

As a check that the choice of knot spacing ($\tau_k = 0.5$) is not creating a significant bias via covariance of the celestial signal with the low-frequency atmospheric estimate (see §4.2.4), we created maps with τ_k from 0.15 s to 1.5 s for ACT-CL J0245−5301 and ACT-CL J0638−5358. The temperature profiles for the latter are plotted in the middle panel of Fig. 6.4. Even the shortest spacing does not produce a profile that is significantly different from the others. Its knot spacing, $\tau_k = 0.15$ s, is the only one from the ensemble with a corresponding angular scale smaller than the map size. We conclude that the results are not biased by having knots of too high a frequency.

6.2.2.3 Attempts at Profile Fitting

In §1.1.5.1 and §1.1.5.2 we showed that comparisons to X-ray measurements can yield measurements of the Hubble constant and the gas-mass fraction, and probe the details of cluster structure. However, a joint analysis requires some modelling of the cluster so that length scales can be compared.

A popular choice is the spherical, isothermal β-model (Cavaliere & Fusco-Femiano, 1978):

$$n_e(\mathbf{r}) = n_{e0}\left[1 + \left(\frac{r}{r_c}\right)^2\right]^{-3\beta/2} \quad\longrightarrow\quad \Delta T_{SZ} = \Delta T_0\left[1 + \left(\frac{\theta}{\theta_c}\right)^2\right]^{(1-3\beta)/2}, \tag{6.3}$$

where $\mathbf{r}$ has its origin at the cluster center and r_c defines a "core radius" for the cluster. Fits to real clusters have parameters in the range $0.6 \lesssim \beta \lesssim 1$ and $15'' \lesssim \theta_c \lesssim 60''$ (e.g., LaRoque et al.,

[2] We thank the authors for kindly sharing their code for this calculation with us.

[3] However, note that the distances are large enough that there is no overlap between them.

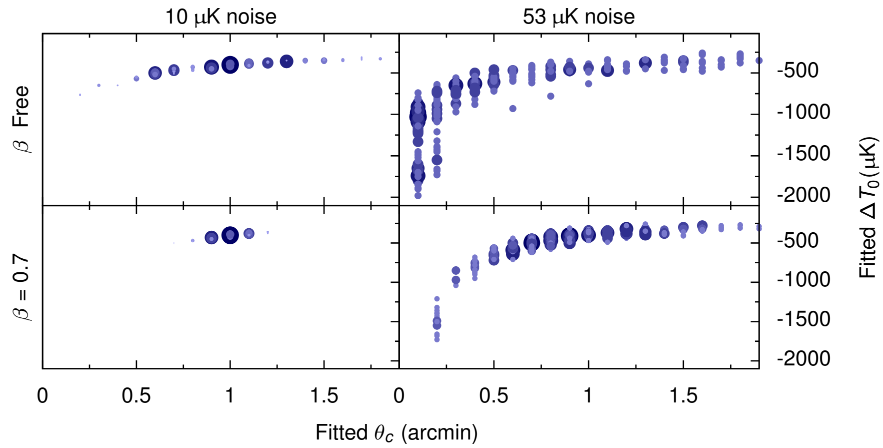

Figure 6.5: Some results of β-profile fits to simulated maps. The parameters for the simulation were $\Delta T_0 = -390\,\mu\text{K}$, $\beta = 0.7$, and $\theta_c = 1'$. Two noise levels were tested, 10 μK rms at 1 square arcminute *(left)* and 53 μK *(right)*. For each noise level, several hundred maps of random noise were generated and were fit with the β-model. Two types of fit were done: one with all parameters free *(top)*, and one with β fixed to the (known) input value *(bottom)*. The plots show the results of the fit in the ΔT_0–θ_c plane. Larger dots indicate that more fits returned values at that position in parameter space. Fits to the lower noise recover the input parameters with good fidelity, but are unable to perform well in the 53 μK maps.

2006). It has been used with some success for joint SZ–X-ray studies (e.g., Bonamente et al., 2008), though it does have some known flaws (Hallman et al., 2007). Other models with more realistic gas temperature profiles show promise and are beginning to replace the β-profile (e.g., Bode et al., 2009; Mroczkowski et al., 2009; Umetsu et al., 2009). Nevertheless as a first step towards modelling our clusters, we chose the β-model because of its simplicity and the numerous examples in the literature.

We performed β-model fits by calculating χ^2 in our 148 GHz maps for a grid of $(\Delta T_0, \theta_c, \beta)$ covering the expected parameter space. The models were convolved with the telescope beam before computing χ^2. The fits were inconclusive. In general, the reduced-χ^2 was significantly greater than unity. The covariance between β and θ_c was substantial, with θ_c often tending to large ($> 1'$) values. The latter occurred even if β was fixed to 0.7 or 1.

To investigate whether the poorness of the fits is due to noise in the maps or rather to a fundamental inconsistency between the β-model and our data, we turn to simulations. Synthetic maps with a β-profile were generated, convolved with the beam, and white noise was added. Different parameter combinations were used, with $0.7 \le \beta \le 1.3$, $0.5 \le \theta_c \le 2.0$, and ΔT_0 chosen so that in all maps, the central decrement was $-250\,\mu\text{K}$, commensurate with the depths of the largest clusters in our real maps. For each parameter set, hundreds of maps with different random noise realizations were generated and the β-model was fit to each. The scatter on the fit results allowed us to quantify the precision of the fits.

We found that with a low white noise level of 10 μK rms on 1 square arcminute scales, our fits recovered the input parameters with good precision, but that when the noise was raised to 53 μK (similar to the noise in our real maps), the fits had almost no precision at all. As an example, Fig. 6.5 shows the plane of ΔT_0–θ_c fits for the two noise levels with an input of $\theta_c = 1'$, $\beta = 0.7$. Even when β is held fixed at its known value, the precision is low in the higher noise maps. These results show that the poorness of the fits in our real maps is expected.

On the other hand, recovery of the integrated Compton-y parameter was more robust. In the maps with 53 μK noise, the mean value of $Y(\theta)$ matches the input model and has a standard

Table 6.3: Literature references for known cluster data, mainly compiled by J. Hughes and F. Menanteau.

Catalog Name	Optical	X-Ray	SZ
Abell S0295[a]	Abell et al. (1989), Edge et al. (1994)	Voges et al. (1999), Fukazawa et al. (2004)	—
Abell 3128	Rose et al. (2002)	Werner et al. (2007)	—
SPT-CL 0509−5342	Menanteau & Hughes (2009)[b]	—	Staniszewski et al. (2008)
Abell S0520	Abell et al. (1989), Guzzo et al. (1999)	Böhringer et al. (2004), Zhang et al. (2008)	Staniszewski et al. (2008)
SPT-CL 0547−5345	Menanteau & Hughes (2009)[b]	—	Staniszewski et al. (2008)
Abell S0592	Abell et al. (1989)	de Grandi et al. (1999), Hughes et al. (2009)	—
1E 0657−56	Tucker et al. (1998), Clowe et al. (2007),	Markevitch et al. (2002), Markevitch (2006) Zhang et al. (2006), Zhang et al. (2008)	Andreani et al. (1998) Gomez et al. (2004), Halverson et al. (2008b)

[a] The Mass was inferred from the mass-luminosity relation in Reiprich & Böhringer (2002).

[b] This paper also uses X-ray data.

deviation of $\sim$10–15% for $\theta < 6'$.

6.2.3 Comparisons with Previous Measurements

All but two of the clusters presented in this chapter had been discovered in other surveys (c.f. Table 6.1). The ACT has made the first SZ detections of four of these (Abell S0295, Abell 3128 (NE), Abell S0259, and Abell 3404). J. Hughes and F. Menanteau did an extensive review of the literature on the X-ray, optical, and SZ analyses observations of the clusters. The details are in Hincks et al. (2009), and here we only summarize and discuss some of the more salient points that comparisons with our data afford.

Cluster properties from the literature are in Table 6.2 (shaded columns). The errors on the luminosity L_X are $<$ 20%, and those on the masses are somewhat large, about 50%. Masses are sometimes given in the form M_ξ, defined as the mass within a radius R_ξ having a mean mass density $\langle\rho\rangle$ that is ξ times greater than the critical density, i.e., $\langle\rho\rangle = \xi \times 3H^2/(8\pi G)$. A flat ΛCDM cosmology with $\Omega_M = 0.3$ and $H_0 = 70\,\mathrm{km\,s^{-1}\,Mpc^{-1}}$ is assumed for calculation of angular diameter distances D_A. The Y_{2500} values are discussed in §6.2.3.4, below. Table 6.3 lists the literature references that were used for compiling all of these values.

In the following sections we comment on some of the individual clusters, before comparing intergrated Compton-y values.

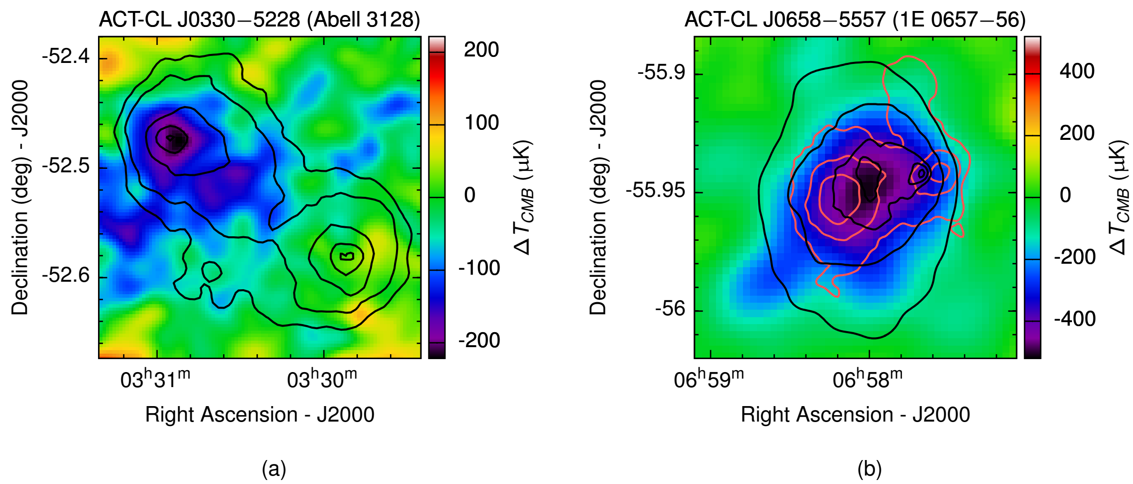

Figure 6.6: Maps of ACT clusters with superimposed X-ray and lensing contours. The map of ACT-CL J0330−5228 (a) has X-ray contours from two separate *XMM-Newton* observations (Obs Ids 0400130101 and 0400130201) with a total exposure time of 104 ks. The two observations were mosaicked into a single image over the range 0.2–2.0 keV. Contour values are from 1.25×10^{-8} to 1.25×10^{-7} photons/cm^2/s/arcsec^2. The SZ signal appears to be a detection of the high-redshift, NE component of this system—see text. The map of ACT-CL J0658−5556 (b) shows X-ray contours in black and lensing in orange. The X-ray contours come from an 85 ks-long *Chandra* observation (Obs Id 3184) and correspond to the 0.5-2.0 keV band. Contour values are 4×10^{-7} to 2×10^{-9} photons/cm^2/s/arcsec^2. The lensing data are from Clowe et al. (2007) with contours running from κ = 0.12 to 0.39.

6.2.3.1 ACT-CL J0330−5228 (Abell 3128)

One of the more interesting clusters in our sample is ACT-CL J0330−5228, which is associated with Abell 3128. The X-ray observations show two clear peaks separated by about 12′. A detailed analysis of Abell 3128 with X-ray and optical data by (Werner et al., 2007) concluded that most of the X-ray emission in the north-east (NE) component comes from a distant cluster at z = 0.44 unassociated with the cluster responsible for the south-west (SW) component, which is a member of the nearby (z = 0.06) Horologium-Reticulum supercluster. They estimate a mass of M_{500} = $3.4 \times 10^{14}\,M_\odot$ for the high-redshift cluster, about that twice that of the SW cluster, though they caution that the systematic error is large.

Fig. 6.6a shows our map with superimposed X-ray contours. ACT-CL J0330−5228 is clearly associated with the NE component and we see no obvious SZ flux at the position of the SW peak. Based on the map noise, our nondetection of this component is at the 100 μK level to 2σ.

6.2.3.2 ACT-CL J0658−5556 (1E 0657−56)

The cluster 1E 0657−56 is a famous merging system that has been called “the most interesting cluster in the universe” (Markevitch, 2006). We have detected it with large signficance as ACT-CL J0658−5556. It is highly dynamic, consisting of a smaller cluster, the “Bullet”, which has fallen through a larger cluster at the supersonic speed of 4700 km s^{-1}, almost perpendicular to the line-of-sight. This has created a hot shock-front of gas with temperatures $\gtrsim$ 15 keV (Markevitch et al., 2002). Recently, Clowe et al. (2007) presented weak lensing measurements, which they use to infer a mass distribution and conclude that the system provides strong evidence for the existence of dark matter. Fig. 6.6b shows our SZ map with superimposed X-ray and lensing contours.

The Bullet cluster was first observed with the SZ effect on the Swedish-ESO Submillimetre Telescope (SEST) by Andreani et al. (1998), who gave a central compton-y value of $(2.6 \pm 0.79) \times 10^{-4}$. ACBAR (Gomez et al., 2004) reported a central decrement of $\approx 180\,\mu$K per 4.5′ FWHM beam. The most recent measurement before ours comes from APEX (Halverson et al., 2008a). All three experiments were done at about 150 GHz, and the first two also made measurements of the SZ increment.

Halverson et al. (2008a) were able to fit a β-profile to their SZ map, obtaining a central temperature decrement of $\Delta T = (-771 \pm 71)\,\mu$K, a central Compton-$y$ parameter of $(3.24 \pm 0.3) \times 10^{-4}$ (for T_e = 10.6 keV), a core radius of $\theta_c = (2.37 \pm 0.3)'$, and an index $\beta = 1.15 \pm 0.13$. Numerically integrating their β-profile data yields $Y(2') = 2.46 \times 10^{-10}$, $Y(4') = 5.61 \times 10^{-10}$, and $Y(6') = 7.76 \times 10^{-10}$. These values are considerably larger than ours, especially at the larger radii.

The central decrement temperature can also be compared. In the APEX source-masked map, smoothed to a FWHM resolution of 1.42′, the decrement is about $-660\,\mu$K. Because the ACT beam is larger than that of APEX, it is not as easy to get a precise temperature at that resolution. The smoothing kernel is small compared to the beam size and does not greatly reduce pixel-to-pixel noise, making it difficult to quote a cluster depth in the map. However, convolving the ACT map with a 0.85′ FWHM Gaussian gives roughly the same smoothing as APEX, and the central decrement is somewhere in the range -600 to $-700\,\mu$K, consistent with their value. If the ACT map is smoothed to the ACBAR resolution, the central decrement is around $-330\,\mu$K, almost twice the amplitude of their measurement.

There is a slight offset in the SZ position reported by ACBAR from the X-ray position, which might suggest that the bright millimeter galaxy located within the bullet cluster found by Wilson et al. (2008) and Rex et al. (2009) contaminates the SZ signal at 150 GHz. However, there is no such offset in our map nor in that from APEX. Wilson et al. (2008) report a brightness of (13.5 ± 1) mJy for the point source at 270 GHz. Taking the spectral index β = 3.5 used by Rex et al. (2009), we expect the brightness at 148 GHz to be about 1.6 mJy, which corresponds to a CMB temperature of about 20 μK in our instrument (c.f. Table 1.3). While this will slightly decrease the amplitude of the SZ decrement in the ACT map, it is a small effect and is currently well below the map noise.

6.2.3.3 South Pole Telescope Clusters

The South Pole Telescope (SPT) is complementary to the ACT in terms of its sensitivity, resolution, and sky coverage. Last year, their first science paper introduced SZ detections of four clusters, three of them previously undiscovered (Staniszewski et al., 2008). We detect three of them: SPT-CL 0547−5345 (ACT-CL J0546−5346), SPT-CL 0509−5342 (ACT-CL J0509−5345), and Abell S0520 (SPT-CL 0517−5430, ACT-CL J0516−5432).

There is no published information on the size of the SZ decrements for the SPT clusters (either in terms of temperature or the Compton-y parameter), so no substantial comparison can be made at this time. That both experiments have detected three clusters with high significance is strong evidence that these are massive clusters, a conclusion also reached by Menanteau & Hughes (2009) based on optical and X-ray data.

A notable feature present in both the ACT and SPT maps is the bright spot to the north-west-north of SPT-CL 0509−5342 (ACT-CL J0509−5345). There are no objects listed in NED within 3′ of this feature's location in the ACT map. The possibility that this is a point source is discussed more below in §6.3.2.

We are unable to confirm the SZ detection of SPT-CL 0528−5300. Fig. 6.7 shows a map centered on the SPT coordinates, where there is no measureable decrement for a putative decrement at the map center. Based on the map noise, we report a 2σ non-detection at the 90 μK level. The follow-up study by Menanteau & Hughes (2009) provided good further evidence for the existence of this cluster, so it is reasonable to expect that with better sensitivity, it will be detected by the ACT in future studies.

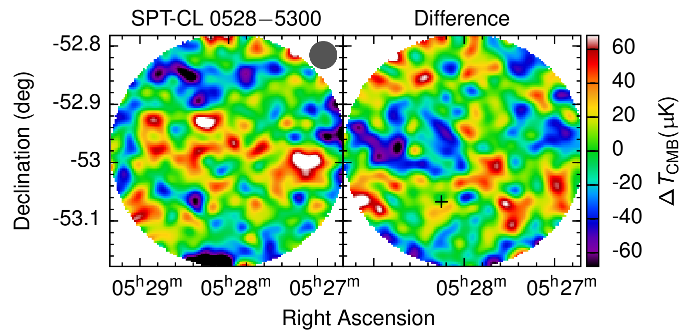

Figure 6.7: A map and corresponding difference map centered on the coordinates of SPT-CL 0528−5300. The noise in our map is 45 μK (per square arcminute), so we have a 2σ non-detection at the 90 μK level. Future ACT maps with better sensitivity may well make a detection.

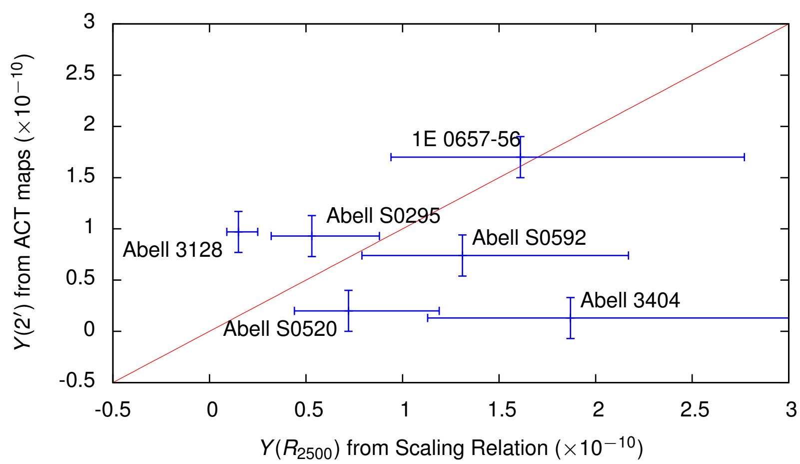

Figure 6.8: A comparison of integrated-Y values predicted by the Y-kT scaling relation of (Bonamente et al., 2008) with the values measured in the ACT maps (c.f. Table 6.2). Errorbars on $Y(R_{2500})$ come from the uncertainties in the scaling relations.

6.2.3.4 Comparing Integrated Compton-y Values

To compare our measurements with previously-known clusters that have X-ray measurements, J. Hughes compiled a list of integrated-Y values based on the Y-kT scaling relations of Bonamente et al. (2008). The Y values are given at a radius of R_{2500} and are listed in Table 6.2, with uncertainties coming from the errors on the scaling relation. While we do not have Y_{2500} for our clusters, estimates range from $1'$ to $3'$, allowing for a rough comparison to our $Y(2')$ values.

Fig. 6.8 compares the predicted and measured Y values. They agree to within 2σ for four of the clusters, but two—ACT-CL J0330−5228 (Abell 3128 (NE)) and Abell 3404 (ACT-CL J0645−5413)—are not in as good agreement.

6.2.4 Discussion

Our high-significance maps of previously known galaxy clusters demonstrate that the ACT can easily detect massive galaxy clusters of $M \lesssim 1 \times 10^{15}\, M_\odot$ (c.f. Table 6.2). Lower detection thresholds will yield less massive clusters, as will the higher sensitivity maps that better mapmaking analysis and more data will produce. Since the size of the SZ signal scales roughly linearly with the mass, it is reasonable to expect that we will reach our target high-z detection limit of a few $\times 10^{14}\,M_{\odot}$. A possible cause for concern is that we do not make a significant detection of SPT-CL 0528$-$5300. However, recent weak-lensing measurements of the SPT clusters' masses indicates that this one might have a mass lower than any of the clusters in our sample (McInnes et al., 2009).

Our comparison of $Y(2')$ measured from our maps with $Y(R_{2500})$ inferred from X-ray temperatures via a scaling relation, though rudimentary, shows that the size of our detections is in the predicted range (c.f. Fig. 6.8), but the presence of outliers points to the need for further study. ACT-CL J0330$-$5228 (Abell 3128 (NE)) has a higher Y than predicted. It is a complex system (c.f. 6.2.3.1) and our measurement might be an indication that the mass is larger than was previously thought. More investigation in the optical, X-ray and SZ will be needed to draw any conclusions. The other outlier, Abell 3404 (ACT-CL J0645$-$5413), has a Y value more than ten times lower than predicted. The average CMB temperature in the $2'$ aperture would have to be about $-500\,\mu$K to give the predicted Y value. One might postulate that a large, positive signal is contaminating the SZ decrement. The magnitude seems too large for it to be a bright spot in the primary CMB. A point source with a brightness of about 0.3 Jy would be required to offset the the predicted decrement to the ACT measured value. However, the uncertainty in the predicted value is large, and a point source of only 0.05 Jy would reconcile the measurement and the prediction to 2σ. Again, more study in the optical and X-ray is needed. Analysis of the ACT 218 GHz channel could also be used to test the point source hypothesis.

The potential for direct comparison of our cluster maps to X-ray and optical data is illustrated in Fig. 6.6. Our strong detection (12.8 SNR) of the NE component of Abell 3128 and our non-detection of the SE component provides additional evidence that the distant cluster is more massive, perhaps by even more than a factor of two as currently estimated. It is a compelling example of the nearly redshift-independent mass selection of the SZ effect. In the other panel, the ACT measurement of the Bullet cluster (1E 0657$-$56) follows the X-ray contours more closely than the lensing, since the SZ signal traces gas rather than dark matter.

The only cluster in our sample with quantitative SZ measurements from other experiments is the Bullet cluster (1E 0657$-$56). In §6.2.3.2 we observed that the integrated Y values we measure differ from those given by the β-model fitted to the APEX map, especially at increasing radius. This indicates that either their beta profile is a poor description of the Bullet cluster, or that the ACT map is missing power in the profile wings, perhaps due to the $6'$ mask being too small. There are no Y values computed directly from the APEX map, so a direct comparison cannot be made, which might be especially useful in their source-masked data which were processed in a more similar manner to ours. Nevertheless, the temperature of the central decrement in the ACT map appears to be consistent with the APEX source-masked map's decrement, when the smoothing is about the same in both maps. The same is not true for the ACBAR map, which measures a lower central temperature than both ACT and APEX, although there is no quoted uncertainty in the ACBAR value.

Joint analysis of of clusters observed in the X-ray and SZ often relies on the ability to fit a model to both datasets. It might also prove useful for comparison to other SZ measurements, as exemplified by our difficulty interpreting our data on the Bullet cluster in relation to the APEX analysis. We have done an initial study of the feasibility of describing our maps with the isothermal β-model (§6.2.2.3) and concluded that the noise in our maps is currently too high for this approach. This underscores the importance of achieving lower noise in future maps. Fitting of more realistic models might also give better results. J. B. Juin, R. Warne, and F. Rojas Aracena are currently investigating the possibility of achieving good model fits to the current cluster maps.

Table 6.4: Flux measurements of three ACT point sources. See text for details.

Name	148 GHz (Jy)	218 GHz (Jy)	277 GHz (Jy)
ACT-PS J0540−5418 (PMN J0540−5418)	0.43 ± 0.03	0.30 ± 0.03	0.13 ± 0.04
ACT-PS J0549−5246 (PMN J0549−5246)	0.19 ± 0.02	0.14 ± 0.02	0.27 ± 0.11
ACT-PS J0509−5337	0.039 ± 0.009	0.049 ± 0.007	0.070 ± 0.023

6.3 Point Sources

Mapmaking of point sources is motivated by the need for telescope pointing characterization (§6.1.3). However, since we have maps at all three frequencies for the sources used for pointing calibration, it is worth doing preliminary analysis on their characteristics.

We measure the peak RJ temperature of the point sources in each map by fitting an Airy pattern as described in §5.2.2.2. Conversion to units of flux is done using the factors listed in Table 1.3; the values are quoted in Janskies (Jy), a common unit in radio astronomy. The uncertainty in the fluxes comes from five places: the Airy peak fitting error, the statistical error in the temperature calibration (see Table 5.4), the systematic uncertainty of the temperature of Uranus (about 6%), the uncertainty in the solid angles, and the uncertainties in the filter bandpass measurements (the latter two are incorporated in the errors listed in Table 1.3.)

In the following sections we study three sources. The two radio sources used for pointing calibration are analyzed in §6.3.1. Additionally, in §6.3.2 we examine a possible IR point source discovered in our map of ACT-CL J0509−5345.

6.3.1 The Bright Radio Sources PMN J0540−5418 and PMN J0549−5246

Both of the sources used for pointing calibration, PMN J0540−5418 and PMN J0549−5246, are radio sources appearing in the Parkes-MIT-NRAO (PMN) surveys (Wright et al., 1994) which observed them at 4.85 GHz. The Sydney University Molonglo Sky Survey (SUMSS) provides fluxes for both at 843 MHz (Mauch et al., 2003). Additionally, PMN J0540−5418 appears in the the Australia Telescope 20 GHz (AT20G) Survey Bright Source Sample at 20 GHz, 8 GHz, and 5 GHz (Massardi et al., 2008), as well as the WMAP5 source catalog at 22.8 GHz, 33 GHz, 40.7 GHz, and 60.8 GHz (Wright et al., 2009). Fig. 6.9 plots the spectra of the sources, combining the ACT data (shown in Table 6.4) and the measurements from the literature just cited.

PMN J0540−5418 exhibits a peak around 30−40 GHz in its spectrum and looks like a gigahertz-peaked spectrum (GPS). Radio sources with GPS include a class of "high-frequency peakers" (HFP) with peaks above 5 GHz (Dallacasa et al., 2002). Most known HFP have peaks below 20 GHz (Labiano et al., 2007; Hancock, 2009), but these catalogs are compiled with low-frequency data compared to the ACT and WMAP bands. The spectra are probably due to synchrotron radiation, with self-absorption causing the turnover at low frequencies. They are compact (i.e., ~ 1 kpc) and are generally thought to be young sources where radio jets at the core of a host galaxy are beginning to pierce through the core of a host galaxy (Orienti, 2009). The size of the core seems to be anticorrelated with the peak frequency: high peak frequencies tend to have more compact sources (O'Dea & Baum, 1997).

Snellen et al. (1998) and Hancock (2009) fit GPS with the equation:

$$I_\nu = \frac{I_p}{1 - e^{-1}} \left(\frac{\nu}{\nu_p}\right)^k \left[1 - e^{-(\nu/\nu_p)^{m-k}}\right], \tag{6.4}$$

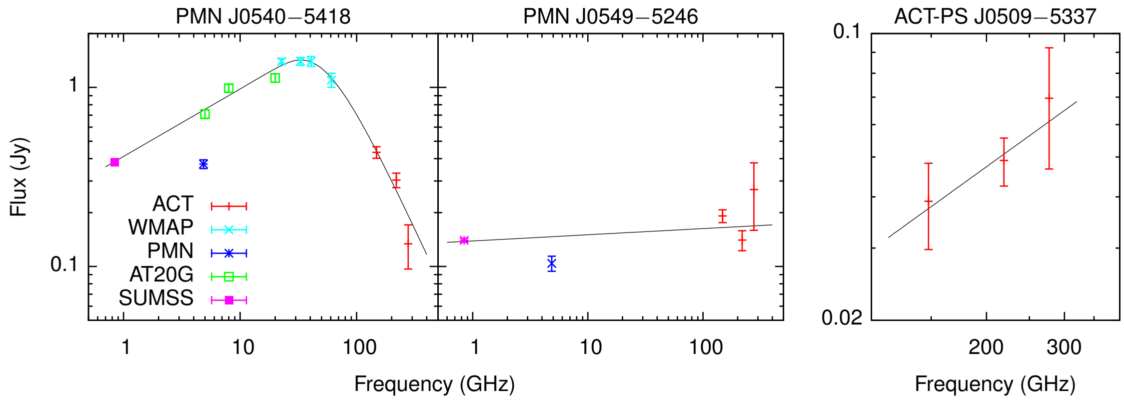

Figure 6.9: *Left:* The spectra of PMN J0540−5418 and PMN J0549−5246, with ACT fluxes contributing at the highest three frequencies. The other points are from the catalogs cited in the text. In the PMN J0540−5418 panel, the solid black line is the best fit to Eq. 6.4. It peaks at (56 ± 5) GHz. In the PMN J0549−5246 panel, the black line is a fit to a simple power law $I_\nu \propto \nu^\alpha$. The best fit, $\alpha = 0.035 \pm 0.034$, is consistent with a flat spectrum. *Right:* The spectrum of ACT J0509−5337, assuming that the slightly-offset brightest points in the three maps are due to the same source—see text for details. The spectral index is $\alpha = 0.8 \pm 0.3$.

where I_p and ν_p are the peak intensity and frequency, respectively, and k and m are the optically thick and thin spectral indices. We fit Eq. 6.4 to ACT data for PMN J0540−5418 together with the existing data in the literature, obtaining $\chi^2 = 15$ for 8 degrees of freedom (DOF). The best fit is shown in Fig. 6.9, and has best-fit values of $I_p = (1.19 \pm 0.04)$ Jy, $\nu_p = (56 \pm 5)$ GHz, $k = 0.38 \pm 0.02$, and $m = -1.4 \pm 0.1$. The optically thick index, k, is not close to the expected value of 2.5 for synchrotron radiation (e.g., Rohlfs & Wilson, 1999, §9.9), but is similar to many of the fitted values of Snellen et al. (1998). It should be noted that the PMN datum (the blue point in the plot) was excluded from the fit. It could be that the source is variable, especially as this apparently spurious point was measured more than ten years before the others.

PMN J0549−5246 appears to have a relatively flat spectrum, though there are only two other radio measurements available. It is included in the Combined Radio All-Sky Targeted Eight GHz Survey (CRATES) flat-spectrum catalog (Healey et al., 2007). Flat spectra are often associated with emission from compact cores and can be used for identifying blazar candidates. A fit to the data shown in Fig. 6.9 gives an index $\alpha = 0.035 \pm 0.034$ with $\chi^2 = 3.6$ for 3 DOF, which is consistent with a flat spectrum. However, the rise in the spectrum suggested by the ACT data is perhaps in tension with the slight negative index between 843 MHz and 4.85 GHz. Measurements in the 10 GHz to 100 GHz range would be useful.

6.3.2 An Infrared Point Source Near ACT-CL J0509−5345?

The bright spot near north of ACT-CL J0509−5345 (c.f. Fig. 6.2) is of interest because it also appears in the South Pole Telescope map of the same cluster, SPT-CL 0509−5342 (Staniszewski et al., 2008), but does not appear in any catalogs available to NED.

To investigate, we made maps in all three frequencies of this source. To achieve maps as clean as possible, we reduced the mapmaking knot spacing to $\tau = 0.25$ s, and for the 218 GHz and 277 GHz maps, used a quadratic curve for stripe-removal instead of a straight line. The maps are 0.3° in radius, and a $4'$ mask was used during stripe-removal. Fig. 6.10 shows maps for all three arrays.

Bright spots appear in all three maps near the same position, but there are clear offsets between them that are larger than the pointing uncertainties (c.f. §6.1.3), especially in the 218 GHz map. We

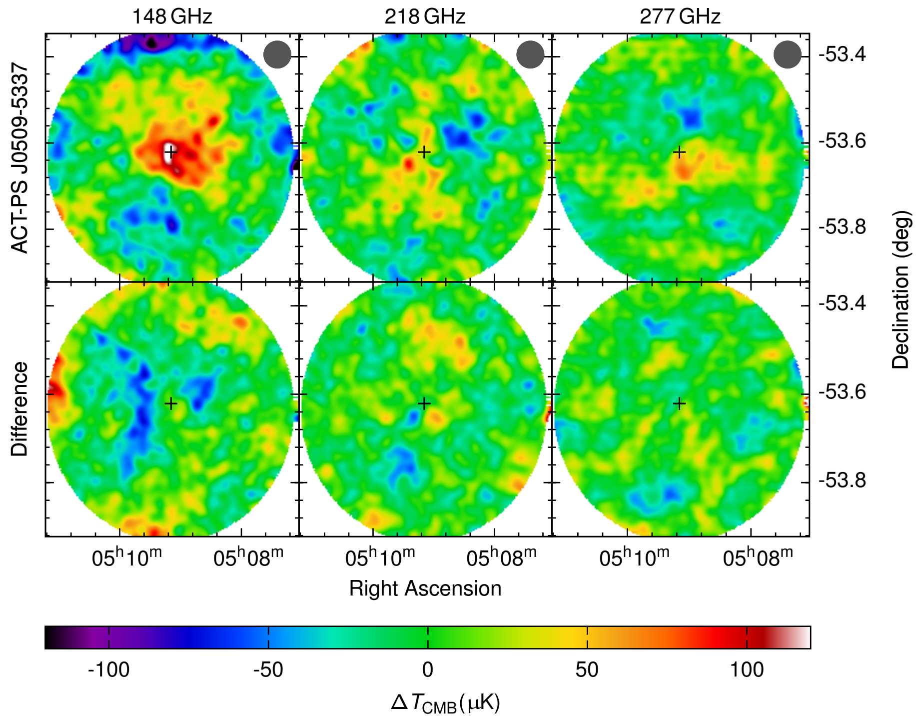

Figure 6.10: Maps and companion difference maps of ACT-PS J0509-5337 in all three frequencies. The offset in the location of the brightest points in these maps is still not fully understood, but is likely due to noise in the 218 GHz and 277 GHz maps. See text for more discussion.

have carefully checked the pointing of all three arrays using the other bright point sources, as already described, so these offsets cannot be explained by a pointing error. It is also notable that the difference map has a dark spot near the location of the bright spot in the signal map of 218 GHz.

It is possible that this is not a point source. It could be an large, compact hot spot in the primary CMB, which is still below the noise level of the 218 GHz and 277 GHz frequencies. Less likely is that it is a point source with a very steep, negative spectral index and only has large flux at 148 GHz. For the rest of this section, however, we assume that there is a single point source that appears in all the maps. The offsets might be explained by high noise in 148 GHz and 218 GHz. This is somewhat plausible, as straight-line stripe-removal still left the maps very noisy, necessitating the use of a quadratic-curve stripe-removal. The residual striping could have smeared out the signal and caused the peak to be offset from the true position.

We take the brightest point in the 2′ FWHM Gaussian-smoothed 148 GHz map as the center of the point source, which has right ascension of $05^{h}09^{m}13^{s}$ and declination $-53°37'39''$, and tentatively designate it ACT-PS J0509$-$5337. However, in the flux measurements described below, we use the brightest points in the 218 GHz and 277 GHz maps as the centers for their respective analysis.

The raw maps are too noisy to fit an Airy pattern to the peaks as we did for the bright radio sources (§6.3.1), but if they are smoothed with a 2′ FWHM Gaussian kernel the fit becomes possible. However, the smoothing dilutes the true peak temperature, which we need to recover before converting to units of intensity. Instead of attempting to analytically calculate the effect of the convolution of the Gaussian kernel with our beam, we instead fit the peak heights of the bright sources from §6.3.1 in smoothed maps and use the ratio between the smoothed and unsmoothed heights to correct the height measured in the smoothed ACT-PS J0509−5337 map. The smoothed/unsmoothed ratios are similar for the two bright sources for 148 GHz (2% difference) and 218 GHz (5% difference), though somewhat different for 277 GHz (30% difference). We include these discrepancies as errors in the peak measurements, adding them in quadrature in the uncertainty estimation. The Airy pattern fit error was corrected in the same way: the ratio of the fit errors in the smoothed and unsmoothed maps of the bright sources allows us to estimate the unsmoothed fit error for ACT-PS J0509−5337. Otherwise, the error analysis is the same as described in §6.3.1.

Table 6.4 shows the fluxes we obtained, and they are plotted in the right panel of Fig. 6.9. The spectral index from our three data points is $\alpha = 0.8 \pm 0.3$, which would imply that, assuming it is real, it is an IR source. If this is extrapolated to lower frequencies it is not surprising that it is not found in radio catalogs: at 1 GHz, for example, it would have a flux of only (0.8 ± 1) mJy. At higher frequencies we can ask if it might have been detected by the Infrared Astronomical Satellite (IRAS). At IRAS's longest wavelength of 100 μm, the extrapolated flux is (0.4 ± 0.4) Jy, and at the shortest wavelength of 12 μm it is (2 ± 3) Jy. The upper bounds of these extrapolations are within the detection limits of the IRAS Point Source Catalog (PSC) (Beichman et al., 1988), but there are no matches to within $3'$ of our source; neither does it appear in the Faint Point Source Catalog (FSC). This might indicate that the spectrum peaks at wavelengths $\lesssim 100\,\mu$m.

We reiterate that these results are tentative and are based on the hypothesis that the bright spots in the maps from the three frequency channels (Fig. 6.10) correspond to a single source, despite apparent offsets in position. Future maps from the ACT or the SPT, which also has multi-frequency data of this sky region, could help to determine whether ACT-PS J0509-5337 is indeed a newly discovered IR galaxy.

6.4 Conclusions

After two seasons of observing with the ACT, we are now producing our first cosmological results. The experiment is working well: we have one of the largest telescopes capable of making sensitive, wide-area observations of the millimeter sky at one of the best sites in the world. Chapter 2 gave an indication of the complexity behind the experiment and showed how we met some of the key performance requirements, such as smooth motion control and high precision synchronization between data acquisition systems.

Despite the quality of our instrument, analysis of the data is challenging, due to their volume as well as the presence of noise and contamination from atmospheric emission. Much of this dissertation has been devoted to describing techniques for reducing the data that address these challenges. In Chapter 3 we looked at the lowest level of data processing in the time stream: deconvolving filters, removing common-mode detector noise, measuring detector time constants, solving for array pointing, and calibrating gains. Chapter 4 described the Cottingham Method for estimating the atmospheric signal in the data so that it might be separated from the celestial signal we aim to study. The technique, first developed more than twenty years ago, has proved successful for a modern experiment, and it is hoped that the addition of some new approaches introduced here, such as processing multiple detectors simultaneously, is an important contribution to the CMB mapmaking community.

One of the most important aspects of calibration for a CMB experiment is knowledge of the beams. They act as spatial filters on all the observations and must be deconvolved or otherwise accounted for in the maps to make precise astrophysical and cosmological measurements. In Chapter 5 we mapped the beams down to the −40 dB level. This sets a new precedent for precision beam measurements in CMB instruments. Our beam knowledge directly affects all data analysis—that presented in this thesis and that still being done.

Using the beam information and all of the data analysis tools we have just summarized, we have made some of the first maps from ACT data of galaxy clusters visible via the SZ effect, and have also had a preliminary look at radio and IR galaxies. Discovery and analysis of the clusters in particular is a major goal of the project since they hold great potential for helping us understand cosmic evolution. We have presented a group of the clusters detected in our current survey maps. Many in our selection had been previously discovered in the optical, allowing us to confirm the reality of our detections. Initial comparisons of the size of our SZ decrements with values predicted from X-ray observations are favorable. At the same time, apparent discrepancies between our measurements and others demonstrate the need for further analysis and the importance that follow-up X-ray and optical observations for joint analysis will play.

In addition to the known clusters that we have detected, we also introduced two previously undetected cluster candidates. For one of them, we were able to make preliminary maps in all three of the ACT frequency bands that showed the characteristic SZ spectrum. It is reasonable to say that the ACT is beginning to meet its full potential, and the work in this dissertation shows that a large catalog of massive galaxies at a wide range of redshifts is within our reach.

Bibliography

Abell, G. O., Corwin, H. G., Jr., & Olowin, R. P. “A catalog of rich clusters of galaxies.” *ApJS*, **70**:1–138, 1989.

Aboobaker, A. M. *A new millimeter-wave camera for CMB observations*. Ph.D. thesis, Princeton University, United States, 2006.

Abramowitz, M. & Stegun, I. A., eds. *Handbook of Mathematical Functions with Formulas, Graphs and Mathematical Tables*. National Bureau of Standards, 1964.

Alpher, R. A. & Herman, R. “Evolution of the Universe.” *Nature*, **162**:774–775, 1948.

Andreani, P., Boehringer, H., Dall’Oglio, G., Martinis, L., Shaver, P., Lemke, R., -\AA. Nyman, L., Booth, R., Pizzo, L., Whyborn, N., Tanaka, Y., & Liang, H. “The enhancement and decrement of the Sunyaev-Zeldovich effect towards the ROSAT Cluster RXJ0658-5557.” *ArXiv Astrophysics e-prints*, 1998. (arXiv:astro-ph/9811093)

Bahcall, N. A., Ostriker, J. P., Perlmutter, S., & Steinhardt, P. J. “The Cosmic Triangle: Revealing the State of the Universe.” *Science*, **284**:1481–+, 1999. (arXiv:astro-ph/9906463)

Battistelli, E. S., Amiri, M., Burger, B., Devlin, M. J., Dicker, S. R., Doriese, W. B., Dünner, R., Fisher, R. P., Fowler, J. W., Halpern, M., Hasselfield, M., Hilton, G. C., Hincks, A. D., Irwin, K. D., Kaul, M., Klein, J., Knotek, S., Lau, J. M., Limon, M., Marriage, T. A., Niemack, M. D., Page, L., Reintsema, C. D., Staggs, S. T., Swetz, D. S., Switzer, E. R., Thornton, R. J., & Zhao, Y. “Automated SQUID tuning procedure for kilo-pixel arrays of TES bolometers on the Atacama Cosmology Telescope.” In W. D. Duncan, W. S. Holland, S. Withington, & J. Zmuidzinas, eds., “Proc. SPIE,” volume 7020, p. 702028. SPIE, 2008a.

Battistelli, E. S., Amiri, M., Burger, B., Halpern, M., Knotek, S., Ellis, M., Gao, X., Kelly, D., MacIntosh, M., Irwin, K., & Reintsema, C. “Functional description of read-out electronics for time-domain multiplexed bolometers for millimeter and sub-millimeter astronomy.” *J. Low Temp. Phys.*, **151** (3-4):908–914, 2008b.

Beichman, C. A., Neugebauer, G., Habing, H. J., Clegg, P. E., & Chester, T. J., eds. *Infrared astronomical satellite (IRAS) catalogs and atlases. Volume 1: Explanatory supplement*, volume 1. 1988.

Bennett, C. L., Banday, A. J., Gorski, K. M., Hinshaw, G., Jackson, P., Keegstra, P., Kogut, A., Smoot, G. F., Wilkinson, D. T., & Wright, E. L. “Four-Year COBE DMR Cosmic Microwave Background Observations: Maps and Basic Results.” *ApJ*, **464**:L1+, 1996. (arXiv:astro-ph/9601067)

Bennett, C. L., Halpern, M., Hinshaw, G., Jarosik, N., Kogut, A., Limon, M., Meyer, S. S., Page, L., Spergel, D. N., Tucker, G. S., Wollack, E., Wright, E. L., Barnes, C., Greason, M. R., Hill, R. S., Komatsu, E., Nolta, M. R., Odegard, N., Peiris, H. V., Verde, L., & Weiland, J. L. “First-Year Wilkinson Microwave Anisotropy Probe (WMAP) Observations: Preliminary Maps and Basic Results.” *ApJS*, **148**:1–27, 2003. (arXiv:astro-ph/0302207)

Benoît, A., Ade, P., Amblard, A., Ansari, R., Aubourg, É., Bargot, S., Bartlett, J. G., Bernard, J.-P., Bhatia, R. S., Blanchard, A., Bock, J. J., Boscaleri, A., Bouchet, F. R., Bourrachot, A., Camus, P., Couchot, F., de Bernardis, P., Delabrouille, J., Désert, F.-X., Doré, O., Douspis, M., Dumoulin, L., Dupac, X., Filliatre, P., Fosalba, P., Ganga, K., Gannaway, F., Gautier, B., Giard, M., Giraud-Héraud, Y., Gispert, R., Guglielmi, L., Hamilton, J.-C., Hanany, S., Henrot-Versillé, S., Kaplan, J., Lagache, G., Lamarre, J.-M., Lange, A. E., Macías-Pérez, J. F., Madet, K., Maffei, B., Magneville, C., Marrone, D. P., Masi, S., Mayet, F., Murphy, A., Naraghi, F., Nati, F., Patanchon, G., Perrin, G., Piat, M., Ponthieu, N., Prunet, S., Puget, J.-L., Renault, C., Rosset, C., Santos, D., Starobinsky, A., Strukov, I., Sudiwala, R. V., Teyssier, R., Tristram, M., Tucker, C., Vanel, J.-C., Vibert, D., Wakui, E., & Yvon, D. "The cosmic microwave background anisotropy power spectrum measured by Archeops." *A&A*, **399**:L19–L23, 2003. (arXiv:astro-ph/0210305)

Benson, B. A., Church, S. E., Ade, P. A. R., Bock, J. J., Ganga, K. M., Henson, C. N., & Thompson, K. L. "Measurements of Sunyaev-Zel'dovich Effect Scaling Relations for Clusters of Galaxies." *ApJ*, **617**:829–846, 2004. (arXiv:astro-ph/0404391)

Benson, B. A., Church, S. E., Ade, P. A. R., Bock, J. J., Ganga, K. M., Hinderks, J. R., Mauskopf, P. D., Philhour, B., Runyan, M. C., & Thompson, K. L. "Peculiar Velocity Limits from Measurements of the Spectrum of the Sunyaev-Zeldovich Effect in Six Clusters of Galaxies." *ApJ*, **592**:674–691, 2003. (arXiv:astro-ph/0303510)

Bertin, E. & Arnouts, S. "SExtractor: Software for source extraction." *A&AS*, **117**:393–404, 1996.

Birkinshaw, M. "The Sunyaev-Zel'dovich effect." *Phys. Rep.*, **310**:97–195, 1999. (arXiv:astro-ph/9808050)

Birkinshaw, M., Hughes, J. P., & Arnaud, K. A. "A measurement of the value of the Hubble constant from the X-ray properties and the Sunyaev-Zel'dovich effect of Abell 665." *ApJ*, **379**:466–481, 1991.

Blanchard, A. & Schneider, J. "Gravitational lensing effect on the fluctuations of the cosmic background radiation." *A&A*, **184**:1–2, 1987.

Bode, P., Ostriker, J. P., & Vikhlinin, A. "Exploring the Energetics of Intracluster Gas with a Simple and Accurate Model." *ApJ*, **700**:989–999, 2009. (arXiv:0905.3748)

Böhringer, H., Schuecker, P., Guzzo, L., Collins, C. A., Voges, W., Cruddace, R. G., Ortiz-Gil, A., Chincarini, G., De Grandi, S., Edge, A. C., MacGillivray, H. T., Neumann, D. M., Schindler, S., & Shaver, P. "The ROSAT-ESO Flux Limited X-ray (REFLEX) Galaxy cluster survey. V. The cluster catalogue." *A&A*, **425**:367–383, 2004. (arXiv:astro-ph/0405546)

Bojanov, B. D., Hakopian, H. A., & Sahakian, A. A. *Spline Functions and Multivariate Interpolations*. Kluwer Academic Publishers, 1993.

Bonamente, M., Joy, M., LaRoque, S. J., Carlstrom, J. E., Nagai, D., & Marrone, D. P. "Scaling Relations from Sunyaev-Zel'dovich Effect and Chandra X-Ray Measurements of High-Redshift Galaxy Clusters." *ApJ*, **675**:106–114, 2008. (arXiv:0708.0815)

Bonamente, M., Joy, M. K., LaRoque, S. J., Carlstrom, J. E., Reese, E. D., & Dawson, K. S. "Determination of the Cosmic Distance Scale from Sunyaev-Zel'dovich Effect and Chandra X-Ray Measurements of High-Redshift Galaxy Clusters." *ApJ*, **647**:25–54, 2006. (arXiv:astro-ph/0512349)

Bond, J. R. "Theory and Observations of the Cosmic Background Radiation." In R. Schaeffer, J. Silk, M. Spiro, & J. Zinn-Justin, eds., "Cosmology and Large Scale Structure," pp. 469–+. 1996.

Borgani, S. & Kravtsov, A. "Cosmological simulations of galaxy clusters." *ArXiv e-prints*, 2009. (arXiv:0906.4370)

Born, M. & Wolf, E. *Principles of Optics*. Cambridge University Press, 7th (expanded) edition, 1999.

Boughn, S. P., Cheng, E. S., Cottingham, D. A., & Fixsen, D. J. "Limits of Gaussian fluctuations in the cosmic microwave background at 19.2 GHz." *ApJ*, **391**:L49–L52, 1992.

Brown, M. L., Ade, P., Bock, J., Bowden, M., Cahill, G., Castro, P. G., Church, S., Culverhouse, T., Friedman, R. B., Ganga, K., Gear, W. K., Gupta, S., Hinderks, J., Kovac, J., Lange, A. E., Leitch, E., Melhuish, S. J., Memari, Y., Murphy, J. A., Orlando, A., O'Sullivan, C., Piccirillo, L., Pryke, C., Rajguru, N., Rusholme, B., Schwarz, R., Taylor, A. N., Thompson, K. L., Turner, A. H., Wu, E. Y. S., & Zemcov, M. "Improved measurements of the temperature and polarization of the CMB from QUaD." *ArXiv e-prints*, 2009. (arXiv:0906.1003)

Burigana, C., Malaspina, M., Mandolesi, N., Danse, L., Maino, D., Bersanelli, M., & Maltoni, M. "A preliminary study on destriping techniques of PLANCK/LFI measurements versus observational strategy." *ArXiv Astrophysics e-prints*, 1999. (arXiv:astro-ph/9906360)

Carlstrom, J. E., Holder, G. P., & Reese, E. D. "Cosmology with the Sunyaev-Zel'dovich Effect." *ARA&A*, **40**:643–680, 2002. (arXiv:astro-ph/0208192)

Cavaliere, A. & Fusco-Femiano, R. "The Distribution of Hot Gas in Clusters of Galaxies." *A&A*, **70**:677–+, 1978.

Clowe, D., Randall, S. W., & Markevitch, M. "Catching a bullet: direct evidence for the existence of dark matter." *Nuclear Physics B Proceedings Supplements*, **173**:28–31, 2007. (arXiv:astro-ph/0611496)

Cottingham, D. A. *A Sky Temperature Survey at 19.2 GHz Using a Balloon Borne Dicke Radiometer for Anisotropy Tests of the Cosmic Microwave Background*. Ph.D. thesis, Princeton University, United States, 1987.

Dallacasa, D., Stanghellini, C., Centonza, M., & Furnari, G. "High frequency peakers." *New Astronomy Review*, **46**:299–302, 2002.

Das, S. *Astrophysical uses of CMB lensing*. Ph.D. thesis, Princeton University, United States, 2008.

Dawson, K. S., Holzapfel, W. L., Carlstrom, J. E., Joy, M., LaRoque, S. J., & Reese, E. D. "A Preliminary Detection of Arcminute-Scale Cosmic Microwave Background Anisotropy with the BIMA Array." *ApJ*, **553**:L1–L4, 2001. (arXiv:astro-ph/0012151)

de Boor, C. *A Practical Guide to Splines*. Springer, revised edition, 2001.

de Grandi, S., Böhringer, H., Guzzo, L., Molendi, S., Chincarini, G., Collins, C., Cruddace, R., Neumann, D., Schindler, S., Schuecker, P., & Voges, W. "A Flux-limited Sample of Bright Clusters of Galaxies from the Southern Part of the ROSAT All-Sky Survey: The Catalog and LOG N-LOG S." *ApJ*, **514**:148–163, 1999. (arXiv:astro-ph/9902067)

Delabrouille, J. "Analysis of the accuracy of a destriping method for future cosmic microwave background mapping with the PLANCK SURVEYOR satellite." *A&AS*, **127**:555–567, 1998.

Dicke, R. H., Peebles, P. J. E., Roll, P. G., & Wilkinson, D. T. "Cosmic Black-Body Radiation." *ApJ*, **142**:414–419, 1965.

Dickinson, C., Battye, R. A., Carreira, P., Cleary, K., Davies, R. D., Davis, R. J., Genova-Santos, R., Grainge, K., Gutiérrez, C. M., Hafez, Y. A., Hobson, M. P., Jones, M. E., Kneissl, R., Lancaster, K., Lasenby, A., Leahy, J. P., Maisinger, K., Ödman, C., Pooley, G., Rajguru, N., Rebolo, R., Rubiño-Martin, J. A., Saunders, R. D. E., Savage, R. S., Scaife, A., Scott, P. F., Slosar, A., Sosa Molina, P., Taylor, A. C., Titterington, D., Waldram, E., Watson, R. A., & Wilkinson, A. "High-sensitivity measurements of the cosmic microwave background power spectrum with the extended Very Small Array." *MNRAS*, **353**:732–746, 2004. (arXiv:astro-ph/0402498)

Edge, A. C., Boehringer, H., Guzzo, L., Collins, C. A., Neumann, D., Chincarini, G., de Grandi, S., Duemmler, R., Ebeling, H., Schindler, S., Seitter, W., Vettolani, P., Briel, U., Cruddace, R., Gruber, R., Gursky, H., Hartner, G., MacGillivray, H. T., Schuecker, P., Shaver, P., Voges, W., Wallin, J., Wolter, A., & Zamorani, G. "A giant arc in a ROSAT-detected cluster of galaxies." *A&A*, **289**:L34–L36, 1994. (arXiv:astro-ph/9407078)

Ettori, S., Dolag, K., Borgani, S., & Murante, G. "The baryon fraction in hydrodynamical simulations of galaxy clusters." *MNRAS*, **365**:1021–1030, 2006. (arXiv:astro-ph/0509024)

Ettori, S., Morandi, A., Tozzi, P., Balestra, I., Borgani, S., Rosati, P., Lovisari, L., & Terenziani, F. "The cluster gas mass fraction as a cosmological probe: a revised study." *ArXiv e-prints*, 2009. (arXiv:0904.2740)

Fowler, J. W. "A Simple, Constant Pointing Model for ACT.", 2007. Internal ACT Memo

Fowler, J. W., Niemack, M. D., Dicker, S. R., Aboobaker, A. M., Ade, P. A. R., Battistelli, E. S., Devlin, M. J., Fisher, R. P., Halpern, M., Hargrave, P. C., Hincks, A. D., Kaul, M., Klein, J., Lau, J. M., Limon, M., Marriage, T. A., Mauskopf, P. D., Page, L., Staggs, S. T., Swetz, D. S., Switzer, E. R., Thornton, R. J., & Tucker, C. E. "Optical design of the Atacama Cosmology Telescope and the Millimeter Bolometric Array Camera." *Appl. Opt.*, **46** (17):3444–3454, 2007.

Fukazawa, Y., Makishima, K., & Ohashi, T. "ASCA Compilation of X-Ray Properties of Hot Gas in Elliptical Galaxies and Galaxy Clusters: Two Breaks in the Temperature Dependences." *PASJ*, **56**:965–1009, 2004. (arXiv:astro-ph/0411745)

Funke, J. "ACT 6 Meter Radiotelescope [sic] Application Manual.", 2007. Internal ACT Memo

Ganga, K., Cheng, E., Meyer, S., & Page, L. "Cross-correlation between the 170 GHz survey map and the COBE differential microwave radiometer first-year maps." *ApJ*, **410**:L57–L60, 1993.

Goldstein, J. H., Ade, P. A. R., Bock, J. J., Bond, J. R., Cantalupo, C., Contaldi, C. R., Daub, M. D., Holzapfel, W. L., Kuo, C., Lange, A. E., Lueker, M., Newcomb, M., Peterson, J. B., Pogosyan, D., Ruhl, J. E., Runyan, M. C., & Torbet, E. "Estimates of Cosmological Parameters Using the Cosmic Microwave Background Angular Power Spectrum of ACBAR." *ApJ*, **599**:773–785, 2003. (arXiv:astro-ph/0212517)

Gomez, P., Romer, A. K., Peterson, J. B., Chase, W., Runyan, M., Holzapfel, W., Kuo, C. L., Newcomb, M., Ruhl, J., Goldstein, J., & Lange, A. "Sunyaev-Zeldovich Observations of Massive Clusters of Galaxies." In G. Bertin, D. Farina, & R. Pozzoli, eds., "Plasmas in the Laboratory and in the Universe: New Insights and New Challenges," volume 703 of *American Institute of Physics Conference Series*, pp. 361–366. 2004.

Guzzo, L., Böhringer, H., Schuecker, P., Collins, C. A., Schindler, S., Neumann, D. M., de Grandi, S., Cruddace, R., Chincarini, G., Edge, A. C., Shaver, P. A., & Voges, W. "The REFLEX cluster survey: observing strategy and first results on large-scale structure." *The Messenger*, **95**:27–32, 1999. (arXiv:astro-ph/9903396)

Hallman, E. J., Burns, J. O., Motl, P. M., & Norman, M. L. "The β-Model Problem: The Incompatibility of X-Ray and Sunyaev-Zeldovich Effect Model Fitting for Galaxy Clusters." *ApJ*, **665**:911–920, 2007. (arXiv:0705.0531)

Halverson, N. W., Lanting, T., Ade, P. A. R., Basu, K., Bender, A. N., Benson, B. A., Bertoldi, F., Cho, H. ., Chon, G., Clarke, J., Dobbs, M., Ferrusca, D., Guesten, R., Holzapfel, W. L., Kovacs, A., Kennedy, J., Kermish, Z., Kneissl, R., Lee, A. T., Lueker, M., Mehl, J., Menten, K. M., Muders, D., Nord, M., Pacaud, F., Plagge, T., Reichardt, C., Richards, P. L., Schaaf, R., Schilke, P., Schuller, F., Schwan, D., Spieler, H., Tucker, C., Weiss, A., & Zahn, O. "Sunyaev-Zel'dovich Effect Observations of the Bullet Cluster (1E 0657-56) with APEX-SZ." *ArXiv e-prints*, 2008a. (arXiv:0807.4208)

Halverson, N. W., Lanting, T., Ade, P. A. R., Basu, K., Bender, A. N., Benson, B. A., Bertoldi, F., Cho, H. ., Chon, G., Clarke, J., Dobbs, M., Ferrusca, D., Guesten, R., Holzapfel, W. L., Kovacs, A., Kennedy, J., Kermish, Z., Kneissl, R., Lee, A. T., Lueker, M., Mehl, J., Menten, K. M., Muders, D., Nord, M., Pacaud, F., Plagge, T., Reichardt, C., Richards, P. L., Schaaf, R., Schilke, P., Schuller, F., Schwan, D., Spieler, H., Tucker, C., Weiss, A., & Zahn, O. "Sunyaev-Zel'dovich Effect Observations of the Bullet Cluster (1E 0657-56) with APEX-SZ." *ArXiv e-prints*, 2008b. (arXiv:0807.4208)

Halverson, N. W., Leitch, E. M., Pryke, C., Kovac, J., Carlstrom, J. E., Holzapfel, W. L., Dragovan, M., Cartwright, J. K., Mason, B. S., Padin, S., Pearson, T. J., Readhead, A. C. S., & Shepherd, M. C. "Degree Angular Scale Interferometer First Results: A Measurement of the Cosmic Microwave Background Angular Power Spectrum." *ApJ*, **568**:38–45, 2002. (arXiv:astro-ph/0104489)

Hanany, S., Ade, P., Balbi, A., Bock, J., Borrill, J., Boscaleri, A., de Bernardis, P., Ferreira, P. G., Hristov, V. V., Jaffe, A. H., Lange, A. E., Lee, A. T., Mauskopf, P. D., Netterfield, C. B., Oh, S., Pascale, E., Rabii, B., Richards, P. L., Smoot, G. F., Stompor, R., Winant, C. D., & Wu, J. H. P. "MAXIMA-1: A Measurement of the Cosmic Microwave Background Anisotropy on Angular Scales of $10' - 5^\circ$." *ApJ*, **545**:L5–L9, 2000. (arXiv:astro-ph/0005123)

Hancock, P. J. "High frequency GPS sources in the AT20G survey." *Astronomische Nachrichten*, **330**:180–+, 2009. (arXiv:0901.4592)

Healey, S. E., Romani, R. W., Taylor, G. B., Sadler, E. M., Ricci, R., Murphy, T., Ulvestad, J. S., & Winn, J. N. "CRATES: An All-Sky Survey of Flat-Spectrum Radio Sources." *ApJS*, **171**:61–71, 2007. (arXiv:astro-ph/0702346)

Hincks, A. D. "Characterising Transition Edge Sensors for the Atacama Cosmology Telescope.", 2005. Princeton Doctoral Experimental Project Summary

Hincks, A. D., Acquaviva, V., Ade, P., Aguirre, P., Amiri, M., Appel, J. W., Barrientos, L. F., Battistelli, E. S., Bond, J. R., Brown, B., Burger, B., Chervenak, J., Das, S., Devlin, M. J., Dicker, S., Doriese, W. B., Dunkley, J., Dünner, R., Essinger-Hileman, T., Fisher, R. P., Fowler, J. W., Hajian, A., Halpern, M., Hasselfield, M., Hernández-Monteagudo, C., Hilton, G. C., Hilton, M., Hlozek, R., Huffenberger, K., Hughes, D., Hughes, J. P., Infante, L., Irwin, K. D., Jimenez, R., Juin, J. B., Kaul, M., Klein, J., Kosowsky, A., Lau, J. M., Limon, M., Lin, Y. ., Lupton, R. H., Marriage, T., Marsden, D., Martocci, K., Mauskopf, P., Menanteau, F., Moodley, K., Moseley, H., Netterfield, C. B., Niemack, M. D., Nolta, M. R., Page, L. A., Parker, L., Partridge, B., Quintana, H., Reid, B., Sehgal, N., Sievers, J., Spergel, D. N., Staggs, S. T., Stryzak, O., Swetz, D., Switzer, E., Thornton, R., Trac, H., Tucker, C., Verde, L., Warne, R., Wilson, G., Wollack, E., & Zhao, Y. "The Atacama Cosmology Telescope (ACT): Beam Profiles and First SZ Cluster Maps." *ArXiv e-prints*, 2009. (arXiv:0907.0461)

Hincks, A. D., Ade, P. A. R., Allen, C., Amiri, M., Appel, J. W., Battistelli, E. S., Burger, B., Chervenak, J. A., Dahlen, A. J., Denny, S., Devlin, M. J., Dicker, S. R., Doriese, W. B., Dünner, R., Essinger-Hileman, T., Fisher, R. P., Fowler, J. W., Halpern, M., Hargrave, P. C., Hasselfield, M., Hilton, G. C., Irwin, K. D., Jarosik, N., Kaul, M., Klein, J., Lau, J. M., Limon, M., Lupton, R. H., Marriage, T. A., Martocci, K. L., Mauskopf, P., Moseley, S. H., Netterfield, C. B., Niemack, M. D., Nolta, M. R., Page, L., Parker, L. P., Sederberg, A. J., Staggs, S. T., Stryzak, O. R., Swetz, D. S., Switzer, E. R., Thornton, R. J., Tucker, C., Wollack, E. J., & Zhao, Y. "The effects of the mechanical performance and alignment of the Atacama Cosmology Telescope on the sensitivity of microwave observations." In W. D. Duncan, W. S. Holland, S. Withington, & J. Zmuidzinas, eds., "Proc. SPIE," volume 7020, p. 70201P. SPIE, 2008.

Hinshaw, G., Weiland, J. L., Hill, R. S., Odegard, N., Larson, D., Bennett, C. L., Dunkley, J., Gold, B., Greason, M. R., Jarosik, N., Komatsu, E., Nolta, M. R., Page, L., Spergel, D. N., Wollack, E., Halpern, M., Kogut, A., Limon, M., Meyer, S. S., Tucker, G. S., & Wright, E. L. "Five-Year Wilkinson Microwave Anisotropy Probe Observations: Data Processing, Sky Maps, and Basic Results." *ApJS*, **180**:225–245, 2009. (arXiv:0803.0732)

Holder, G. P. & Carlstrom, J. E. "Understanding Cluster Gas Evolution and Fine-Scale Cosmic Microwave Background Anisotropy with Deep Sunyaev-Zeldovich Effect Surveys." *ApJ*, **558**:515–519, 2001. (arXiv:astro-ph/0105229)

Holzapfel, W. L., Ade, P. A. R., Church, S. E., Mauskopf, P. D., Rephaeli, Y., Wilbanks, T. M., & Lange, A. E. "Limits on the Peculiar Velocities of Two Distant Clusters Using the Kinematic Sunyaev-Zeldovich Effect." *ApJ*, **481**:35–+, 1997. (arXiv:astro-ph/9702223)

Huffenberger, K. M. & Seljak, U. "Prospects for ACT: Simulations, power spectrum, and non-Gaussian analysis." *New Astronomy*, **10**:491–515, 2005. (arXiv:astro-ph/0408066)

Hughes, J. P., Menanteau, F., Sehgal, N., Infante, L., & Barrientos, F. "X-ray Clusters in the ACT Strip." In "Bulletin of the American Astronomical Society," volume 41 of *Bulletin of the American Astronomical Society*, pp. 336–+. 2009.

Irwin, K. D. & Hilton, G. C. *Transition-Edge Sensors*. Springer, 2005.

Itoh, N., Kohyama, Y., & Nozawa, S. "Relativistic Corrections to the Sunyaev-Zeldovich Effect for Clusters of Galaxies." *ApJ*, **502**:7–+, 1998. (arXiv:astro-ph/9712289)

Itoh, N. & Nozawa, S. "Relativistic corrections to the Sunyaev-Zeldovich effect for extremely hot clusters of galaxies." *A&A*, **417**:827–832, 2004.

Joye, W. A. & Mandel, E. "New Features of SAOImage DS9." In H. E. Payne, R. I. Jedrzejewski, & R. N. Hook, eds., "Astronomical Data Analysis Software and Systems XII," volume 295 of *Astronomical Society of the Pacific Conference Series*, pp. 489–+. 2003.

Kashlinsky, A., Atrio-Barandela, F., Kocevski, D., & Ebeling, H. "A Measurement of Large-Scale Peculiar Velocities of Clusters of Galaxies: Results and Cosmological Implications." *ApJ*, **686**:L49–L52, 2008. (arXiv:0809.3734)

Keihänen, E., Kurki-Suonio, H., & Poutanen, T. "MADAM- a map-making method for CMB experiments." *MNRAS*, **360**:390–400, 2005. (arXiv:astro-ph/0412517)

Keihänen, E., Kurki-Suonio, H., Poutanen, T., Maino, D., & Burigana, C. "A maximum likelihood approach to the destriping technique." *A&A*, **428**:287–298, 2004. (arXiv:astro-ph/0304411)

Komatsu, E. & Seljak, U. "Universal gas density and temperature profile." *MNRAS*, **327**:1353–1366, 2001. (arXiv:astro-ph/0106151)

Komatsu, E. & Seljak, U. “The Sunyaev-Zel’dovich angular power spectrum as a probe of cosmological parameters.” *MNRAS*, **336**:1256–1270, 2002. (arXiv:astro-ph/0205468)

Kosowsky, A. & Turner, M. S. “CBR anisotropy and the running of the scalar spectral index.” *Phys. Rev. D*, **52**:1739–+, 1995. (arXiv:astro-ph/9504071)

Labiano, A., Barthel, P. D., O’Dea, C. P., de Vries, W. H., Pérez, I., & Baum, S. A. “GPS radio sources: new optical observations and an updated master list.” *A&A*, **463**:97–104, 2007. (arXiv:astro-ph/0611600)

LaRoque, S. J., Bonamente, M., Carlstrom, J. E., Joy, M. K., Nagai, D., Reese, E. D., & Dawson, K. S. “X-Ray and Sunyaev-Zel’dovich Effect Measurements of the Gas Mass Fraction in Galaxy Clusters.” *ApJ*, **652**:917–936, 2006. (arXiv:astro-ph/0604039)

LaRoque, S. J., Carlstrom, J. E., Reese, E. D., Holder, G. P., Holzapfel, W. L., Joy, M., & Grego, L. “The Sunyaev-Zel’dovich Effect Spectrum of Abell 2163.” *ArXiv Astrophysics e-prints*, 2002. (arXiv:astro-ph/0204134)

Lau, J., Benna, M., Devlin, M., Dicker, S., & Page, L. “”experimental tests and modeling of the optimal orifice size for a closed cycle 4he sorption refrigerator”.” *”Cryogenics”*, **46** (1):”809–814”, 2006a.

Lau, J., Fowler, J., Marriage, T., Page, L., Leong, J., Wishnow, E., Henry, R., Wollack, E., Halpern, M., Marsden, D., & Marsden, G. “Millimeter-wave antireflection coating for cryogenic silicon lenses.” *Appl. Opt.*, **45**:3746–3751, 2006b. (arXiv:astro-ph/0701091)

Lau, J. M. *CCAM: A Novel Millimeter-Wave Instrument Using A Close-Packed TES Bolometer Array*. Ph.D. thesis, Princeton University, United States, 2007.

Lewis, A. & Challinor, A. “Weak gravitational lensing of the CMB.” *Phys. Rep.*, **429**:1–65, 2006. (arXiv:astro-ph/0601594)

Lewis, A., Challinor, A., & Lasenby, A. “Efficient Computation of Cosmic Microwave Background Anisotropies in Closed Friedmann-Robertson-Walker Models.” *ApJ*, **538**:473–476, 2000. (arXiv:astro-ph/9911177)

Maino, D., Burigana, C., Górski, K. M., Mandolesi, N., & Bersanelli, M. “Removing 1/f noise stripes in cosmic microwave background anisotropy observations.” *A&A*, **387**:356–365, 2002. (arXiv:astro-ph/0202271)

Markevitch, M. “Chandra Observation of the Most Interesting Cluster in the Universe.” In A. Wilson, ed., “The X-ray Universe 2005,” volume 604 of *ESA Special Publication*, pp. 723–+. 2006.

Markevitch, M., Gonzalez, A. H., David, L., Vikhlinin, A., Murray, S., Forman, W., Jones, C., & Tucker, W. “A Textbook Example of a Bow Shock in the Merging Galaxy Cluster 1E 0657-56.” *ApJ*, **567**:L27–L31, 2002. (arXiv:astro-ph/0110468)

Marriage, T. A. *Detectors for the Atacama Cosmology Telescope*. Ph.D. thesis, Princeton University, United States, 2006.

Marriage, T. A., Chervenak, J. A., & Doriese, W. B. “Testing and assembly of the detectors for the Millimeter Bolometric Array Camera on ACT.” *Nuc Inst & Meth. in Phys Res A*, **559**:551–553, 2006.

Mason, B. S., Pearson, T. J., Readhead, A. C. S., Shepherd, M. C., Sievers, J., Udomprasert, P. S., Cartwright, J. K., Farmer, A. J., Padin, S., Myers, S. T., Bond, J. R., Contaldi, C. R., Pen, U., Prunet, S., Pogosyan, D., Carlstrom, J. E., Kovac, J., Leitch, E. M., Pryke, C., Halverson, N. W., Holzapfel, W. L., Altamirano, P., Bronfman, L., Casassus, S., May, J., & Joy, M. "The Anisotropy of the Microwave Background to l = 3500: Deep Field Observations with the Cosmic Background Imager." *ApJ*, **591**:540–555, 2003. (arXiv:astro-ph/0205384)

Massardi, M., Ekers, R. D., Murphy, T., Ricci, R., Sadler, E. M., Burke, S., de Zotti, G., Edwards, P. G., Hancock, P. J., Jackson, C. A., Kesteven, M. J., Mahony, E., Phillips, C. J., Staveley-Smith, L., Subrahmanyan, R., Walker, M. A., & Wilson, W. E. "The Australia Telescope 20-GHz (AT20G) Survey: the Bright Source Sample." *MNRAS*, **384**:775–802, 2008. (arXiv:0709.3485)

Mather, J. C., Cheng, E. S., Eplee, R. E., Jr., Isaacman, R. B., Meyer, S. S., Shafer, R. A., Weiss, R., Wright, E. L., Bennett, C. L., Boggess, N. W., Dwek, E., Gulkis, S., Hauser, M. G., Janssen, M., Kelsall, T., Lubin, P. M., Moseley, S. H., Jr., Murdock, T. L., Silverberg, R. F., Smoot, G. F., & Wilkinson, D. T. "A preliminary measurement of the cosmic microwave background spectrum by the Cosmic Background Explorer (COBE) satellite." *ApJ*, **354**:L37–L40, 1990.

Mather, J. C., Fixsen, D. J., Shafer, R. A., Mosier, C., & Wilkinson, D. T. "Calibrator Design for the COBE Far-Infrared Absolute Spectrophotometer (FIRAS)." *ApJ*, **512**:511–520, 1999. (arXiv:astro-ph/9810373)

Matthews, J. & Walker, R. L. *Mathematical Methods of Physics*. Addison Wesley, 1965.

Mauch, T., Murphy, T., Buttery, H. J., Curran, J., Hunstead, R. W., Piestrzynski, B., Robertson, J. G., & Sadler, E. M. "SUMSS: a wide-field radio imaging survey of the southern sky - II. The source catalogue." *MNRAS*, **342**:1117–1130, 2003. (arXiv:astro-ph/0303188)

Mauskopf, P. D., Ade, P. A. R., de Bernardis, P., Bock, J. J., Borrill, J., Boscaleri, A., Crill, B. P., DeGasperis, G., De Troia, G., Farese, P., Ferreira, P. G., Ganga, K., Giacometti, M., Hanany, S., Hristov, V. V., Iacoangeli, A., Jaffe, A. H., Lange, A. E., Lee, A. T., Masi, S., Melchiorri, A., Melchiorri, F., Miglio, L., Montroy, T., Netterfield, C. B., Pascale, E., Piacentini, F., Richards, P. L., Romeo, G., Ruhl, J. E., Scannapieco, E., Scaramuzzi, F., Stompor, R., & Vittorio, N. "Measurement of a Peak in the Cosmic Microwave Background Power Spectrum from the North American Test Flight of Boomerang." *ApJ*, **536**:L59–L62, 2000. (arXiv:astro-ph/9911444)

McInnes, R. N., Menanteau, F., Heavens, A. F., Hughes, J. P., Jimenez, R., Massey, R., Simon, P., & Taylor, A. N. "First lensing measurements of SZ-discovered clusters." *ArXiv e-prints*, 2009. (arXiv:0903.4410)

Menanteau, F. & Hughes, J. P. "Physical Properties of Four SZE-Selected Galaxy Clusters in the Southern Cosmology Survey." *ApJ*, **694**:L136–L139, 2009. (arXiv:0811.3596)

Meyer, S. S., Cheng, E. S., & Page, L. A. "A measurement of the large-scale cosmic microwave background anisotropy at 1.8 millimeter wavelength." *ApJ*, **371**:L7–L9, 1991.

Miller, A., Beach, J., Bradley, S., Caldwell, R., Chapman, H., Devlin, M. J., Dorwart, W. B., Herbig, T., Jones, D., Monnelly, G., Netterfield, C. B., Nolta, M., Page, L. A., Puchalla, J., Robertson, T., Torbet, E., Tran, H. T., & Vinje, W. E. "The QMAP and MAT/TOCO Experiments for Measuring Anisotropy in the Cosmic Microwave Background." *ApJS*, **140**:115–141, 2002. (arXiv:astro-ph/0108030)

Miller, A. D., Caldwell, R., Devlin, M. J., Dorwart, W. B., Herbig, T., Nolta, M. R., Page, L. A., Puchalla, J., Torbet, E., & Tran, H. T. "A Measurement of the Angular Power Spectrum of the Cosmic Microwave Background from L = 100 to 400." *ApJ*, **524**:L1–L4, 1999. (arXiv:astro-ph/9906421)

Moodley, K., Warne, R., Goheer, N., & Trac, H. “Detection of Hot Gas in Galaxy Groups Via the Thermal Sunyaev-Zel’Dovich Effect.” *ApJ*, **697**:1392–1409, 2009. (arXiv:0809.5172)

Mroczkowski, T., Bonamente, M., Carlstrom, J. E., Culverhouse, T. L., Greer, C., Hawkins, D., Hennessy, R., Joy, M., Lamb, J. W., Leitch, E. M., Loh, M., Maughan, B., Marrone, D. P., Miller, A., Muchovej, S., Nagai, D., Pryke, C., Sharp, M., & Woody, D. “Application of a Self-Similar Pressure Profile to Sunyaev-Zel’Dovich Effect Data from Galaxy Clusters.” *ApJ*, **694**:1034–1044, 2009. (arXiv:0809.5077)

Niemack, M. D. “Measuring two-millimeter radiation with a prototype multiplexed TES receiver for ACT.” In “Society of Photo-Optical Instrumentation Engineers (SPIE) Conference Series,” volume 6275 of *Presented at the Society of Photo-Optical Instrumentation Engineers (SPIE) Conference*. 2006.

Niemack, M. D. *Towards Dark Energy: Design, Development, and Preliminary Data from ACT*. Ph.D. thesis, Princeton University, United States, 2008.

Niemack, M. D., Zhao, Y., Wollack, E., Thornton, R., Switzer, E. R., Swetz, D. S., Staggs, S. T., Page, L., Stryzak, O., Moseley, H., Marriage, T. A., Limon, M., Lau, J. M., Klein, J., Kaul, M., Jarosik, N., Irwin, K. D., Hincks, A. D., Hilton, G. C., Halpern, M., Fowler, J. W., Fisher, R. P., Dünner, R., Doriese, W. B., Dicker, S. R., Devlin, M. J., Chervenak, J., Burger, B., Battistelli, E. S., Appel, J., Amiri, M., Allen, C., & Aboobaker, A. M. “A kilopixel array of TES bolometers for ACT: Development, testing, and first light.” *J. Low Temp. Phys.*, **151** (3-4):690–696, 2008.

Nolta, M. R., Dunkley, J., Hill, R. S., Hinshaw, G., Komatsu, E., Larson, D., Page, L., Spergel, D. N., Bennett, C. L., Gold, B., Jarosik, N., Odegard, N., Weiland, J. L., Wollack, E., Halpern, M., Kogut, A., Limon, M., Meyer, S. S., Tucker, G. S., & Wright, E. L. “Five-Year Wilkinson Microwave Anisotropy Probe Observations: Angular Power Spectra.” *ApJS*, **180**:296–305, 2009. (arXiv:0803.0593)

Nozawa, S., Itoh, N., Suda, Y., & Ohhata, Y. “An improved formula for the relativistic corrections to the kinematical Sunyaev-Zeldovich effect for clusters of galaxies.” *Nuovo Cimento B Serie*, **121**:487–500, 2006. (arXiv:astro-ph/0507466)

O’Dea, C. P. & Baum, S. A. “Constraints on Radio Source Evolution from the Compact Steep Spectrum and GHz Peaked Spectrum Radio Sources.” *AJ*, **113**:148–161, 1997.

Orienti, M. “High frequency peakers.” *Astronomische Nachrichten*, **330**:167–+, 2009.

Padin, S., Cartwright, J. K., Mason, B. S., Pearson, T. J., Readhead, A. C. S., Shepherd, M. C., Sievers, J., Udomprasert, P. S., Holzapfel, W. L., Myers, S. T., Carlstrom, J. E., Leitch, E. M., Joy, M., Bronfman, L., & May, J. “First Intrinsic Anisotropy Observations with the Cosmic Background Imager.” *ApJ*, **549**:L1–L5, 2001. (arXiv:astro-ph/0012211)

Page, L. A., Cheng, E. S., & Meyer, S. S. “A large-scale cosmic microwave background anisotropy measurement at millimeter and submillimeter wavelengths.” *ApJ*, **355**:L1–L4, 1990.

Pascale, E., Ade, P. A. R., Bock, J. J., Chapin, E. L., Chung, J., Devlin, M. J., Dicker, S., Griffin, M., Gundersen, J. O., Halpern, M., Hargrave, P. C., Hughes, D. H., Klein, J., MacTavish, C. J., Marsden, G., Martin, P. G., Martin, T. G., Mauskopf, P., Netterfield, C. B., Olmi, L., Patanchon, G., Rex, M., Scott, D., Semisch, C., Thomas, N., Truch, M. D. P., Tucker, C., Tucker, G. S., Viero, M. P., & Wiebe, D. V. “The Balloon-borne Large Aperture Submillimeter Telescope: BLAST.” *ApJ*, **681**:400–414, 2008. (arXiv:0711.3465)

Patanchon, G., Ade, P. A. R., Bock, J. J., Chapin, E. L., Devlin, M. J., Dicker, S., Griffin, M., Gundersen, J. O., Halpern, M., Hargrave, P. C., Hughes, D. H., Klein, J., Marsden, G., Martin, P. G., Mauskopf, P., Netterfield, C. B., Olmi, L., Pascale, E., Rex, M., Scott, D., Semisch, C., Truch, M. D. P., Tucker, C., Tucker, G. S., Viero, M. P., & Wiebe, D. V. "SANEPIC: A Mapmaking Method for Time Stream Data from Large Arrays." *ApJ*, **681**:708–725, 2008. (arXiv:0711.3462)

Peebles, P. J. E., Page, L. A., & Partridge, R. B., eds. *Finding the Big Bang*. Cambridge University Press, 2009.

Penzias, A. A. & Wilson, R. W. "A Measurement of Excess Antenna Temperature at 4080 Mc/s." *ApJ*, **142**:419–421, 1965.

Pérez-Beaupuits, J. P., Rivera, R. C., & Nyman, L.-A. "Height and velocity of the turbulence layer at chajnantor estimated from radiometric measurements." Memo 542, Atacama Large Millimeter Array (ALMA), 2005.

Perlmutter, S., Aldering, G., Goldhaber, G., Knop, R. A., Nugent, P., Castro, P. G., Deustua, S., Fabbro, S., Goobar, A., Groom, D. E., Hook, I. M., Kim, A. G., Kim, M. Y., Lee, J. C., Nunes, N. J., Pain, R., Pennypacker, C. R., Quimby, R., Lidman, C., Ellis, R. S., Irwin, M., McMahon, R. G., Ruiz-Lapuente, P., Walton, N., Schaefer, B., Boyle, B. J., Filippenko, A. V., Matheson, T., Fruchter, A. S., Panagia, N., Newberg, H. J. M., Couch, W. J., & The Supernova Cosmology Project. "Measurements of Omega and Lambda from 42 High-Redshift Supernovae." *ApJ*, **517**:565–586, 1999. (arXiv:astro-ph/9812133)

Press, W. H. & Schechter, P. "Formation of Galaxies and Clusters of Galaxies by Self-Similar Gravitational Condensation." *ApJ*, **187**:425–438, 1974.

Press, W. H., Teukolsky, S. A., Vetterling, W. T., & Flannery, B. P. *Numerical Recipes in C: The Art of Scientific Computing*. Cambridge University Press, 2nd edition, 1992.

Pryke, C., Ade, P., Bock, J., Bowden, M., Brown, M. L., Cahill, G., Castro, P. G., Church, S., Culverhouse, T., Friedman, R., Ganga, K., Gear, W. K., Gupta, S., Hinderks, J., Kovac, J., Lange, A. E., Leitch, E., Melhuish, S. J., Memari, Y., Murphy, J. A., Orlando, A., Schwarz, R., Sullivan, C. O., Piccirillo, L., Rajguru, N., Rusholme, B., Taylor, A. N., Thompson, K. L., Turner, A. H., Wu, E. Y. S., & Zemcov, M. "Second and Third Season QUaD Cosmic Microwave Background Temperature and Polarization Power Spectra." *ApJ*, **692**:1247–1270, 2009.

Radford, S. J. E. & Chamberlin, R. A. "Atmospheric Transparency at 225 GHz over Chajnantor, Mauna Kea, and the South Pole." Memo 334, Atacama Large Millimeter Array (ALMA), 2000.

Reese, E. D., Carlstrom, J. E., Joy, M., Mohr, J. J., Grego, L., & Holzapfel, W. L. "Determining the Cosmic Distance Scale from Interferometric Measurements of the Sunyaev-Zeldovich Effect." *ApJ*, **581**:53–85, 2002. (arXiv:astro-ph/0205350)

Reichardt, C. L., Ade, P. A. R., Bock, J. J., Bond, J. R., Brevik, J. A., Contaldi, C. R., Daub, M. D., Dempsey, J. T., Goldstein, J. H., Holzapfel, W. L., Kuo, C. L., Lange, A. E., Lueker, M., Newcomb, M., Peterson, J. B., Ruhl, J., Runyan, M. C., & Staniszewski, Z. "High-Resolution CMB Power Spectrum from the Complete ACBAR Data Set." *ApJ*, **694**:1200–1219, 2009a. (arXiv:0801.1491)

Reichardt, C. L., Zahn, O., Ade, P. A. R., Basu, K., Bender, A. N., Bertoldi, F., Cho, H. ., Chon, G., Dobbs, M., Ferrusca, D., Halverson, N. W., Holzapfel, W. L., Horellou, C., Johansson, D., Johnson, B. R., Kennedy, J., Kneissl, R., Lanting, T., Lee, A. T., Lueker, M., Mehl, J., Menten, K. M., Nord, M., Pacaud, F., Richards, P. L., Schaaf, R., Schwan, D., Spieler, H., Weiss, A., & Westbrook, B. "Constraints on the High-l Power Spectrum of Millimeter-wave Anisotropies from APEX-SZ." *ArXiv e-prints*, 2009b. (arXiv:0904.3939)

Reiprich, T. H. & Böhringer, H. "The Mass Function of an X-Ray Flux-limited Sample of Galaxy Clusters." *ApJ*, **567**:716–740, 2002. (arXiv:astro-ph/0111285)

Rephaeli, Y. "Cosmic microwave background comptonization by hot intracluster gas." *ApJ*, **445**:33–36, 1995.

Rex, M., Ade, P. A. R., Aretxaga, I., Bock, J. J., Chapin, E. L., Devlin, M. J., Dicker, S. R., Griffin, M., Gundersen, J. O., Halpern, M., Hargrave, P. C., Hughes, D. H., Klein, J., Marsden, G., Martin, P. G., Mauskopf, P., Netterfield, C. B., Olmi, L., Pascale, E., Patanchon, G., Scott, D., Semisch, C., Thomas, N., Truch, M. D. P., Tucker, C., Tucker, G. S., Viero, M. P., & Wiebe, D. V. "A Bright Submillimeter Source in the Bullet Cluster (1E0657–56) Field Detected with BLAST." *ArXiv e-prints*, 2009. (arXiv:0904.1203)

Rex, M., Chapin, E., Devlin, M. J., Gundersen, J., Klein, J., Pascale, E., & Wiebe, D. "BLAST autonomous daytime star cameras." In "Society of Photo-Optical Instrumentation Engineers (SPIE) Conference Series," volume 6269 of *Society of Photo-Optical Instrumentation Engineers (SPIE) Conference Series*. 2006.

Riess, A. G., Filippenko, A. V., Challis, P., Clocchiatti, A., Diercks, A., Garnavich, P. M., Gilliland, R. L., Hogan, C. J., Jha, S., Kirshner, R. P., Leibundgut, B., Phillips, M. M., Reiss, D., Schmidt, B. P., Schommer, R. A., Smith, R. C., Spyromilio, J., Stubbs, C., Suntzeff, N. B., & Tonry, J. "Observational Evidence from Supernovae for an Accelerating Universe and a Cosmological Constant." *AJ*, **116**:1009–1038, 1998. (arXiv:astro-ph/9805201)

Rohlfs, K. & Wilson, T. L. *Tools of Radio Astronomy*. Springer, 3rd edition, 1999.

Rose, J. A., Gaba, A. E., Christiansen, W. A., Davis, D. S., Caldwell, N., Hunstead, R. W., & Johnston-Hollitt, M. "Multiple Merging Events in the Double Cluster A3128/A3125." *AJ*, **123**:1216–1246, 2002. (arXiv:astro-ph/0112346)

Ruhl, J. E., Ade, P. A. R., Bock, J. J., Bond, J. R., Borrill, J., Boscaleri, A., Contaldi, C. R., Crill, B. P., de Bernardis, P., De Troia, G., Ganga, K., Giacometti, M., Hivon, E., Hristov, V. V., Iacoangeli, A., Jaffe, A. H., Jones, W. C., Lange, A. E., Masi, S., Mason, P., Mauskopf, P. D., Melchiorri, A., Montroy, T., Netterfield, C. B., Pascale, E., Piacentini, F., Pogosyan, D., Polenta, G., Prunet, S., & Romeo, G. "Improved Measurement of the Angular Power Spectrum of Temperature Anisotropy in the Cosmic Microwave Background from Two New Analyses of BOOMERANG Observations." *ApJ*, **599**:786–805, 2003. (arXiv:astro-ph/0212229)

Sachs, R. K. & Wolfe, A. M. "Perturbations of a Cosmological Model and Angular Variations of the Microwave Background." *ApJ*, **147**:73–+, 1967.

Saklatvala, G., Withington, S., & Hobson, M. P. "Simulations of astronomical imaging phased arrays." *Journal of the Optical Society of America A*, **25**:958–+, 2008. (arXiv:0709.0461)

Schroeder, D. J. *Astronomical Optics*. Academic Press, 2nd edition, 2000.

Schumaker, L. L. *Spline Functions: Basic Theory*. Cambridge University Press, 3rd edition, 2007.

Scott, P. F., Carreira, P., Cleary, K., Davies, R. D., Davis, R. J., Dickinson, C., Grainge, K., Gutiérrez, C. M., Hobson, M. P., Jones, M. E., Kneissl, R., Lasenby, A., Maisinger, K., Pooley, G. G., Rebolo, R., Rubiño-Martin, J. A., Sosa Molina, P. J., Rusholme, B., Saunders, R. D. E., Savage, R., Slosar, A., Taylor, A. C., Titterington, D., Waldram, E., Watson, R. A., & Wilkinson, A. "First results from the Very Small Array - III. The cosmic microwave background power spectrum." *MNRAS*, **341**:1076–1083, 2003. (arXiv:astro-ph/0205380)

Scoville, N., Aussel, H., Brusa, M., Capak, P., Carollo, C. M., Elvis, M., Giavalisco, M., Guzzo, L., Hasinger, G., Impey, C., Kneib, J.-P., LeFevre, O., Lilly, S. J., Mobasher, B., Renzini, A., Rich, R. M., Sanders, D. B., Schinnerer, E., Schminovich, D., Shopbell, P., Taniguchi, Y., & Tyson, N. D. “The Cosmic Evolution Survey (COSMOS): Overview.” *ApJS*, **172**:1–8, 2007. (arXiv:astro-ph/0612305)

Sehgal, N., Trac, H., Huffenberger, K., & Bode, P. “Microwave Sky Simulations and Projections for Galaxy Cluster Detection with the Atacama Cosmology Telescope.” *ApJ*, **664**:149–161, 2007. (arXiv:astro-ph/0612140)

Seidelmann, P. K., ed. *Explanatory Supplement to the Astronomical Almanac*. University Science Books, revised edition, 1992.

Seljak, U. “Gravitational Lensing Effect on Cosmic Microwave Background Anisotropies: A Power Spectrum Approach.” *ApJ*, **463**:1–+, 1996. (arXiv:astro-ph/9505109)

Sharp, M. K., Marrone, D. P., Carlstrom, J. E., Culverhouse, T., Greer, C., Hawkins, D., Hennessy, R., Joy, M., Lamb, J. W., Leitch, E. M., Loh, M., Miller, A., Mroczkowski, T., Muchovej, S., Pryke, C., & Woody, D. “A Measurement of Arcminute Anisotropy in the Cosmic Microwave Background with the Sunyaev-Zel’dovich Array.” *ArXiv e-prints*, 2009. (arXiv:0901.4342)

Shimon, M. & Rephaeli, Y. “Quantitative description of the Sunyaev-Zeldovich effect: analytic approximations.” *New Astronomy*, **9**:69–82, 2004. (arXiv:astro-ph/0309098)

Sievers, J. L., Mason, B. S., Weintraub, L., Achermann, C., Altamirano, P., Bond, J. R., Bronfman, L., Bustos, R., Contaldi, C., Dickinson, C., Jones, M. E., May, J., Myers, S. T., Oyarce, N., Padin, S., Pearson, T. J., Pospieszalski, M., Readhead, A. C. S., Reeves, R., Shepherd, M. C., Taylor, A. C., & Torres, S. “Cosmological Results from Five Years of 30 GHz CMB Intensity Measurements with the Cosmic Background Imager.” *ArXiv e-prints*, 2009. (arXiv:0901.4540)

Snellen, I. A. G., Schilizzi, R. T., de Bruyn, A. G., Miley, G. K., Rengelink, R. B., Roettgering, H. J., & Bremer, M. N. “A new sample of faint Gigahertz Peaked Spectrum radio sources.” *A&AS*, **131**:435–449, 1998. (arXiv:astro-ph/9803140)

Snyder, J. P. *Map Projections - A Working Manual*. U.S. Geological Survey Profesional Paper 1395. U.S. Geological Survey, 1987.

Staniszewski, Z., Ade, P. A. R., Aird, K. A., Benson, B. A., Bleem, L. E., Carlstrom, J. E., Chang, C. L., Cho, H. ., Crawford, T. M., Crites, A. T., de Haan, T., Dobbs, M. A., Halverson, N. W., Holder, G. P., Holzapfel, W. L., Hrubes, J. D., Joy, M., Keisler, R., Lanting, T. M., Lee, A. T., Leitch, E. M., Loehr, A., Lueker, M., McMahon, J. J., Mehl, J., Meyer, S. S., Mohr, J. J., Montroy, T. E., Ngeow, C. ., Padin, S., Plagge, T., Pryke, C., Reichardt, C. L., Ruhl, J. E., Schaffer, K. K., Shaw, L., Shirokoff, E., Spieler, H. G., Stalder, B., Stark, A. A., Vanderlinde, K., Vieira, J. D., Zahn, O., & Zenteno, A. “Galaxy clusters discovered with a Sunyaev-Zel’dovich effect survey.” *ArXiv e-prints*, 2008. (arXiv:0810.1578)

Sunyaev, R. A. & Zel’dovich, Y. B. “The Spectrum of Primordial Radiation, its Distortions and their Significance.” *Comments on Astrophysics and Space Physics*, **2**:66–+, 1970.

Sunyaev, R. A. & Zel’dovich, Y. B. “The Observations of Relic Radiation as a Test of the Nature of X-Ray Radiation from the Clusters of Galaxies.” *Comments on Astrophysics and Space Physics*, **4**:173–+, 1972.

Sutton, D., Johnson, B. R., Brown, M. L., Cabella, P., Ferreira, P. G., & Smith, K. M. “Map making in small field modulated CMB polarization experiments: approximating the maximum likelihood method.” *MNRAS*, **393**:894–910, 2009. (arXiv:0807.3658)

Swetz, D. S. *The Atacama Cosmology Telescope*. Ph.D. thesis, University of Pennsylvania, 2009.

Swetz, D. S., Ade, P. A. R., Allen, C., Amiri, M., Appel, J. W., Battistelli, E. S., Burger, B., Chervenak, J. A., Dahlen, A. J., Das, S., Denny, S., Devlin, M. J., Dicker, S. R., Doriese, W. B., Dünner, R., Essinger-Hileman, T., Fisher, R. P., Fowler, J. W., Gao, X., Hajian, A., Halpern, M., Hargrave, P. C., Hasselfield, M., Hilton, G. C., Hincks, A. D., Irwin, K. D., Jarosik, N., Kaul, M., Klein, J., Knotek, S., Lau, J. M., Limon, M., Lupton, R. H., Marriage, T. A., Martocci, K. L., Mauskopf, P., Moseley, S. H., Netterfield, C. B., Niemack, M. D., Nolta, M. R., Page, L., Parker, L. P., Reid, B. A., Reintsema, C. D., Sederberg, A. J., Sehgal, N., Sievers, J. L., Spergel, D. N., Staggs, S. T., Stryzak, O. R., Switzer, E. R., Thornton, R. J., Tucker, C., Wollack, E. J., & Zhao, Y. "Instrument design and characterization of the Millimeter Bolometer Array Camera on the Atacama Cosmology Telescope." In W. D. Duncan, W. S. Holland, S. Withington, & J. Zmuidzinas, eds., "Proc. SPIE," volume 7020, p. 702008. SPIE, 2008.

Switzer, E. R. *Small-Scale Anisotropies of the Cosmic Microwave Background: Experimental and Theoretical Perspectives*. Ph.D. thesis, Princeton University, United States, 2008.

Switzer, E. R., Allen, C., Amiri, M., Appel, J. W., Battistelli, E. S., Burger, B., Chervenak, J. A., Dahlen, A. J., Das, S., Devlin, M. J., Dicker, S. R., Doriese, W. B., Dünner, R., Essinger-Hileman, T., Gao, X., Halpern, M., Hasselfield, M., Hilton, G. C., Hincks, A. D., Irwin, K. D., Knotek, S., Fisher, R. P., Fowler, J. W., Jarosik, N., Kaul, M., Klein, J., Lau, J. M., Limon, M., Lupton, R. H., Marriage, T. A., Martocci, K. L., Moseley, S. H., Netterfield, C. B., Niemack, M. D., Nolta, M. R., Page, L., Parker, L. P., Reid, B. A., Reintsema, C. D., Sederberg, A. J., Sievers, J. L., Spergel, D. N., Staggs, S. T., Stryzak, O. R., Swetz, D. S., Thornton, R. J., Wollack, E. J., & Zhao, Y. "Systems and control software for the atacama cosmology telescope." In A. Bridger & N. M. Radziwill, eds., "Proc. SPIE," volume 7019, p. 70192L. SPIE, 2008.

Tegmark, M. "The Angular Power Spectrum of the Four-Year COBE Data." *ApJ*, **464**:L35+, 1996. (arXiv:astro-ph/9601077)

Tegmark, M. "CMB mapping experiments: A designer's guide." *Phys. Rev. D*, **56**:4514–4529, 1997. (arXiv:astro-ph/9705188)

Thornton, R. J., Ade, P. A. R., Allen, C., Amiri, M., Appel, J. W., Battistelli, E. S., Burger, B., Chervenak, J. A., Devlin, M. J., Dicker, S. R., Doriese, W. B., Essinger-Hileman, T., Fisher, R. P., Fowler, J. W., Halpern, M., Hargrave, P. C., Hasselfield, M., Hilton, G. C., Hincks, A. D., Irwin, K. D., Jarosik, N., Kaul, M., Klein, J., Lau, J. M., Limon, M., Marriage, T. A., Martocci, K. L., Mauskopf, P., Moseley, S. H., Niemack, M. D., Page, L., Parker, L. P., Reidel, J., Reintsema, C. D., Staggs, S. T., Stryzak, O. R., Swetz, D. S., Switzer, E. R., Tucker, C., Wollack, E. J., & Zhao, Y. "Opto-mechanical design and performance of a compact three-frequency camera for the millimeter bolometer array camera on the atacama cosmology telescope." In W. D. Duncan, W. S. Holland, S. Withington, & J. Zmuidzinas, eds., "Proc. SPIE," volume 7020, p. 70201R. SPIE, 2008.

Tristram, M., Patanchon, G., Macías-Pérez, J. F., Ade, P., Amblard, A., Ansari, R., Aubourg, É., Benoît, A., Bernard, J.-P., Blanchard, A., Bock, J. J., Bouchet, F. R., Bourrachot, A., Camus, P., Cardoso, J.-F., Couchot, F., de Bernardis, P., Delabrouille, J., Désert, F.-X., Douspis, M., Dumoulin, L., Filliatre, P., Fosalba, P., Giard, M., Giraud-Héraud, Y., Gispert, R., Guglielmi, L., Hamilton, J.-C., Hanany, S., Henrot-Versillé, S., Kaplan, J., Lagache, G., Lamarre, J.-M., Lange, A. E., Madet, K., Maffei, B., Magneville, C., Masi, S., Mayet, F., Nati, F., Perdereau, O., Plaszczynski, S., Piat, M., Ponthieu, N., Prunet, S., Renault, C., Rosset, C., Santos, D., Vibert, D., & Yvon, D. "The CMB temperature power spectrum from an improved analysis of the Archeops data." *A&A*, **436**:785–797, 2005. (arXiv:astro-ph/0411633)

Tucker, W., Blanco, P., Rappoport, S., David, L., Fabricant, D., Falco, E. E., Forman, W., Dressler, A., & Ramella, M. "1E 0657-56: A Contender for the Hottest Known Cluster of Galaxies." *ApJ*, **496**:L5+, 1998. (arXiv:astro-ph/9801120)

Umetsu, K., Birkinshaw, M., Liu, G.-C., Wu, J.-H. P., Medezinski, E., Broadhurst, T., Lemze, D., Zitrin, A., Ho, P. T. P., Huang, C.-W. L., Koch, P. M., Liao, Y.-W., Lin, K.-Y., Molnar, S. M., Nishioka, H., Wang, F.-C., Altamirano, P., Chang, C.-H., Chang, S.-H., Chang, S.-W., Chen, M.-T., Han, C.-C., Huang, Y.-D., Hwang, Y.-J., Jiang, H., Kesteven, M., Kubo, D. Y., Li, C.-T., Martin-Cocher, P., Oshiro, P., Raffin, P., Wei, T., & Wilson, W. "Mass and Hot Baryons in Massive Galaxy Clusters from Subaru Weak-Lensing and AMiBA Sunyaev-Zel'Dovich Effect Observations." *ApJ*, **694**:1643–1663, 2009. (arXiv:0810.0969)

Voges, W., Aschenbach, B., Boller, T., Bräuninger, H., Briel, U., Burkert, W., Dennerl, K., Englhauser, J., Gruber, R., Haberl, F., Hartner, G., Hasinger, G., Kürster, M., Pfeffermann, E., Pietsch, W., Predehl, P., Rosso, C., Schmitt, J. H. M. M., Trümper, J., & Zimmermann, H. U. "The ROSAT all-sky survey bright source catalogue." *A&A*, **349**:389–405, 1999. (arXiv:astro-ph/9909315)

Weinberg, S. *Gravitation and Cosmology: Principles and Applications of the General Theory of Relativity*. Wiley, 1972.

Weinberg, S. *Cosmology*. Oxford University Press, USA, 2008. ISBN 0198526822.

Werner, N., Churazov, E., Finoguenov, A., Markevitch, M., Burenin, R., Kaastra, J. S., & Böhringer, H. "Complex X-ray morphology of Abell 3128: a distant cluster behind a disturbed cluster." *A&A*, **474**:707–716, 2007. (arXiv:0708.3253)

White, M. "Contribution of long-wavelength gravitational waves to the cosmic microwave background anisotropy." *Phys. Rev. D*, **46**:4198–4205, 1992. (arXiv:hep-ph/9207239)

White, M. & Srednicki, M. "Window functions of cosmic microwave background experiments." *ApJ*, **443**:6–10, 1995. (arXiv:astro-ph/9402037)

White, S. D. M., Navarro, J. F., Evrard, A. E., & Frenk, C. S. "The baryon content of galaxy clusters: a challenge to cosmological orthodoxy." *Nature*, **366**:429–433, 1993.

Wilson, G. W., Hughes, D., Aretxaga, I., Ezawa, H., Austermann, J. E., Doyle, S., Ferrusca, D., Hernandez-Curiel, I., Kawabe, R., Kitayama, T., Kohno, K., Kuboi, A., Matsuo, H., Mauskopf, P. D., Murakoshi, Y., Montana, A., Natarajan, P., Oshima, T., Ota, N., Perera, T., Rand, J., Scott, K. S., Tanaka, K., Tsuboi, M., Williams, C. C., Yamaguchi, N., & Yun, M. S. "A bright, dust-obscured, millimeter-selected galaxy beyond the Bullet Cluster (1E0657-56)." *ArXiv e-prints*, 2008. (arXiv:0803.3462)

Withington, S., Saklatvala, G., & Hobson, M. P. "Theoretical Analysis of Astronomical Phased Arrays." *ArXiv e-prints*, 2007. (arXiv:0707.1580)

Wright, A. E., Griffith, M. R., Burke, B. F., & Ekers, R. D. "The Parkes-MIT-NRAO (PMN) surveys. 2: Source catalog for the southern survey (delta greater than -87.5 deg and less than -37 deg)." *ApJS*, **91**:111–308, 1994.

Wright, E. L. "Dark Flow Detected — Not!", 2008. http://www.astro.ucla.edu/∼wright/dark-flow-errors.html. Retrieved 25 July 2009

Wright, E. L., Chen, X., Odegard, N., Bennett, C. L., Hill, R. S., Hinshaw, G., Jarosik, N., Komatsu, E., Nolta, M. R., Page, L., Spergel, D. N., Weiland, J. L., Wollack, E., Dunkley, J., Gold, B., Halpern, M., Kogut, A., Larson, D., Limon, M., Meyer, S. S., & Tucker, G. S. "Five-Year Wilkinson Microwave Anisotropy Probe Observations: Source Catalog." *ApJS*, **180**:283–295, 2009. (arXiv:0803.0577)

Zhang, Y.-Y., Böhringer, H., Finoguenov, A., Ikebe, Y., Matsushita, K., Schuecker, P., Guzzo, L., & Collins, C. A. "X-ray properties in massive galaxy clusters: XMM-Newton observations of the REFLEX-DXL sample." *A&A*, **456**:55–74, 2006. (arXiv:astro-ph/0603275)

Zhang, Y.-Y., Finoguenov, A., Böhringer, H., Kneib, J.-P., Smith, G. P., Kneissl, R., Okabe, N., & Dahle, H. "LoCuSS: comparison of observed X-ray and lensing galaxy cluster scaling relations with simulations." *A&A*, **482**:451–472, 2008. (arXiv:0802.0770)

Zhao, Y., Allen, C., Amiri, M., Appel, J. W., Battistelli, E. S., Burger, B., Chervenak, J. A., Dahlen, A. J., Denny, S., Devlin, M. J., Dicker, S. R., Doriese, W. B., Dünner, R., Essinger-Hileman, T., Fisher, R. P., Fowler, J. W., Halpern, M., Hilton, G. C., Hincks, A. D., Irwin, K. D., Jarosik, N., Klein, J., Lau, J. M., Marriage, T. A., Martocci, K. L., Moseley, S. H., Niemack, M. D., Page, L., Parker, L. P., Sederberg, A., Staggs, S. T., Stryzak, O. R., Swetz, D. S., Switzer, E. R., Thornton, R. J., & Wollack, E. J. "Characterization of transition edge sensors for the millimeter bolometer array camera on the atacama cosmology telescope." In W. D. Duncan, W. S. Holland, S. Withington, & J. Zmuidzinas, eds., "Proc. SPIE," volume 7020, p. 70200O. SPIE, 2008.